

Particulate wear debris of coated lightweight disc brakes

Asmawi Bin Sanuddin

Submitted in accordance with the requirements for the degree of
Doctor of Philosophy

The University of Leeds
School of Mechanical Engineering

November, 2020

The candidate confirms that the work submitted is his/her own, except where work which has formed part of jointly-authored publications has been included. The contribution of the candidate and the other authors to this work has been explicitly indicated below. The candidate confirms that appropriate credit has been given within the thesis where reference has been made to the work of others.

Paper	Chapter
A. B. Sanuddin, S. Kosarieh, C. A. Gilkeson, P. C. Brooks and D. C. Barton, " Design and assessment of a test rig for airborne brake wear debris measurements", Proceedings of the Eurobrake 2019 Conference, Paper EB2019-MDS-005. EuroBrake 2019, Dresden, Germany, 2019.	Ch. 1, 2, 3 and 4
A. B. Sanuddin, S. Kosarieh, C. A. Gilkeson, P. C. Brooks and D. C. Barton, "Airflow Simulation and Measurement of Brake Wear Particle Emissions with a Novel Test Rig", Journal of Engineering, 2020.	Ch. 1, 2, 3, 4 and 5

The candidate undertook major tasks of the work presented in these published papers, such as undertaking experimental works, design, analysing and presenting the results. The co-authors reviewed all aspects of the publication and provided comments.

This copy has been supplied on the understanding that it is copyright material and that no quotation from the thesis may be published without proper acknowledgement.

The right of Asmawi Bin Sanuddin to be identified as Author of this work has been asserted by him in accordance with the Copyright, Designs and Patents Act 1988.

© 2020 The University of Leeds and Asmawi Bin Sanuddin

Acknowledgements

First of all, I would like to express my deep and sincere thanks to my supervisor, Professor David Barton for his valuable guidance and support throughout this PhD work. I have been very fortunate to work under his supervision. His motivation, encouragement, advice and patience during the preparation of this thesis are greatly appreciated.

I am highly grateful to my co-supervisors Dr. Peter Brooks, Dr. Shahriar Kosarieh and Dr. Carl Gilkeson for all the help during my PhD research and believed in me more than I did myself. Their support and encouragement kept me motivated to complete this work. I also wish to sincerely thank the technical staff, Mr. Tony Weise for his technical support and for being a great friend.

I would like to express my deepest gratitude to Professor Suman Shrestha from Keronite International Ltd for giving me an overview of the Plasma Electrolytic Oxidation process. His gracious hospitality during my visit to the Keronite was absolutely breathtaking. Also, I would like to thank TMD Friction Ltd and the Keronite for providing me with the materials used in this project.

Special thanks to the Ministry of Higher Education Malaysia and Universiti Malaysia Perlis for their financial support throughout my study.

I am grateful to all my friends for their continuous moral support and sharing experiences, knowledge and advice.

Finally, I would like to express my most heartfelt gratitude to my family in Malaysia for their infinite love and support.

Abstract

Stringent regulations on exhaust emissions (e.g. Regulation (EC) No 443/2009) have put automotive companies under tremendous pressure to improve vehicle fuel economy and reduce the carbon dioxide emissions. The use of lightweight disc brake rotors is one of the solutions to meet this legislative requirement. Due to significant reductions in exhaust emissions, the proportion of non-exhaust emissions has increased in recent years. Airborne brake wear emissions are the major contributor to the non-exhaust emissions and they can adversely affect human health and the environment (Grigoratos and Martini, 2015). In this study, the performance of conventional grey cast iron (GCI) and novel Plasma Electrolytic Oxidation Aluminium (PEO-Al) rotors with regard to particle size and mass distribution, morphology and chemical composition was investigated and characterised for comparison purposes.

Experiments were conducted using a newly developed test rig which was based upon the existing Leeds full-scale disc brake dynamometer. The brake head of the dynamometer was enclosed and a ducting system was used to supply clean air from the laboratory and exhaust it to the outside environment. A sampling probe in the outlet duct was connected to a Dekati ELPI®+ Electrical Low Pressure Impactor to collect and measure airborne particles in different size ranges from 10 µm down to the nano-particle range. Computational Fluid Dynamics (CFD) simulations were performed to predict airflow behaviour within the brake enclosure and in the vicinity of the sampling point. The CFD results suggested good evacuation of brake wear particles from the enclosure and a near uniform air flow regime in the outlet duct near the sampling probe.

Both GCI and PEO-Al brake rotors were tested under steady-state drag brake test conditions. Braking test parameters of sliding speed, hydraulic pressure, rotor surface temperature and coefficient of friction were monitored during the tests for each rotor material. Hydraulic pressures of 5, 10 and 15 bar at 135 rpm rotational speed were selected as three typical braking test conditions to be studied. Measurement of brake wear emissions was carried out using the Dekati ELPI®+ along with an isokinetically designed sampling probe.

Generally, the coefficient of friction measured during steady-state conditions was greater for the GCI rotor (0.43-0.49) as compared to the PEO-Al rotor (0.25-0.28). However, the ELPI®+ results showed that the PEO-Al rotor tended to produce lower wear debris particle emissions than the conventional GCI rotor in the critical size range of 1 µm – 10 µm especially under low applied pressures. Based on SEM-EDX analysis, the percentage of Fe in the PEO-Al debris was about threefold lower than that from the GCI rotor. This is an important result given the reported link between sub-micron airborne particles containing Fe and its oxides with neurological diseases such as Alzheimer's.

Table of Contents

Acknowledgements	ii
Abstract	iii
Table of Contents	iv
List of Figures	viii
List of Tables	xv
Nomenclature	xvii
Abbreviations	xix
Chapter 1 : Introduction	1
1.1 Background and rationale.....	1
1.2 Aim and objectives	5
1.3 Thesis outline	6
Chapter 2 : Literature review	8
2.1 Overview	8
2.2 Introduction to automotive disc brakes	8
2.3 Materials for disc brake friction pairs	10
2.3.1 Brake rotor materials	10
2.3.2 Brake pad materials	14
2.4 Particulate matter	16
2.4.1 Particle size concept	16
2.4.2 Particulate matter basics.....	18
2.4.3 Air quality standards.....	19
2.4.4 Effect of particulate matters.....	21
2.4.5 Traffic-related particulate matter	23
2.4.6 Brake wear particle emissions.....	26
2.4.6.1 Particle mass distribution.....	27
2.4.6.2 Particle number distribution	29
2.4.6.3 Chemical characterisation	31
2.5 Measurements of brake wear particle emissions.....	34
2.5.1 Brake testing assembly	35
2.5.2 Braking test cycle	37
2.6 Particle instruments	39
2.6.1 Introduction to inertial classifiers	39
2.6.2 Dekati Electrical Low Pressure Impactor.....	41

2.7	Isokinetic sampling principle.....	43
2.8	Characterisation tools.....	45
2.9	Keronite PEO surface treatment technology	46
2.10	Applications of Computational Fluid Dynamics in braking simulations	48
2.11	Summary	49
Chapter 3 : Materials and experimental methods		51
3.1	Introduction.....	51
3.2	Disc brake pair materials.....	51
3.3	Remanufacture of the PEO-Al rotor.....	53
3.3.1	Preparation of Al rotor for PEO treatment (surface masking)	53
3.3.2	PEO surface treatment process	55
3.4	Brake Dynamometer.....	57
3.5	Measurement of the brake rotor runout and thickness variation.....	59
3.5.1	Brake rotor thickness variation	59
3.5.2	Brake rotor runout	61
3.6	Extraction and particle capture system.....	64
3.7	Airflow velocity calibration	67
3.8	Design of sampling probe.....	68
3.9	Test procedures	71
3.9.1	Bedding-in process	71
3.9.2	Preliminary dynamometer test.....	72
3.9.3	Airborne brake wear particle measurement and debris collection	73
3.10	Impactor and charger cleaning.....	75
3.11	Gravimetric analysis	77
3.12	Brake wear particle characterisation.....	79
3.13	Summary	80
Chapter 4 : Particulate sampling method: guidance using computational fluid dynamics		81
4.1	Introduction.....	81
4.2	Mathematical modelling.....	82
4.2.1	Governing equations	82
4.2.2	Reynolds number	83
4.2.3	Turbulence models.....	84

4.3	Numerical simulations of airflow in the extraction system.....	85
4.3.1	Geometry and boundary conditions	85
4.3.2	Mesh generation and solver settings.....	87
4.3.3	General flow behaviour	92
4.3.4	Validation	94
4.4	Numerical simulations of airflow in the sampling probe.....	97
4.4.1	Geometry and boundary conditions	97
4.4.2	Mesh generation and solver settings.....	98
4.4.3	General flow behaviour	99
4.5	Summary	101
Chapter 5 : Results for grey cast iron rotor		102
5.1	Introduction.....	102
5.2	Brake dynamometer tests.....	102
5.2.1	Preliminary tests.....	102
5.2.2	Repeatability tests.....	104
5.3	Particulate matter measurement	106
5.3.1	Background measurement	106
5.3.2	Brake wear emission measurement	106
5.3.2.1	Real-time particle measurement.....	107
5.3.2.2	Particle number distribution	109
5.3.2.3	Particle mass distribution.....	110
5.3.2.4	Airborne particulate matter classification	112
5.4	Gravimetric analysis	113
5.5	Microstructural analysis	116
5.6	Elemental composition evaluation	124
5.6.1	EDX mapping analysis for the blank PC foil.....	124
5.6.2	EDX mapping analysis for the collected particles.....	124
5.6.3	Elemental weight percentage comparisons.....	135
5.6.4	EDX mapping analysis for the brake pad	136
5.7	Summary	138
Chapter 6 : Results for PEO-treated lightweight aluminium alloy rotor		140
6.1	Introduction.....	140
6.2	Brake dynamometer tests.....	140

6.2.1	Preliminary tests.....	140
6.2.2	Repeatability tests.....	142
6.3	Brake wear emission measurement	143
6.3.1	Real-time particle measurement	143
6.3.2	Particle number distribution.....	145
6.3.3	Particle mass distribution	147
6.3.4	Airborne particulate matter classification.....	149
6.4	Microstructural analysis.....	150
6.5	Elemental composition evaluation	155
6.5.1	EDX analysis for the collected particles	155
6.5.2	Elemental weight percentage comparisons.....	159
6.5.3	EDX analysis for the brake pad.....	161
6.6	Summary	163
Chapter 7 : Discussion		165
7.1	Introduction.....	165
7.2	Friction performance and temperature	165
7.3	Brake wear emission measurement	169
7.3.1	Real-time particle measurements.....	169
7.3.2	Typical particle number distributions	171
7.3.3	Typical particle mass distributions.....	172
7.3.4	Overall average particulate number and mass distributions	174
7.4	Post-test PM characterisation.....	175
7.4.1	Microstructural analysis.....	175
7.4.2	Elemental composition evaluation.....	176
7.5	Health relevance of brake wear particles.....	178
7.6	Evaluations of current methodology	179
7.7	Overall assessment of GCI and PEO-Al rotors.....	181
Chapter 8 : Conclusions and future work.....		183
8.1	Conclusions.....	183
8.2	Suggestions for future work.....	187
References.....		189
Appendix A.....		198
Appendix B.....		199

List of Figures

Figure 2.1: A graphical representation of automotive braking system (Post, 2014).	10
Figure 2.2: Typical (a) drum (Akebono, 2020) and (b) disc brake systems (Wahlström, 2009).	10
Figure 2.3: Illustration of equivalent particle diameters.	17
Figure 2.4: Relative size of particulate matter (USEPA, 2018).....	19
Figure 2.5: Example of how the Andersen cascade impactor simulates the human respiratory system (Andrade-Lima et al., 2012).	22
Figure 2.6: UK emissions of (a) PM ₁₀ and (b) PM _{2.5} from road transport (DEFRA, 2019a).	25
Figure 2.7: Particle mass distribution of brake abrasion dust for different braking temperatures (Iijima et al., 2007).....	29
Figure 2.8: Example of SEM images showing particle features at different size intervals (Verma et al., 2016).	33
Figure 2.9: Example of EDS spectra at different particle size intervals (Verma et al., 2016).	33
Figure 2.10: Schematic representation of brake testing assemblies: [top (Iijima et al., 2008) and bottom (Hagino et al., 2016)].	36
Figure 2.11: Schematic illustration of a traditional impactor (Dekati, 2016).	40
Figure 2.12: (a) Actual photo and (a) schematic diagram of the ELPI®+ units (Dekati, 2016).	41
Figure 2.13: an impactor stage of the Dekati ELPI®+ (Dekati, 2016).	42
Figure 2.14: Schematics of a thin-walled sampling probe.....	43
Figure 2.15: Schematic diagram of isokinetic particle sampling (Welker, 2012).	44
Figure 2.16: SEM micrographs of an as-prepared surface of (a) Keronite and (b) hard-anodised coatings (Shrestha and Dunn, 2007).	48

Figure 3.1: (a) GCI and (b) PEO-Al brake rotors with its corresponding brake pad.....	52
Figure 3.2: Brake rotor components, (a) outboard cheek, (b) inboard cheek and (c) inner ring.....	53
Figure 3.3: Two halves of the rotor in a) machined, b) polished, c) tape-covered and d) masked conditions.	55
Figure 3.4: Jigs installation on the two halves of the rotor.	56
Figure 3.5: Two halves of the rotor (a) at the beginning of the PEO process, (b) after some time of the PEO process, (c) before de-masking and (d) after de-masking.	57
Figure 3.6: General layout of the full scale disc brake dynamometer (Alnaqi, 2014).	58
Figure 3.7: Measured point on the rubbing surface of the PEO-Al rotor (left) and GCI rotor (right).....	60
Figure 3.8: (a) adapter set-up on the dynamometer and measurements of PEO-Al rotor runout on (b) top hat, (c) rotor inner and (d) rotor outer edges.....	61
Figure 3.9: Runout of the PEO-Al rotor at the three different locations (without addition of shims).	63
Figure 3.10: Runout of the PEO-Al rotor with and without the addition of shims.	64
Figure 3.11: Photographs of the dynamometer extraction system.....	66
Figure 3.12: (a) an anemometer mounting on the duct and (b) an image of the fan speed control.	68
Figure 3.13: Mean value of the average velocity for the three readings at each fan setting.	68
Figure 3.14: Full dimensions of the sampling probe (not to scale).....	70
Figure 3.15: An assembled view of fitting elements for the sampling probe on the duct (a) 2D drawing and (b) actual installation.....	71

Figure 3.16: Conditions of the PEO-Al rotor rubbing surface.	72
Figure 3.17: Example of the greased PC foils secured on the collection plates.	74
Figure 3.18: Impactor and charger cleaning procedures: (a) disassembling impactor parts, (b) cleaning parts in the bath, (c) drying the charger and impactor parts and (d) assembling all parts.	76
Figure 3.19: Weighing procedure for airborne brake wear particles: (a) samples storing and labelling, (b) particles collection on the foils and (c) samples weighing in the balance.	78
Figure 3.20: Samples preparation and positioning inside the SEM and EDX instrument.	79
Figure 4.1: 3D model of the brake dynamometer extraction system from various orientations (all units in mm).	87
Figure 4.2: A typical computational grid filling the fluid volume in the brake dynamometer extraction system.	90
Figure 4.3: Velocity profiles at tapping 4 for various CFD meshes.	91
Figure 4.4: Air pathlines in the dynamometer extraction system.	93
Figure 4.5: Resultant velocity contours viewed from above at five key locations.	93
Figure 4.6: Radial velocity profile at the velocity test point (VTP) and four tappings of the duct.	94
Figure 4.7: Plan view inside the outlet duct in a plane coincident with the velocity test points.	95
Figure 4.8: Velocity contours (m/s) at the velocity test cross-section.	96
Figure 4.9: Velocity profiles from the experimental and simulation studies.	97
Figure 4.10: 3D schematic of the sampling probe flow simulation.	98
Figure 4.11: 3D domain of the probe flow simulation with computational grid.	99

Figure 4.12: Velocity magnitude contours in a vertical slice of the domain (right) including a close-up view at the nozzle inlet (left).....	100
Figure 4.13: Velocity profile at the inlet of the sampling probe.....	100
Figure 5.1: Position of the thermocouple at the leading side of the brake rotor.	105
Figure 5.2: Rotor temperature variation with time for the three tests at each braking condition.....	105
Figure 5.3: Comparison of particle concentrations in the laboratory and ducting system environments.	106
Figure 5.4: Particle concentration variation with time for three different pressures.	108
Figure 5.5: Particle concentration variation with time for the three tests of P10.	108
Figure 5.6: Particle number distribution measurements for (a) background and (b-d) brake application at 5, 10 & 15 bar hydraulic pressure, respectively.....	110
Figure 5.7: Mass distribution measurements for (a) background and (b-d) brake application at 5, 10 & 15 bar hydraulic pressure, respectively.	111
Figure 5.8: Brake wear emissions of $PM_{0.1}$, $PM_{2.5}$ and PM_{10} based on average (a) particle number and (b) particle mass concentrations.	113
Figure 5.9: Particle mass distributions for (a) test P05D, (b) test P10D and (c) test P15D.....	116
Figure 5.10: PC foil position on the bottom of the enclosure.....	117
Figure 5.11: Rotor temperature variation with time for the three braking conditions during particle collections.	118
Figure 5.12: Brake wear particles collected on polycarbonate foils for the corresponding stage number.	118
Figure 5.13: Micrographs for the test P05E.	120
Figure 5.14: Micrographs for the test P10E.	121

Figure 5.15: Micrographs for the test P15E.	122
Figure 5.16: Micrographs of the collected particles on the bottom of the enclosure at 3000x magnifications for (a) test P05E, (b) test P10E and (c) test P15E.....	123
Figure 5.17: EDX images and elemental weight percentages of the greased PC foil.	126
Figure 5.18: An illustration of the examined area within a dark spot on a PC foil.	127
Figure 5.19: EDX map images for the test P05E.	128
Figure 5.20: EDX map images for the test P10E.	129
Figure 5.21: EDX map images for the test P15E.	130
Figure 5.22: EDX spectrum for the corresponding test.	131
Figure 5.23: Weight percentage of elements for the test P05E.....	132
Figure 5.24: Weight percentage of elements for the test P10E.....	133
Figure 5.25: Weight percentage of elements for the test P15E.....	134
Figure 5.26: Comparison of elemental percentages by weight for the three conditions (a) Fe, (b) Ba, (c) Cr, (d) Ca, (e) S and (f) Si.	135
Figure 5.27: EDX images and elemental weight percentages of the brake pad.....	137
Figure 6.1: Rotor temperature variation with time for the two brake conditions.....	141
Figure 6.2: Rotor temperature variation with time for the two brake conditions.....	142
Figure 6.3: Particle number concentration variation with time for two different pressures.	144
Figure 6.4: Particle number concentration variation with time for the three tests at 10 bar pressure.	144

Figure 6.5: Particle number distribution measurements for (a & c) background and (b & d) brake application at 5 & 10 bar hydraulic pressure, respectively.	146
Figure 6.6: Particle number distribution measurements for the brake application at (a-c) 5 bar and (d-f) 10 bar hydraulic pressure.	147
Figure 6.7: Particle mass distribution measurements for (a & c) background and (b & d) brake application at 5 & 10 bar hydraulic pressure, respectively.	148
Figure 6.8: Particle mass distribution measurements for the brake application at (a-c) 5 bar and (d-f) 10 bar hydraulic pressure.	149
Figure 6.9: Brake wear emissions of PM _{0.1} , PM _{2.5} and PM ₁₀ based on average (a) particle number and (b) particle mass concentrations. ...	150
Figure 6.10: PC foil position on the bottom of the enclosure.	151
Figure 6.11: Rotor temperature variation with time for the two brake conditions during particle collections.	151
Figure 6.12: Micrographs for the test P05J.	153
Figure 6.13: Micrographs for the test P10J.	154
Figure 6.14: Micrographs of the collected particles on the bottom of the enclosure at 3000x magnifications for (a) test P05J and (b) test P10J.	155
Figure 6.15: EDX spectrum at stage 12 for the two brake conditions.	156
Figure 6.16: Weight percentage of elements for the test P05J.	158
Figure 6.17: Weight percentage of elements for the test P10J.	159
Figure 6.18: Comparison of elemental percentages by weight for the two conditions (a) Fe, (b) Cu, (c) Cr, (d) Ca, (e) S (f) Si, (g) Al and (h) Mg.	160
Figure 6.19: EDX images and elemental weight percentages of the brake pad.	162

Figure 7.1: Temporal changes in the coefficient of friction for the two brake rotor materials at (a) 5 and (b) 10 bar brake pressures.	167
Figure 7.2: Rotor temperature variation with time for the two brake rotor materials at (a) 5 and (b) 10 bar brake pressures.	168
Figure 7.3: Particle number concentration variation with time at (a) 5 bar and (b) 10 bar brake pressures for the two brake rotors studied within the particle size range of 0.383 to 10 μm	171
Figure 7.4: Particle number distribution measurements during brake application for (a & c) GCI and (b & d) PEO-Al rotors at the corresponding 5 & 10 bar hydraulic pressures.	172
Figure 7.5: Particle mass distribution measurements during brake application for (a & c) GCI and (b & d) PEO-Al rotors at the corresponding 5 & 10 bar hydraulic pressures.	173
Figure 7.6: Brake wear emissions of $\text{PM}_{0.1}$, $\text{PM}_{2.5}$ and PM_{10} based on average (a & b) particle number and (c & d) particle mass concentrations for the two brake rotor materials.	175
Figure 7.7: Comparison of elemental percentages by weight for two brake rotor materials at 5 and 10 bar brake pressures (a & b) Fe, (c & d) Al and (e & f) S.	177
Figure 7.8: Comparison of weight percentages for two different elements, (a) Ba and (b) Al at 5 and 10 bar brake pressures.	178

List of Tables

Table 2.1: Physical properties of brake rotor materials (Barton, 2011; Hussain, 2018).....	14
Table 2.2: Possible composition of a brake pad (Chan and Stachowiak, 2004; Xiao et al., 2016; Grigoratos and Martini, 2015).	15
Table 2.3: A typical composition of an NAO brake pad (Barton, 2011).	16
Table 2.4: Air quality standards for PM _{2.5} and PM ₁₀	20
Table 2.5: Bandings of air pollution level for PM _{2.5} and PM ₁₀ (DEFRA, 2019b).....	21
Table 2.6: Health advice and recommended actions (DEFRA, 2019b).	21
Table 2.7: Summary of literature studies regarding airborne particle mass size distributions. Adapted from Grigoratos and Martini (2015).	28
Table 2.8: Summary of literature studies regarding airborne particle number size distributions. Adapted from Grigoratos and Martini (2015).	30
Table 2.9: Potential test cycle for brake emission measurement (Alemani et al., 2014).....	38
Table 2.10: Selected list of commercially available impactors (Marple and Olson, 2011).	40
Table 2.11: Typical process parameters for Keronite PEO process (Shrestha and Dunn, 2007).	47
Table 3.1: Ra values for the two halves of the rotor in μm	54
Table 3.2: Rotor thickness variation for PEO-Al and GCI rotors.	60
Table 3.3: The possible value of the internal diameter of the probe.....	69
Table 3.4: Test parameters for the bedding-in process.....	72
Table 4.1: Skewness comparison for the model with different element counts.	89
Table 5.1: Steady-state rotor temperature ($^{\circ}\text{C}$) at each condition.	104
Table 5.2: Three braking conditions for subsequent tests.....	104

Table 5.3: Mass concentration calculation for the test P05D.	114
Table 5.4: Mass concentration calculation for the test P10D.	114
Table 5.5: Mass concentration calculation for the test P15D.	115
Table 6.1: Two brake conditions for subsequent tests.	141

Nomenclature

V_s	Settling velocity	[cm/s]
D_p	Particle diameter	[μm]
ρ_p	Particle density	[g/cm ³]
\dot{V}	Airflow rate	[m ³ /s]
v	Mean velocity	[m/s]
u	Local velocity components of flow in the x-direction	[m/s]
v	Local velocity components of flow in the y-direction	[m/s]
w	Local velocity components of flow in the z-direction	[m/s]
ρ	Fluid density	[kg/m ³]
p	Static pressure	[N/m ²]
t	Time	[s]
μ	Dynamic viscosity	[kg/ms]
T	Absolute temperature	[K]
λ	Thermal conductivity	[W/mK]
C_p	Specific heat capacity of the fluid	[J/kgK]
M	Mach number	[---]
Re	Reynolds number	[---]
D	Internal diameter of the pipe	[m]
V_{avg}	Average velocity of the fluid	[m/s]
k	Turbulent kinetic energy	[J/kg]
ε	Dissipation rate of turbulence	[J/kgs]
ν_T	Eddy viscosity	[m ² /s]
P	Production term	[J/kgs]
C_μ	Turbulence model constant	[---]
σ_k	Turbulence model constant	[---]
σ_ε	Turbulence model constant	[---]

$C_{\varepsilon 1}$	Turbulence model constant	[---]
$C_{\varepsilon 2}$	Turbulence model constant	[---]
D_H	Hydraulic diameter	[m]
I	Turbulent intensity	[---]
U	Inlet fluid velocity	[m/s]
y	The first layer thickness	[m]
y^+	Non-dimensional parameter	[---]
τ_w	Wall shear stress	[N/m ²]
W_1	Initial mass	[mg]
W_2	Final mass	[mg]
ΔC	Mass concentration	[mg/m ³]

Abbreviations

Al	Aluminium
Al-MMC	Aluminium Metal Matrix Composite
Al ₂ O ₃	Alumina
APS	Aerodynamic Particle Sizer Spectrometer
Ba	Barium
BaSO ₄	Barium Sulphate
Bi	Bismuth
BLPI	Berner Low Pressure Impactor
BNC	Bayonet Neill-Concelman
Br	Bromine
BSPT	British Standard Pipe Taper
C	Carbon
Ca	Calcium
CaCO ₃	Calcium Carbonate
CAD	Computer-Aided Design
CFD	Computational Fluid Dynamics
Cl	Chlorine
CMC	Carbon Reinforced Ceramic Matrix Composite
Co	Cobalt
COF	Coefficient of Friction
Cr	Chromium
Cr ₂ O ₃	Chromium Oxide
Cu	Copper
CuSO ₄	Copper Sulphate

CO ₂	Carbon Dioxide
DAQI	Daily Air Quality Index
DC	Direct Current
DEFRA	Department for Environment Food and Rural Affairs
DOE	Design of Experiments
EDS	X-Ray Energy Dispersive Spectrometer
EDX	Energy-Dispersive X-ray
EEA	European Environment Agency
ELPI	Electrical Low Pressure Impactor
Fe	Iron
FEA	Finite Element Analysis
FeO	Iron(II) Oxide
Fe ₂ O ₃	Iron(III) Oxide
Fe ₃ O ₄	Iron(II,III) Oxide
FMPS	Fast Mobility Particle Sizer
GCI	Grey Cast Iron
HEPA	High-Efficiency Particulate Air
Hg	Mercury
HV	High Voltage
ICP-AES	Inductively Coupled Plasma Atomic Emission Spectroscopy
ICP-MS	Inductively Coupled Plasma Mass Spectrometry
JASO	Japanese Automotive Standards Organization
K	Potassium
KNO ₂	Potassium Nitrite
LM	Low Metallic

LPI	Low Pressure Impactor
Mg	Magnesium
MgO	Magnesium Oxide
Mn	Manganese
MO	Molybdenum
MOT	Maximum Operating Temperature
MOULD	Micro-Orifice Uniform Deposit Impactor
Na	Sodium
NAO	Non-Asbestos Organic
Ni	Nickel
NO ₂	Nitrogen Dioxide
NPT	National Pipe Thread
O	Oxygen
O ₃	Ozone
OPS	Optical Particle Sizer
P	Phosphorus
PC	Polycarbonate
PEO	Plasma Electrolytic Oxidation
PEO-Al	PEO-Treated Lightweight Aluminium Alloy
Pb	Lead
Pd	Palladium
PM	Particulate Matter
RANS	Reynolds Averaged Navier Stokes
RTV	Rotor Thickness Variation
S	Sulphur
SAE	Society of Automotive Engineering

Sb	Antimony
Se	Selenium
SEM	Scanning Electron Microscope
Si	Silicon
SiC	Silicon Carbide
SM	Semi-Metallic
SMPS	Scanning Mobility Particle Sizer
Sn	Tin
SnSO ₄	Tin Sulphate
SO ₂	Sulphur Dioxide
Sr	Strontium
SST	Menter Shear Stress Transport
Tb	Terbium
TEM	Transmission Electron Microscope
Ti	Titanium
V	Vanadium
VTP	Velocity Test Point
W	Tungsten
WHO	World Health Organization
WLTP	Worldwide Harmonized Light Vehicles Test Procedure
XRD	X-Ray Diffraction
XRF	X-ray Fluorescence
Zn	Zinc
ZnO	Zinc Oxide
Zr	Zirconium

Chapter 1 : Introduction

1.1 Background and rationale

Most modern vehicles are equipped with various safety features such as brake systems, seatbelts, airbags, lights, etc. The brake system is a key safety component that allows a driver to stop or slow down the vehicle in a controlled and repeatable fashion. In a disc brake system, the brake rotor is employed along with two brake pads to create friction on both sides of the rotor rubbing surfaces. The frictional torque generated by this interaction acts through the road wheel to retard the vehicle forward velocity by dissipating the kinetic energy associated with the forward motion of the vehicle.

Many types of brake rotor are produced nowadays but the lightweight ones have become increasingly the focus of attention among many researchers in the automotive industry since the introduction of new legislation (Regulation (EC) No 443/2009). This legislation, which was introduced in 2009, required passenger cars sold in 2020 to achieve fleet average emissions of 95 grams of CO₂ per kilometre (g/km) (European Federation for Transport and Environment, 2011). One way to meet this legislative requirement is to improve fuel consumption by reducing the weight of a vehicle. Potentially significant savings can be achieved by reducing the weight of the disc brake rotor. In order to reduce the weight of this rotor, researchers have explored the possibility of replacing the conventional grey cast iron or steel brake rotors with alternative lightweight materials (Alnaqi et al., 2014). Recent studies have shown that aluminium alloys are a good alternative for replacing these conventional ferrous materials because of their excellent properties such as low density, high specific heat and high thermal conductivity. Hussain (2018) indicates that for a medium-sized passenger car, the unsprung mass reduction can be estimated at around 20 kg by the use of aluminium alloy based material in the brake rotor.

Despite its excellent properties, the lightweight aluminium alloy brake rotor possesses some major limitations because of thermomechanical properties. Such alloys have low maximum operating temperature and do not exhibit sufficient wear resistance. Therefore, it is essential to protect the rubbing surface of an aluminium rotor with high temperature resistant materials such as alumina (Al_2O_3) or silicon carbide (SiC) (Agbeleye et al., 2020). The function of the substrate material can be improved by applying some form of surface treatment process. There are three processes commonly applied to improve the desired surface properties of lightweight materials such as aluminium alloys, namely, plasma electrolytic oxidation (PEO), anodising and thermal spraying processes (Alnaqi et al., 2018; Bensalah et al., 2009; Watremez et al., 1996). The PEO process is similar to the anodising process except much higher voltages are applied in the former (Gulden et al., 2020). The application of the PEO process produces coating layers of higher hardness, density and wear-resistance as well as better adhesion to the substrate compared to the anodising process. Alnaqi et al. (2014) reported that the PEO process improves the thermal and friction performance of the wrought aluminium brake rotor up to rubbing surface temperatures of 500°C . Nevertheless, the PEO process has a number of shortcomings that requires careful consideration during its operation. One of its apparent drawbacks is that it consumes large amounts of energy, thus the application is only economical for samples with a small area. Another drawback is related to the inherent porosity which may exceed its optimal percentage if the process parameters are not controlled properly.

Recently, a significant increase in airborne brake wear particulate matter (PM) in urban areas has attracted much interest among researchers from around the world. The brake wear particles are generated when sliding contact between the brake pads and the rotor takes place across the interface and the energy is dissipated by the friction generated, which in turn drives the wear process. The brake wear particles are produced by the friction created when the brake pads squeeze against the rotor. They contribute significantly to non-exhaust emissions alongside tyre and road wear as well as resuspension of deposited road dust. Several studies reported that the non-exhaust emissions have become the major

contributor to the traffic-related PM. Their proportion has surpassed the proportion of exhaust emissions every year and this trend is projected to increase even more in the future. The main reason behind this trend is the strict enforcement of regulations regarding exhaust emissions leading to a decline in use of diesel engines whereas no proper such regulations have been established for non-exhaust emissions (Perricone et al., 2016; Grigoratos and Martini, 2015; DEFRA, 2019a).

Theoretically, brake-related emissions have become one of the main sources of urban outdoor air pollution and they can induce large-scale impacts on air quality (DEFRA, 2019a). Poor air quality is known to cause negative effects on the environment and human health. Environmental pollution has been linked to global warming, climate change and acid rain as well as causing harm to other living species (Manisalidis et al., 2020). High levels of environmental pollution can create a white or brown haze that affects human visibility (USEPA, 2018). Driving in low visibility conditions requires extreme caution because unwanted incidents may happen unexpectedly. The emission of airborne brake wear particles in the atmosphere is not only causing adverse effects to the environment but also to human health. Numerous studies have reported the relationship between adverse health effects and the characteristics of PM. It was shown that the particle size of PM is an important factor in influencing how the particles are deposited in the respiratory system and its subsequent effect on human health (Kumar et al., 2013; Pope et al., 2002). Samet et al. (2000) showed that the concentrations of PM in the environment may be associated with human mortality. There is consistent evidence linking the level of PM concentration with the mortality rate from cardiovascular and respiratory illnesses. Furthermore, the chemical composition of particles may also have similar effects on human health (Magari et al., 2002; Kelly and Fussel, 2012; Pope et al., 2007; Ostro et al., 2007). Toxic substances which typically include compounds of Fe, Cu, Ni, Cr, Zn, Al, Pb, Se, Pd and Mn are often discovered in PM. From the aforementioned effects, it is important to consider both size distributions and composition characteristics of brake wear debris.

Accurate measurements of airborne brake-related PM in an open atmosphere is quite challenging because the airborne particles collected may originate from other sources. The changeable wind velocity and direction often affects the sampling results. Most of the research studies on brake wear particles found in the literature were conducted inside a laboratory either in open or closed systems. Since a standardised procedure is not available for this kind of experiment, a variety of test rigs and testing protocols have been constructed around the world. This has often led to different and even conflicting results. However, the basis of the findings is usually the same. Most of the studies attempted to observe the particle concentrations and the presence of chemical elements in brake wear debris. In general, particle measurements are sensitive to the design of the test rig, the choice of cycle, the particle measurement instrument and the characterisation technique. Moreover, the measurement is also different in the way the representative sample is obtained e.g. whether it is isokinetically sampled, or not. Under isokinetic sampling, a probe needs to be manufactured following the underlying isokinetic principles particularly for the nozzle inlet section to avoid sampling errors and biased results.

In the current study, the measurement of brake wear emissions was conducted using a newly developed test rig. The system was based upon the existing Leeds full-scale disc brake dynamometer which is designed to simulate real world drag brake applications such as controlling the vehicle speed during a long mountain descent. This rig includes an actuation system, LabView data acquisition program, ducting system and an environmentally-controlled chamber around the brake head. In addition, a Dekati ELPI[®]+ Electrical Low Pressure Impactor was commissioned along with a custom-made probe in order to capture and measure brake wear particles. The probe was designed and manufactured to comply with the isokinetic concept. The ELPI[®]+ unit allows measurement of airborne particle size distribution and concentration in real time with a sampling rate of 1 Hz. The instrument can also be used to collect airborne particles on filters for subsequent gravimetric and chemical analyses.

Both grey cast iron (GCI) and novel Plasma Electrolytic Oxidation Aluminium (PEO-Al) rotors were tested according to the newly developed procedures. To

the author's knowledge, there are no standard procedures in the literature regarding the capture and measurement of brake wear particles under drag braking conditions. Two key aims of the test procedures developed are to attain a steady-state temperature at the rotor rubbing surface and acquire sufficient particles for the subsequent analysis. Material characterisation of the particles generated from the two types of brake rotor was conducted using a Hitachi TM3030Plus SEM to evaluate their morphology and chemical composition.

Alongside these experimental studies, Computational Fluid Dynamics (CFD) simulations were performed to predict the velocity profile in the vicinity of the sampling point and guide the experiments by identifying suitable locations for taking particulate samples. The velocity profile obtained was validated with the experimental results.

Different brake rotors may have different thermal and tribological responses during operation. These properties influence the number and characteristics of brake wear particles emitted. This is important for health and environmental concerns. It is postulated that the lightweight PEO-Al alloy brake rotor, which is the main subject of the current research, is not only capable of reducing the weight of a vehicle but also capable of reducing non-exhaust emissions to the atmosphere. This result will provide further confidence and justification in utilising the proposed lightweight brake rotor for replacing the conventional ferrous ones.

1.2 Aim and objectives

The overall aim of the project is to investigate and characterise the performance of novel PEO-treated lightweight disc brake rotors compared with conventional grey cast iron rotor systems, particularly in relation to the release of harmful wear particles into the environment. This aim is realised through the implementation of the following objectives:

- 1) To commission a new air extraction system for the Leeds brake dynamometer and to design and manufacture an isokinetic sampling probe in order to extract representative air samples for analysis.

- 2) To develop fluid dynamics simulations in order to provide details of the velocity profile of the air flowing through the extraction system, particularly in the vicinity of the sampling probe.
- 3) To carry out preliminary tests on the modified brake dynamometer and develop a test protocol for generating, measuring and collecting airborne brake wear particles using a state-of-the-art Dekati real-time particle analyser.
- 4) To investigate the effect of different drag brake operational conditions (applied pressure and rotor surface temperature) on the particle size and mass distribution, morphology and elemental composition of wear particulates generated from a conventional GCI brake rotor.
- 5) To study and compare the airborne wear particle characteristics (size and mass distribution and chemical composition) for a novel lightweight PEO-Al brake rotor with those from the corresponding GCI rotor under similar drag brake operating conditions.

1.3 Thesis outline

This thesis contains seven further chapters and their contents are summarised as follows:

Chapter 2 outlines the foundation of the disc brake system as well as materials for the disc brake friction pair. It describes the background information on airborne particulate matter and brake wear particles and discusses a review of particle measurements and characterisation. In addition, the concepts of isokinetic sampling and Computational Fluid Dynamics (CFD) simulations are explained briefly.

Chapter 3 explains the new dynamometer extraction system and disc brake pair materials used. The chapter describes the particle measurement, collection and characterisation methods used in the current study. Explanations about the sampling probe design and PEO surface treatment applied to the aluminium rotor process are also provided.

Chapter 4 introduces the CFD simulation technique used. It describes two airflow simulations: (1) through the whole extraction system and (2) through the sampling probe. A comparison of analytical predictions and experimental studies is also presented.

Chapter 5 presents the results of wear debris generated from the GCI rotor. These include the results of initial and repeatability tests on the full-scale disc brake dynamometer, particulate matter measurement, gravimetric analysis, microstructural analysis and elemental composition evaluation.

Chapter 6 presents the results of wear debris generated from the lightweight PEO-Al rotor. These include the results of repeatability tests on the full-scale disc brake dynamometer, particulate matter measurement, gravimetric analysis, microstructural analysis and elemental composition evaluation.

Chapter 7 discusses the key finding of the research as well as the limitations of the current methodology.

Chapter 8 presents the main conclusions of the thesis and provides suggestions for future work.

Chapter 2 : Literature review

2.1 Overview

This chapter provides research background information in the relevant areas studied. It begins with a brief introduction to automotive disc brakes, followed by an explanation of the brake pad and rotor materials. A comprehensive discussion on the particulate matter which includes particle size concept, particulate matter basics, air quality standards, effect of particulate matters, traffic-related particulate matter and brake wear particle emissions is then provided. A review of the braking test stands and cycles that were reported in the literature is also given. The particle instrument that has been utilised for this research is explained. Other topics that are reviewed in this chapter are brake wear particle characterisation, isokinetic sampling principle, Keronite PEO surface treatment technology and applications of Computational Fluid Dynamics in braking simulations. Finally, a summary of the findings from the literature is presented and described.

2.2 Introduction to automotive disc brakes

An automotive brake system (see Figure 2.1) is one of the most crucial parts of a vehicle as it is used to maintain, slow down or stop the vehicle's motion. Failure of this system will result in the loss of control in a vehicle and it might potentially cause death. Most brakes commonly use friction between two contact surfaces to convert the kinetic energy into heat energy when stopping a vehicle. There are two types of frictional brakes commonly available in automotive applications, namely disc (axial) and drum (radial) brakes (Limpert, 1999). The disc brake is designed to function by means of squeezing pads against either side of a rotating disc, while in a drum brake a set of shoes are pressed outward against the inner

surface of a rotating drum. The main features of a typical automotive drum brake are illustrated in Figure 2.2 (a). In the past, all vehicles used drum brakes on all four wheels. However, more recently, modern vehicles have utilised disc brakes on the front wheels, and many vehicles have discs on the rear wheels as well. Due to their superior stopping ability over the drum brakes (i.e. better performance in wet conditions), there is a growing trend to have them on the rear wheels despite higher costs associated with them. In this research, only the disc brake type will be considered and discussed.

A disc brake generally consists of three main components namely the calliper, rotor (disc) and brake pads. The brake calliper is a structure that houses the brake pads and one or more pistons. The calliper is assembled over the rotor like a clamp and at each side a brake pad is inserted between the calliper and the rotor. Each brake pad is typically made from a steel backplate which has a friction material bonded to it. The pad on the outside of the rotor is called the outboard brake pad and the one on the inside (towards the vehicle) is called the inboard brake pad. During operation, these two pads will squeeze the rotor to create friction in order to slow or stop a vehicle. The rotor is usually made of conventional grey cast iron and it is fitted to a vehicle through a wheel hub assembly (Day, 2014). The main features of a typical automotive disc brake are illustrated in Figure 2.2 (b).

The basic operation of an automotive disc brake involves a driver depressing a brake pedal using their foot. The force applied will then create significant hydraulic pressure in the master cylinder. As a result, the brake fluid is pressurised along the brake lines to the hydraulically activated pistons in each calliper. The force from this piston is transmitted to compress the brake pads against the rotating rotor. The contact between the stationary brake pads and the moving rotor will produce the necessary sliding friction which enables a vehicle to decelerate or stop.

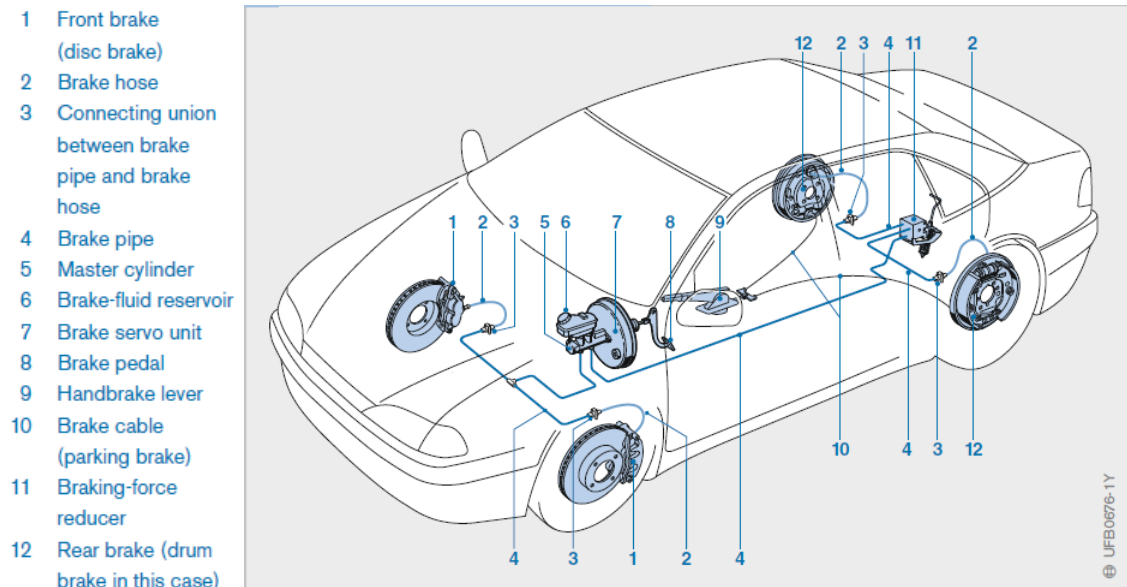


Figure 2.1: A graphical representation of automotive braking system (Post, 2014).

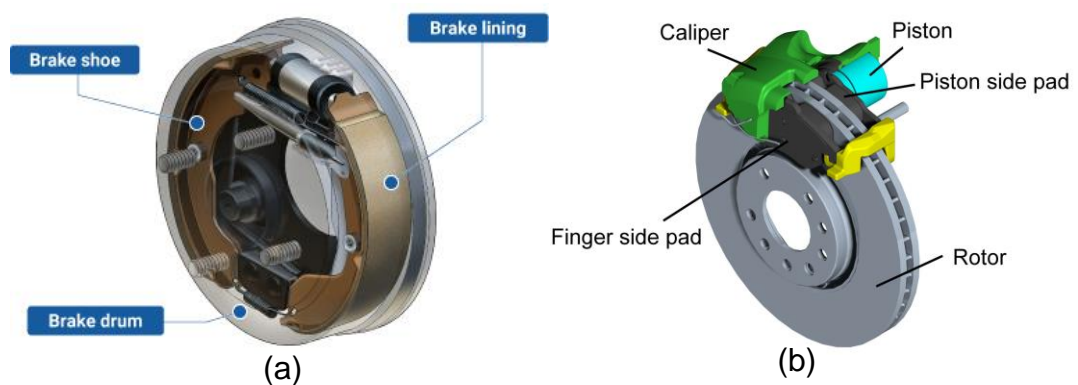


Figure 2.2: Typical (a) drum (Akebono, 2020) and (b) disc brake systems (Wahlström, 2009).

2.3 Materials for disc brake friction pairs

2.3.1 Brake rotor materials

An automotive braking system is a group of mechanical, electronic and hydraulically activated components that use friction to retard the road wheel and therefore the vehicle. The kinetic energy of the vehicle is first converted to thermal energy which is then dissipated through the disc brake and other parts through conduction. It is widely accepted that approximately 90% of the dissipated thermal energy is absorbed by the brake rotor and the remainder

being absorbed by the pad (Yan et al., 2016; Thornton et al., 2011). The amount of absorbed heat is in fact dependent on the specific heat capacity of the components. Under extreme braking events such as repeated high speed braking and continuous downhill braking, the frictional heat generated is expected to increase the temperature significantly at the sliding surface. This high temperature will lead the disc brake to experience overheating and perhaps softening of materials (Alnaqi et al., 2014). Yan et al. (2015a) summarised the effect of overheating of the disc brake. They revealed that such overheating can result in or aggravate brake fade, increased wear of the friction pair, brake disc coning and thermal fatigue cracking, as well as thermal judder of the brake system. Therefore, the brake rotor must have the ability to absorb and dissipate the heat energy quickly during an extreme braking event (Wahid, 2018). Good thermal conductivity and high mechanical strength are the main factors in selecting materials for the brake rotor. Other important factors that should be considered include high specific heat capacity, sufficient maximum operating temperature, low coefficient of thermal expansion, low density, resistance to wear, low cost and ease of manufacture (Barton, 2011).

The most commonly used material for conventional automotive brake rotors is grey cast iron. This material is also known as flake graphite iron and contains approximately 3.5% of graphite in flake form which can offer a reasonable thermal conductivity. Small quantities of alloying elements are usually added to iron in order to enhance the desired properties. Elements such as chromium and molybdenum provide better mechanical strength and improve heat cracking behaviour but at the expense of manufacturability. However, the addition of copper and nickel not only improves the mechanical strength but also imparts the cast iron with better manufacturability characteristics. Other alloying elements used are titanium and manganese for improving friction performance and hardenability, respectively (Thornton et al., 2011; Barton, 2011).

Numerous studies have been reported to improve the performance of disc brakes such as applying surface treatment to the disc (Gorjan et al., 2016; Bensalah et al., 2009; Malayoglu et al., 2011), the use of a ventilated disc design for cooling enhancement (Jiang et al., 2012; Mew et al., 2015; Pevec et al., 2012;

Yan et al., 2015b; Sisson, 1978) and optimisation of the geometry of the disc brake (Lü and Yu, 2016; Palmer et al., 2009; Grieve et al., 1998).

Currently, traffic-related emissions have become an important focus of many researchers in the automotive industry. Stringent legislation regarding exhaust emissions have forced automobile manufacturers to improve the overall fuel consumption of their vehicles (Bielaczyc and Woodburn, 2019). Much effort has been invested to reduce the weight of vehicles through the application of lightweight materials. The disc brake rotor is one of the vehicle components which has received attention in the area of weight reduction. There are several alternative rotor materials such as aluminium metal matrix composites (Al-MMC), carbon-carbon composites and carbon reinforced ceramic matrix composites (CMCs) (Barton, 2011). Additionally, aluminium alloy is also a good alternative for lightening the mass of brake rotors because of its excellent properties such as low density, high specific heat capacity and high thermal conductivity. Since this alloy has a low maximum operating temperature (MOT), it is crucial to protect its rubbing surface through some kind of coating. Table 2.1 shows typical properties of the commonly used rotor materials including the alumina coating that will be of interest later in the current study.

The potential application of lightweight brake rotors in small to medium-sized passenger vehicles has been studied by Grieve et al. (1998). Finite Element Analysis (FEA) was used to investigate the permissible vehicle mass that could keep the temperature below the MOT limit of the generic Al-MMC rotor material. The results showed that the Al-MMC rotor was safe for use in a vehicle with a gross mass of less than 1100 kg. However, this critical temperature can be further reduced by optimising the rotor material or by improving the rotor design. Using Taguchi techniques, Grieve et al. (1998) also found that the rotor cheek thickness, the cooling rate to the rotor surfaces and the conductivity of the rotor material are the most influential factors for the optimised Al-MMC rotor.

The thermal and tribological performance of alumina coated lightweight brake rotors has been investigated by Alnaqi et al. (2018). In their study, two different types of small scale solid brake rotor, namely, aluminium alloy (6082-T6) and Al-MMC (6061/40SiC) rotors were surface-treated through the plasma electrolytic

oxidation (PEO) process. The PEO alumina layer was found to be more uniform and durable on the surface of the aluminium alloy rotor than on the Al-MMC. Both alumina coated brake rotors demonstrated an acceptable range of friction coefficients ($\mu = 0.28-0.34$) throughout the dynamometer tests. The coating layer also significantly improved the hardness value of both the aluminium alloy and the Al-MMC rotors. In terms of thermal performance, both coated rotors have been shown to offer higher maximum surface temperatures when compared to their corresponding plain rotor i.e. non-coated. These coated aluminium alloy and Al-MMC rotors are capable of withstanding a maximum surface temperature of the order of 550°C and 500°C, respectively. This work was then continued by Hussain (2018), who used a full-scale coated ventilated aluminium alloy (6082) brake rotor in his study. Due to health and safety concerns regarding fumes generated during braking tests, the maximum temperature was limited to 300°C. Hussain (2018) found that the coefficient of friction for the alumina coated brake rotor was around 0.5 and these values were uniform and stable at a higher temperature during braking tests. According to Blau (2001), typical values of friction coefficient for brake material pairs vary between 0.3 and 0.6. Additionally, the pin-on-disc tests revealed that the alumina coated rotor surface has a wear rate 15 times lower than that of the grey cast iron rotor surface.

Many techniques have been proposed in the literature to modify the surface of disc brake rotors. The modifications have been used to protect and improve the wear resistance, especially for lightweight alloy rotors. The PEO process (Alnaqi et al., 2018), anodizing (Bensalah et al., 2009) and thermal spraying (Watremez et al., 1996) are commonly used techniques for the surface treatment. Anodizing is an electrochemical process that converts aluminium into its oxide by making an appropriate selection of the electrolyte and the anodizing conditions. Similarly, PEO is an electrochemical process that generates an oxide coating on a metal substrate in an aqueous electrolyte through a series of localised electrical discharge events. In contrast, the thermal spraying technique is a coating process that sprays melted (heated) materials onto a substrate surface. Malayoglu et al. (2011) performed a comparison between PEO and hard anodized coatings. Results show that the PEO coating exhibited better elastic modulus, hardness, wear resistance and adhesion strength properties compared

to the hard anodized coating. It is also mentioned in Alnaqi et al. (2018) that the PEO process can provide a good thermal barrier because of the low thermal conductivity and good wear resistance of aluminium oxide. However, the PEO process is too expensive for the treatment of large workpieces since significant amounts of electricity and energy are required. If the process parameters are not properly controlled, the inherent porosity of a workpiece will also become a major concern (Tsai and Chou, 2018).

Table 2.1: Physical properties of brake rotor materials (Barton, 2011; Hussain, 2018).

Rotor material	Density (kgm ⁻³)	Specific heat (Jkg ⁻¹ K ⁻¹)	Thermal conductivity (Wm ⁻¹ K ⁻¹)	Coefficient of thermal expansion (x10 ⁻⁶ K ⁻¹)	MOT (°C)
Grey cast iron (high carbon)	7150	438	50	10	~700
20% SiC-reinforced Al MMC	2800	800	180	17.5	~450
Carbon-carbon composite	1750	1000	40-150	0.7	>1000
Carbon reinforced SiC-CMC	2300	1000	10	4	>900
Aluminium alloy (6082)	2700	895	180	24	450
Alumina coating	3030	828	1.6	-	>1000

2.3.2 Brake pad materials

During any braking event, wear debris is generated when sliding frictional contact occurs between the disc and the pad. This wear debris (brake-related PM) is known to originate from wear of the pad and the disc (Wahlström and Olofsson, 2015). Typically, a brake pad material can wear by around 80% of its initial volume during its lifetime (Ciudin et al., 2014). Therefore, brake pads or linings (friction materials) are usually manufactured with complex chemical compositions and vary from one manufacturer to another, depending on the type of brake, to prevent excessive wear. Each type of friction material has its own

formulation and the detailed composition is not provided by manufacturers. However, the main components of these friction materials generally consist of abrasives, friction modifiers, fillers and reinforcements and binder materials (Mosleh et al., 2004). The possible composition of each of these components and their corresponding function is shown in Table 2.2.

Table 2.2: Possible composition of a brake pad (Chan and Stachowiak, 2004; Xiao et al., 2016; Grigoratos and Martini, 2015).

Constituents	Composition	Functions
Reinforcing fibres	Metallic chips (i.e. Steel, brass, copper), aramid (i.e. Kelvar), glass, ceramic (i.e. Aluminium oxide, silicon carbide), sepiolite (i.e. Magnesium silicate), potassium titanate.	Provide mechanical strength
Binders	Phenolic resin, silicon-modified resin, cyanate ester resin	Hold the frictional components together
Filler	1) Inorganic: Mica, barium sulphate, vermiculite, calcium carbonate, magnesium oxide, molybdenum trioxide 2) Organic: Cashew dust, rubber	Improve manufacturability and reduce brake noise
Frictional additives 1) Lubricants 2) Abrasive	Graphite, metal sulphides (i.e. lead, antimony, tin & copper sulphides) Zirconium oxide, zirconium silicate, aluminium oxide, Chromium oxide, quartz	Modify friction coefficients and wear rates

Due to serious health concerns, today's friction materials are not allowed to contain asbestos. Thus asbestos brake pads have generally been replaced by a variety of new brake pad compositions. These new brake pads can be categorised into three groups: non-asbestos organic (NAO), semi-metallic (SM)

and low metallic (LM). NAO brake pads have low wear rates and demonstrate relatively low brake noise but degrade braking efficiency at elevated brake temperatures (poor fade). A typical composition of an NAO brake pad is shown in Table 2.3. SM brake pads contain a high amount of steel fibre and iron powder, they exhibit low wear and average fade but are noisier than other types. LM brake pads have a relatively high content of abrasives which increases friction and improves fade. However, they possess the drawbacks of high wear rates and are noise prone (Sanders et al., 2003). LM is the most commonly used type of brake pad in Europe. The demand for LM brake pads has been high since the implementation of strict braking performance requirements. The brake pad material is required to pass the obligatory braking test that simulates extreme braking conditions (Lapinus, 2020).

Table 2.3: A typical composition of an NAO brake pad (Barton, 2011).

Constituent	Percentage by weight
Whiting (chalk)	38
Bronze powder	15
Graphite	10
Vermiculite	8
Phenolic resin	8
Steel fibres	6
Rubber particles	5
'Friction dust'	5
Sand	3
Aramid fibres	2

2.4 Particulate matter

2.4.1 Particle size concept

In addition to chemical composition, the behaviour of PM is often determined by their physical properties namely particle size, particle shape and mechanical properties. One of the most important physical properties of PM is the particle

size. PM is known as monodisperse when its particles have the same size but it is known as polydisperse when its particles vary in size. Particles with a spherical shape can be described by a universal dimension such as the diameter. For non-spherical particles, the size is more difficult to define; thus, it is convenient to use other parameters as a measure of particle size. These parameters are often expressed in terms of particle settling velocity. There are two commonly used parameters to define the particle size; a) aerodynamic diameter and b) Stokes diameter. The aerodynamic diameter is described as the diameter of a unit-density sphere (1 g/cm^3) that would have the same settling velocity as the particle under consideration. In contrast, the Stokes diameter is described as the diameter of a sphere that would have the same density and settling velocity as the particle under consideration. Figure 2.3 illustrates the definition of aerodynamic and Stokes diameters. Furthermore, the concept of equivalent diameter is also commonly used to assign a size to a particle. The particle size is often defined according to a specific physical property which is measured by a specific technique. For instance, the mobility equivalent diameter is used if the electrical mobility of a particle is measured (Kulkarni et al., 2011; Lazaridis and Colbeck, 2014).

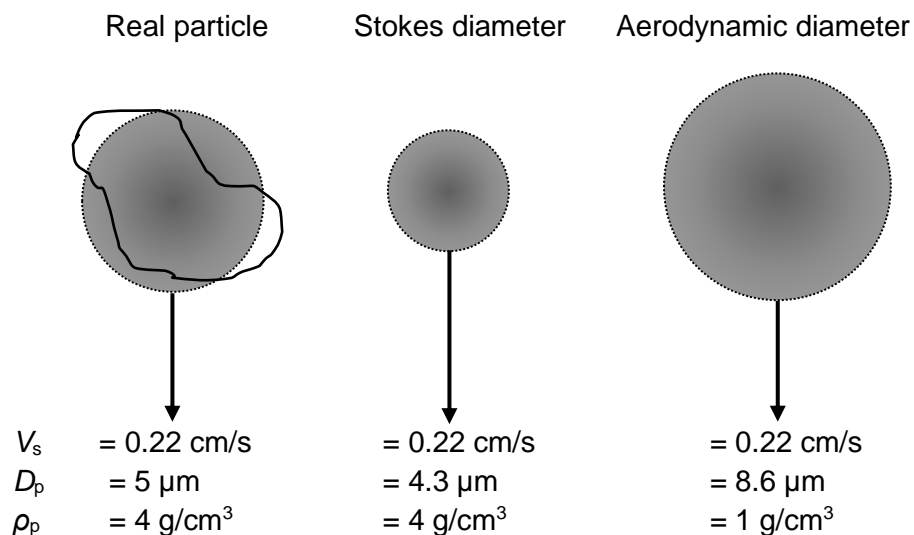


Figure 2.3: Illustration of equivalent particle diameters.

2.4.2 Particulate matter basics

Particulate matter (PM) is a complex mixture of solid and liquid particles that are suspended in the air for extended periods of time. These particles may include both organic and inorganic particles such as dust, dirt, fly ash, soot, pollen, smoke and drops of liquid (USEPA, 2018). PM can exist as a primary and/or a secondary component. The primary components are emitted directly from the source into the atmosphere while the secondary ones are formed by physical and chemical reactions of gaseous pollutants. PM sources can be natural or anthropogenic. Most PM is generated from a variety of man-made activities such as manufacturing, construction, road transportation, agricultural operations, combustion processes and energy production. Other PM sources may naturally be present in the atmosphere because of volcanoes, forest fires, dust storms and living vegetation. PM varies widely in size, composition and origin. Furthermore, PM comes in many sizes and shapes; some particles are large enough to be seen with the naked eye while others are very small and practically invisible.

Particulate matter is often divided according to mass with particles categorised into two distinct size ranges: (i) coarse and (ii) fine. The coarse fraction contains particles with an aerodynamic diameter between 2.5 μm and 10 μm ($\text{PM}_{2.5}$ - PM_{10}), whereas the fine fraction contains particles with an aerodynamic diameter of up to 2.5 μm ($\text{PM}_{2.5}$). Occasionally particles are also grouped into $\text{PM}_{0.1}$ (particles with an aerodynamic diameter smaller than 0.1 μm) since they contribute greatly to the total number of particles, compared to the total mass of particles (Berghmans et al., 2009). All of these particles are grouped into an ultrafine fraction. The coarse particles are typically produced through mechanical processes by breaking up even larger solid particles, for example dust and fly ash while the fine and ultrafine particles are largely formed from the condensation of gases which mainly come from fossil fuel combustion. Figure 2.4 illustrates a relative estimation of the PM size in comparison with the average diameter of a human hair.

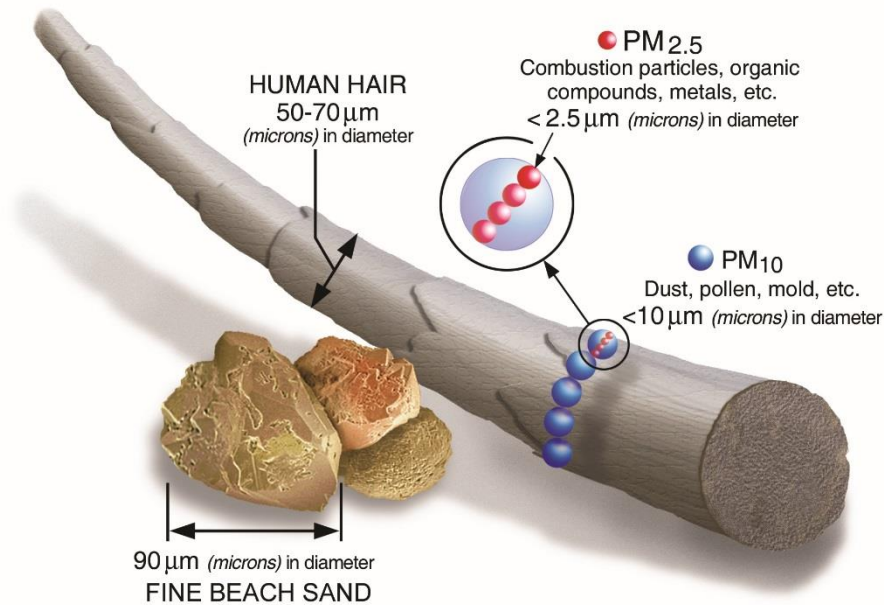


Figure 2.4: Relative size of particulate matter (USEPA, 2018).

2.4.3 Air quality standards

Air pollution has a detrimental impact on the world population and has become a significant threat to human health. There are more than 2 millions premature deaths recorded each year due to diseases associated with the exposure of humans to air pollution (WHO, 2006). In the European Union, premature deaths are about 400,000 and traffic-related emissions are known to have contributed to many of these (Peikertova and Filip, 2016). It was found by EPUK (2019) that air pollution costs the UK economy over £20 billion a year. Air quality guidelines or standard references are generally based on scientific studies in order to reduce the economic and health impacts from air pollution. These standards are established not only to save human lives but also to prevent potential damage to flora and fauna. These standards control the quality of air by limiting the concentration levels of a specific atmospheric pollutant such as sulphur dioxide, (SO_2), nitrogen dioxide (NO_2), ozone (O_3) and both $\text{PM}_{2.5}$ and PM_{10} particles. Table 2.4 provides air quality standards for $\text{PM}_{2.5}$ and PM_{10} that are recommended by the World Health Organization (WHO, 2006) and European Environment Agency (EEA, 2016).

The WHO (WHO, 2006) offers guidance in reducing air pollution of PM_{2.5} and PM₁₀. They recommend an annual average concentration of 10 µg/m³ and 20 µg/m³ as the long-term guideline and a 24-hour average concentration of 25 µg/m³ and 50 µg/m³ as the short-term guideline for PM_{2.5} and PM₁₀, respectively. Directive 2008/50/EC (Council of the European Union) has set legally binding limits to be maintained for the concentrations of PM₁₀. The annual and 24-hr mean concentrations are fixed at 40 µg/m³ and 50 µg/m³, respectively. Additionally, the directive has also set a target value of 25 µg/m³ for PM_{2.5} to be achieved by 2020.

Table 2.4: Air quality standards for PM_{2.5} and PM₁₀.

Organisation	Average time	PM_{2.5} (µg/m³)	PM₁₀ (µg/m³)
WHO	24 h	25	50
	Annual	10	20
European Union	24 h	-	50
	Annual	25	40

In the United Kingdom, the daily air quality index (DAQI) is designed to provide information regarding the concentration levels of air pollution which can be used for health advice and recommended actions. The DAQI consists of numbers from 1 to 10 and it is divided into four bands. The lowest and highest numbers indicate low and very high concentrations, respectively. Five types of pollutants are usually measured, namely SO₂, NO₂, O₃, PM_{2.5} and PM₁₀. Table 2.5 illustrates the bandings of the daily air quality index for PM_{2.5} and PM₁₀ while Table 2.6 shows the corresponding health advice and recommended actions. The Department for Environment Food & Rural Affairs (DEFRA) use the data from the DAQI to predict the level of air pollution every day. The concept is somewhat similar to the weather forecast which allows the public to plan ahead and make better decisions to stay safe.

Table 2.5: Bandings of air pollution level for PM_{2.5} and PM₁₀ (DEFRA, 2019b).

Index	1	2	3	4	5	6	7	8	9	10
Band	Low	Low	Low	Moderate	Moderate	Moderate	High	High	High	Very High
PM_{2.5} (µgm⁻³)	0-11	12-23	24-35	>36-41	>42-47	>48-53	54-58	59-64	65-70	71 or more
PM₁₀ (µg/m³)	0-16	17-33	34-50	51-58	59-66	67-75	76-83	84-91	92-100	101 or more

Table 2.6: Health advice and recommended actions (DEFRA, 2019b).

Air Pollution Banding	Value	Accompanying health messages for at-risk individuals	Accompanying health messages for the general population
Low	1-3	Enjoy your usual outdoor activities.	Enjoy your usual outdoor activities.
Moderate	4-6	Adults and children with lung problems, and adults with heart problems, who experience symptoms, should consider reducing strenuous physical activity, particularly outdoors.	Enjoy your usual outdoor activities.
High	7-9	Adults and children with lung problems, and adults with heart problems, should reduce strenuous physical exertion, particularly outdoors, and particularly if they experience symptoms. People with asthma may find they need to use their reliever inhaler more often. Older people should also reduce physical exertion.	Anyone experiencing discomfort such as sore eyes, cough or sore throat should consider reducing activity, particularly outdoors.
Very High	10	Adults and children with lung problems, adults with heart problems, and older people, should avoid strenuous physical activity. People with asthma may find they need to use their reliever inhaler more often.	Reduce physical exertion, particularly outdoors, especially if you experience symptoms such as cough or sore throat.

2.4.4 Effect of particulate matters

Investigating particulate matter toxicity involves several key factors such as size distribution, agglomeration state, chemical composition, surface area, chemistry and charge. Particle size and chemical composition are likely to be the most important factors (Grigoratos and Martini, 2015). Studies have shown that the size of particles is an important factor for causing adverse health problems to human beings (Pope III and Dockery, 2006; Calcabrini et al., 2004). Particle sizes

of less than 10 μm in diameter were studied the most because they caused the greatest problems to the human respiratory system (respiratory tract). The deposition of inhalable particles in this system depends on their aerodynamic dimensions. For example, coarse particles (PM_{10}) are typically deposited in the nose and throat, while fine ($\text{PM}_{2.5}$) and ultrafine ($\text{PM}_{0.1}$) particles generally penetrate deep into lungs, and some may even get into the bloodstream. Looking at this in more detail, the Andersen cascade impactor is a device used to study air samples which can measure the full particle size distribution seen in the human respiratory tract; the comparison is illustrated in Figure 2.5.

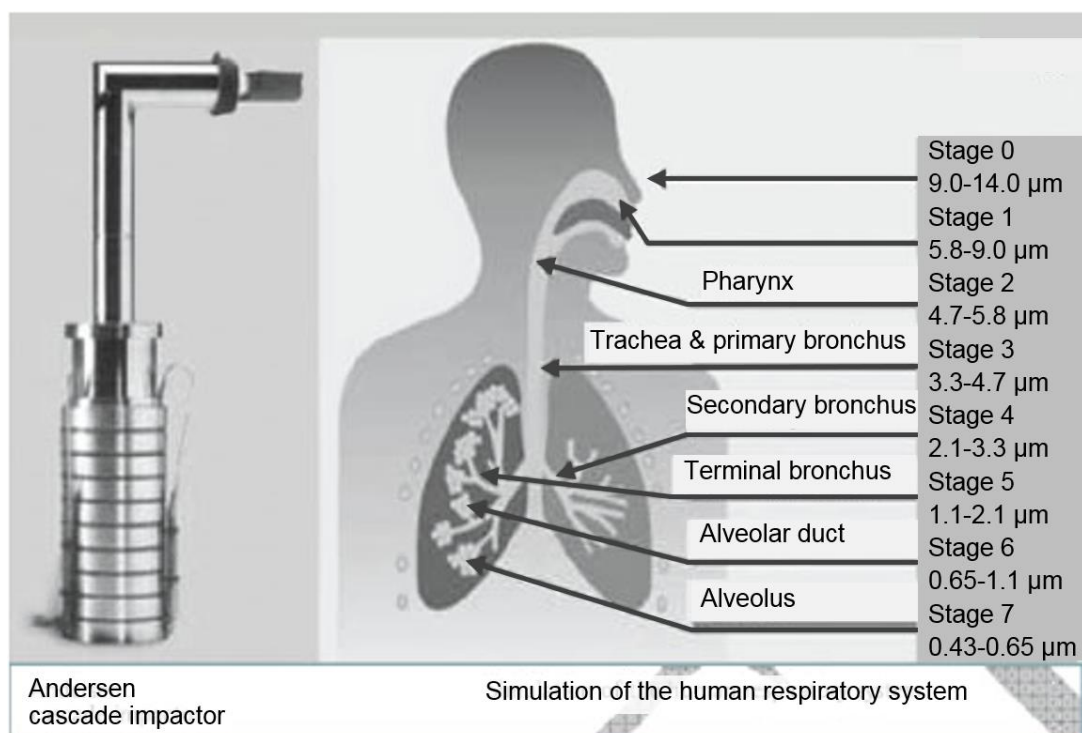


Figure 2.5: Example of how the Andersen cascade impactor simulates the human respiratory system (Andrade-Lima et al., 2012).

Several studies have also reported the relationship between the concentrations of PM in the air with human mortality. Samet et al. (2000) claimed that they have found consistent evidence to associate the level of PM_{10} with the rate of death from all causes, especially from cardiovascular and respiratory illnesses. Based on their results, each increase of $10 \mu\text{g}\text{m}^{-3}$ in the PM_{10} level is associated with a 0.51% increase in rate of death from all causes and 0.68% increase in mortality

from cardiovascular and respiratory illnesses. Similarly, Pope III et al. (2002) reported that each $10 \mu\text{g m}^{-3}$ increase in fine particles was associated with approximately 4%, 6% and 8% increased risk of all causes, cardiopulmonary and lung cancer mortality, respectively. Furthermore, Borja-Aburto et al. (1998) also found that a $10 \mu\text{g m}^{-3}$ increase in the level of $\text{PM}_{2.5}$ could be associated with a 1.4% increase in mortality.

Besides studies that investigate the effect of PM concentrations, there are also studies focused on establishing a significant relationship between chemical composition of particles and adverse effects on human health. Magari et al. (2002) suggested that significant alterations in cardiac autonomic function occurred when humans are exposed to airborne metals (V, Ni, Cr, Pb, Cu and Mn). These results underline the adverse health effects of metallic components of ambient $\text{PM}_{2.5}$. Other adverse health effects caused by chemical composition from numerous researchers have been summarised by Grigoratos and Martini (2015) who described Fe, Cu, Ni, Cr, Zn, Al, Pb, Se, Pd and Mn as toxic substances.

2.4.5 Traffic-related particulate matter

Particulate matter (PM) originating from road vehicles can generally be divided into two categories: exhaust and non-exhaust emissions. Products of combustion from engines primarily contribute to exhaust emission. However, brake, tyre and road wear as well as resuspension of existing road debris are also key sources of non-exhaust emissions. Among these sources, brake-related PM is a major contributor to non-exhaust emissions, particularly in urban areas which correlate with high frequency and severity of braking events (Grigoratos and Martini, 2015). Perricone et al., (2016) found that non-exhaust emissions can contribute up to 50-85% of total traffic-related PM_{10} emissions. Harrison et al. (2012) estimated the contributions of brake, tyre and resuspended dust in ambient air as $55.3 \pm 7.0\%$, $10.7 \pm 2.3\%$ and $38.1 \pm 9.7\%$ (mean \pm standard error), respectively.

Stringent regulations regarding exhaust particulate emissions have only been recently established and no proper regulations are in place regarding non-

exhaust emissions; this means that they are effectively unregulated. Thus, as the former are strictly being controlled, the proportions of the latter to traffic-related emissions are increasingly becoming more significant. As such, there is a need to better understand the behaviour of non-exhaust particulates, especially in light of the fact that they are known to adversely affect human health, as well as the environment.

In the United Kingdom, DEFRA (2019a) reported that non-exhaust particles currently contribute 60% and 73% by mass of primary $PM_{2.5}$ and PM_{10} emissions from road transport, respectively, and that emissions are expected to increase to a greater extent in the forthcoming years. The trends in UK primary non-exhaust and exhaust emissions of PM_{10} and $PM_{2.5}$ from road traffic for the period of 2000 to 2030 are shown in Figure 2.6. Data from 2000 to 2016 represent actual vehicle activities, while data from 2017 to 2030 are the projections made by an expert committee of the Department for Environment, Food and Rural Affairs (DEFRA). As can be seen from Figure 2.6, the exhaust emissions for both PM_{10} and $PM_{2.5}$ show a steady decline up to 2020 and they are predicted to continue decreasing in a gradual manner until 2030. On the other hand, for the three primary components of non-exhaust emissions, tyre wear, brake wear and road abrasion (road wear), these demonstrate a gradual increase over the entire time period of the projection. By 2030, it is anticipated that total UK road transport emissions will be dominated by non-exhaust emissions for both PM_{10} and $PM_{2.5}$.

Despite numerous publications and widespread scientific community dialogue, research on non-exhaust emissions is still in its early stages; to date, no standardised test protocols have been established. Different sampling and measurement setups by research groups studying non-exhaust emissions have frequently led to inconsistent results and even contradictory conclusions. Studying these emissions is extremely challenging because of the nature and complexity of PM generation from various sources. The characteristics of PM may differ depending on driving behaviour (frequency and severity of braking), vehicle's speed, weather condition and maintenance history (Grigoratos and Martini, 2015). Another main issue that may arise during measuring or collecting the wear particles from fieldwork is the difficulty in distinguishing the origin of

these particles. It becomes more difficult for the study if the tested components reach a plausibly high temperature. There is a possibility that the friction processes are accompanied by chemical reactions at the contact interface of a brake pair which result in the formation of new species with different chemical properties, when compared to the original bulk materials (Peikertova and Filip, 2016; Hagino et al., 2015). Furthermore, air sampling results also have a tendency to be affected by the changeable wind velocity and direction when conducted in the field. In this study, only brake wear particle emissions in a controlled laboratory environment will be considered.

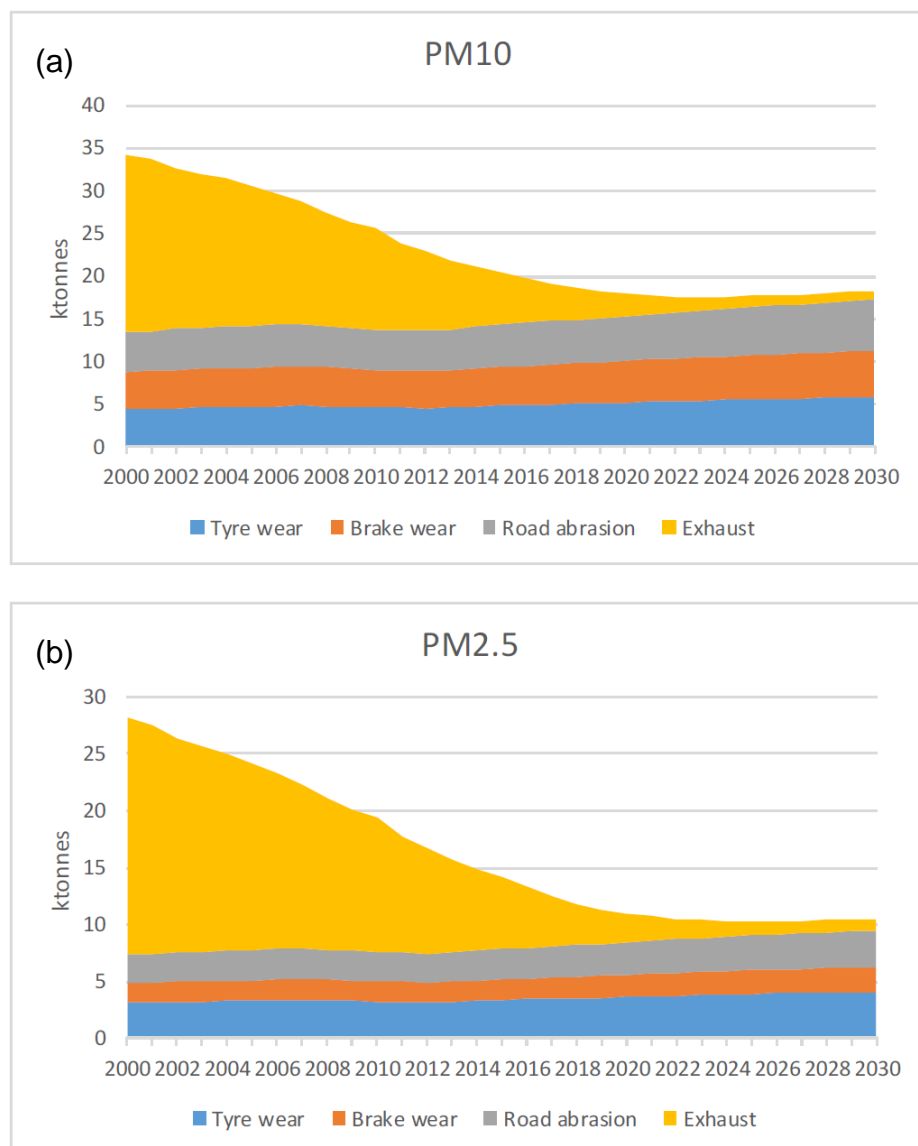


Figure 2.6: UK emissions of (a) PM₁₀ and (b) PM_{2.5} from road transport (DEFRA, 2019a).

2.4.6 Brake wear particle emissions

Previous research has mentioned that brake wear particles contribute up to 20% of total traffic-related emissions (Gasser et al., 2009). These particles are formed and released during frictional contact between brake pads and a rotor when hydraulic pressure is exerted on the spinning rotor. The wear debris released may partially deposit on the vehicle's components and some other debris may become airborne particulates. Both Garg et al. (2000) and Sanders et al. (2003) have highlighted that a significant proportion of brake PM is airborne with the former estimating that 35% of PM is airborne and the latter indicating 50%. Other studies have also shown that approximately 30% (Iijima et al., 2008) and up to 21% (Hagino et al., 2016) of brake wear particles were emitted as airborne particles, and these may vary in size, shape and composition.

There are several factors that affect the characteristics of brake wear particles. Kukutschová et al. (2011) describe that sliding speed, contact pressure and temperature influence the generation of brake wear debris. They investigated the morphology of airborne brake wear particles generated from low-metallic brake pads using a brake dynamometer. The results showed that the generated particles with a size range of 10 nm to 20 µm were released into the air as airborne particulates. The study also suggested that the generation of brake wear particles was dependent on the brake interface temperature; the number of nanoparticles gradually become greater when the average temperature of the rotor approached 300°C. Iijima et al. (2007) found that the number distributions of the brake wear particles had a peak in the fine particle region and this peak gradually shifted to the coarse side as the rotor temperature increased. The size of brake wear particles also becomes larger as the contact pressures increases (Hussain et al., 2014; Mosleh et al., 2004).

Investigating brake wear particles involves two important parameters that affect human health which are particle size and chemical composition. The particle size distribution is commonly expressed in terms of the particle number concentration and the particle mass concentration as described in Sections 2.4.6.1 and 2.4.6.2, respectively. The determination of chemical composition is described in Section 2.4.6.3.

2.4.6.1 Particle mass distribution

Airborne brake wear particles are segregated and collected by various particle counting instruments and multi-cascade impactors. Particles passing through the collection plate in the impactor/counter are classified according to their aerodynamic size. In the case of an impactor, a filter is utilised to collect these particles at each stage. The mass distribution is then calculated from the weight of the filter before and after sampling work. On the other hand, if a particle counting instrument is employed, then the mass distribution is determined in real-time and the values are obtained directly from the instrument. Two kinds of laboratory studies regarding airborne brake wear particle measurement can commonly be found in the literature. These studies are related to the investigation of particles by means of brake dynamometers and pin-on-disc tests. As summarised in Table 2.7, most researchers have found that the particle mass distributions are unimodal. Maximum peaks reported range from 0.1 to 6 μm . Comparisons are in fact not easy to draw, as the findings are primarily collected through various research methods, particle measurement instruments and brake pad types.

Using an enclosed chamber, Hagino et al. (2016) investigated the emissions of airborne brake wear particles under transient driving cycles and found a unimodal particle mass distribution with a size range of 0.68-3.5 μm . In their study, a Low Pressure Impactor (LPI) was utilised in order to classify the sizes of airborne particles. Likewise, Sanders et al. (2003) also reported a unimodal particle mass distribution when testing different types of brake pads under typical urban driving conditions. Some other studies have investigated the mass size distributions of airborne particles for different types of brake pad and braking temperatures (Iijima et al., 2007; Garg et al., 2000). Iijima et al. (2007) have reported that the mass distribution curve was shifted slightly to the coarse side when the braking temperatures increase. Figure 2.7 shows the particle mass distributions of brake abrasion dust for different braking temperatures. The plotted graph displays the mass concentration which has a peak in the size range of 3-6 μm . Another study by these authors employed similar measurement setups, except the brake dynamometer was fully encapsulated in a chamber;

results showed a unimodal particle mass distribution occurring at 2 μm (Iijima et al., 2008). In contrast, Garg et al. (2000) have reported varying trends in the mass size distribution for different braking temperatures. For NAO brake pad, the distribution varied from unimodal at 100°C to bimodal at 200°C and 300°C. Kukutschová et al. (2011) utilised the Berner Low Pressure Impactor (BLPI) and a dynamometer to collect the generated brake wear particles and their findings revealed that the particle mass concentration intensifies between 2 and 4 μm .

Table 2.7: Summary of literature studies regarding airborne particle mass size distributions. Adapted from Grigoratos and Martini (2015).

Researcher	Testing method	Brake pair materials	Size-classified instrument	Mass size distribution
Hagino et al. (2016)	Closed brake dynamometer	Pad – NAO brake pad Disc – Cast iron	LPI (0.06-12 μm)	Unimodal (0.68-3.5 μm)
Nosko et al. (2015)	Closed pin-on-disc rig	Pad – Low metallic pad Disc – Cast iron	FMPS (0.0056-0.56 μm) OPS (0.3-10 μm)	Unimodal (2.2 μm)
Kukutschová et al. (2011)	Closed brake dynamometer	Pad – Low metallic pad Disc – Cast iron	BLPI (0.025-13.6 μm)	Unimodal (2-4 μm)
Iijima et al. (2008)	Closed brake dynamometer	Pad – NAO brake pad Disc – Cast iron	APS (0.5-20 μm)	Unimodal (2.0 μm)
Iijima et al. (2007)	Open brake dynamometer	Pad – NAO brake pad Disc – Cast iron	APS (0.5-20 μm)	Unimodal (3-6 μm)
Sanders et al. (2003)	Open brake dynamometer	Pad – NAO, LM, SM Disc – Not stated	MOUDI & ELPI	Unimodal (4-5 μm)
Garg et al. (2000)	Closed brake dynamometer	Pad – NAO, SM Disc – Not stated	MOUDI (0.1-18 μm)	Unimodal & Bimodal

Notes: ELPI – Electric low-pressure impactor
MOULDI – Micro-orifice uniform deposit impactor
APS – Aerodynamic particle sizer spectrometer
OPS – Optical particle sizer
FMPS – Fast mobility particle sizer

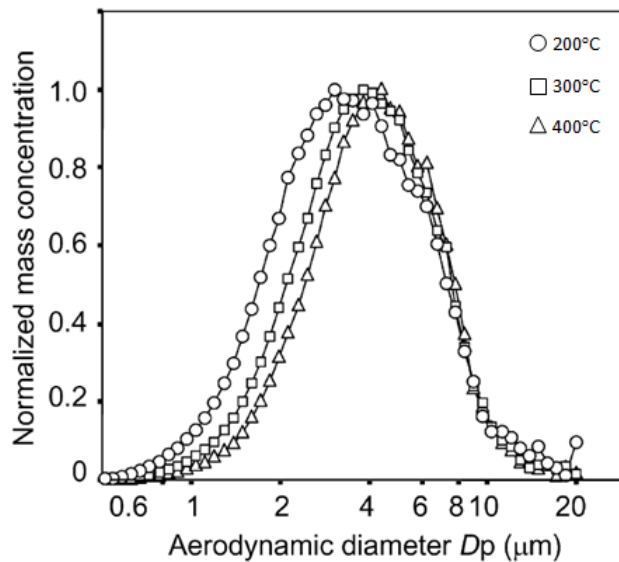


Figure 2.7: Particle mass distribution of brake abrasion dust for different braking temperatures (Iijima et al., 2007).

2.4.6.2 Particle number distribution

In order to acquire more important information about airborne brake wear particles, it is necessary to study their particle number distributions. This property is normally measured by using real-time particle counting instruments. Table 2.8 shows a summary of literature studies regarding airborne particle number size distributions. The table outlines the results obtained using various testing methods, particle measuring instruments and brake pad types. Iijima et al. (2007) used a Aerodynamic Particle Sizer (APS) as part of their study. They conducted brake dynamometer tests using three types of pads and different braking temperatures and reported a unimodal (1-2 μm) particle number distribution. Sanders et al. (2003) also conducted brake dynamometer tests and concluded that the wear debris generated under typical urban driving conditions had a maximum peak in the range of 0.5-2 μm . Different trends (bimodal) are also reported by Mosleh et al. (2004). They tested a commercial truck brake pad against a cast iron rotor using the pin-on-disc testing method. In their study, the size distribution of wear particles was measured under different sliding speeds and nominal contact pressures. Under low speed tests, they found that the first peak occurred around 350 nm for all nominal contact pressures. However for the second peak, the values of 2, 7, and 15 μm were obtained for pressures at 0.125,

0.375 and 0.625 MPa, respectively. Kukutschová et al. (2011) who used a Scanning Mobility Particle Sizer (SMPS) reported that the maximum particle number concentration occurs at 100 and 300 nm. Similarly, Wahlström et al. (2010) also found a bimodal size distribution using the GRIMM aerosol spectrometer. They reported that these two distinct peaks appeared at a particle size of approximately 280 nm and 350 nm.

Table 2.8: Summary of literature studies regarding airborne particle number size distributions. Adapted from Grigoratos and Martini (2015).

Researcher	Testing method	Brake pair materials	Size-classified instrument	particle number distribution
Nosko et al. (2015)	Closed pin-on-disc rig	Pad – Low metallic pad Disc – Cast iron	FMPS (0.0056-0.56 µm) OPS (0.3-10 µm)	Unimodal (0.9, 0.19 & 0.011 µm)
Kukutschová et al. (2011)	Closed brake dynamometer	Pad – Low metallic pad Disc – Cast iron	SMPS (10-445 nm)	Bimodal (100 & 300 nm)
Wahlström et al. (2010)	Closed brake dynamometer	Pad – NAO, LM Disc – Cast iron	GRIMM (0.25-32µm)	Bimodal (280 nm & 350 nm)
Iijima et al. (2007)	Open brake dynamometer	Pad – NAO brake pad Disc – Cast iron	APS (0.5-20 µm)	Unimodal (1-2 µm)
Mosleh et al. (2004)	Open pin-on-disc rig	Pad – SM brake pad Disc – Cast iron	Laser scattering analyser (0.04-262µm)	Bimodal (350 nm & 2-15µm)
Sanders et al. (2003)	Closed brake dynamometer	Pad – NAO, LM, SM Disc – Not stated	ELPI	Unimodal (0.5-2µm)

Nosko et al. (2015) conducted tests on an encapsulated pin-on-disc rig to investigate the effect of temperature on airborne brake wear particles. The pin samples used were milled out from low-metallic pads and the rotating counterparts were made of cast iron. The emission of the brake wear particles was measured by an Optical Particle Sizer (OPS) and a Fast Mobility Particle Sizer (FMPS) in the overall size range of 0.0056 to 10 µm. The result showed that the particle number concentration intensifies at three particle size regimes and that the particle size decreases as the rotor temperature increases. Coarse particles (0.56-10 µm) dominate at the temperature below 95°C and have a peak

at 0.9 μm . Whereas, fine (0.1–0.56 μm) and ultrafine (0.0056–0.1 μm) particles intensify at the temperature between 95 and 188°C and at the temperature above 188°C, respectively. Both fine and ultrafine particles recorded a respective peak at 0.19 and 0.011 μm . Moreover, the authors also reported that the particle mass concentration occurs at a peak of 2.2 μm .

2.4.6.3 Chemical characterisation

Many properties of brake wear particles such as size, microstructure, morphology, chemical composition and phase composition can be acquired through the study of wear debris characterisation. From these properties, much useful information regarding wear mechanisms, environmental and health effects and surface interaction phenomena can be disclosed. For example, the larger sheet-like wear debris is often associated with delamination and fatigue wear, whereas the smaller particles are due to abrasive and/or adhesive wear (Mosleh et al., 2004). The effect of many influential braking factors such as temperature, sliding speed, contact pressure, pad formulation, brake type, history of the friction pair, braking frequency and the severity of braking events on the properties of wear debris can also be identified and differentiated (Glišović et al., 2016; Ciudin et al., 2014).

The brake wear particle size and morphology are usually examined using a scanning electron microscope (SEM). For instance, Verma et al. (2016) have reported microstructural features of airborne brake wear particles that were collected based on their size ranges. These features and their corresponding EDX spectra are shown in Figures 2.8 and 2.9, respectively. From the SEM images, Verma et al. (2016) observed that finer particles are typically clustered in small assemblies, while coarser particles appear to be uniformly distributed on the collection substrate surface. According to EDX analysis, they found that the emitted particles mainly comprised Fe, Mg, Al, Cu, Sn, Zn as well as oxygen and carbon elements. Moreover, dominant phases such as Fe_3O_4 , MgO, ZnO, Fe, Fe_2O_3 and Cu were also identified when the airborne particles were analysed using X-ray diffraction (XRD). Hussain et al. (2014) used a grey cast iron disc and two types of brake pads (NAO and SM) to characterise the brake wear particles. They found that the size of the particles becomes greater as the applied

brake pressure increases. However, the disc brake speed does not show any significant effect on the size and shape of the brake wear particles. The observed particle size ranged from 0.3 to 0.7 μm and its shape mostly appears to be like a flake with many sharp edges. Hussain et al. (2014) also reported the existence of chemical elements such as C, O₂, Mg, Al, Si, S, Fe, Ba, Tb and Ca (only in SM) in the brake wear debris.

Sanders et al. (2003) investigated the chemical composition of brake wear particles generated from three lining types; NAO, LM and SM using an X-ray fluorescence (XRF) analyser. The analysis showed that Fe, Cu, Si, Ba, K and Ti are the highest percentage of the elements in brake wear particles. Other elements detected are Mg, Al and Ca. Hulskotte et al. (2014) conducted an experimental analysis to examine the chemical composition of brake friction pairs commonly used in the Netherlands. To obtain representative results for the European personal car fleet, the friction pairs were collected from the eight most typical car brands in Europe in several auto repair workshops. In total, 65 used brake pads and 15 brake discs were examined by an XRF analyser in order to acquire their chemical composition. The dominant element content observed in the brake pads was Fe, Cu, Zn, Sn and Sb, however Al, Si, Zr, Ti, Cr, Mo, Mn, V, Ni, Bi, W, P, Pb and Co were also present in a small percentage. The brake discs were found to contain more than 95% Fe and approximately 2-3% Si.

The concentrations of several inorganic elements may also be determined by inductively coupled plasma mass spectrometry (ICP-MS) and Inductively coupled plasma atomic emission spectroscopy (ICP-AES). Hagino et al. (2016) utilised NAO braking pads and analysed the generated airborne particles using ICP-MS. They reported the existence of Fe, Cu, Ba, Sb, Na, Al, K, Ca, Ti, V, Cr, Mg, Mn, Zn, Sr, Zr and Mo in the size-classified wear dust and concluded that the first four elements were identified as a key tracer of airborne brake wear particles. Another study conducted by Iijima et al. (2007) showed the presence of K, Ti, Fe, Cu, Zn, Sb and Ba in the size-classified wear dust when airborne particles were analysed by ICP-MS and ICP-AES.

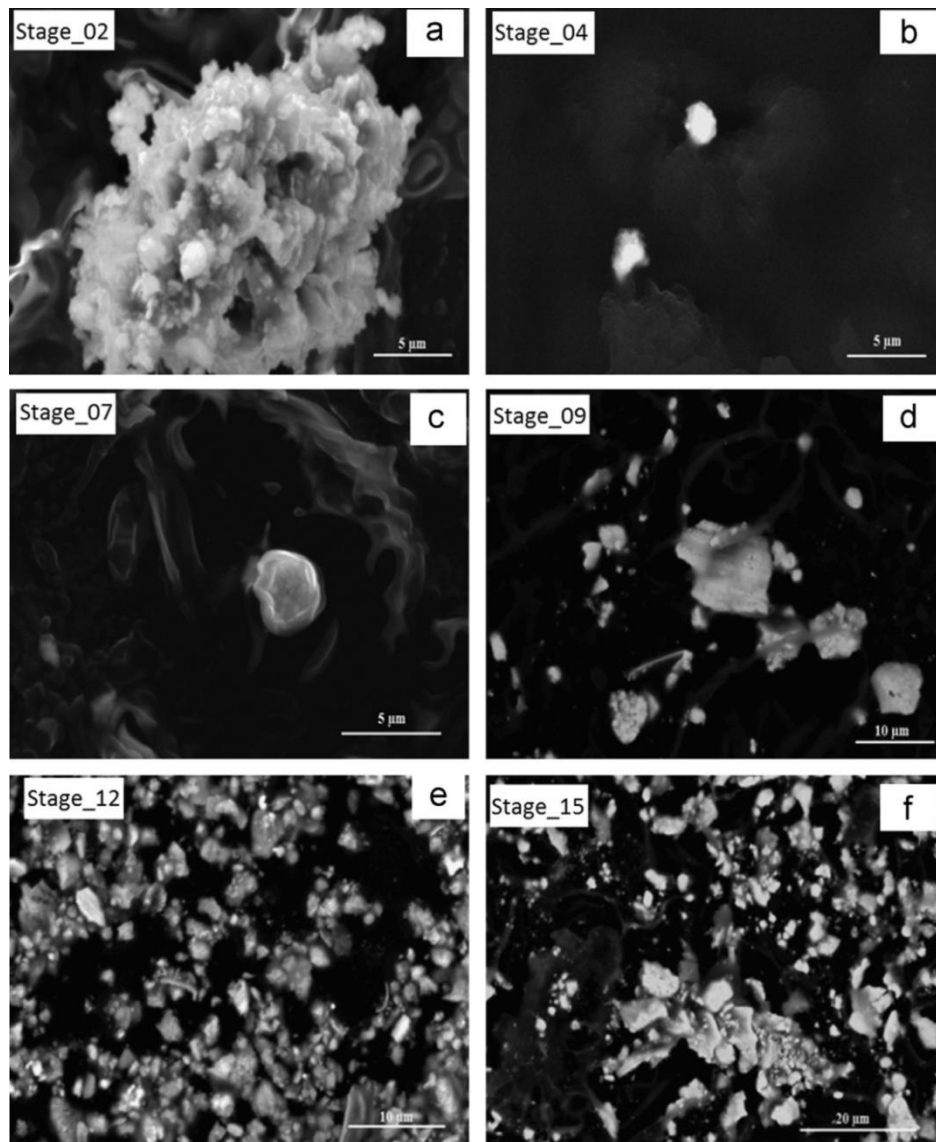


Figure 2.8: Example of SEM images showing particle features at different size intervals (Verma et al., 2016).

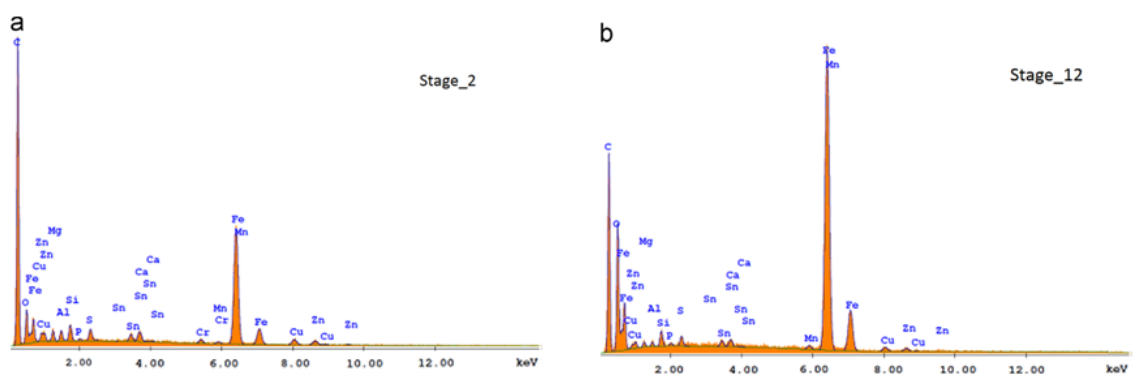


Figure 2.9: Example of EDS spectra at different particle size intervals (Verma et al., 2016).

2.5 Measurements of brake wear particle emissions

Lab-based and field-based experiments are the most commonly used methods for the study of airborne brake wear particle emissions. The field study is more complicated as the airborne particles measured or collected may originate from other sources. The difficulty arises when different airborne particles need to be distinguished not only from the non-exhaust particulate emissions but also from the tailpipe particulate emissions. The field measurement of airborne brake wear particles has been commonly performed in roadside environments, road tunnels, and motorway exit sites. Moreover, the particles were also measured during on-road driving either on a high-speed test track or on a public road. Only few field studies have been reported in the literature. For example Harrison et al. (2012) carried out experiments at the roadside and background sites in 2007, 2009, 2010 and 2011 to quantify the contributions of non-exhaust particulate components in ambient air. In addition, Kwak et al. (2013) conducted tests on a high-speed circuit and round track by fitting a vehicle with particle instruments to measure and estimate the mass distributions of brake wear, tyre wear and road surface abrasion.

Since it is not a trivial task to obtain a representative brake wear sample from a field study, research on brake wear debris has mainly been performed inside a laboratory either in open or closed systems. Generally speaking, laboratory studies can be carried out based on three testing configurations; a) brake dynamometer (Perricone et al., 2016), b) pin-on-disc (Wahlström et al., 2017) and c) chassis dynamometer (Mathissen et al., 2019). The brake dynamometer configurations are usually equipped with brake components of real size and constructed with an environmental chamber and filters to control the cleanliness of the air. These configurations enable braking tests to simulate real-world driving conditions and subsequently reduce the testing expenditure when comparing to the test at full vehicle level. The apparent drawback is that brake dynamometer testing is not able to replicate aerodynamics similar to the real-world test.

The pin-on-disc configurations are generally equipped with a small scale pin and disc which is very different in size compared to real test conditions. The

distinction also includes the braking parameters used such as sliding speed, contact pressure, wear rate and deceleration. Braking tests performed via these configurations will generate lower energy per area which can affect the wear rate and also the particle generation. Thus, the pin-on-disc test is commonly preferable for studying the fundamentals of braking phenomena prior to full-scale tests. The chassis dynamometer configurations are basically developed with a roller assembly to support and operate a full-scale vehicle in a controlled environment. Using these configurations, real-world test conditions can be simulated which are similar to driving a vehicle on a real road (Mathissen et al., 2019).

2.5.1 Brake testing assembly

Studies dealing with the wear and particulate emissions at the sliding interface have been conducted based on laboratory measurements. Due to the lack of any proper sampling methodologies, many different measurement procedures have been developed and employed. For example, Blau and Meyer (2003) utilised a specially developed instrument called a sub-scale disc brake testing system to study the characteristics of both conventional and unconventional brake material wear particles. They also developed and used an adhesive extraction method to remove the loose wear samples of wear debris for examination. On the other hand, Sanders et al. (2003) used a dynamometer bench to determine the emission rate of lining materials and the data obtained were compared to other methods including wind tunnel and test track measurements. Hagino et al. (2015) used a laboratory brake dynamometer that was equipped with an enclosing chamber and a constant volume sampling system to investigate the mass emission of airborne brake wear particles under different driving conditions. Using the same dynamometer assembly, Hagino et al. (2016) tested NAO friction materials to investigate particle sizes and chemical compositions of brake wear particles from brake pads and rotors (or lining and drum) without contamination from dust and/or tyre wear. In addition, abrasion tests were conducted by Iijima et al. (2008) to determine the antimony emissions originating from automotive braking using a full-size brake dynamometer assembly with an enclosed chamber. In Figure 2.10, two layouts of the testing assembly used in different

studies are presented from Iijima et al. (2008) and Hagino et al. (2016), respectively.

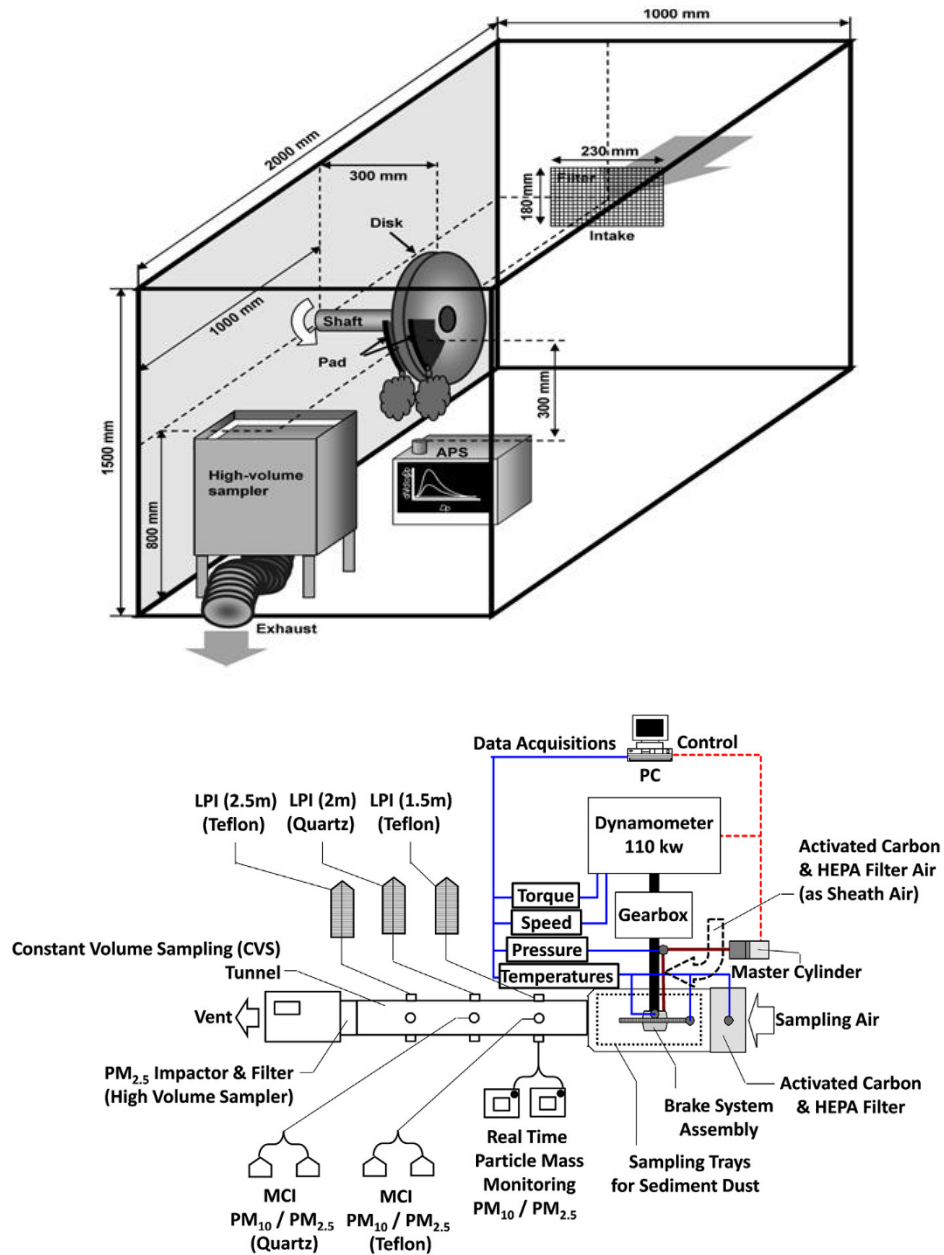


Figure 2.10: Schematic representation of brake testing assemblies: [top (Iijima et al., 2008) and bottom (Hagino et al., 2016)].

Perricone et al. (2016) have proposed a novel test stand for measuring the brake emissions by redesigning an inertial disc brake dynamometer. In their study, the test stand was evaluated by measuring the number and size distributions of the brake wear emissions. In addition, computational fluid dynamics simulations were carried out to ascertain that no vortices were present during the

development of the velocity profile of the sampled aerosol and that the aerosol inside the chamber was well mixed. Generally, the results have shown that the test stand is suitable as a standard test to assess the emissions of airborne brake particles in future legislation, especially in the case of urban conditions. Mosleh et al. (2004) performed laboratory tests to investigate the geometrical and morphological characteristics of brake wear particles using the pin-on-disc testing apparatus. They revealed that the size distribution of brake wear particles varies with the continuity or discontinuity of the sliding contact. They added that the smaller brake wear particles are generated for repeated braking events (discontinuous sliding conditions). The results also revealed brake wear debris scatter into two distinct populations. The first population averages approximately 350 nm in diameter and these particles were assumed to originate from the cast iron disc because of the high content of Fe, C and O. In contrast, the second population of wear debris has a size larger than 1 µm and it was found that these particles contain aluminum, magnesium, antimony, silicon, sulfur, and copper. The presence of these elements in the particles suggested that they are generated from the brake pad material.

2.5.2 Braking test cycle

As mentioned previously, standard test protocols related to non-exhaust emissions of airborne brake wear particles are not yet established. One of the test parameters that need to be standardised is the braking test cycle. Numerous test cycles have been applied by researchers in the literature. Alemani et al. (2014) have utilised SAEJ2707 Method B (Wear Test Procedure on Inertia Dynamometer for Brake Friction Materials) to evaluate brake wear particulate emissions. This standard is commonly developed for wear studies, however they made the assumption that, since particulate matter emitted from disc brakes is linked to the wear between pads and discs, this test cycle is also suitable for the evaluation of particulate emissions. A full test condition for the SAEJ2707 Method B requires a long time to complete the full running-in of the pads and disc. In order to shorten the time, the number of stops within each block was reduced. In their study, they reduced 50% of the stops suggested in the

SAEJ2707 for initial burnish and only 10% of the stops were performed for other blocks. The test cycle that was modified from the SAEJ2707 is shown in Table 2.9.

Iijima et al. (2007) applied JASO C427-88 (Brake Lining, Pad Friction Dynamometer Testing) to evaluate brake wear emissions. The braking tests began with a burnish process at a disc temperature of 200°C and a constant equivalent vehicle deceleration of 3.0 m/s². Following the burnishing process, repetitive braking was applied to the brake disc until its temperature increased from room temperature to 200°C. Then, further braking was applied for a total of 20 repetitions: 5 times for achieving stabilisation and 15 times for measuring the particle size distribution. For tests at disc temperatures of 300°C and 400°C, a similar procedure was followed. However, at 400°C the initial speed was set to 80 km/h.

The Japanese JC08 transient emission test cycle was also employed by Hagino et al. (2016) to simulate driving on an urban road. The test cycle represents driving in congested city traffic, including idling periods and frequently alternating acceleration and deceleration. Indeed, the braking frequencies and patterns of a vehicle were based on the actual travelling conditions of the vehicle. At the end of the test cycle, driving on a highway away from an urban environment was simulated with a maximum speed of 81.6 km/h.

Table 2.9: Potential test cycle for brake emission measurement (Alemani et al., 2014).

Block	Initial Speed [km/h]	Final Speed [km/h]	Initial Disc Brake Temperature [°C]	Braking Deceleration [g]	Number of Stops [N]
Burnish	50	4	100	0.25	50
Town block #1	50	4	150	0.25	20
Highway block #1	150	80	150	0.4	10
Country road block #1	80	4	200	0.35	20
Country road block #2	100	4	125	0.4	20
Highway cycle #2	180	80	100	0.5	5
Town block #2	50	4	150	0.25	20
County road block #3	100	4	125	0.4	20
Hill descent block	80	4	350	0.35	5

2.6 Particle instruments

2.6.1 Introduction to inertial classifiers

Several techniques may be used to collect particles for size classification and sampling analysis, including inertia classification, gravitational sedimentation, centrifugal and thermal precipitation. Among these techniques, inertial classifiers are widely applied in the sampling of particles. Inertial classifiers are available in three types: impactors, virtual impactors and cyclones.

The impactors have been extensively used to capture particles of various size ranges for the determination of aerosol mass size distributions. The most common impactor contains a flat plate, which is placed just under an acceleration nozzle. The aerosol sample is pumped through the nozzle and forced to make a sharp turn after facing the plate. Particles with a large enough aerodynamic diameter will slip across the airflow lines and impact upon the plate while small enough particles will remain in the flow.

Virtual impactors are a more recent development and they have a special technique for collecting particles, differing from that of the traditional impactors. This technique allows virtual impactors to retain the particles collected in the airborne state after classification so that these airborne particles can be transported to other instruments or filters for further analysis. This type of impactor is somewhat similar to the traditional impactor, except that the impaction plate has been replaced by a collection probe. In the virtual impactor, the classification occurs in the collection probe after the aerosol sample exits the acceleration nozzle and enters the probe. Particles with a large enough aerodynamic diameter will travel deeper through the probe (within minor flow) and collected on a filter while small enough particles will remain in the major flow until being directed into the next separation stage.

Cyclones are much more difficult to analyse in theory and mainly differ in terms of their capacity to collect much larger quantities of particles than the traditional impactors. During operation, the aerosol sample enters a cyclone and impacts the cylinder's internal surface tangentially. The aerosol travels in a spiral path inside a cylindrical chamber of the cyclone. Particles with a large enough

aerodynamic diameter are deposited on the inner surface of the cylinder, while relatively small particles may slip through the cylinder.

Based on the literature, Marple and Olson (2011) have summarised the commercially available impactors as represented in Table 2.10. Figure 2.11 illustrates an example schematic diagram of a traditional impactor.

Table 2.10: Selected list of commercially available impactors (Marple and Olson, 2011).

Manufacturer ^a	Sampler Name	Flow Rate (L/min)	Number of Stages	Cutpoints (range, μm)	Comments ^b
<i>Cascade Impactors for Ambient Air Sampling</i>					
<i>COP, NSE, TFS, TIS, WES</i>	Eight Stage Non-Viable Cascade Impactor	28	8	0.4–10	
<i>DEK</i>	ELPI (Electrical Low Pressure Impactor)	10, 30	13	0.03–10	1
<i>DEK</i>	Low Pressure Impactor	10, 30	13	0.03–10	
<i>DEK</i>	PM-10 Impactor	10, 30	3	10, 2.5, 1.0	
<i>HAU</i>	Type LPI	25, 30, 80	6–12	0.0085–16	
<i>INT</i>	Mercer Style (02-001 to 02-011)	0.5, 1, 2, 5	7	0.35–12	2
<i>INT</i>	Multi-jet Style (02-012 to 02-021)	10, 15, 20, 25, 28	7	0.3–12	
<i>MSP</i>	MOUDI (Micro-orifice impactor model 100)	30	8	0.18–10	
<i>MSP</i>	MOUDI (Micro-orifice impactor model 110)	30	10	0.056–10	3
<i>MSP</i>	Nano-MOUDI (model 115)	10	3	0.01–0.032	3
<i>MSP</i>	Nano-MOUDI II (model 125)	10	13	0.01–10	3
<i>MSP</i>	Nano-MOUDI II (model 122)	30	13	0.01–10	3
<i>MSP</i>	Cleanroom Cascade Impactor	3	6	0.05–10	
<i>MSP</i>	High Flow Cascade Impactor	100	6	0.25–10	
<i>CMI</i>	QCM Real-Time Impactor, PC-2	0.25	10	0.05–25	4
<i>CMI</i>	QCM Real-Time Impactor, PC-2H	2	10	0.05–10	4
<i>CMI</i>	QCM Real-Time Impactor, PC-6H	2	6	0.05–6.0	4
<i>ZAA</i>	Air-O-Cell Impactor	15	1	1.0	5
<i>SKC</i>	IMPACT Sampler	10	1	2.5 or 10	

1. Uses electrometers connected to each impactor stage for counting charges on particles for real-time measurement.
2. One round jet per stage.
3. Micro-orifice plates of 2000 jets on bottom stages (6000 jets on Model 122).
4. Uses vibrating quartz crystal collection surfaces as mass-to-frequency transducers for real-time measurement.
5. Plastic rectangular slit cassette.

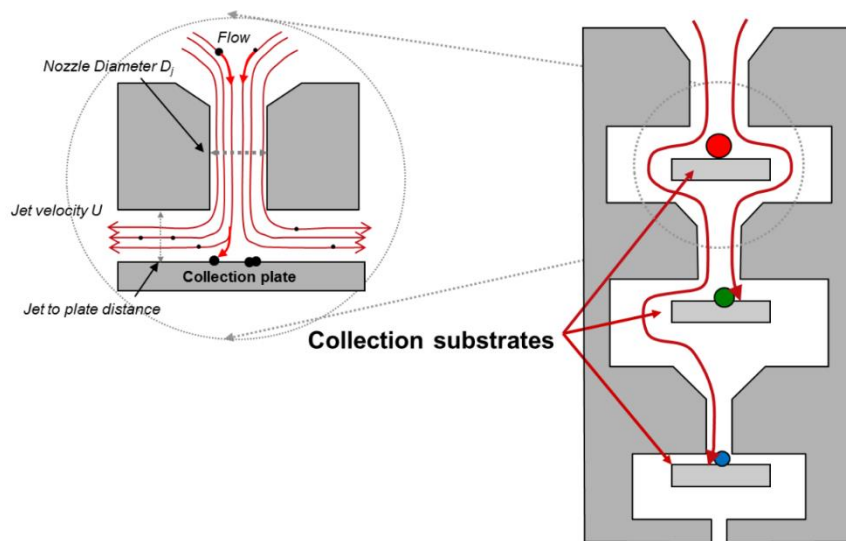


Figure 2.11: Schematic illustration of a traditional impactor (Dekati, 2016).

2.6.2 Dekati Electrical Low Pressure Impactor

Figures 2.12 (a) and (b) show the actual photo and schematic diagram of the Dekati ELPI®+ (Electrical Low Pressure Impactor), respectively. The ELPI®+ unit which was used in the present study is an electronic measuring instrument used to determine airborne particle size distributions in real time and to collect representative samples for subsequent analysis (chemical and gravimetric analysis). This unit can either be used as a stand-alone instrument or run on an external computer with the ELPI®+ VI programme. It allows measurement of airborne particle size distributions at a sampling rate of 1 Hz or 10 Hz.

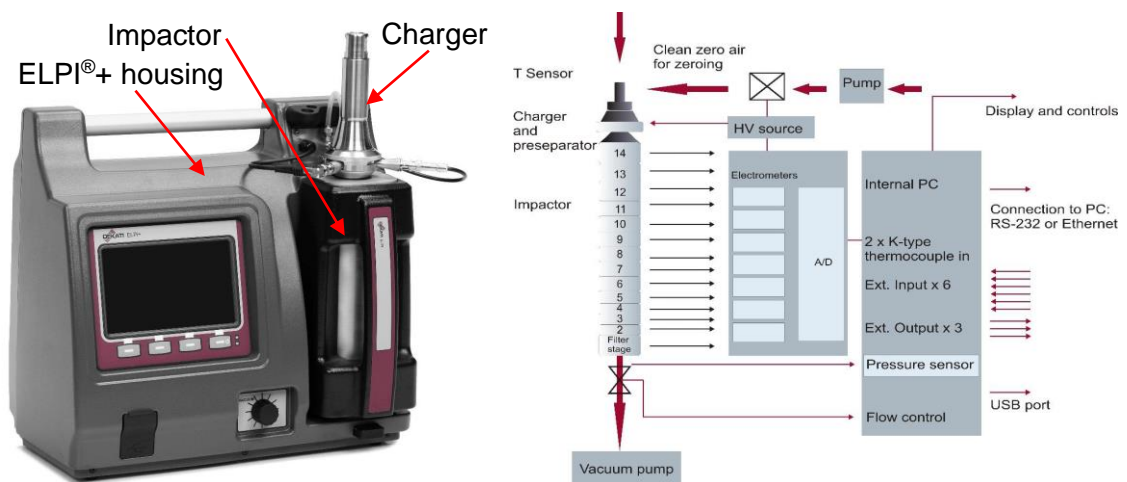


Figure 2.12: (a) Actual photo and (a) schematic diagram of the ELPI®+ units (Dekati, 2016).

The ELPI®+ unit is fitted with a zero air (flush) pump at the top and an external vacuum pump at the bottom. The function of the flush pump is to feed HEPA-filtered air into a charger and the impactor. A HEPA filter is installed at the ELPI®+ inlet to provide the clean air. The vacuum pump is used to draw air into the instrument with the necessary 10 lpm nominal air flow. The recommended vacuum pump capacity is 25 m³/hour when running at 40 mbar absolute pressure.

The Instrument has 14-stage cascade impactor including a back-up filter stage (stage no. 1). These stages can classify particles with a size range of 6 nm to 10 µm. Each stage of the impactor is connected with a sensitive electrometer for measuring electrical currents. Additionally, a pre-separator stage (stage no. 15)

is also placed on top of the impactor to remove particles larger than 10 μm in size. Each stage is electrically insulated from other stages using PEEK™ insulators.

An impactor stage consists of several parts such as PEEK™ insulator, O-rings, jet plate, collection plate and substrate holder ring. These parts are assembled in the ELPI®+ unit as illustrated in Figure 2.13. All the stages have the same part arrangement except for the back-up filter stage. The filter stage does not have a collection plate on its lower side. It is specially designed with many layers of fine mesh to entrap particles in the range of 6 nm-16nm. This stage is the only stage functioning without a filter.

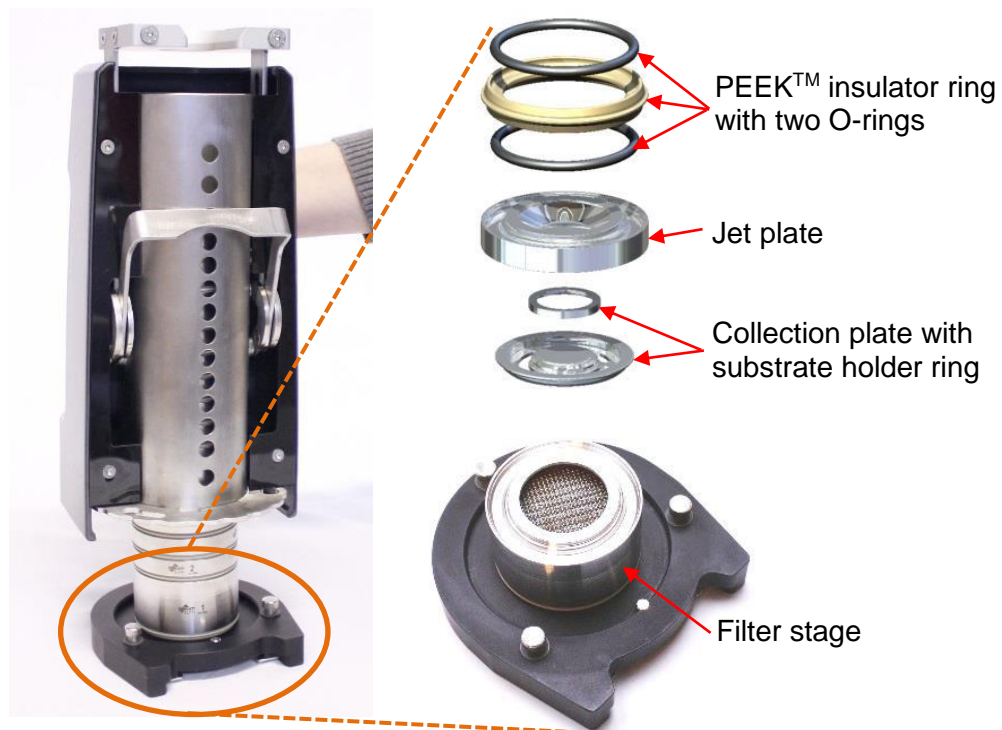


Figure 2.13: an impactor stage of the Dekati ELPI®+ (Dekati, 2016).

During operation, particles entering the instrument are charged to a certain charge level in a corona charger. The charged particles are then classified in the impactor according to their aerodynamic size. Charged particles larger than the cut-off size of a particular impactor stage are collected on the respective collection plate. Such particles produce an electrical current that can be measured and registered by the electrometer for each stage of the impactor. The number concentration of particles is determined on the basis that its value is

directly proportional to the current on the same stage. Other properties such as area, volume and mass are directly calculated from these results by assuming a particle density of 1 g/m^3 .

2.7 Isokinetic sampling principle

Obtaining a representative aerosol sample from a moving air stream often requires an appropriate selection of an aerosol sampling probe. Isokinetic sampling is a preferred concept because it can greatly minimise sampling errors. Isokinetic sampling is an equal or uniform sampling of moving particles and gases (air) in a duct. This is achieved as the air enters the sampling probe inlet at the same velocity and direction as the air in the duct. The sampling probe must therefore be positioned parallel to the local free-stream. Furthermore, under isokinetic conditions the nozzle inlet should have a thin-walled, sharp-edged form in order to minimise air streamline distortion in the neighbourhood of the inlet (Belyaev and Levin, 1974; Brockmann, 2011; Hinds, 1982). An illustration of a sampling probe with relevant dimensions is shown in Figure 2.14. According to Belyaev and Levin (1974), a nozzle is viewed as “thin-walled” if $D/d \leq 1.1$, regardless of t/d and β or, for $D/d \geq 1.1$, if $t/d \leq 0.05$ and $\beta \leq 15^\circ$.

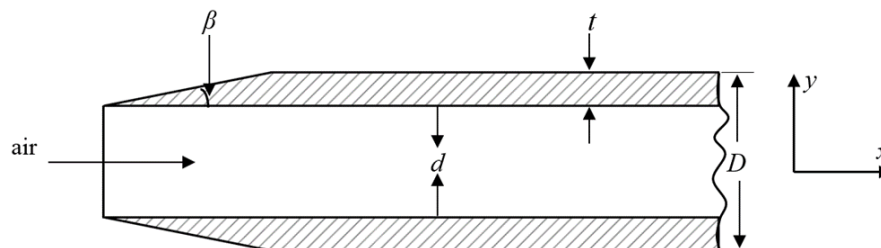


Figure 2.14: Schematics of a thin-walled sampling probe.

Figure 2.15 illustrates the difference between isokinetic and non-isokinetic sampling and depicts how the air carries particles passing through the probe. Under isokinetic conditions, the air velocity entering the nozzle inlet is equal to the free-stream velocity; thus, particles will move following the flow lines of the main stream and the sample stream. Particle sizes with a true representation of the main flow will be collected, resulting in 100% sampling efficiency. In the

super-isokinetic case, the sampling velocity is greater than the free-stream velocity and the local air stream direction will be converged into the nozzle inlet. Due to inertia, large particles will keep moving straight without turning their direction; however, small particles will follow the air stream direction. As a result, more small particles will be sampled compared to the large particles, for the super-isokinetic case. When the sampling velocity is less than the free-stream velocity, the condition is said to be sub-isokinetic. The air stream direction will be diverted around the nozzle inlet and cause small particles to flow around the probe, without entering the inlet. Conversely, large particles will keep following the flow lines and are sampled. As a result, more large particles will be sampled compared to the small particles (Welker, 2012; Wilcox, 1956). This illustrates the importance of achieving isokinetic sampling.

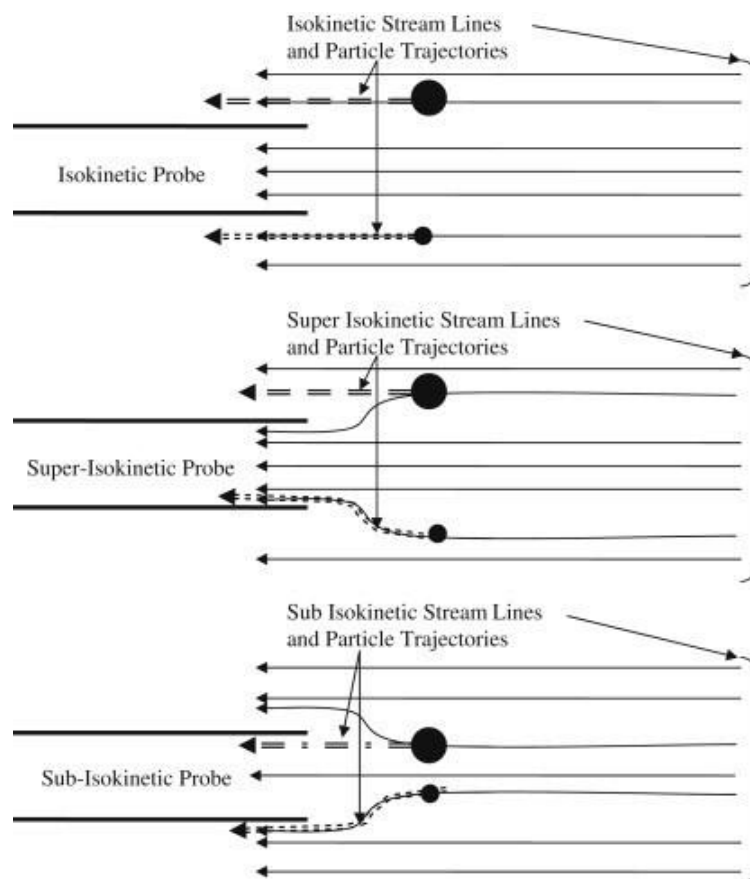


Figure 2.15: Schematic diagram of isokinetic particle sampling (Welker, 2012).

2.8 Characterisation tools

The scanning electron microscope (SEM) is widely utilised in many applications such as forensic, biological, medical and materials sciences. The SEM is a type of electron microscope that scans the surface of solid specimens using a focused electron beam to create the desired image. There are some advantages to the SEM over other microscopes. SEM can generate three-dimensional images while the transmission electron microscope (TEM) can generate only two-dimensional images. However, TEM can produce images with higher magnification and resolution than those produced by SEM. In the case of SEM, it is possible to examine larger samples with a diameter of 200 mm compared to that of the TEM where only a sample diameter of about 3 mm is possible. In comparison to the conventional optical microscope, SEM delivers better high-resolution images of about 1 nm resolution. Using SEM, sub micron-scale features of a sample can be observed with high magnification of up to 1,000,000 times (Vernon-Parry, 2000). In the SEM an image is produced when electrons interact with atoms in the sample. This interaction generates various signals that can be used to obtain information about the sample including surface morphology (size, shape and texture), crystalline structure and crystal orientations.

The SEM is also capable of performing analyses at selected point locations on the sample in order to obtain chemical information. This approach is usually carried out using a variety of techniques, including the integration of the SEM with the X-ray energy dispersive spectrometer (EDS). EDS is an analytical technique used to identify and quantify the surface elemental composition of a sample. The compositional information can be determined at an individual point or at an imaged area which can provide an overall mapping of the sample. In this technique, X-ray energies are released when an electron beam is applied to the surface of the sample. The energies of the X-ray are essentially the characteristics of the atomic structure of the elements. The energy dispersive detector measures the number and energy of the X-rays released and provides information on the elemental composition (Ebnesajjad, 2014).

2.9 Keronite PEO surface treatment technology

Plasma electrolytic oxidation (PEO) is an electrochemical surface treatment process that provides protection against corrosion, wear and heat for lightweight metal alloys such as aluminium, magnesium and titanium. Keronite is a global technology company that can offer the most advanced PEO technology for a wide range of applications in various industries. Established in 2000 in Cambridge, the company began with a simple mission to advance materials science through PEO technology. Since then, Keronite has become the world leader in innovative surface treatment technology. There are two fundamental benefits of Keronite PEO coatings namely extending the life and reducing the weight of components. Keronite coatings are far superior compared to anodising and thermal sprays (Keronite, 2020).

Keronite has developed a special form of PEO process to transform the substrate metal surface into a hard, dense, wear-resistant and adhesive oxide layer. The process employs nontoxic and dilute alkaline electrolytes which are free from chrome and other heavy metals. During the process, a lightweight metal is submerged in an electrolytic bath and millions of very short-lived plasma discharges are generated by an electrical potential. The plasma is used to modify the growing oxide layer (oxide-based ceramic) and alter the microstructure of the substrate to provide excellent corrosion resistance and fatigue strength. The PEO coatings can be tailored to produce the desired key characteristics by changing process parameters (Keronite, 2007). Table 2.11 shows a typical set of process parameters used during Keronite PEO of aluminium alloy (AA7075).

Studies have shown that Keronite PEO coating can offer extremely good surface properties. Shrestha and Dunn (2007) investigated the coating microstructure and surface damage of the Keronite layer and made comparisons with those for a hard anodised coating. In these experiments, the Keronite PEO coating was applied to AA7075 aluminium alloy. Scanning electron microscopy (SEM) micrographs showed that the surface of an as-prepared Keronite layer was composed of particle-like structures that tend to be more irregular and spherical in shape. In contrast, the surface layer of the hard anodised coating contained

several voids and micro-porosity. At the sharp edge of the coating, the Keronite layer had a good and uniform coating coverage and no sign of cracks was found on the surface; however, the hard anodised layer showed the presence of wide-opening cracks on it. Figure 2.16 shows SEM micrographs of the as-prepared surface of the Keronite and hard-anodised coatings. Another surface test (fretting test) revealed that the Keronite coating showed superiority over the hard-anodised coating. The presence of surface damage (extensive surface cracks) could only be seen in the tested hard-anodised coating. However, there was no visible surface damage in the tested Keronite coating. Shrestha et al. (2006) revealed that the Keronite coating was four times harder than the hard-anodised coating. This extreme hardness was believed due to the structure of the coating which was composed of different phases. The study showed that the Keronite coating mainly consisted of the crystalline γ -Al₂O₃ phase while the hard-anodised coating contained the amorphous phase. Malayoglu et al. (2011) investigated mechanical and tribological properties of 6082 aluminium alloy which was surface-treated by Keronite PEO and hard anodising processes. They found that the hardness, elastic modulus, adhesion strength and wear resistance of the Keronite coating were better than those of the hard-anodised coating.

Table 2.11: Typical process parameters for Keronite PEO process (Shrestha and Dunn, 2007).

Process parameter	Value
Pre-treatment	Degrease only
Electrolyte	Proprietary alkaline free of Cr, V or other heavy metals
Total salt content (%)	<4
Typical pH	7-12
Nominal thickness (μm)	15-60
Coating rate ($\mu\text{m}/\text{min}$)	1 - 4
Voltage (V)	200 - 900
Process temperature ($^{\circ}\text{C}$)	12 to 30
Surface appearance	Grey to Charcoal black

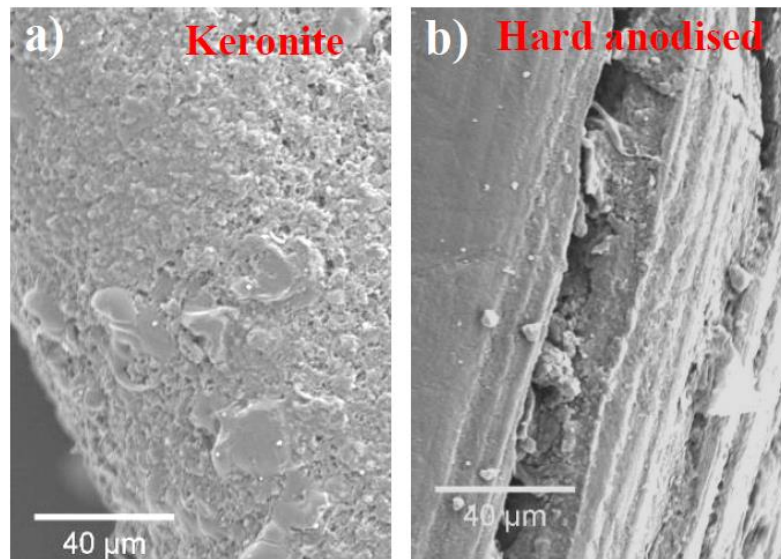


Figure 2.16: SEM micrographs of an as-prepared surface of (a) Keronite and (b) hard-anodised coatings (Shrestha and Dunn, 2007).

2.10 Applications of Computational Fluid Dynamics in braking simulations

Computational Fluid Dynamics (CFD) is a powerful tool to numerically simulate and predict fluid-flow phenomena based on the governing Navier-Stokes equations. CFD can be employed to solve and analyse multiple problems for fluids engineering. The rapid development of computers and CFD-based software packages makes solving times quicker and attracts great interest. Several areas of CFD applications include aerospace and defense industries, automotive engineering, chemical and mineral processing, biomedical science and engineering, power generation, sports, etc. In automotive engineering, CFD is commonly used to improve automotive design and to meet certain requirements and specifications by optimising engineering components and systems (Tu et al., 2013). The demand for high-performance disc brakes has encouraged numerous researchers to focus their studies on the disc brake cooling area (Palmer et al., 2009; Qian 2002; Nutwell and Ramsay, 2009; Galindo-López and Tirovic, 2012; Belhocine and Wan Omar, 2018). With the aid of CFD analysis, they have found that the geometric design of ventilated brake rotors is an essential factor in the improvement of the cooling process of the

rotors. For example, Belhocine and Wan Omar (2018) has utilised CFD analysis to investigate the behaviour of airflow around automotive disc brake rotors for both solid and ventilated designs. The results showed that the ventilated brake rotor has better convective heat dissipation compared to the solid one.

The application of CFD simulation in emissions of brake wear is relatively recent. In the literature, very few related studies have been reported. Perricone et al. (2016) performed simulations of fluid dynamics to analyse airflow behaviour in the newly developed brake testing rig using the StarCCM+® CFD code. They concluded that the sampled aerosol inside the chamber is well mixed and the velocity of the airstream is fully developed in the sampling pipe. Agudelo et al. (2019) used a Design of Experiments (DOE) and CFD to understand how the flow within an enclosed chamber and relevant operating conditions affect response variables such as turbulence intensity, mean velocity profiles and residence times. The DOE factors considered include airflow level, brake size, rotor style, caliper position, brake rotational direction, brake rotational speed and fixture style. The airflow level and brake rotational speed were found to be the most significant factors that influence the outputs of the simulations.

2.11 Summary

This chapter has outlined various aspects of disc brake technology and particulate matter background information. Although no legislation for non-exhaust emissions exist, general standards or guidelines have been implemented to control air quality in European countries. Air pollution has been shown to adversely affect humans by either particle size or chemical composition. The proportion of non-exhaust emissions in traffic-related emission is more substantial nowadays relative to that from recent decades. Brake wear particulate emissions have been reported to exceed non-exhaust emissions and this attracts much interest in the scientific community. Numerous particle collection methods have been proposed and utilised since no proper standards are available. The braking test cycles employed were also different but many of them performed repeated full stop braking. The application of the drag brake condition to generate the brake wear particles was not found in literature. Most

studies focussed on the particle mass distribution, particle number distribution and chemical composition. In general, the findings indicate discrepancies and cannot be readily comparable due to variations in testing methods, particle measuring instruments and brake pad types.

Particulate matter measurement instruments used are mostly based on the inertial principle. Several studies have applied isokinetic sampling principle to achieve an aspiration efficiency of 100%. CFD simulations have potential to be used in brake wear particle emission studies, particularly for predicting the behaviour of airflow inside the enclosure which houses the brake assembly.

Lightweight disc brake rotors have recently received much attention from many researchers after legislation on exhaust emissions was introduced. It is estimated that using a lightweight brake rotor in a vehicle can reduce approximately two-thirds of the weight compared to a conventional brake rotor. Despite the advantage of weight reduction, the lightweight brake rotor has quite a low maximum operating temperature and this can affect its thermal performance. It is therefore crucial to protect the rubbing surface of the rotor through some kind of coating. This coated lightweight brake rotor is predicted not only to be capable of reducing the weight of a vehicle but also capable of reducing the non-exhaust emissions in the atmosphere. An initial finding has demonstrated that the alumina coated lightweight brake rotor (aluminium alloy) has a wear rate 15 times lower than that for the grey cast iron rotor, suggesting that it produces substantially less particulate emissions than for the cast iron type (Hussain, 2018). However, further investigation needs to be conducted using a more reliable experimental setup in order to verify this hypothesis.

Chapter 3 : Materials and experimental methods

3.1 Introduction

This chapter describes the disc brake pair materials and the experimental techniques employed in the current research for measuring and collecting airborne brake wear particulate matter. It also provides information concerning the existing dynamometer system and the design of a sampling probe to assist particle measurement and collection. The calibration of airflow velocity in the system using an anemometer is explained in detail. Moreover, the rotor thickness variation (RTV) and runout are elaborated for both grey cast iron (GCI) and PEO-Al rotors. All braking test procedures covered in this chapter are newly developed methods aiming to generate sufficient airborne particles for subsequent analysis. Procedures for impactor cleaning and gravimetric analysis were developed based on the manufacturer's manual. Scanning Electron Microscopy (SEM) and Energy-Dispersive X-ray Analysis (EDX) are two material characterisation techniques that were used to analyse the airborne brake wear particles.

3.2 Disc brake pair materials

Two kinds of brake rotor, namely the conventional GCI and PEO-Al rotors, were employed in the present study for investigating airborne brake wear particle emissions. The existing Rover 75 brake rotor (commercial GCI rotor) was previously used by another student (Budinsky, 2018) and it had already undergone the standard burnishing process. This rotor has an outside diameter of 284 mm and an original thickness of 22 mm. It was manufactured with a vented section in between the two braking contact surfaces to provide effective cooling for the part. The standard NAO brake pads (Mintex MDB1189) were utilised

along with the Rover 75 rotor to form the friction pair. These commercial brake pads have a contact area of approximately 2400 mm².

The second brake rotor was designed and developed by Hussain (2018) using in-house facilities. The rotor was constructed using lightweight aluminium alloy (Al-6082) as a substrate and the PEO treatment was applied to its rubbing surfaces by Keronite International Ltd. The details of the PEO surface treatment process are explained further in Section 3.3. Generally speaking, the PEO-Al rotor consists of two separate parts containing the rubbing surfaces with a vented section in between them. The completely assembled PEO-Al rotor has a thickness of 25 mm and an outside diameter of 280 mm. The brake pads used with this coated rotor were specially designed and supplied by TMD Friction Ltd. The contact area of each pad is approximately 2960 mm². The details regarding the formulation are confidential and remain the intellectual property of the company. Figure 3.1 shows images of the Rover 75 and PEO-Al brake rotors alongside the corresponding brake pads.

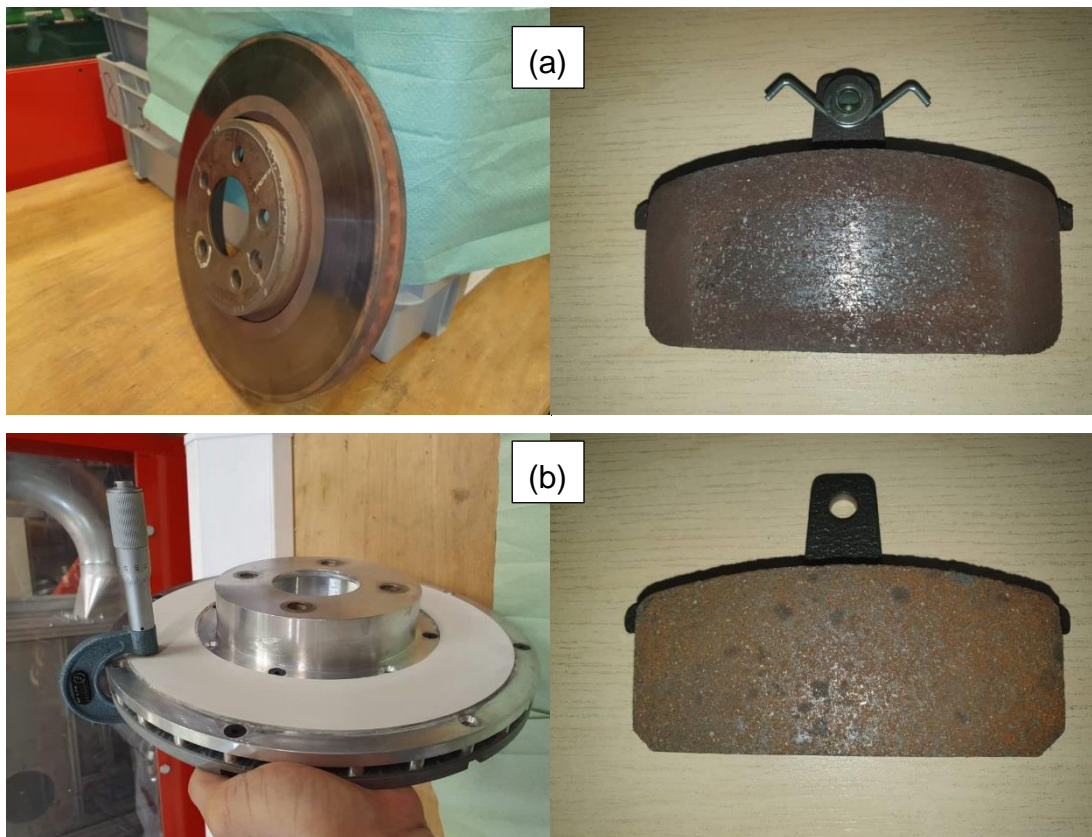


Figure 3.1: (a) GCI and (b) PEO-Al brake rotors with its corresponding brake pad.

3.3 Remanufacture of the PEO-Al rotor

The existing PEO-Al rotor was intended to be employed in the current braking tests for measurements and collections of the airborne brake wear particles. The rotor was initially tested on the dynamometer to investigate the generation of a steady-state temperature on the rubbing surface as different pressures were applied. However, results showed that cyclic torque fluctuations were somewhat higher than expected and constant temperatures could not be attained. Therefore, the decision was made to recoat the rotor as the old rubbing surfaces were found to contain some considerably wide and deep grooves.

Before the retreatment process was carried out, the old coating layer was removed from the rubbing surfaces of the rotor by conventional machining operations. The brake rotor was then disassembled into three components namely outboard cheek (with top hat), inboard cheek and inner ring (containing vanes) as shown in Figure 3.2.

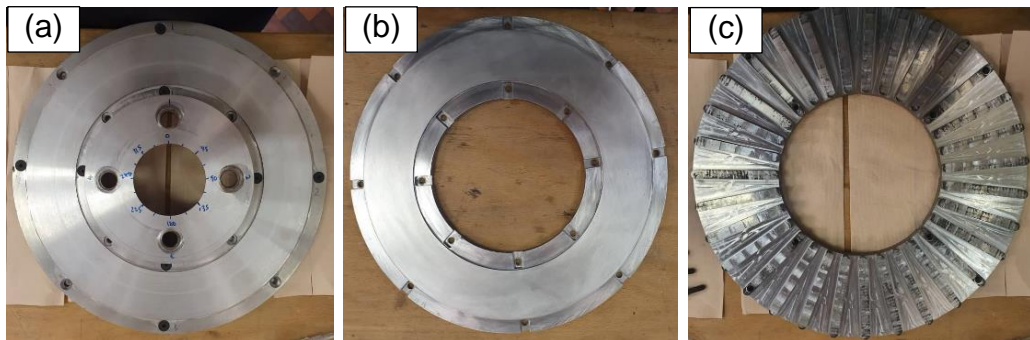


Figure 3.2: Brake rotor components, (a) outboard cheek, (b) inboard cheek and (c) inner ring.

3.3.1 Preparation of Al rotor for PEO treatment (surface masking)

Keronite recommended that the surface roughness of the rotor rubbing surfaces should be less than approximately $0.5 \mu\text{m}$ before the treatment process. The Ra values of the rotor rubbing surfaces were measured using the Talysurf – PGI 800 instrument. The reading was taken at four points (at 90° increments) across the surface. It was found that the two halves of the rotor (outboard and inboard cheeks) have Ra value around $1.0 \mu\text{m}$ after the above machining operations

(See Figure 3.3 (a)). Abrasive paper was utilised to polish the two rubbing surfaces of the rotor by hand. Paper with a grit range of P600 was first applied, followed by P1000 grit paper. Figure 3.3 (b) displays the rubbing surface of the two halves of the rotor after final polishing. The surface roughness of the two halves of the rotor was measured and the results are represented in Table 3.1. Overall, the values obtained were of the order of 0.5 μm and this result was considered acceptable for the PEO process.

Table 3.1: Ra values for the two halves of the rotor in μm .

Measured point	Outboard cheek	Inboard cheek
Ra 1 (90°)	0.5941	0.6820
Ra 2 (180°)	0.4401	0.6769
Ra 3 (270°)	0.4868	0.6408
Ra 4 (360°)	0.4983	0.6531
Average	0.5048	0.6632

Since only the rubbing surfaces of the rotor would be coated, the other surfaces needed to be covered by a special masking material (Suprawax 114) so they were protected from the PEO process. Masking tape was used to protect the rubbing surfaces of the rotor from droplets of the green Suprawax 114 that might possibly drop down during the masking process. Electrical tape was also used to cover the screw holes to ease the masking and de-masking processes. A screw hole on each half of the rotor was left uncovered so that a jig could be fixed into it. However, these two holes were temporarily covered by a screw, washer and nut before the masking process. Figure 3.3 (c) shows the two halves of the rotor ready for the masking process.

Using a fine brush, the green Suprawax 114 was applied on all surfaces of the two halves of the rotor except the rubbing surfaces that were covered by the masking tape. The Suprawax 114 was applied layer by layer on the surfaces until it became thick enough to resist the PEO treatment. The succeeding layer was applied only when the preceding layer had completely dried. Figure 3.3 (d) shows the two halves of the rotor after the masking process and ready for the jig installation.

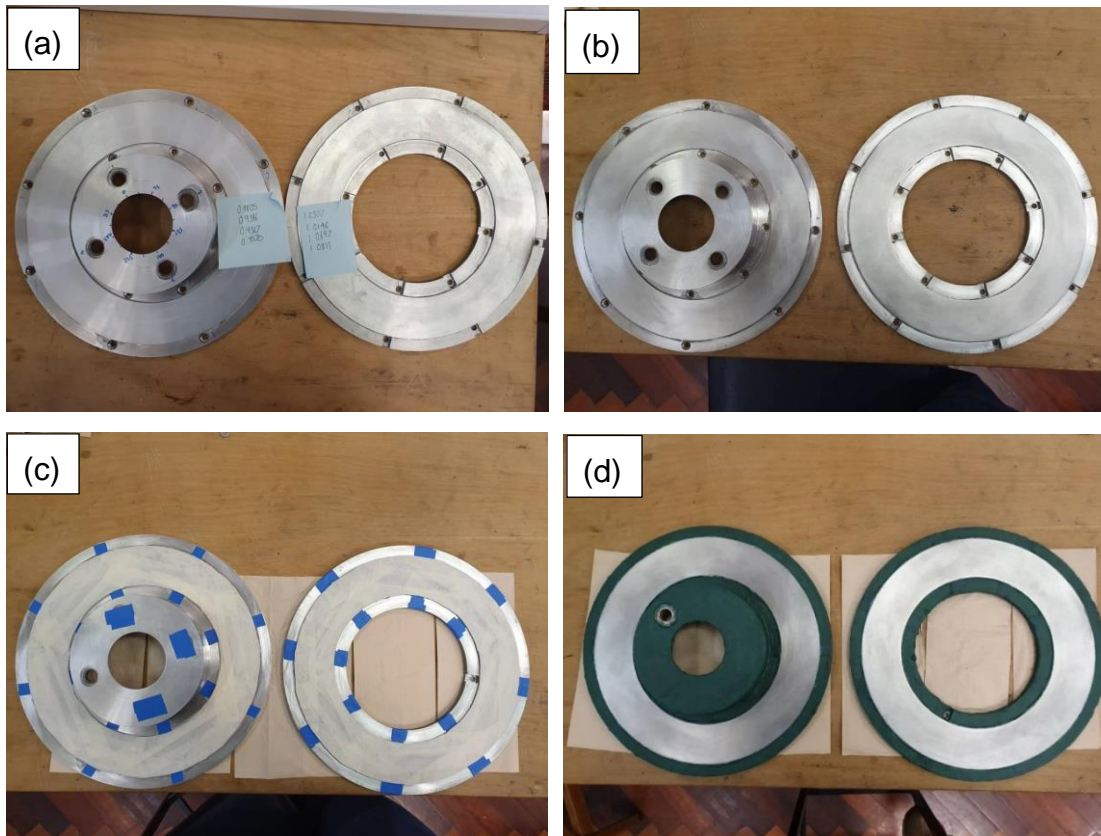


Figure 3.3: Two halves of the rotor in a) machined, b) polished, c) tape-covered and d) masked conditions.

3.3.2 PEO surface treatment process

The masked rotor halves were taken to Keronite for the surface treatment process through Plasma Electrolytic Oxidation (PEO). The two halves of the rotor were each fixed with a jig for connecting them to the high voltage electrical source. This allows a large current density to flow to the rotor halves when a high voltage is applied thereby creating a plasma discharge. Prior to the process, the uncovered surface of the rotor halves was degreased by spraying acetone and then rinsing it with water. Figure 3.4 shows the two halves of the rotor with the installed jig on them ready for the PEO treatment.

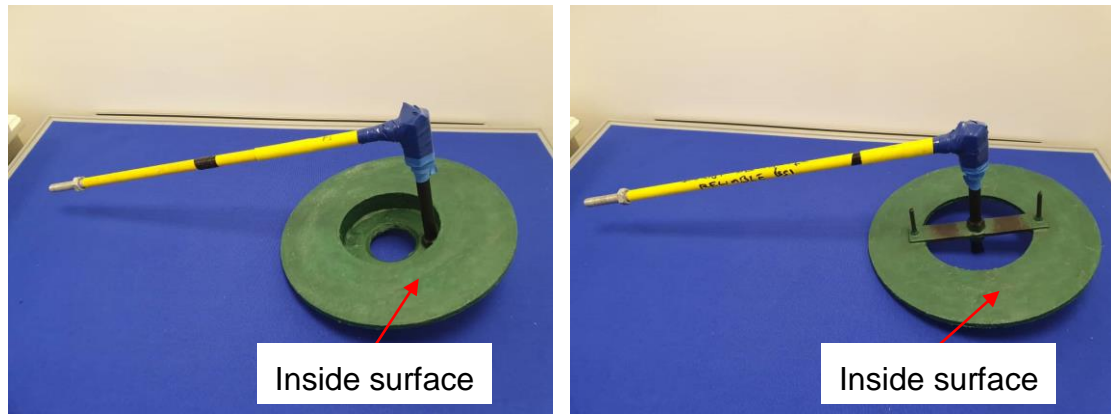


Figure 3.4: Jigs installation on the two halves of the rotor.

In the PEO process, the two masked rotor halves act as an anode while the stainless steel electrolyte container acts as a cathode. The process commenced when the rotor halves were immersed into the 1000 litre bath of electrolyte of a low concentrated alkaline solution as shown in Figure 3.5 (a). The process parameters were set by the Keronite company representative and these details are classified. The coating thickness was targeted to be around 50 μm which is similar to the previous coating thickness. In fact, the cost of a coating increases as the coating layer becomes thicker. Therefore, the value was chosen based on a trade-off between the cost and a certain amount of wear that can be tolerated while the coating is still sufficiently thick to act as a thermal barrier. A high voltage of over 200 volts was applied during the process and this creates an intense plasma which results in oxidation on the surface of the aluminium alloy. The high energy caused the oxide layer to transform into (mainly) crystalline alumina (Al_2O_3). Figure 3.5 (b) exhibits the formation of thin coating layers on the rubbing surfaces of the two rotor halves during the PEO process. After some time, the two rotor halves were taken out from the tank and the thickness was measured at different points using an ultrasonic thickness gauge. The treatment process was then resumed until a thickness of around 50 μm was attained. Overall, the rotor was immersed in the bath for about 4 hours to complete the process. The final thickness measured was within the range of 45 – 50 μm for both halves of the rotor. The PEO coated rubbing surfaces before and after de-masking are shown in Figures 3.5 (c) and (d), respectively.

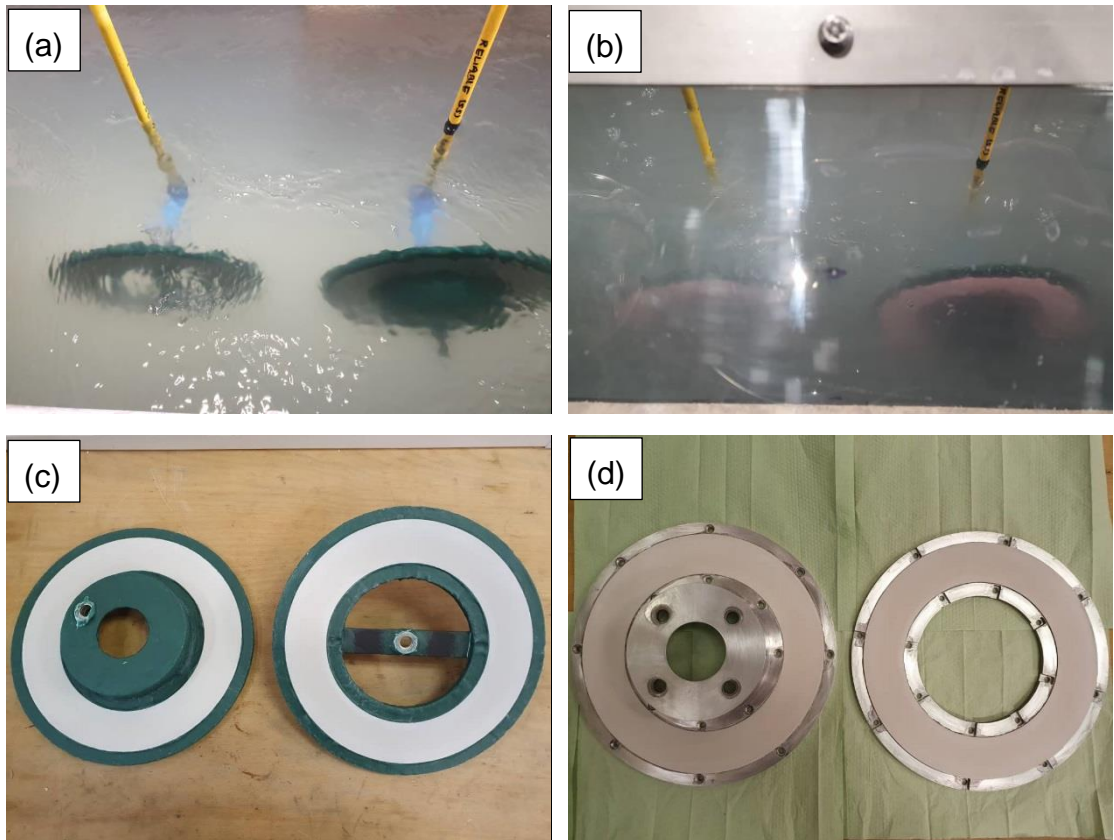


Figure 3.5: Two halves of the rotor (a) at the beginning of the PEO process, (b) after some time of the PEO process, (c) before de-masking and (d) after de-masking.

3.4 Brake Dynamometer

In this project, the determination of brake wear emissions is properly conducted inside a laboratory with full control of the environment. A wear debris extraction system was developed based upon an existing full-scale disc brake dynamometer which was fitted with either the cast iron or PEO-Al rotor and the corresponding asbestos-free pads. The main components of the brake dynamometer include a DC electric motor, drive belt, torque transducer, actuation system, brake caliper and sliding thermocouple. Figure 3.6 shows the general layout of the existing full-scale disc brake dynamometer. A 45 kW electric motor is employed to drive the main shaft and the brake rotor through a drive belt unit. To measure the brake torque and rotation speed, a torque transducer (Torquemaster TM213) is situated between the two bearings. The torque transducer was able to measure the brake torque and the rotation speed up to

limits of 500 Nm and 1500 rpm, respectively. Furthermore, the brake dynamometer is fitted with an actuation system to apply hydraulic pressures on both sides of the brake rotor via a purpose-built 4-piston caliper. A K-type sliding thermocouple is used to measure temperatures on the mean rubbing surface of the brake rotor at both sides of the brake caliper. The test parameters are controlled and monitored using a LabView data acquisition program which was developed by a previous student (Budinsky, 2018). These parameters are stored in a single file which can be retrieved for further processing. The applied hydraulic pressure and the rotation speed can be controlled independently while other parameters such as brake torque and coefficient of friction are derived from the measured parameters. The temperature parameter depends on the heat generation on the rubbing surface of the brake rotor and can be monitored throughout the test.

This brake dynamometer is capable of applying drag braking conditions only. The Labview software can maintain the constant speed braking condition at pre-set hydraulic pressures and rotational speeds.

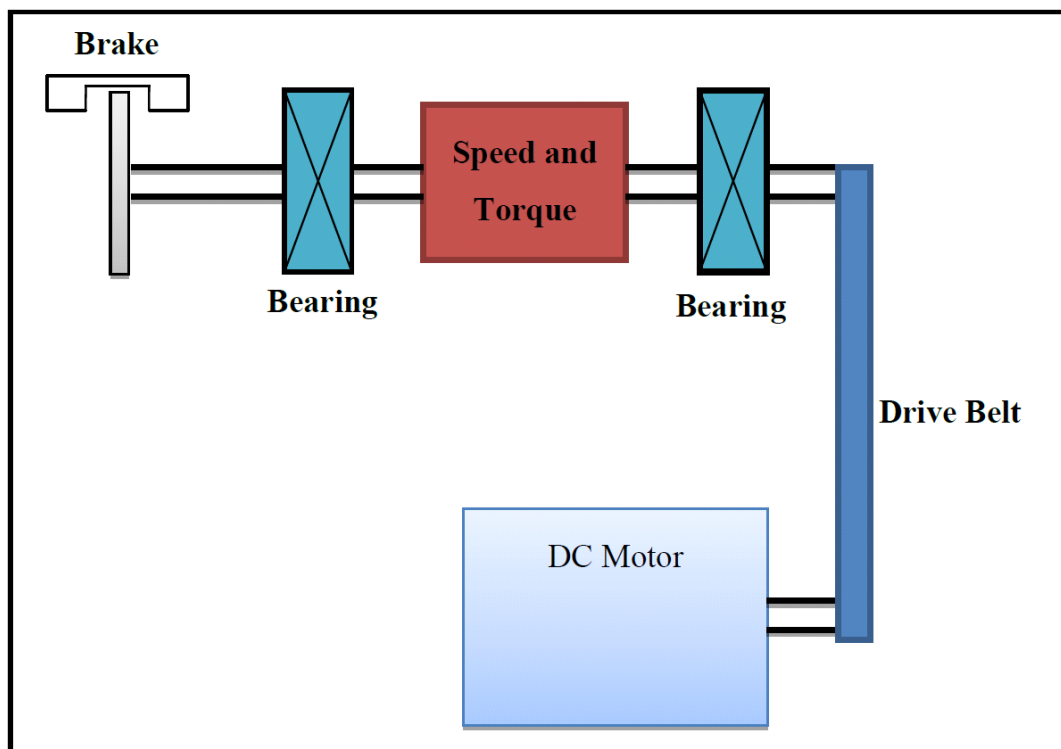


Figure 3.6: General layout of the full scale disc brake dynamometer (Alnaqi, 2014).

3.5 Measurement of the brake rotor runout and thickness variation

A brake rotor with a non-uniform thickness or axial runout has a great tendency to induce cyclic torque fluctuations in a disc brake system. Measurement of the rotor thickness variation (RTV) was conducted to investigate the extent to which the two braking contact surfaces of a brake rotor lie parallel with each other. Maximum parallelism must be attained to prevent the occurrence of torque pulsation in the brake disc system. The RTV is specified to be 0.1 mm maximum in order to keep the torque variation as low as possible (Hussain, 2018). Another problem commonly arising in a brake disc system is the occurrence of rotor axial runout. The runout is measured on the dynamometer to determine the amount of wobbling in the brake rotor as it is rotated. The brake rotor runout must be kept minimal so that the disc brake does not vibrate excessively when in operation. High rotor runout also leads to uneven wear of the brake rotor and pad surfaces and this may also result in a variation in the rotor thickness. It is good practice to maintain the rotor runout to less than 0.08 mm (Day, 2014). However, some manufacturers allow higher runout than others and this can be up to 0.2 mm (Carley, 2008). Therefore, measuring the RTV and rotor runout was important in this study to allow corrective action to be taken before the brake rotors are utilised. This will allow the brake system to work properly without major problems.

3.5.1 Brake rotor thickness variation

As mentioned in Section 3.2, the GCI brake rotor is a commercial brake rotor that was precisely manufactured with highly developed facilities in a company. The brake rotor should have gone through a detailed product quality inspection to verify whether it meets relevant quality requirements. As a result, a GCI brake rotor with top-quality production and assembly tolerances was utilised in this study. On the contrary, the PEO-Al rotor was made using in-house facilities. Thus, this custom-made rotor may have some shortcomings in terms of machining and assembly inconsistencies. A more detailed RTV measurement was therefore performed on the PEO-Al rotor compared with the GCI rotor. The

measurement was performed on the rubbing surface area of the rotor with a micrometer. The thickness of the PEO-Al rotor was measured at 16 equidistant circumferential points while for the GCI rotor, only 4 equidistant points were taken for the measurement, as illustrated in Figure 3.7. For the PEO-Al rotor, the measurement was carried out after the use of 0.1 mm aluminium shims between the brake rotor vane plate and the inboard cheek in order to reduce the variation.

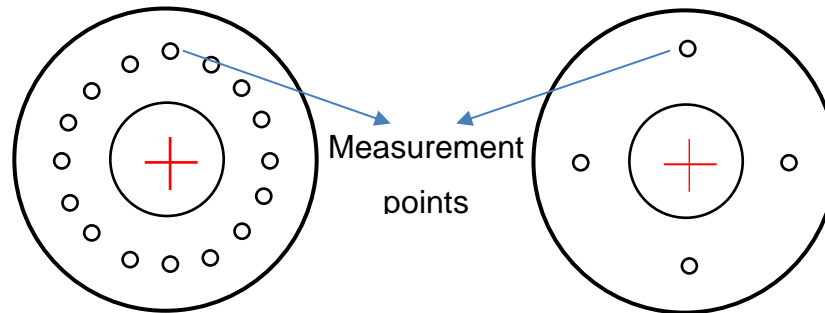


Figure 3.7: Measured point on the rubbing surface of the PEO-Al rotor (left) and GCI rotor (right).

Table 3.2: Rotor thickness variation for PEO-Al and GCI rotors.

Location (°)	Thickness (mm)	
	PEO-Al rotor	GCI rotor
0/360	24.670	21.690
22.5	24.695	-
45.0	24.710	-
67.5	24.685	-
90.0	24.665	21.640
112.5	24.675	-
135.0	24.680	-
157.5	24.670	-
180.0	24.660	21.640
202.5	24.660	-
225.0	24.660	-
247.5	24.660	-
270.0	24.660	21.670
292.5	24.675	-
315.0	24.695	-
337.5	24.690	-
Max value (mm)	24.710	21.690
Min value (mm)	24.660	21.640
Range (mm)	0.050	0.050
Mean value (mm)	24.676	21.660
Standard deviation	0.016	0.024

Table 3.2 shows the brake rotor thickness values at the various measurement points. This table reveals that the thickness of both rotors only varies slightly with a low standard deviation and maximum RTV of 0.05 mm.

3.5.2 Brake rotor runout

Measurement of the runout with the rotor mounted on the dynamometer was performed using a dial gauge. The way in which the two brake rotors were measured was slightly different. For the GCI rotor, there are two radial locations where the rotor was measured, namely 5 mm from the inner and outer edges of the rubbing surfaces. Only a maximum value was taken during this measurement. In contrast, the coated rotor runout was measured at three locations which were 5 mm from the top hat outer radius, the rubbing surface inner radius and the rubbing surface outer radius as shown in Figures 3.8 (b)-(d), respectively. The runout values were taken at fixed 22.5° angular displacements for one revolution of the rotor.

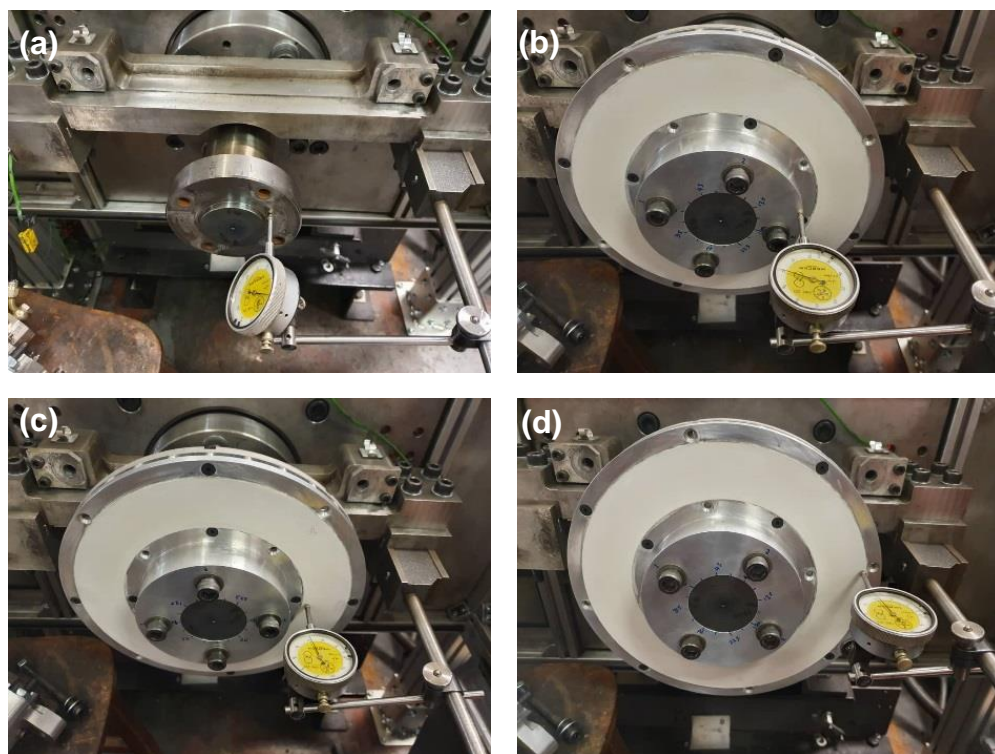


Figure 3.8: (a) adapter set-up on the dynamometer and measurements of PEO-Al rotor runout on (b) top hat, (c) rotor inner and (d) rotor outer edges.

To obtain the lowest possible runout for the PEO-Al rotor, the rotor and adapter need to be bolted together with the best hole combination. The four holes on the top hat of the rotor and on the adapter were marked with a number 1 to 4. The adapter is actually an additional component used to connect the brake rotor to the main shaft and it contains four holes similar to those on the PEO-Al rotor. The measurement of the runout of the adapter on the dynamometer system is exhibited in Figure 3.8 (a). The rotor was bolted to the adapter with the position of the corresponding adapter-to-rotor holes as follows 1/1, 1/2, 1/3 and 1/4. Therefore, four sets of measurements were recorded. Figures 3.8 (b)-(d) shows the runout measurements for these three locations.

Figure 3.9 shows the plotted runout values for the PEO-Al rotor at the three different locations. It can be seen that the lowest runout was obtained for the alignment of the mating surface 1/4. Here the maximum runout recorded was 0.06 mm, 0.06 mm and 0.09 mm for the top hat surface, the inner edge of the rubbing surface and the outer edge of the rubbing surface, respectively. Therefore, the coated rotor was fixed on the adapter according to the 1/4 arrangement of the mating surfaces for all subsequent tests. Additionally, a 0.12 mm aluminium shim was used in order to reduce the rotor runout a bit further. The shim was placed between the adapter surface and the top hat surface of the rotor. Figure 3.10 shows the measured values of the rotor runout at the three different locations without a shim and with the 0.12 mm shim fitted. It can be seen that the use of the 0.12 mm shim minimised the rotor runout to around 0.07 mm maximum and this is therefore crucial to avoid high cyclic torque fluctuations. For the GCl rotor, the maximum runout measured was 0.1 mm for the inner and 0.2 mm for the outer edge of the rubbing surfaces.

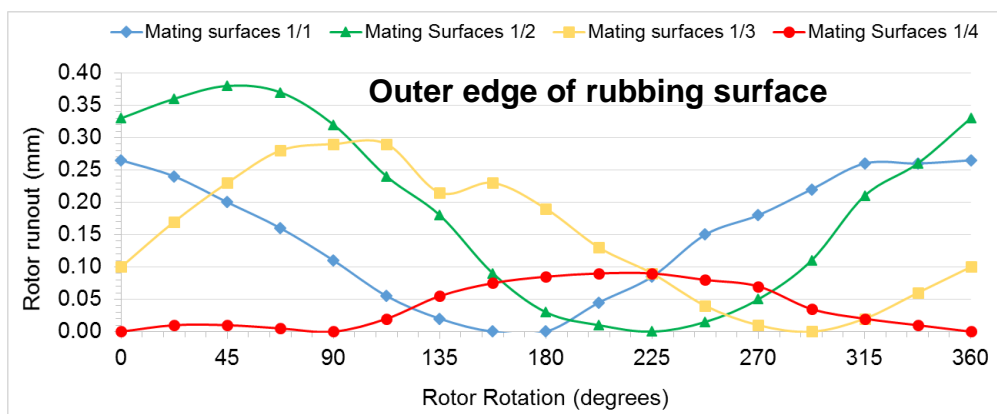
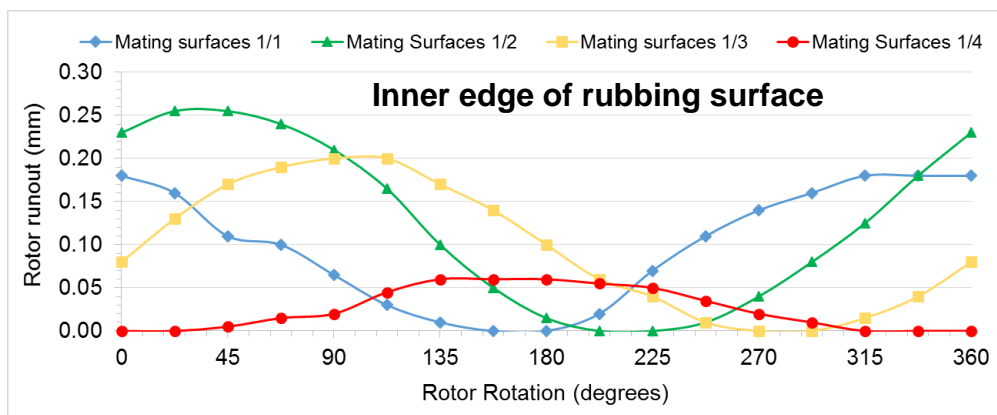
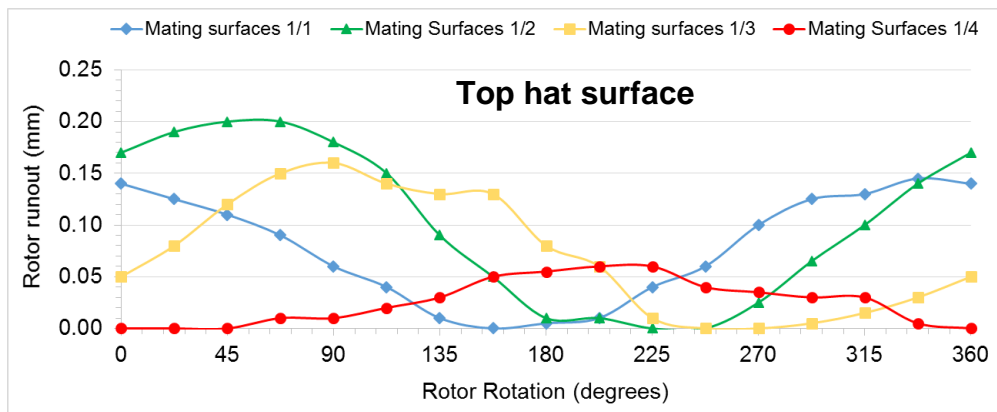


Figure 3.9: Runout of the PEO-Al rotor at the three different locations (without addition of shims).

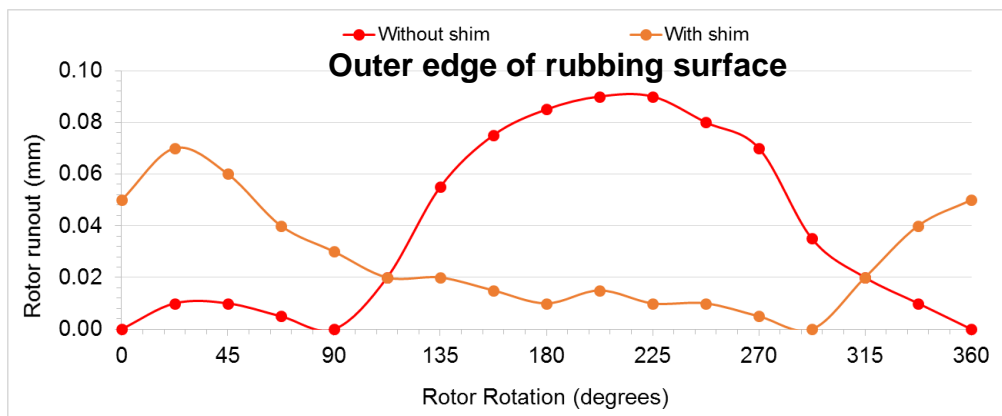
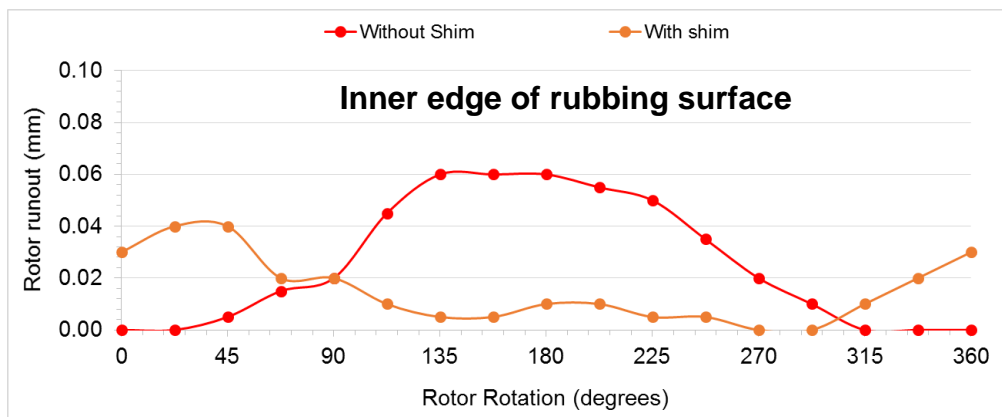
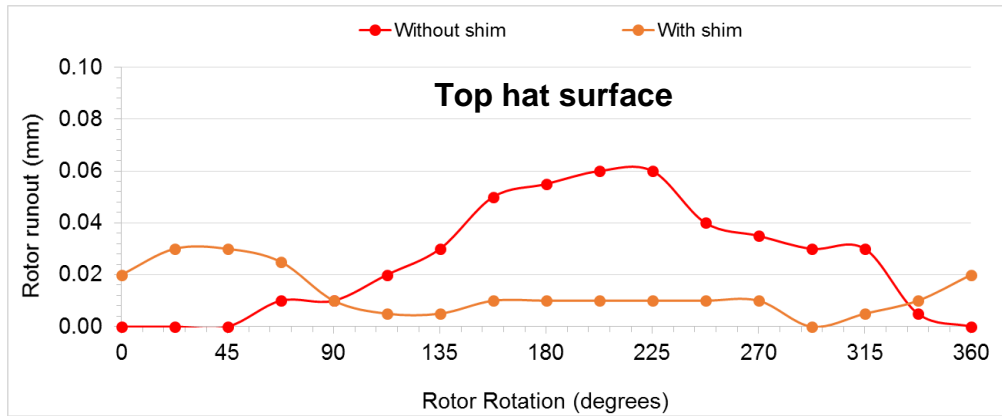


Figure 3.10: Runout of the PEO-Al rotor with and without the addition of shims.

3.6 Extraction and particle capture system

Figure 3.11 shows photographs of the new dynamometer extraction system developed for measuring the brake wear particle emissions. A custom-made hexahedral Perspex box was constructed at the brake end of the main dynamometer shaft in order to seal the air in the immediate vicinity of the brake

assembly and keeping it separate from the laboratory air. The enclosure is connected to HEPA (H14) filters through ducting systems. An inlet duct connects the laboratory air via an inlet HEPA filter to the enclosure while an outlet duct connects the enclosure to an outlet HEPA filter. A further piece of ductwork connects the outlet HEPA filter to a fan with a 4 kW rating on the top of the building. All the ducts were made of galvanised sheet steel and have an inside diameter of 225 mm.

Airflow within the enclosure is controlled by the fan to deliver fresh air through the inlet duct, before it mixes within the brake enclosure and exits through an outlet duct. Incoming and outgoing air is cleaned using the HEPA filters and vented safely to atmosphere on the top of the building. As a safety precaution, a carbon activated filter was employed at the outlet to remove any strong odour and other harmful gases. The speed of the fan can be adjusted by controlling the fan setting to create an air velocity in the range of 6 to 15 m/s. The measurement of the air velocity was carried out using an anemometer at the velocity test point as described below.

Within the outlet duct, four tappings (T1 – T4) and a velocity test point (VTP) were provided for sampling brake wear particulate matter and measuring airflow velocity, respectively (see Figure 3.11). A custom-made sampling probe was utilised at the tap locations to extract representative samples for analysis. Details of the design of the sampling probe based on the isokinetic concept are explained in Section 3.8. To measure and capture brake wear debris, the Dekati ELPI®+ Electrical Low Pressure Impactor is connected to the isokinetic probe at its inlet and a vacuum pump at its outlet using a rubber hose and a vacuum hose, respectively. The ELPI®+ unit operates correctly at the sample flow rate of 10 litres/minute and this flow rate can be obtained by adjusting the impactor low pressure to 40 mbar (± 5 mbar). The impactor low pressure is the downstream pressure measured at the outlet of the ELPI®+ impactor. The value of 40 mbar was set by the manufacturer in the device parameter file in order to acquire the desired sample airflow and particle cut-off diameters. For correct operation, the user is only required to adjust the pressure adjustment valve to the specified pressure value.

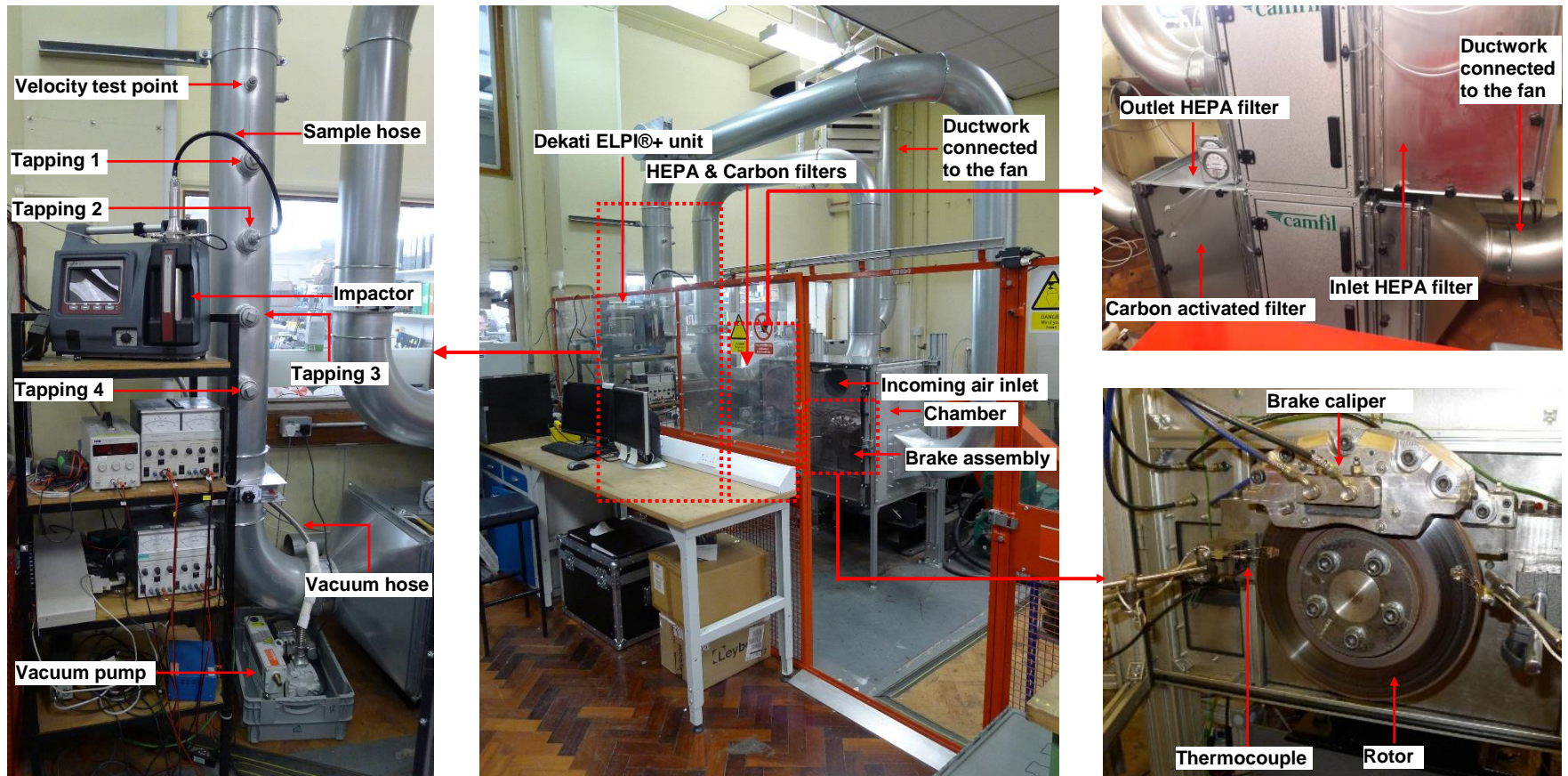


Figure 3.11: Photographs of the dynamometer extraction system.

3.7 Airflow velocity calibration

The calibration of air velocity at the velocity test point of the extraction system was carried out using an airflow TA-2 thermal anemometer (see Figure 3.12). This anemometer was manufactured by TSI Incorporated. The measurement of air velocity was taken at the centre of the outlet duct at different percentages of the fan setting by adjusting the speed control knob. Before the extraction system was turned on, the background air velocity was measured at the same point in order to examine the presence of airflow without the fan power. The measurement showed that the background air velocity passing through the outlet duct was in the range of 0.4 to 0.6 m/s. To ensure the system was stable, the air was allowed to flow through the system for five minutes prior to the actual measurement. In this work, three sets of readings were taken in constant multiples of 5% from 0 to 100% of the fan setting. This was done to minimise any unexpected measurement errors that may occur. Since the anemometer is an analog type, the velocities were recorded over a certain time period. From this range, an average value was calculated for all readings and then the mean and standard deviation of the three sets of the readings were computed. It was found that the lowest and highest possible air velocity within the ducting is 6 m/s and 15 m/s, respectively.

Figure 3.13 plots the mean values of the average velocity of the three readings versus the percentage of the fan setting. Error bars are also added to the graph to represent the corresponding standard deviations to express by how far the three sets of readings differ from the mean value. A standard curve-fitting method was employed to construct a linear line that has the best fit to the series of mean values. A linear interpolation was performed to estimate the percentage value of the fan setting to give the air velocity equal to 6.92 m/s as required for the Dekati isokinetic sampling (see next section). To acquire this air velocity value, it was found that the fan should be set at 5% of its maximum speed.

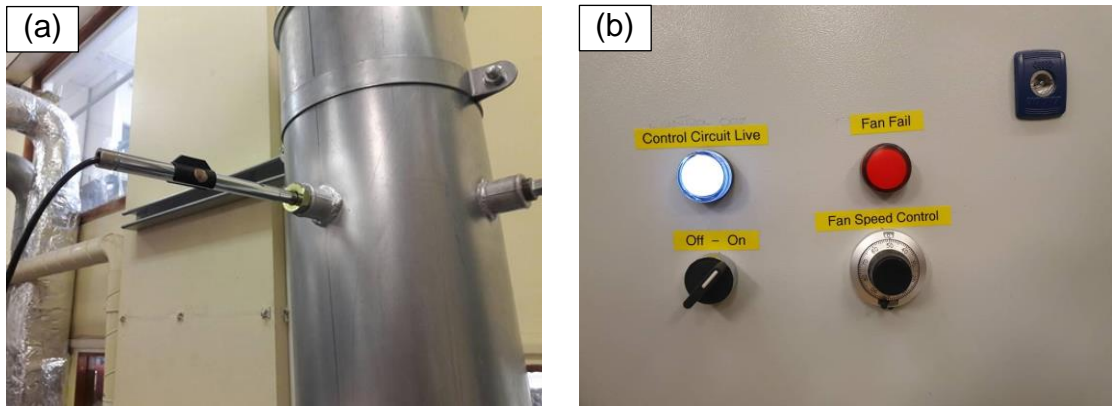


Figure 3.12: (a) an anemometer mounting on the duct and (b) an image of the fan speed control.

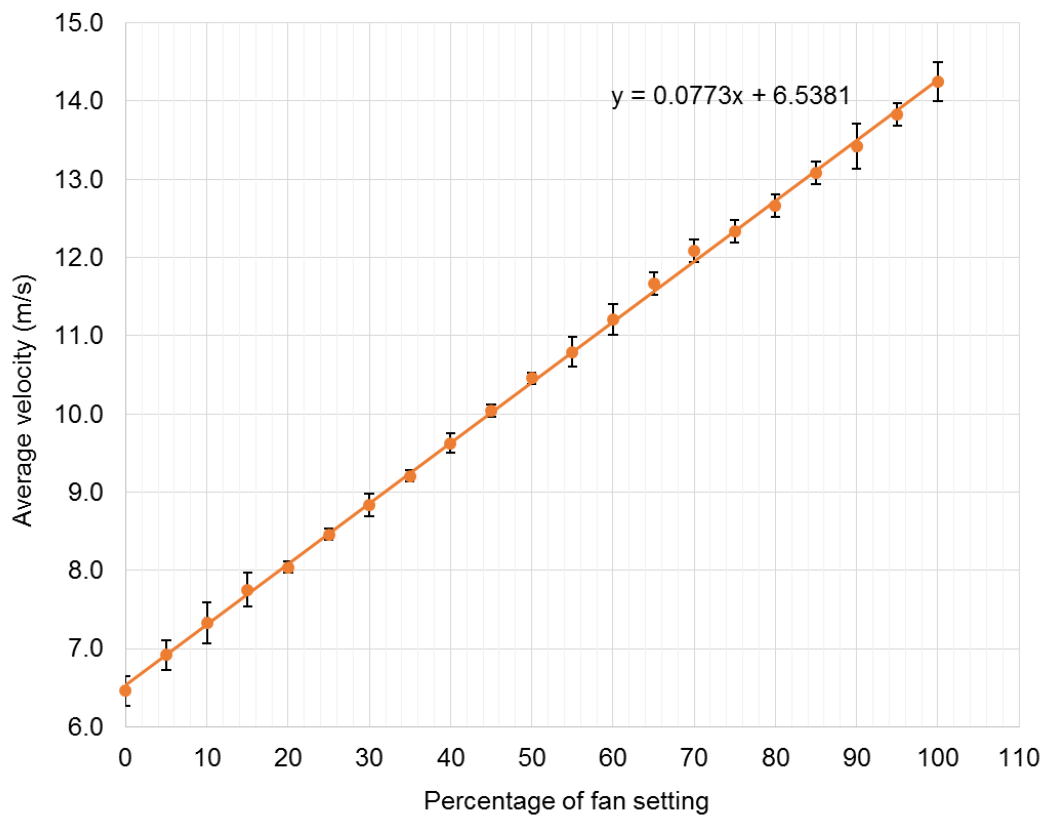


Figure 3.13: Mean value of the average velocity for the three readings at each fan setting.

3.8 Design of sampling probe

An isokinetic sampling concept was applied to the sampling probe design in order to acquire reliable measurement data and avoid sampling errors. The use of a

metal or electrically conductive sampling tube for particle sampling can largely reduce the particle deposition by means of electrostatic effects (Brockmann, 2011). In this study, the sampling probe was made of a standard thin-walled tube (316L stainless steel seamless tube) and its nozzle inlet was tailored to have a sharp-edged form. Furthermore, the orientation of the sampling probe was aligned parallel to the free-stream air that was flowing through the outlet duct. As mentioned in Section 3.7, the mean velocity at the test point (centre of the duct) was measured to be in the range of 6 – 15 m/s and since the Dekati ELPI[®]₊ Electrical Low Pressure Impactor would be utilised, the airflow rate passing through the sampling probe should be equal to 10 litres/minute. From these two parameters, the internal diameter of the sampling probe, d , can be determined using the continuity equation as follows:

$$d = \sqrt{\frac{4\dot{V}}{\pi v}} \quad (3.1)$$

Where \dot{V} is the airflow rate in m³/s and v is the mean velocity at the inlet of the probe in m/s. As a result, Table 3.3 is presented to show the calculated internal diameter as a function of the corresponding airstream velocities.

Table 3.3: The possible value of the internal diameter of the probe.

Mean velocity (m/s)	Internal diameter (mm)
6	5.947
6.92	5.538
7	5.506
8	5.150
9	4.856
10	4.607
11	4.392
12	4.205
13	4.040
14	3.893
15	3.761

From Table 3.3, it can be seen that the minimum and maximum internal diameters that can be considered for the sampling probe are approximately 3.76 and 5.95 mm, respectively. By considering manufacturing constraints, a standard tube size that satisfies the abovementioned requirements should be selected. The chosen tube has an outer diameter of 1/4" (6.35 mm) and a wall thickness of 0.016" (0.4064 mm) giving an internal diameter of 5.537 mm. The mean air velocity was calculated to be 6.92 m/s in the centre of the ducting and the probe inlet. Since the chosen tube has the ratio D/d equal to 1.15 and t/d is greater than 0.05, the condition for the probe to be considered "thin-walled" as elaborated in Chapter 2 were not met. Therefore, a Computational Fluid Dynamics simulation was performed to observe and evaluate the airflow behaviour at the sampling probe inlet in order to minimise the distortion of the ambient flow and the rebound of particles entering the nozzle inlet. The results are elaborated in the next chapter. The final dimensions of the sampling probe chosen are shown in Figure 3.14.

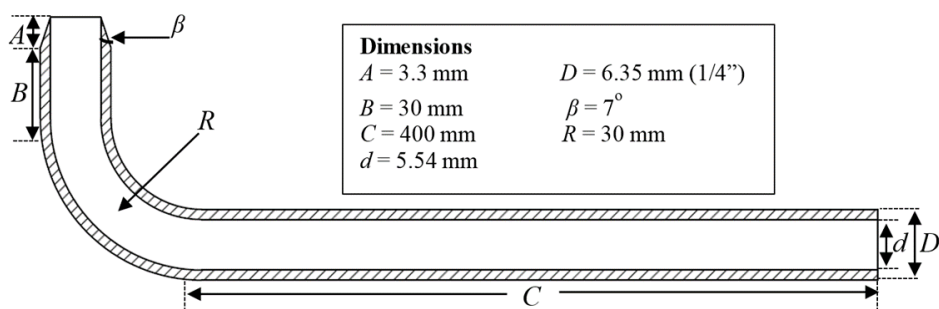


Figure 3.14: Full dimensions of the sampling probe (not to scale).

The sampling probe was specifically designed to withdraw a representative airborne brake wear particle sample from the free airstream and deliver it into the impactor of the Dekati ELPI[®]+. Thus, the probe was securely fitted within one of the tappings in the duct. A BSPT/NPT reducing bush and a Conax probe sealing gland were employed to hold and seal the sampling probe in the right position. Figure 3.15 (a) illustrates a 2D assembled view of the components on the duct with the corresponding dimension. To ensure the nozzle of the probe faces the airstream, a line was drawn on the surface of the probe to indicate the

upward direction of the nozzle. For positioning the probe at the centre of the duct, numbers were written down on the exposed length of the probe to represent the distance from the outer wall of the probe to the far end of the duct wall. The complete installation of the probe on the duct is exhibited in Figure 3.15 (b).

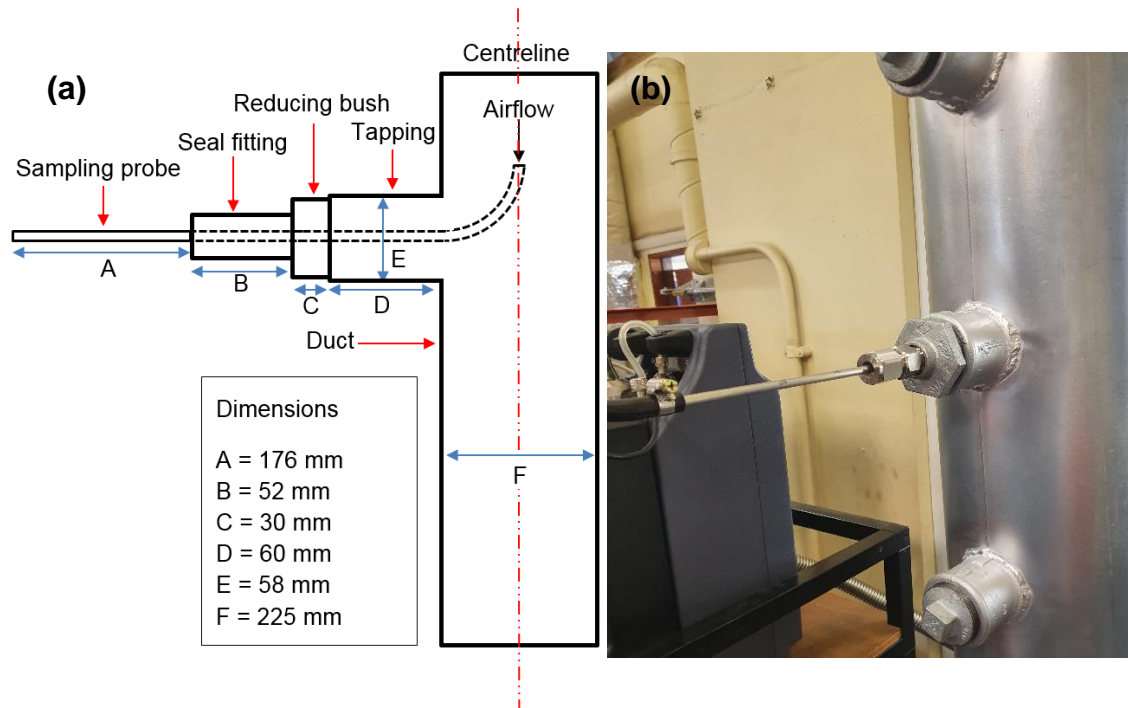


Figure 3.15: An assembled view of fitting elements for the sampling probe on the duct (a) 2D drawing and (b) actual installation.

3.9 Test procedures

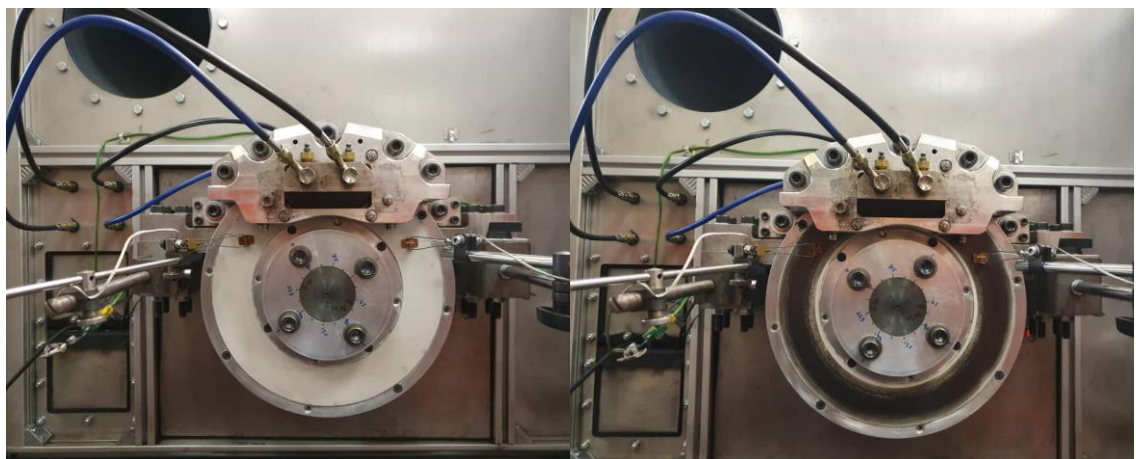
3.9.1 Bedding-in process

Bedding-in new brake pads with a rotor is essential to maximise the brake system performance. Bedding-in tests are carried out to remove impurities from the surface of the brake pads and transfer a thin layer of pad material on to the rotor surface. The process of bedding-in brakes is generally tailored to each friction pair and application. To the author's knowledge, there is no standard bedding-in process for the newly developed coated Al rotor tested under a drag brake application. Therefore, the current bedding-in process followed the conditions suggested by (Hussain, 2018), as indicated in Table 3.4. The test duration given in the table is the time taken when the rotor surface attains 100°C temperature

rise. Figure 3.16 shows the condition of the coated rotor before and after the bedding-in test. It can be seen clearly that a thin transfer layer of brake pad material was deposited on the rubbing surface of the coated rotor as shown in Figure 3.16 (b).

Table 3.4: Test parameters for the bedding-in process.

Test no.	Rotational speed (rpm)	Brake pressure (bar)	Temperature rise (°C)	Test duration (s)
1	100	5	100	2134
2	200	5	100	410
3	300	5	100	297
4	300	5	100	278



(a) Before Bedding-in test

(b) After Bedding-in test

Figure 3.16: Conditions of the PEO-Al rotor rubbing surface.

3.9.2 Preliminary dynamometer test

This test was performed to investigate the rotor temperature change when rotational speed or brake pressure was varied. The test parameters selected were to be used to study their effect on the brake wear emissions. A standard procedure was established to test the two kinds of rotor material and compare various dynamometer parameters. The same drag brake procedure was applied to both GCI and PEO-Al rotors. Before the braking event, the dynamometer was

warmed up for at least 10 minutes and the rotor was then allowed to cool to the ambient temperature (24 – 27°C). When the dynamometer was shown to be functioning consistently, without any sudden stops or slowing down, the dynamometer was run for two minutes without applied forces from the brake caliper. The actual braking tests were carried out for about an hour in order to generate a steady-state temperature on the rubbing surface of the rotor. At the end of the test, the dynamometer was stopped and a single file that recorded the test data was retrieved from the computer.

3.9.3 Airborne brake wear particle measurement and debris collection

In this work, the Dekati ELPI®+ with 14 impactor stages was utilised to sort airborne brake wear particles into different size ranges. Greased aluminium foils were employed in the Dekati to prevent particle bouncing and ease impactor cleaning during and after particle measurements, respectively. These aluminium foils were also used to collect airborne brake wear particles for gravimetric analysis while greased polycarbonate (PC) foils were utilised for chemical analysis. PC foils, as supplied by the manufacturer, were plain without any applied grease. Therefore, a suitable grease was applied to the foils. The AG-10 Apiezon-L grease was used in this study because of its purity and low evaporation properties. To ease the greasing process, Apiezon-L was dissolved in acetone in the grease/solvent ratio of about 1/30-1/20. A fine brush was employed to apply this mixture on the PC foils and the acetone was allowed to volatilise completely off the foils.

Both types of foil for use in the corresponding test were placed on the collection plates and are secured in its place by the substrate holder ring before the impactor was assembled. Figure 3.17 shows an example of the greased PC foils that were placed on the collection plates of the impactor. The impactor was assembled by stacking each numbered impactor stage on top of each other by following the numbering order with number 1 positioned at the bottom. The impactor cover and the charger with the pre-selector stage were added to the

impactor assembly and the assembly then added to the ELPI[®]+ housing (refer Figure 3.18 (d)). Prior to particle measurements and collections, a leakage test was performed to ensure the instrument would work correctly without changing the sample airflow, impactor operation pressures and particle cut-off diameters in the impactor stages.

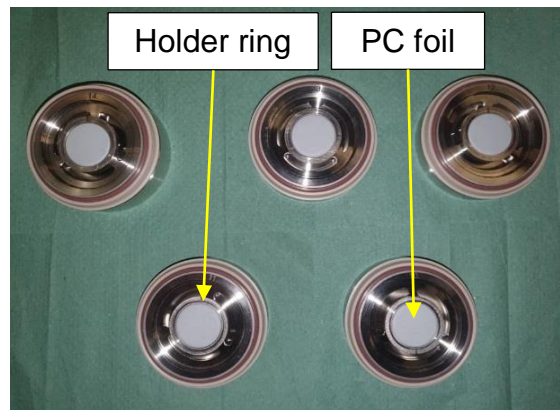


Figure 3.17: Example of the greased PC foils secured on the collection plates.

A standard test procedure was established to generate, measure and collect airborne brake wear particles for both GCI and PEO-Al rotors. Real-time particle measurements and collections of the particles followed the same established procedure. In general, the measurements and collections of particles during a braking event were carried out for 90 minutes to ensure sufficient particles would be measured and collected. At the beginning of the test, the Dekati ELPI[®]+ was switched on at least half an hour prior to data collection to ensure the measured currents were properly stabilised. The impactor low pressure was adjusted to 40 mbar to operate properly and the zero air pump was switched on to allow a clean and filtered air flow through the instrument. A graph of raw current values as a function of time was monitored by looking at the ELPI[®]+ display and when the currents had stabilised, the zeroing process was performed in order to adjust the offset levels of the electrometers. Once the zeroing had been successful completed, the current noise levels were checked and assured to be within the acceptable limits of ± 10 fA.

For real-time particle measurements, the charger was turned on and the current was assured to remain constant at $1.0 \mu\text{A} \pm 0.1 \mu\text{A}$. With the fan switched on,

the background level of the system was measured for 10 minutes. The brake rotor was then allowed to rotate freely without pressure for 2 minutes. After that, the desired hydraulic pressure was applied against the rotating brake rotor and the airborne brake wear particles were measured and recorded for 90 minutes. Similarly, the dynamometer parameters were also recorded for the whole braking test. Once the measurements had finished, the hydraulic pressure was released from the brake rotor and the rotor allowed to freely rotate for 3 minutes.

After the brake dynamometer and particle measurements were stopped, a vacuum cleaner was employed to remove generated particles from inside the system, especially in the enclosure. The remaining airborne particles were flushed out of the system by flowing air through it at maximum fan speed. For particle collections, a similar method was followed but no system background was recorded. In the case of particle collections for the use in gravimetric analysis, the charger was turned off during the test. This is to avoid loss of particles in the corona charger when it is switched on due to electrostatic effects.

3.10 Impactor and charger cleaning

Keeping the ELPI[®]+ unit clean is important to ensure only minimal errors occur during particle measurements. Unclean ELPI[®]+ impactor and charger result in changes in impactor cut-off points and the bouncing effect of particles. During a measurement, particles are often collected on the charger surfaces and also tend to adhere to the impactor parts. Regular cleaning of the impactor and the charger depends on the frequency of their usage and the measured concentrations of particles.

All parts of the impactor and charger were disassembled before the cleaning process. Figure 3.18 (a) shows all parts of the impactor after the disassembly process. The cleaning was carried out in a Decon FS100b heated ultrasonic bath containing tap water. As recommended by the manufacturer, isopropanol was used as a solvent in this work to clean the charger and impactor parts from any dust and dirt. First of all, all parts of the impactor except for the filter stage and O-rings were placed in a beaker which had been previously filled with isopropanol. In the case of the charger parts, the BNC connectors and O-rings

were instructed by the manufacturer not to be washed. Only the same kind of impactor parts were cleaned at a time and the needle assembly from the charger was washed separately. Next, the beaker was placed into the ultrasonic bath and the cleaning time was set to 25 minutes. Figure 3.18 (b) shows the PEEK™ insulator rings in the bath during the process. After the cleaning, all parts were allowed to dry properly as shown in Figure 3.18 (c). After all parts of the charger were re-assembled, electrical contacts between the charger needle and the HV connector as well as the trap cone and the trap connector were measured with a multimeter. The value of electrical resistance measured should be less than 5 Ω . The last stage involved assembling the impactor and charger into the impactor cover as displayed in Figure 3.18 (d).

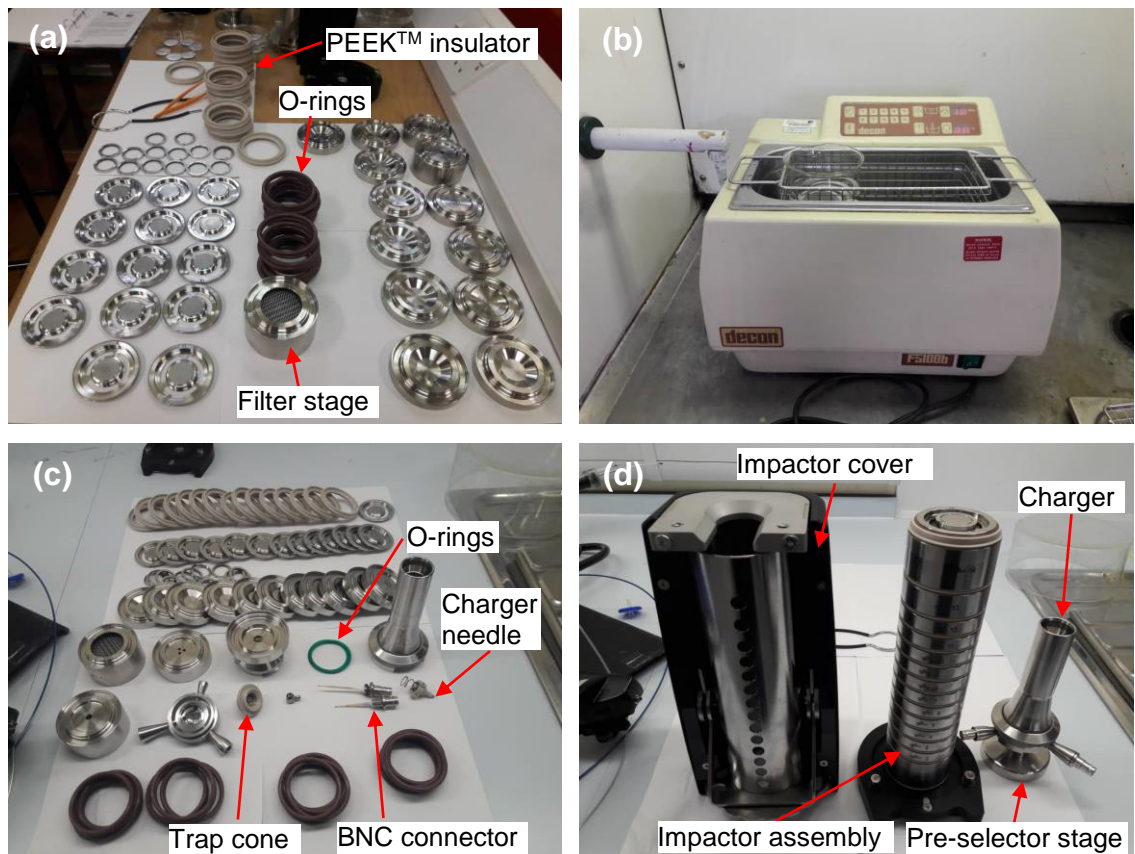


Figure 3.18: Impactor and charger cleaning procedures: (a) disassembling impactor parts, (b) cleaning parts in the bath, (c) drying the charger and impactor parts and (d) assembling all parts.

3.11 Gravimetric analysis

The greased aluminium foils with a diameter of 25 mm were utilised in this analysis as collection substrates. Each foil was stored in a petri dish and numbered in order to allow sample identification (see Figure 3.19 (a)). All the foils before and after the collection were conditioned in a balance room with a constant humidity of 41% and a temperature of 22°C for 24 hours in order to obtain a constant mass. Gravimetric measurements were conducted for all stages except for the filter stage (stage 1) as this cannot be used for chemical and gravimetric analyses. The analysis was done for airborne brake wear particles from the GCI rotor and for different braking conditions.

In this work, the dynamometer was run using the test parameters selected as described in Section 3.9.2. The brake rotor was first allowed to rotate without any brake pressure for 2 minutes. The collections of airborne brake wear particles were performed as soon as a hydraulic pressure was applied on the rubbing surface of the rotor. The braking events took 90 minutes and the brake pressure was released afterwards to allow the rotor to rotate freely without any forces on it for 3 minutes. Generally, the gravimetric measurements were conducted by following procedures outlined in the Dekati Manual. Figure 3.19 (b) shows the collected particulate matter on the Al foils after the impactor was disassembled.

Aluminium foils before and after the braking tests were weighed using a Mettler Toledo XP26 Analytical Balance with a resolution of 1 µg (see Figure 3.19 (c)). All measurements were carried out in the balance room and readings were taken 3 times to ensure consistency. To ease the weighing process, a square weigh boat was employed to quantify the mass of the particles on the Al foils. Before weighing, the microbalance was cleaned using a tissue paper and compressed air to gently wipe the inside. This was done to remove any dust that could possibly cause any errors to the results. Before mass measurement, the balance door was opened and closed several times in order to equilibrate the inside of the balance with the room environment. When the balance was stable and showing zero reading, the boat was placed on the weighing pan and the zero value was set using the tare button. A 1.6165 g metal control pin was used to

validate the instrument and readings were checked before and after measurement of all the samples.

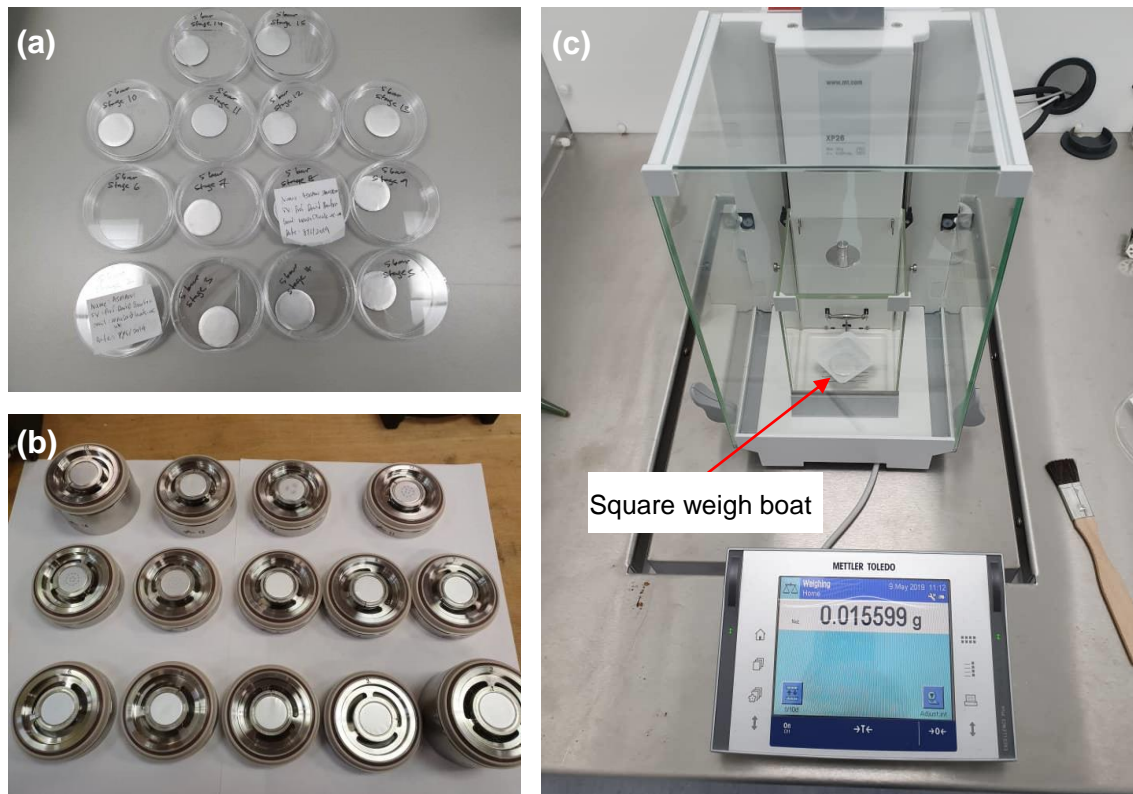


Figure 3.19: Weighing procedure for airborne brake wear particles: (a) samples storing and labelling, (b) particles collection on the foils and (c) samples weighing in the balance.

To take the measurement, the samples were drawn out one by one from the petri dish and placed onto the boat using tweezers. To remove the electrostatic charge, the samples were passed in front of the anti-static ioniser before positioning them onto the boat. The value of mass on the screen was recorded when the reading had stabilised. The procedure was repeated after the weighed sample was removed from the balance and the reading returned to zero value. The mass of the particles for every size interval was calculated in order to determine the mass concentration in mg/m^3 . The mass concentration was calculated by dividing the difference in mass between the samples obtained after and before measurements with the volume of air sampled. A histogram of mass distributions was plotted from the calculated values. The plotted histogram is normalised by dividing the mass concentration in each particle size interval with the width of that interval. The particle size is often conveniently plotted on a

logarithmic size scale so that the same level of detail at all particle size fractions can be seen distinctly.

3.12 Brake wear particle characterisation

For chemical analysis, PC foils were utilised to collect airborne brake wear particles based on particle size ranges. Only 5 foils were used to collect particles in the size range of 1 μm – 10 μm . In terms of particle mass concentration, the brake dust is mainly generated in this coarse particle size range and only a relatively small mass presents as very fine particles of diameter less than 1 μm . Concurrently, a foil was placed on the bottom of the enclosure in order to collect particles that fell down from the braking head. All these particles were collected from the tests of both GCI and PEO-Al rotors and characterised using the Hitachi TM3030Plus SEM. Particle sizes and distributions were examined using SEM while chemical compositions of the collected particles were analysed using EDX techniques.

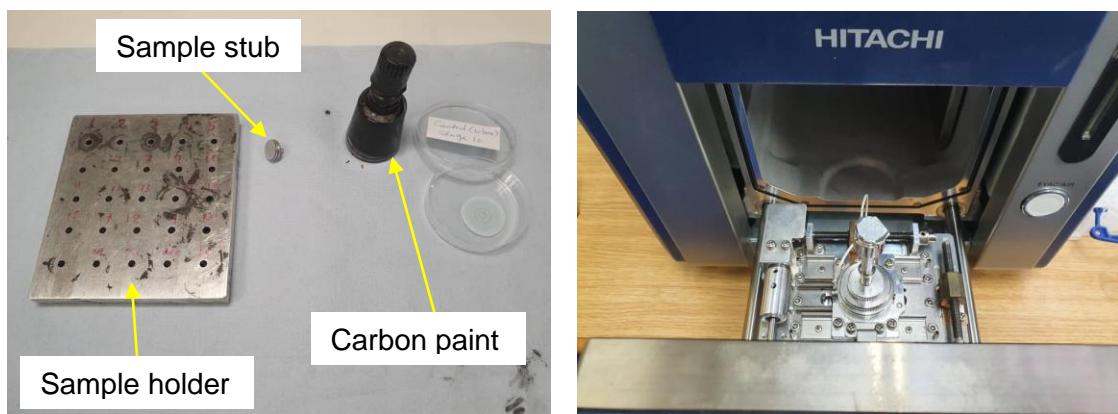


Figure 3.20: Samples preparation and positioning inside the SEM and EDX instrument.

Prior to the SEM examination, samples were properly prepared in order to obtain satisfactory results. Firstly, each foil was cut into a small size of the order of 10 mm so that it can be properly fit on a sample stub. Each sample was mounted into the stub using double-coated conductive carbon tape. The sample was then pressed using tweezers to ensure it strongly adhered to the carbon tape. Carbon paint was applied to the edge of the sample to provide good conductivity for the

foil. Finally, the applied carbon paint was dried using an air dryer. Figure 3.20 shows the various components used during sample preparations and also the sample placed inside the instrument. During sample observation, a high accelerating voltage of 15 kV was used in order to obtain better image sharpness and resolution.

3.13 Summary

This chapter has outlined the experimental procedures for physically and chemically characterising the airborne brake wear particles which were generated from the novel lightweight PEO-Al and standard GCI brake rotors. The coated rotor was made of aluminium alloy (Al-6082) and its rubbing surfaces were treated in the Keronite International Company through the application of the Plasma Electrolytic Oxidation (PEO) process. The coating layer is mainly crystalline alumina (Al_2O_3) which has superior properties such as high hardness, density, wear resistance and good adhesion to the substrate. An isokinetic sampling probe was designed to meet the specifications of the new dynamometer extraction system. The air velocity inside the extraction system was measured with an anemometer to be in the range of 6 to 15 m/s. Prior to actual braking tests, the brake rotor runout and thickness variation for both brake rotors were measured. The runout of the coated rotor was improved by the use of a 0.12 mm shim.

Standard test procedures based on a drag brake application were developed to generate, measure and collect sufficient airborne brake wear particles. The crucial part of the development of these test procedures was to get sufficient particles for the subsequent analysis. Thus, the braking event time that is imposed under steady-state conditions during each friction pair dynamometer evaluation is an important parameter. Several attempts were performed by trial and error to determine an acceptable braking event time which was found to be about 90 minutes. The particles collected were evaluated by gravimetric weighing techniques and characterised morphologically and chemically using SEM and EDX techniques, respectively.

Chapter 4 : Particulate sampling method: guidance using computational fluid dynamics

4.1 Introduction

The study reported in this chapter aims to investigate the flow behaviour of air in the dynamometer extraction system and in the vicinity of a critical component: the sampling probe inlet. Two Computational Fluid Dynamics (CFD) models were set up; firstly global simulations of airflow through the dynamometer extraction system were developed and secondly, more detailed simulations focus on airflow through a localised segment of the duct, which contains the sampling probe. The main objective of the global simulations is to reveal and predict the flow behaviour of air in the enclosed chamber and to gain an understanding of flow patterns in the vicinity of a range of potential sampling points. This is to ascertain that the velocity profile of air is uniform and fully developed at the potential sampling point. The results will guide experiments by identifying a suitable location for taking particulate samples. The purpose of the localised simulations is to examine the velocity profile in the vicinity of the sampling probe inlet and subsequently validate the isokinetic concept that was applied to the newly-designed sampling probe. Both simulations were carried out using the commercial CFD software package, ANSYS Fluent (V16.2). In addition, the velocity magnitudes across the diameter of the outlet duct, obtained from the simulation, were validated with those from the experimental study.

4.2 Mathematical modelling

4.2.1 Governing equations

The fundamental basis of CFD is that the fluid must obey the governing equations of fluid motion, namely the Navier-Stokes equations. These are based on the physical laws of the conservations of mass, momentum and energy (Tu et al., 2013). Fluid flows are usually represented by mathematical statements in partial differential form. In this study, the fluid flow in the dynamometer extraction system was assumed to be steady-state, isothermal and single-phase. The Mach number, M , of the peak airflow speed within the ducting system is 0.02 which is significantly less than the threshold for compressibility ($M = 0.3$) (Cengel and Cimbala, 2006). Therefore, the flow is assumed to be incompressible, whereby the density of air is considered to be constant. These assumptions allow simplifications to be made to the Navier-Stokes equations, allowing them to be solved more easily using commercial CFD packages, such as ANSYS Fluent.

The conservation of mass is given by:

$$\frac{\partial u}{\partial x} + \frac{\partial v}{\partial y} + \frac{\partial w}{\partial z} = 0 \quad (4.1)$$

the momentum equations in the x, y and z directions, respectively, are shown to be:

$$\rho \frac{\partial u}{\partial t} + \rho \left(u \frac{\partial u}{\partial x} + v \frac{\partial u}{\partial y} + w \frac{\partial u}{\partial z} \right) = - \frac{\partial p}{\partial x} + \mu \left(\frac{\partial^2 u}{\partial x^2} + \frac{\partial^2 u}{\partial y^2} + \frac{\partial^2 u}{\partial z^2} \right) \quad (4.2)$$

$$\rho \frac{\partial v}{\partial t} + \rho \left(u \frac{\partial v}{\partial x} + v \frac{\partial v}{\partial y} + w \frac{\partial v}{\partial z} \right) = - \frac{\partial p}{\partial y} + \mu \left(\frac{\partial^2 v}{\partial x^2} + \frac{\partial^2 v}{\partial y^2} + \frac{\partial^2 v}{\partial z^2} \right) \quad (4.3)$$

$$\rho \frac{\partial w}{\partial t} + \rho \left(u \frac{\partial w}{\partial x} + v \frac{\partial w}{\partial y} + w \frac{\partial w}{\partial z} \right) = - \frac{\partial p}{\partial z} + \mu \left(\frac{\partial^2 w}{\partial x^2} + \frac{\partial^2 w}{\partial y^2} + \frac{\partial^2 w}{\partial z^2} \right) \quad (4.4)$$

and the energy equation is given by:

$$\frac{\partial T}{\partial t} + u \frac{\partial T}{\partial x} + v \frac{\partial T}{\partial y} + w \frac{\partial T}{\partial z} = \frac{\lambda}{\rho C_p} \left(\frac{\partial^2 T}{\partial x^2} + \frac{\partial^2 T}{\partial y^2} + \frac{\partial^2 T}{\partial z^2} \right) \quad (4.5)$$

where u , v and w are, respectively, the local velocity components of flow in the x , y , and z directions, ρ is the fluid density, p is the static pressure, t is the time and μ , T , λ and C_p are the dynamic viscosity, the absolute temperature, the thermal conductivity and the specific heat capacity of the fluid, respectively.

4.2.2 Reynolds number

The Reynolds number, Re , is generally used to characterise the flow behaviour of a fluid. It is a dimensionless quantity to determine whether the flow regime is laminar, transitional or turbulent. The flow regime is governed by the ratio of inertial to viscous forces. When the viscous forces are dominant, the flow regime is said to be laminar and it is characterised by smooth and highly ordered fluid flow. However, the flow regime becomes turbulent when the inertial forces begin to dominate. This flow is characterised by rapid and random fluctuations of the fluid. For internal flow in a circular pipe, an Re value less than or equal to 2300 indicates the laminar flow while a value greater than or equal to 4000 indicates turbulent flow. Between 2300 and 4000 the flow is assumed to be in the transitional regime (Cengel and Cimbala, 2006). The Reynolds number can be expressed as follows:

$$Re = \frac{\rho V_{avg} D}{\mu} \quad (4.6)$$

Where, ρ and μ are the fluid density (kg/m^3) and dynamic viscosity (kg/ms), respectively, D is the internal diameter of the pipe (m) and V_{avg} is the average velocity of the fluid (m/s).

4.2.3 Turbulence models

Most of the fluid flows encountered in engineering are likely to be turbulent. In a turbulent flow, a different physical problem requires different treatments. Many different turbulence models have been developed to be accurate for various engineering applications. For example, the Spalart-Allmaras (Spalart and Allmaras, 1992) and SST $k-\omega$ (Menter, 1994) models are generally used in aerospace applications. In low- Re regimes, the standard $k-\omega$ model (Wilcox, 1998) performs well, whereas $k-\varepsilon$ models (Launder et al., 1975) can deal with high- Re regimes and they are known to be robust because they have been validated extensively since 1975. All of these models are known as Reynolds Averaged Navier Stokes (RANS) models because they approximate mean variables of the turbulent flow problems (Tu et al., 2013). In this work, the standard $k-\varepsilon$ model (Launder et al., 1975) is used because this model is generally robust and suitable for engineering flows such as these. It consists of two transport equations representing a general description of the turbulence phenomena. The first equation expresses the transported variable of the turbulent kinetic energy, k , while the second equation expresses the transported variable of the dissipation rate of turbulence, ε . For this model, the transport equations are:

$$\begin{aligned} \frac{\partial k}{\partial t} + u \frac{\partial k}{\partial x} + v \frac{\partial k}{\partial y} + w \frac{\partial k}{\partial z} \\ = \frac{\partial}{\partial x} \left[\frac{v_T}{\sigma_k} \frac{\partial k}{\partial x} \right] + \frac{\partial}{\partial y} \left[\frac{v_T}{\sigma_k} \frac{\partial k}{\partial y} \right] + \frac{\partial}{\partial z} \left[\frac{v_T}{\sigma_k} \frac{\partial k}{\partial z} \right] + P - \varepsilon \end{aligned} \quad (4.7)$$

$$\begin{aligned} \frac{\partial \varepsilon}{\partial t} + u \frac{\partial \varepsilon}{\partial x} + v \frac{\partial \varepsilon}{\partial y} + w \frac{\partial \varepsilon}{\partial z} \\ = \frac{\partial}{\partial x} \left[\frac{v_T}{\sigma_\varepsilon} \frac{\partial \varepsilon}{\partial x} \right] + \frac{\partial}{\partial y} \left[\frac{v_T}{\sigma_\varepsilon} \frac{\partial \varepsilon}{\partial y} \right] + \frac{\partial}{\partial z} \left[\frac{v_T}{\sigma_\varepsilon} \frac{\partial \varepsilon}{\partial z} \right] \\ + \frac{\varepsilon}{k} (C_{\varepsilon 1} P - C_{\varepsilon 2} \varepsilon) \end{aligned} \quad (4.8)$$

Where k is the turbulent kinetic energy, ν_T is the eddy viscosity and ϵ is the turbulence dissipation rate. The production term, P , is defined as:

$$P = 2\nu_T \left[\left(\frac{\partial u}{\partial x} \right)^2 + \left(\frac{\partial v}{\partial y} \right)^2 + \left(\frac{\partial w}{\partial z} \right)^2 \right] + \nu_T \left[\left(\frac{\partial u}{\partial y} + \frac{\partial v}{\partial x} \right)^2 + \left(\frac{\partial v}{\partial z} + \frac{\partial w}{\partial y} \right)^2 + \left(\frac{\partial w}{\partial x} + \frac{\partial u}{\partial z} \right)^2 \right] \quad (4.9)$$

Both Equations 4.7 and 4.8 consists of the following coefficients and constants which have been guided by empiricism; $\nu_T = (C_\mu k^2)/\epsilon$, $C_\mu = 0.09$, $\sigma_k = 1.00$, $\sigma_\epsilon = 1.30$, $C_{\epsilon 1} = 1.44$ and $C_{\epsilon 2} = 1.92$.

4.3 Numerical simulations of airflow in the extraction system

4.3.1 Geometry and boundary conditions

Figure 4.1 shows a CAD model of the dynamometer extraction system including the grey cast iron brake rotor. Key dimensions are labelled based on physical measurements from the lab in which this rig is based. All ducting has an internal diameter of 225 mm. The inlet and outlet ducts consist of four 90-degree bends with an inner curvature radius of 225 mm as illustrated in Figure 4.1 (a). Furthermore, the outlet duct contains an additional bend with the same inner curvature radius but with a different arc of 45 degrees. The box (chamber) that encloses the brake assembly has a volume of approximately 0.45 m³. As this is a fluid dynamics problem, the volume of fluid in the box was modelled using a boolean operation, whereby the geometry of the brake assembly was subtracted from the box air, leaving only the fluid shape. The brake caliper was modelled and simplified as a rectangular prism with a groove through it. The shape of the truncated pyramid at the outlet of the enclosure was simplified into a truncated cone.

The boundary conditions for the inlet and outlet of the domain are shown in Figure 4.1 (a). The inlet velocity of 6.92 m/s and the pressure outlet of 1 atm

(absolute pressure) were taken as the boundary conditions. The brake rotor was specified as a moving wall with a rotational speed of 135 rpm. In this simulation, the value of inlet velocity and rotational speed was selected to replicate those used in the experimental work. The other bounding walls of the computational domain were set as stationary walls with the no-slip condition applied. At the inlet of the system, the velocity profile is assumed to be uniform. Since the domain produces a confined flow regime, it is important to prescribe turbulence levels at the domain inlet and outlet. These are determined from duct flow which is standard practice in CFD (Tu et al., 2013). Accordingly the hydraulic diameter, D_H , and the turbulent intensity, I , are given by:

$$D_H = D \quad (4.10)$$

$$I = 0.16Re_{D_H}^{(-1/8)} \quad (4.11)$$

where D is the duct diameter, Re_{D_H} is the Reynolds number based on the hydraulic diameter, $Re_{D_H} = \frac{\rho U D_H}{\mu}$, ρ is the fluid density, U is the inlet fluid velocity and μ is the fluid viscosity. These equations produced a hydraulic diameter of 0.225 m and a turbulence intensity of 3.76%.

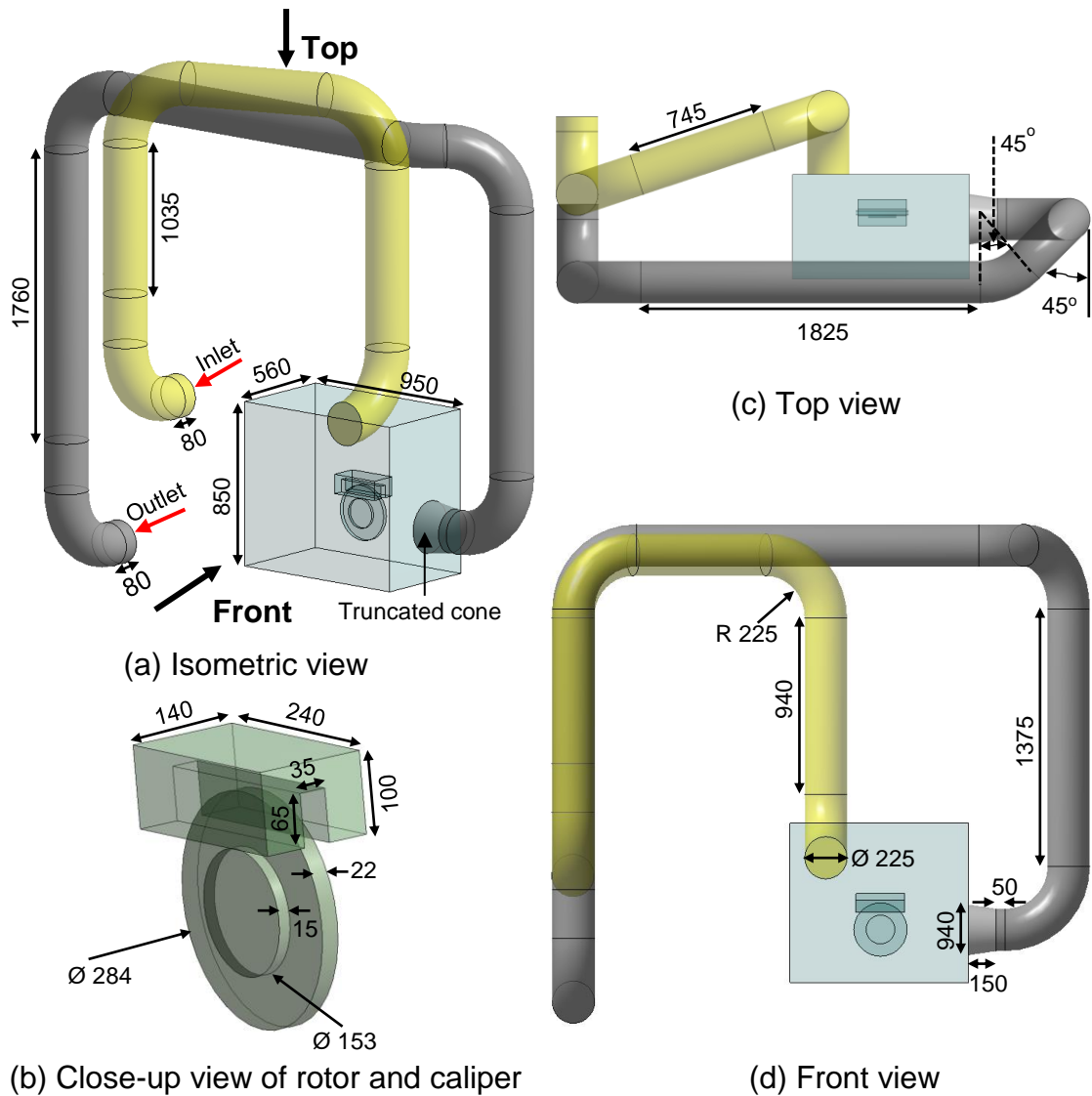


Figure 4.1: 3D model of the brake dynamometer extraction system from various orientations (all units in mm).

4.3.2 Mesh generation and solver settings

Mesh generation is a crucial part of the preprocessing step in the CFD simulation process as it greatly influences the accuracy of results and the time of simulations. The process is challenging and often takes a substantial amount of time to yield a suitable compromise between mesh quality and overall element count, particularly with regard to complex geometries. The most economical element count should be considered in CFD analyses to seek lower computational cost, however, this must not be at the expense of accuracy. Before a simulation can be performed, it is necessary to check the quality of the mesh

because low-quality or coarse meshes often lead to inaccurate results. The element size should be small enough in the regions of high flow gradients to resolve the effect of the velocity gradient on turbulent flow. In the near-wall regions, it is crucial to cluster the mesh of elements normal to the relevant wall to capture the effect of viscosity close to the wall i.e. the boundary layer. A crucial aspect of near-wall mesh design is the correct placement of the first cell height, y , in the mesh, measured normal to the wall surfaces. To help with this, the non-dimensional y^+ value is a parameter that is used to check if the normal distance from the wall to these nodes is correct. The equation for the y^+ calculation is given by:

$$y^+ = y \frac{\sqrt{\rho \tau_w}}{\mu} \quad (4.12)$$

where τ_w is the wall shear stress, ρ is the fluid density, μ is the viscosity and y is the first layer thickness. All of these fluid parameters are obtained from CFD simulations, therefore, for a given value of y (chosen in the mesh), this must be checked using a CFD simulation to evaluate y^+ which must be within a certain range. This process is iterative, with changes to the mesh often needed to obtain a suitable y^+ value. Considering a general boundary layer, when $y^+ < 5$, this is known as the viscous sub-layer and is dominated by viscous effects. The region where both viscous and turbulent effects are equally important is called the log-law layer and this is relevant to the flow problem considered in this chapter. It follows that the mesh requirements are such that the condition $30 < y^+ < 500$ must be satisfied (Versteeg and Malalasekera 2007; Tu et al., 2013).

As well as checking the near-wall mesh refinement, a mesh or grid independence study must be performed to find an optimum number of elements for fast and accurate simulations; having solutions which are affected by the mesh density is undesirable. A coarse mesh may be quick to solve but the results may not be accurate whereas a fine mesh may be accurate although the simulation may take a prohibitively long time for the analysis to be completed. It is therefore good practice to investigate mesh sensitivity.

Accordingly, a grid independence study was performed using a coarse mesh initially and then followed by a finer mesh until the deviations between the desired outputs stabilised. The present work applies local refinement techniques that focus on the areas of the outlet duct and in the vicinity of the brake assembly, where flow gradients are expected to be highest. The number of elements used in the model are approximately 1.6, 1.8, 2.0, 2.2, 2.4 and 2.6 million elements. An inflation of 10 layers of elements was added to the outlet duct walls to capture the shear stress effect close to the wall. The first layer thickness used is 0.001 m and it produces a y^+ of approximately 100 which is in the correct range (Versteeg and Malalasekera 2007; Tu et al., 2013).

Another important consideration in mesh design is the quality of the elements. If they are too distorted to fill the complex domain shape then convergence issues can arise, often leading to unreliable solutions. A useful measure of cell quality is the skewness and if it is below 0.9, simulations will normally converge. Due to the complex geometry of the present 3D model, the skewness of a few elements was high. However, the maximum skewness reported was less than 0.9 which is still within the acceptable range. The number of elements and their corresponding average and maximum skewness are shown in Table 4.1. Overall, the average skewness achieved was around 0.15 and this indicates that most of the elements are of excellent quality.

Table 4.1: Skewness comparison for the model with different element counts.

Number of elements (millions)	1.6	1.8	2.0	2.2	2.4	2.6
Average skewness	0.17	0.17	0.16	0.16	0.15	0.15
Maximum skewness	0.89	0.90	0.90	0.88	0.86	0.84

Figure 4.2 shows the mesh topology of the whole domain of the brake dynamometer extraction system together with their two specific close-up views. A hybrid of hexahedral and tetrahedral elements was generated to simulate the internal flow of air inside the system. An unstructured tetrahedral mesh was used

for the enclosed chamber portion of the domain due to the difficulty of generating a structured mesh in such a complex geometry.

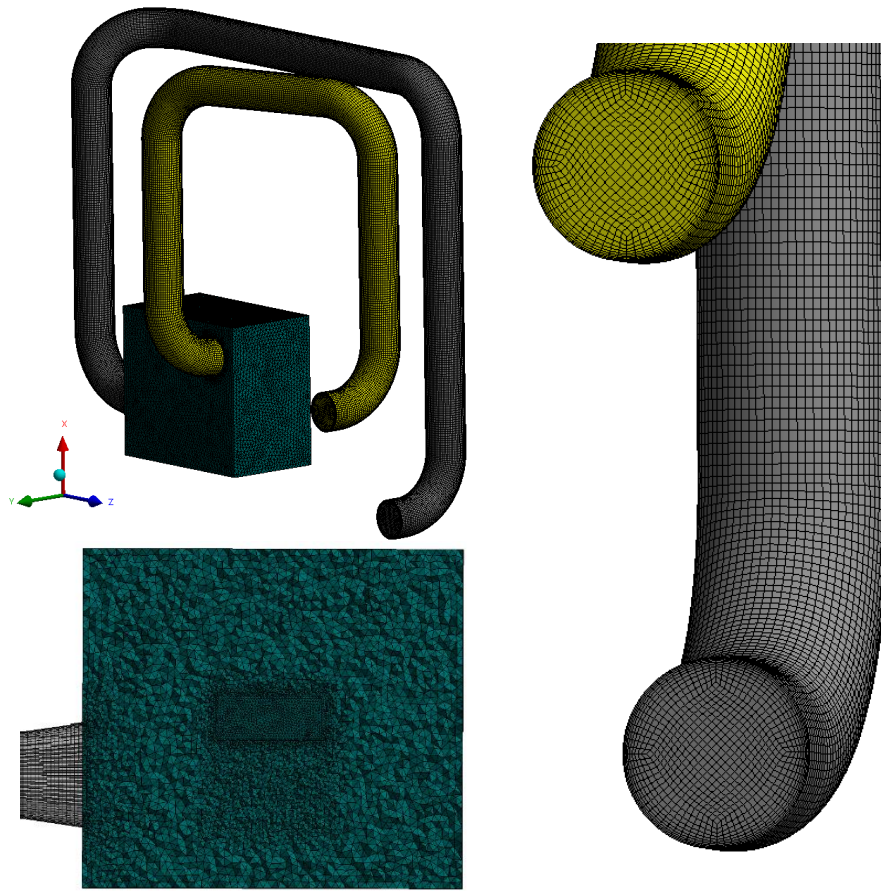


Figure 4.2: A typical computational grid filling the fluid volume in the brake dynamometer extraction system.

Prior to simulations, the CFD solver, Fluent, was set with the boundary conditions described in Section 4.3.1. As already explained, the standard $k-\varepsilon$ turbulence model with standard wall functions (Launder et al., 1975) was used because it accurately predicts flow features away from the wall i.e. in the chamber and centre of the ducting. Standard (sea-level) atmospheric air properties from the Fluent material database were used (density = 1.225 kg/m^3 and viscosity = $1.7894 \times 10^{-5} \text{ kg/ms}$). Also, second order discretisation schemes were set because they are more accurate than first order ones but still economical (Versteeg and Malalasekera, 2007; Tu et al., 2013).

Figure 4.3 shows the velocity profile obtained at tapping 4 (see Figure 3.11) for all meshes used. This region is close to where the sampling probe is in the physical experiment which is why this area is investigated in the CFD model in order to assess grid independence. The graph was plotted by taking cell centre values across the diameter of the outlet duct, for each of the six meshes. To select the optimal number of elements, the velocity profiles in Figure 4.3 were compared in order to find a suitable result. All results shown in the figure have a similar trend with low values at the walls due to the no-slip condition, larger velocities in the centre of the duct and a slight dip in profile at the centre. This shows that the results in this location are relatively insensitive to the mesh density changes. Observing the profiles more closely, the one for 2.6 million elements seems to give a profile which visually appears to be the average of all profiles. Furthermore, this is the finest mesh which means it will show greatest accuracy in other places in the domain. Therefore, the fine 2.6 million element mesh is used in all further analysis of the entire system.

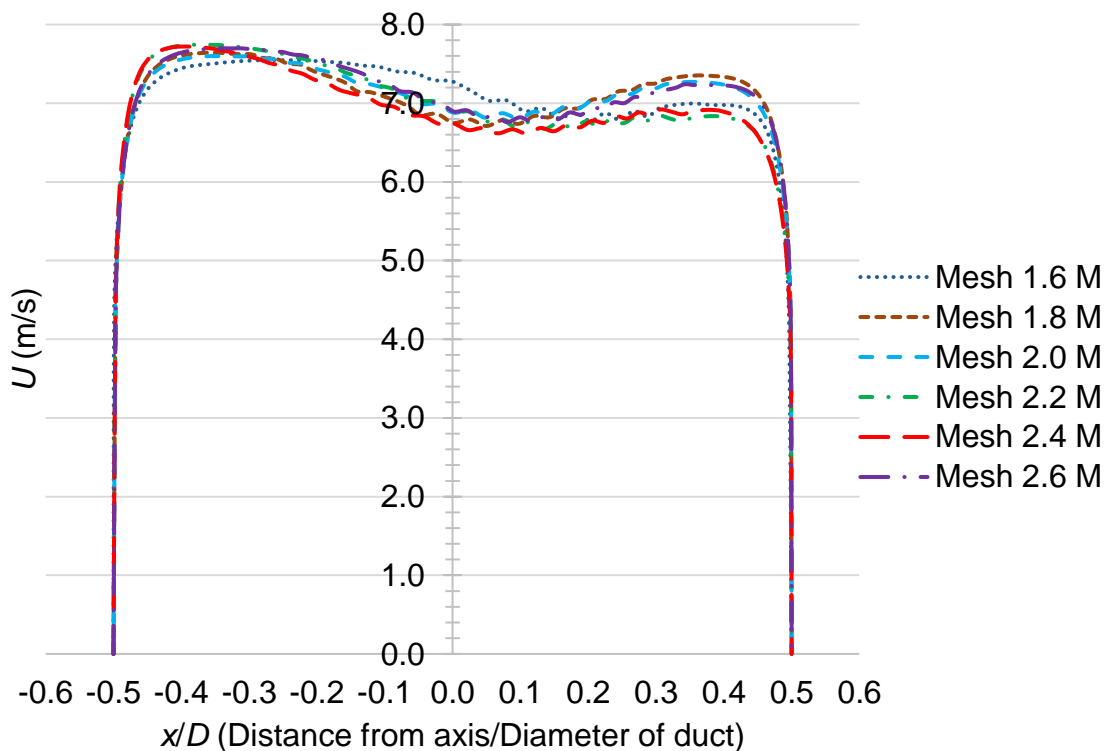


Figure 4.3: Velocity profiles at tapping 4 for various CFD meshes.

4.3.3 General flow behaviour

Figure 4.4 shows air pathlines passing through the entire dynamometer extraction system. The pathlines travelling along the inlet duct are almost uniform and unidirectional before they are discharged into the enclosed chamber. Inside the chamber itself, the flow is complex and dominated by extensive mixing. The turbulence levels present around the brake assembly ensure that airborne particles generated from the brake pads and the rotor are transported from the enclosure to the sampling location. The flow entering the chamber divides into two distinct streams, one circulating below the brake assembly and one above. Both streams then interact as they enter the outlet ducting. It is also noted that the airflow just after the chamber outlet is quite similar to the flow behaviour at the inlet duct. As the flow moves through the ducting, a mild spiraling motion is evident suggesting that there is a rotational component about the duct axis which is likely due to the multiple bends along the outlet ducting.

To comprehend the velocity profile in the vicinity of the sampling tap locations and the velocity test point, velocity contours at these cross-sections, viewed from above the system, are presented in Figure 4.5. These cross-section views show that the velocity magnitude is somewhat higher on the left-hand side of the sampling duct. This might be caused by the preceding bend that the airflow has to follow; it naturally follows the outer radius of this relatively tight bend. As the airflow moves downward along the straight duct section, it is found that the high-velocity region slowly diminishes such that a more uniform velocity profile gradually develops. To obtain a better illustration of the velocity profile at the four tap locations and the velocity test point, a graph of the downward air velocity magnitude, U , against the duct width (denoted by the red lines in Figure 4.5) was plotted, as shown in Figure 4.6. Overall, the shape of all profiles on the left-hand side is almost flat with a steep velocity gradient on the left-hand wall due to the no-slip boundary condition. However, on the right-hand side the velocity magnitude for all locations is noticeably reduced due to flow separation on the tight inner radius of the 90-degree elbow immediately above the VTP location. As the airflow re-attaches, the velocity profile spanning the duct gradually

becomes fuller and flatter as the airflow advances further down towards the outlet.

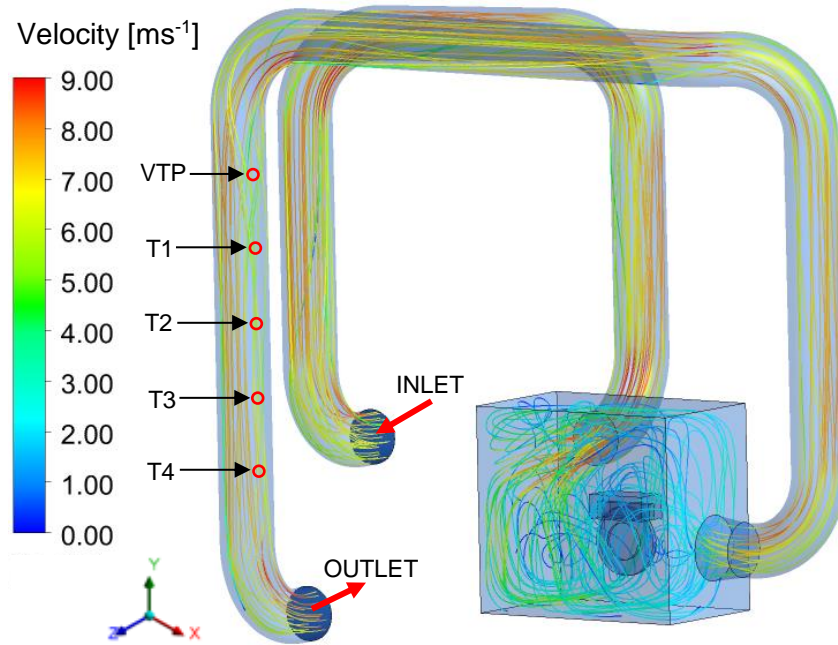


Figure 4.4: Air pathlines in the dynamometer extraction system.

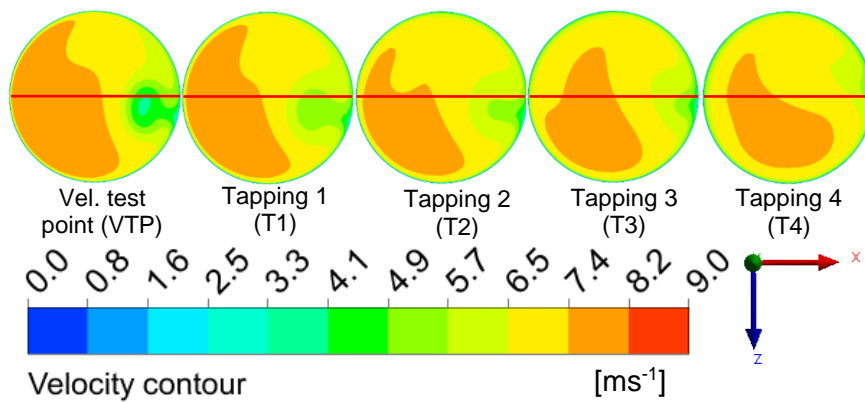


Figure 4.5: Resultant velocity contours viewed from above at five key locations.

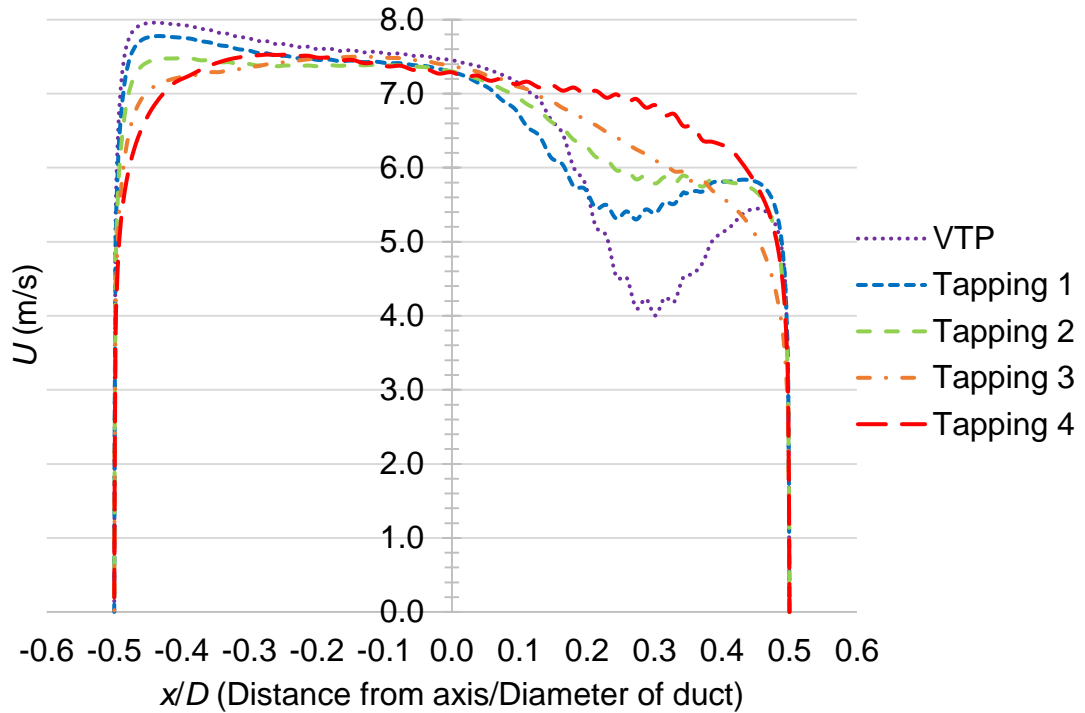


Figure 4.6: Radial velocity profile at the velocity test point (VTP) and four tappings of the duct.

4.3.4 Validation

To provide further confidence in the CFD approach, validation was performed by comparing the velocity profiles obtained from experimental measurements to CFD data at the same locations within the system. The measurement of velocities was carried out using the VelociCheck air velocity meter (model number 8330) along two co-planar lines indicated by A and B, in Figure 4.7. Location A has the same orientation as the z-axis (recall Figure 4.4) while location B is at 90 degrees from location A, aligned in the x-axis. Several readings were taken along each line between the two opposite duct walls. Most velocity readings were measured at equally spaced points 10 mm apart, except for the centre point (6.5 mm spacing). Due to the size of the velocity sensor, the first reading was taken to be at least 16 mm from the far-end wall. However, more measurements were able to be taken near the other opposite wall. The present work utilised 43% of the fan power to achieve the predicted velocity of 10 m/s at the velocity test points. The velocity selected was a medium velocity that can demonstrate representative airflow behaviour in the dynamometer system,

particularly in the vicinity of the velocity test point. To measure the velocity at the desired points, the telescopic probe of the anemometer was marked with a marker for the distance measurement. The velocity measurement was taken when the reading on the anemometer was stable. All points and readings recorded are shown in Appendix A. For the simulation work, the model developed in Section 4.3 was used to simulate the airflow within the system, particularly in the vicinity of the velocity test points. However, the brake rotor was set as a stationary wall with the no-slip condition; this has no impact on flow conditions at the outlet duct. Since the inlet velocity of 10 m/s was used in this simulation, thus the intensity was recalculated to give a value of 4.8% and this value was set in the Fluent.

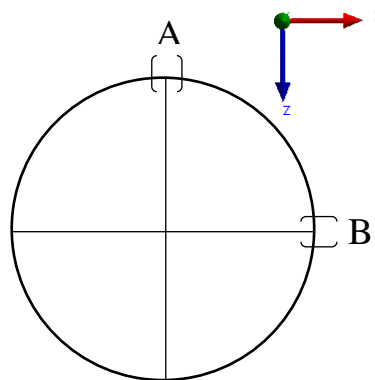


Figure 4.7: Plan view inside the outlet duct in a plane coincident with the velocity test points.

The velocity contours obtained from the CFD simulation can be used to provide a detailed view of the velocity field. Accordingly, velocity contours (absolute velocities) at the cross-section of the sampling tap location are depicted in Figure 4.8. The figure shows that the velocity is higher in the upper left of the cross-section and lower in the bottom right. Several velocities were measured along lines A and B for comparison with that of the experimental study. Figure 4.9 shows the magnitudes of the velocity profile at the specified points obtained from the experimental and simulation results. The velocity profiles of the experimental work are marked with blue and green lines, while the velocity profiles of the simulation work were marked with orange and red lines. From this figure, it can be seen that the velocity profiles for the experimental and CFD studies are

broadly similar. In the case of location A, there is only a slight difference in velocity, which is never more than 10% of the absolute value. The difference in velocity for location B is slightly higher on the right-hand side of the ducting. However, the downward trend in velocity magnitude from the left to right-hand sides is broadly similar in both studies. These results indicate generally good agreement between the experimental and simulation studies. Hence, the CFD model can be regarded as validated and used for future simulation studies of various parameters.

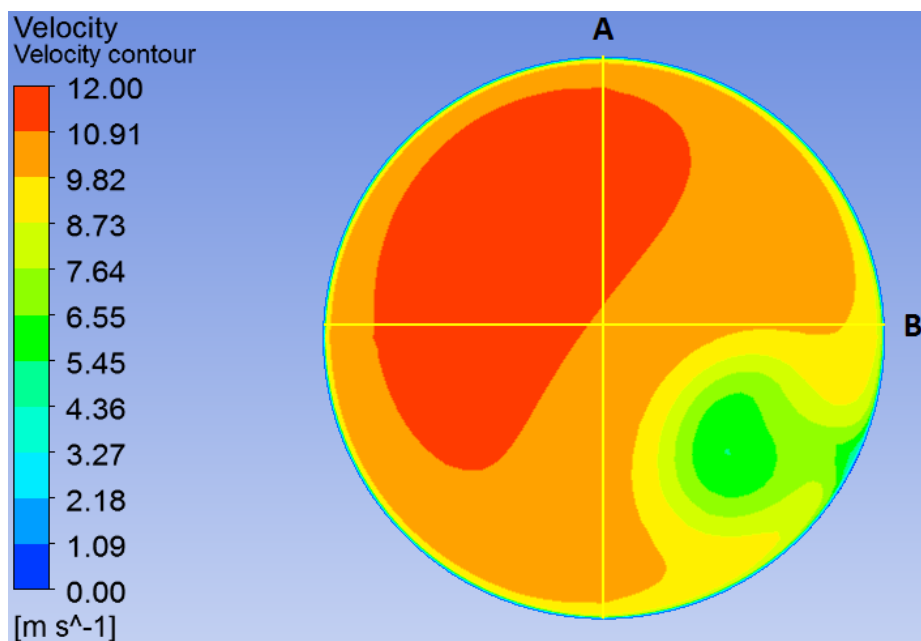


Figure 4.8: Velocity contours (m/s) at the velocity test cross-section.

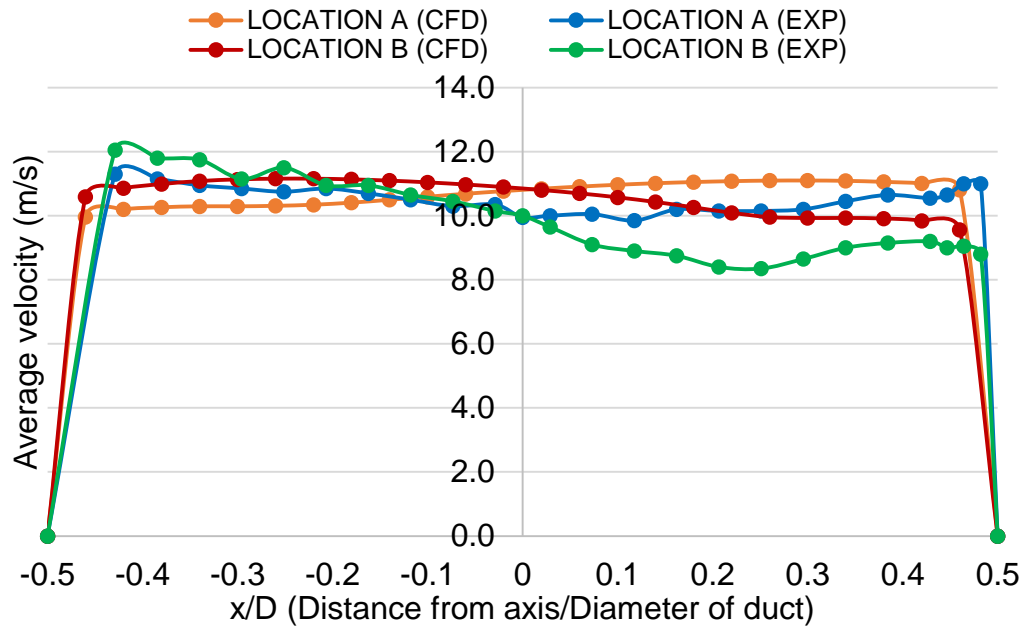


Figure 4.9: Velocity profiles from the experimental and simulation studies.

4.4 Numerical simulations of airflow in the sampling probe

4.4.1 Geometry and boundary conditions

Figure 4.10 shows a 3D schematic of a segment of the duct with the sampling probe mounted within it. The sampling point is designed to operate under isokinetic conditions, thus it is important to understand in more detail the airflow behaviour in this region. The dimensions of the sampling probe in the model follow the geometry as described in Section 3.8 (see Figure 3.14). In this model, a decision was taken to only simulate a small portion of the outlet of system because the grid is very fine in and around the sampling probe. The purpose here, is to ensure isokinetic sampling. The length of the outlet duct was extended 500 mm from the probe nozzle in both downward and upward directions to allow the formation of fully developed flow, at the probe tip. The inlet velocity was taken to be constant over the cross-section of the outlet ducting and equal to 6.92 m/s, matching the experiments. The pressure at the duct outlet was set to be 1 atm (absolute pressure). To obtain the effect of the pump suction, a negative value of inlet velocity (-6.92 m/s) which is equivalent to the Dekati suction rate was applied to the outlet of the sampling probe. Referring to Equations 4.10 and 4.11,

the intensity of 3.8% and hydraulic diameter of 0.225 m were obtained and used for the inlet y and outlet y.

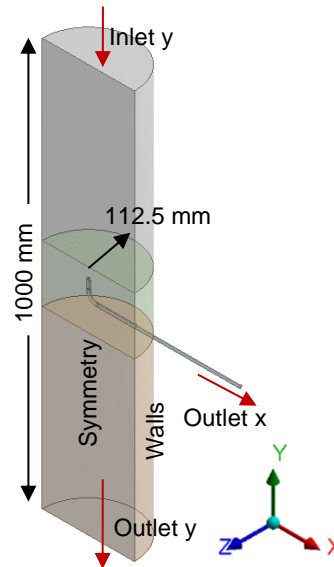


Figure 4.10: 3D schematic of the sampling probe flow simulation.

4.4.2 Mesh generation and solver settings

In this study, the domain was generated with a very fine mesh to capture the flow details in the vicinity of the sampling probe and the results are representative of what would be expected. Thus, the grid independence study was not carried out for this CFD simulation. The flow domain contains approximately 1.45 million elements with a maximum and average skewness of 0.85 and 0.2, respectively. Figure 4.11 shows the mesh generation for the entire domain of the probe simulation. A hexahedral mesh was used for the probe fluid volume, while a tetrahedral mesh was used for the outlet ducting.

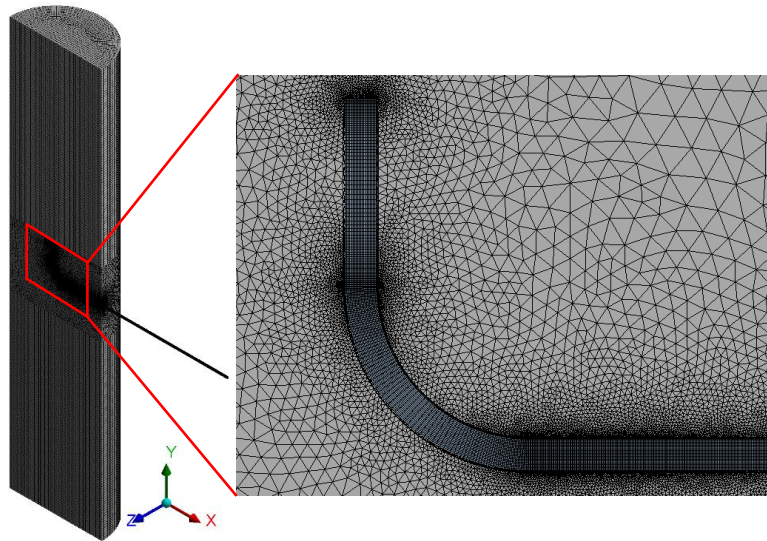


Figure 4.11: 3D domain of the probe flow simulation with computational grid.

For this model, the same general settings were used as for the whole system in the previous section. The solver Fluent was used with the same boundary condition types as stated in Section 4.4.1. The standard k - ϵ turbulence model was used along with second order discretisation schemes and standard atmospheric air properties.

4.4.3 General flow behaviour

Figure 4.12 shows a velocity magnitude contour map from the simulation of the airflow passing through and around the sampling probe. The contours are normalised with respect to the free-stream velocity (taken as the inlet velocity). A close-up view of the contours is enlarged in the vicinity of the nozzle on the left-hand side of Figure 4.12, with the velocity profile plotted in the x-direction across the mouth of the probe in Figure 4.13. It is important to note that there is a slight reduction in velocity at the two sides of the probe tip ($6.5 < U < 6.92$ m/s) compared to the velocity at the centre of the probe (~ 6.92 m/s); this is unavoidable and is due to the no-slip condition assumed on the probe walls. Since the tip is shaped with knife edges, only a small distortion effect is evident which is limited to the vicinity of the probe tip circumference; flow in the centre of the probe is unaffected. It should be noted that if a significant reduction in velocity

were to exist at the probe tip, deviation from the free-stream direction would be noticed. A consequence of this would be incomplete wear debris particle collection from the air entering the probe; this underlines the importance of careful probe design and positioning within the system and the results from the CFD simulation show that this has been achieved.

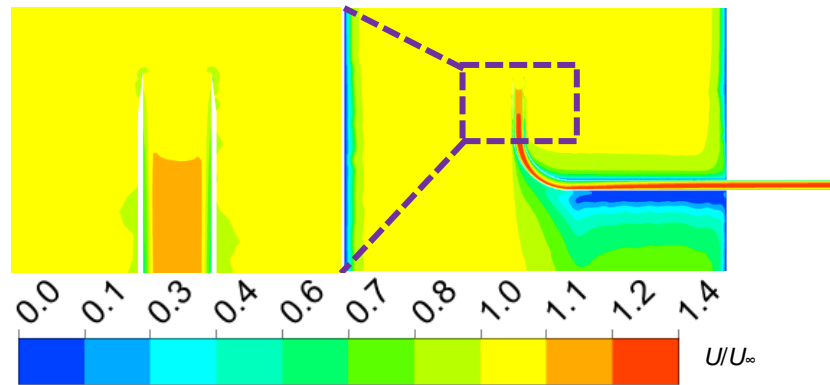


Figure 4.12: Velocity magnitude contours in a vertical slice of the domain (right) including a close-up view at the nozzle inlet (left).

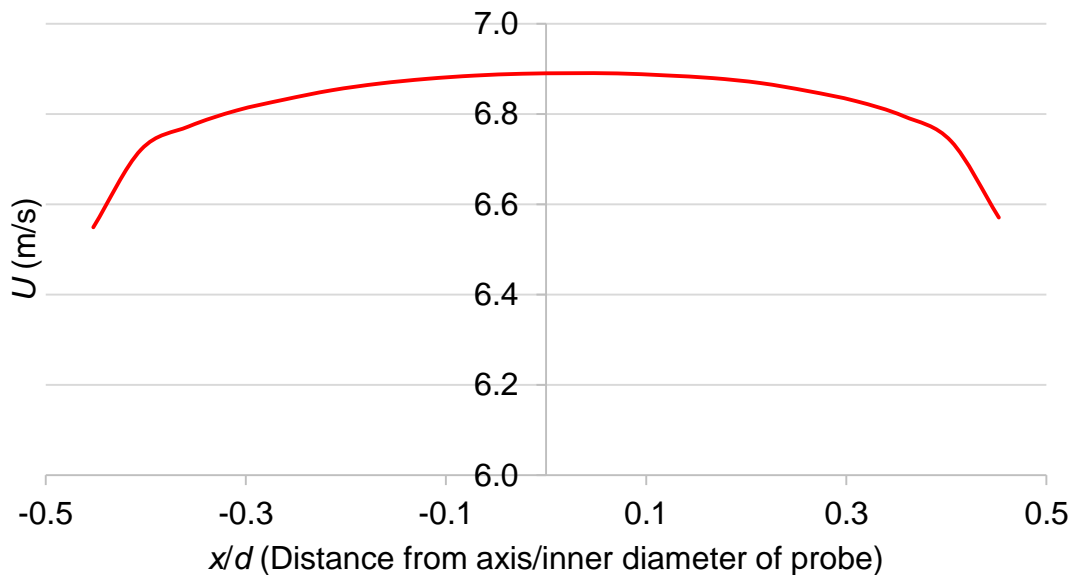


Figure 4.13: Velocity profile at the inlet of the sampling probe.

4.5 Summary

This chapter describes the simulation of airflow in the dynamometer extraction system and within the vicinity of the sampling probe inlet. The first set of CFD simulations showed that a well-mixed air flow pattern exists within the rig which would therefore be expected to contain a wide range of airborne particles. In addition, the velocity profile on the left-hand side of the duct for all tapping positions is generally uniform and this suggests that the sampling point in this particular rig should be taken from this region where the flow is more stable. The deviation between the inlet velocity to the chamber and the velocity at the centre of the tapping locations was computed to be no greater than 8%. The second set of CFD simulation results showed a small flow distortion in the vicinity of the sampling probe inlet, particularly around the tip. However, this is not thought to be significant in terms of the operation of the sampling probe which is confirmed to achieve near isokinetic conditions. It was also found that the experimental and simulation results were in good agreement in terms of the velocity profiles at the velocity test point.

Chapter 5 : Results for grey cast iron rotor

5.1 Introduction

This chapter presents the evaluation of brake wear particulate matter generated from the grey cast iron rotor and its conforming pads. Initially, a preliminary test was conducted to find appropriate brake conditions for use in subsequent tests. Three brake conditions were selected and the corresponding test was run three times to ensure the consistency of the result. At the same time, real-time particle measurements were carried out to investigate the particle number and mass distributions. Prior to the actual braking measurements, the particulate matter in the background air of the laboratory and within the ducting system were recorded using the Dekati ELPI[®]+. The determination of particle mass concentration by the gravimetric method was subsequently evaluated. To investigate the morphology and elemental composition of airborne brake wear particles, a scanning electron microscope (SEM) equipped with an energy-dispersive X-ray spectroscopy (EDX) system was utilised. Finally, the results were compared quantitatively and qualitatively based on particle size range for the three brake conditions.

5.2 Brake dynamometer tests

5.2.1 Preliminary tests

An initial test was conducted to discover appropriate parameters for use in subsequent brake wear emission measurements. These parameters, namely hydraulic pressure and rotor rotational speed, were selected based on the temperature generated at the rubbing surface of the rotor during a drag braking event. It was anticipated that the temperature would attain a steady-state condition following a few minutes after a test commenced. Three conditions that

achieved nearly constant temperatures of 200, 300, and 400°C were selected. Iijima et al. (2007) have mentioned that the rotor temperature of 200°C is more representative of braking during urban driving, while the other two temperatures are produced under extreme braking, such as during a steep hill descent. In this work, a drag brake application was applied to the dynamometer. The fan power of the extraction system was set at 5% of the total capacity in order to generate approximately 7 m/s air velocity at the anemometer test point. The hydraulic pressure was selected in the range of 2.5 and 20.0 bar while the rotational speed was in the range of 45 and 360 rpm as shown in Table 5.1. Each test was run for an hour to try to induce a constant temperature on the rotor rubbing surface or the test was ceased when the temperature of the rubbing surface exceeded 450°C so as to avoid resin content in the pads from charring or evaporation (Chan, 2004).

Table 5.1 shows the temperature generated at the rubbing surface of the rotor during steady-state conditions. The symbol 'X' in the table indicates when tests were not performed because the intended temperatures were not expected to be successfully obtained.

Hydraulic pressures of 5, 10 and 15 bar at a constant speed of 135 rpm were selected as the three braking conditions for subsequent tests and the corresponding steady-state temperatures achieved are shown in bold font in Table 5.1. These conditions closely achieve the desired rotor surface temperatures of 200, 300 and 400°C. Moreover, the variation of the brake pressure value selected is uniform in constant multiples of 5 bar. Assuming the brake pad was compressed uniformly by the actuation load, a mean rubbing radius for the rotor of 115 mm and a pad area of 2400 mm², the hydraulic pressures and rotation speed were converted to mean contact pressure and average sliding speed, respectively as shown in Table 5.2.

Table 5.1: Steady-state rotor temperature (°C) at each condition.

Pressure (bar) \ Speed (rpm)	2.5	5.0	7.5	10.0	12.5	15.0	17.5	20.0
45	X	X	141	X	X	216	X	X
90	88	164	226	280	318	391	409	X
135	90	189	273	315	360	412	X	X
180	X	X	311	X	X	460	X	X
225	150	233	345	470	X	X	X	X
270	X	X	365	X	X	X	X	X
315	X	X	370	X	X	X	X	X
360	X	X	X	X	X	X	X	X

Table 5.2: Three braking conditions for subsequent tests.

Condition no.	Hydraulic brake pressure (bar)	Rotation speed (rpm)	Mean contact pressure (MPa)	Average sliding speed (m/s)
1	5	135	0.264	1.63
2	10	135	0.528	1.63
3	15	135	0.792	1.63

5.2.2 Repeatability tests

Tests at each of the three conditions were repeated three times in order to check for repeatability. All tests follow the same sampling procedure as described in Chapter 3. The rotor surface temperature was measured near the leading edge of the brake rotor using a K-type rubbing thermocouple as shown in Figure 5.1. Figure 5.2 shows the temperature-time history plot for all tests. Annotations in the figure legend have the following meaning; 'P' represents hydraulic pressure and 'A', 'B' and 'C' represent the 3 repetitions, respectively. The results show all temperatures attain a steady-state condition following a few minutes of the

braking process except for the test of P05A where the temperature gradually decreases after reaching a maximum value. Overall, these results confirm that good consistency has been achieved for the three braking conditions, although the result of P05A demonstrates a slight difference from the other results at this low pressure.

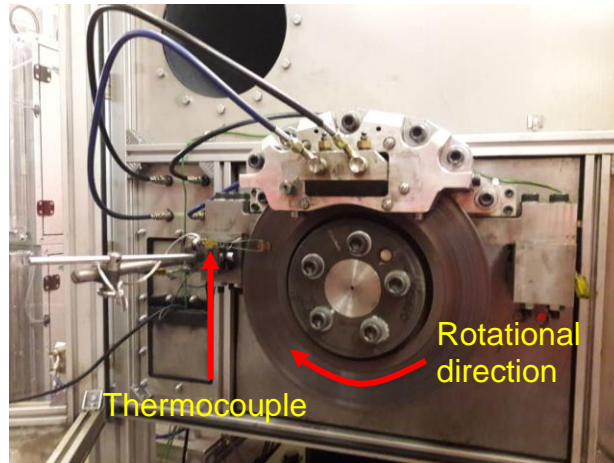


Figure 5.1: Position of the thermocouple at the leading side of the brake rotor.

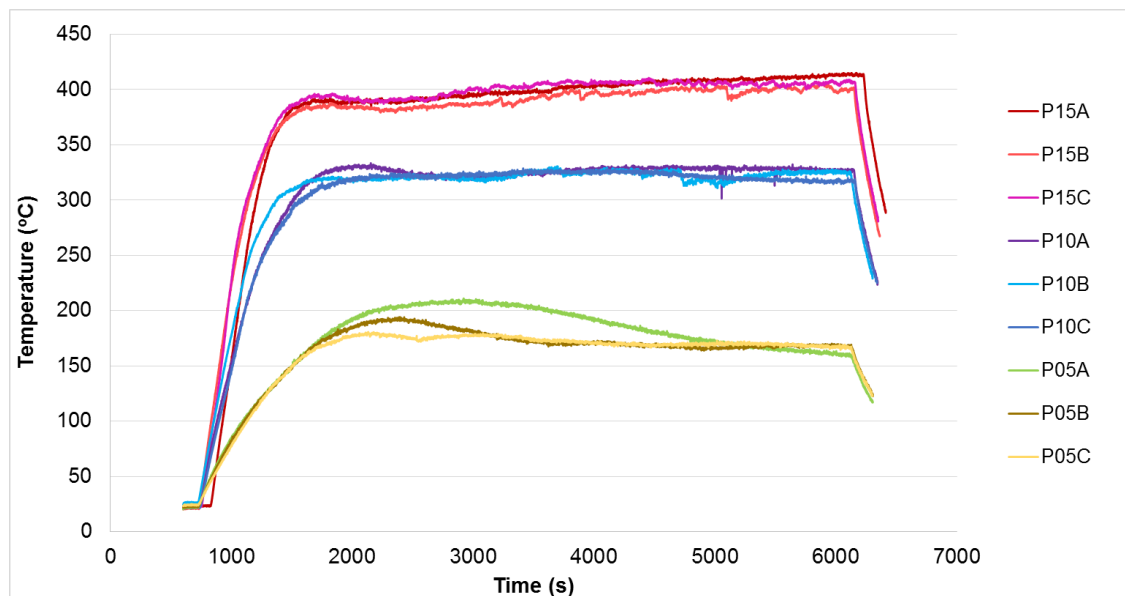


Figure 5.2: Rotor temperature variation with time for the three tests at each braking condition.

5.3 Particulate matter measurement

5.3.1 Background measurement

To investigate the role of the HEPA filter fitted to the inlet duct, measurements of the background (laboratory) air and the air once inside the extraction system were carried out without running the dynamometer. The particle concentrations were measured using the Dekati unit over a duration of 10 minutes. It can be seen from Figure 5.3 that the particle concentrations for both measurements were approximately constant throughout each test. The laboratory background air recorded an order of magnitude higher number concentration of particles compared to that inside the ducting system which indicates that the application of the HEPA filter leads to a clean supply to the system. This result underlines the importance of filtering the air before it enters the dynamometer enclosure.

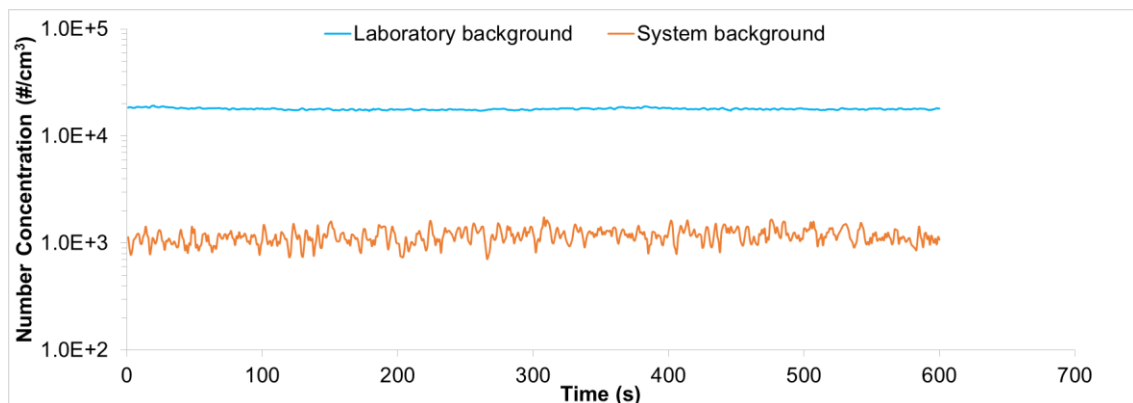


Figure 5.3: Comparison of particle concentrations in the laboratory and ducting system environments.

5.3.2 Brake wear emission measurement

Measurements of particle concentration during each braking event were carried out for 90 minutes (see Chapter 3 for the complete sampling procedure). Prior to this sampling, the background level inside the system was measured at the beginning of the tests for 10 minutes in order to ensure a consistent and acceptable level of cleanliness. Three pressures of 5, 10 and 15 bar at a constant speed of 135 rpm were employed in order to study the effect of the temperature on the particle concentration and mass distribution.

5.3.2.1 Real-time particle measurement

Figure 5.4 presents the particle concentration as a function of time for three different pressures. These particulate numbers are similar to the system background measurements shown in Figure 5.3, which may be due to the inefficacy of the HEPA filter to prevent very fine particles from entering the system. The huge numbers of these very fine particles dominate the number of larger particles that may be released from the friction interface.

The test at the lowest brake pressure of 5 bar, P05C, demonstrates an increasing pattern starting from 1000 seconds of the test duration although the increment is not considerable. The tests P10C and P15C also show a similar trend but starting at 2000 and 4000 seconds into the test cycle, respectively. A related point to consider here is the rate of the temperature rise at the beginning of a test may affect the rate of production of the brake wear debris. The results show that as the rate of temperature rise reduces with time, the rate of debris production increases.

In the case of test P15C, a sudden increase in particle number could be seen starting from 3600 seconds. Wear debris becoming trapped at the friction interface for a longer time may be the reason behind this. The higher the brake pressure, the stronger the brake pad squeezes on the brake rotor and logic dictates that it is then more difficult for the wear debris to escape from the interface. This will allow more debris to accumulate and subsequently agglomerate to produce larger particles. These agglomerates may cause third body abrasion and plowing on the surface of the brake pair and eventually they may break up into loose fragments and be released into the surrounding air (Ciudin et al., 2014).

The particle concentration generally increases with hydraulic pressure. This may be caused by the different temperatures developed during the contact for the three conditions studied. It is postulated that brake materials soften due to the reduction in bonding strength at elevated temperatures. Consequently, more brake particulates are generated with increasing brake rotor temperature.

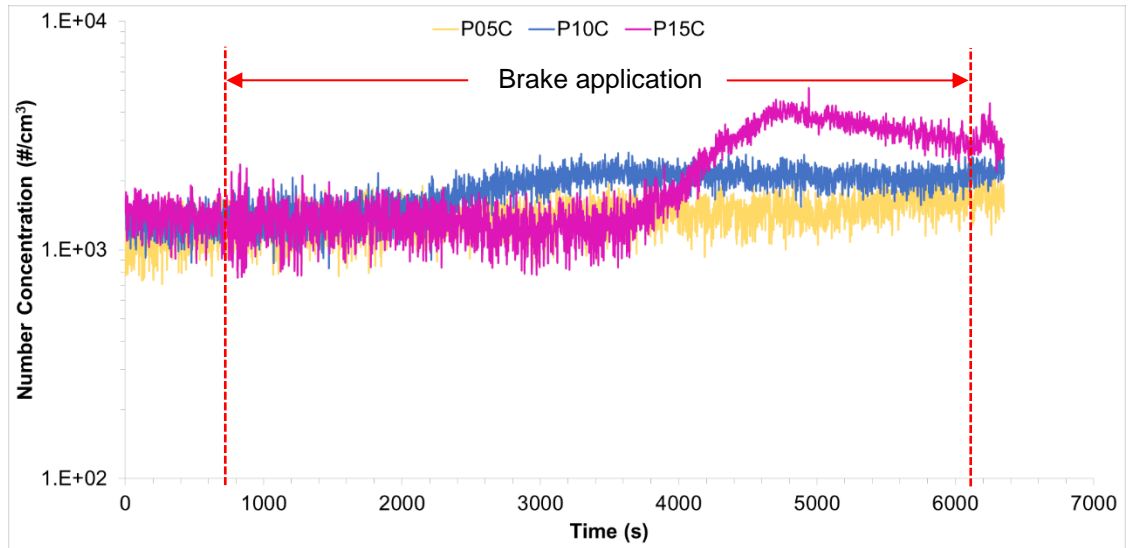


Figure 5.4: Particle concentration variation with time for three different pressures.

To check for repeatability, results of the real-time particle measurement for the three repeated tests of P10 were plotted together as shown in Figure 5.5. It can be seen that only test P10C demonstrates an increasing trend while the other two tests exhibit an insignificant change for the entire period of time. Nevertheless, these three results are fairly parallel at the beginning but then converge up to the end of the test and reduce the level of inconsistency. The lack of consistency shown here is most likely due to the different concentrations of very fine particles in the background air due to changing conditions in the laboratory before the real-time particle measurements commenced.

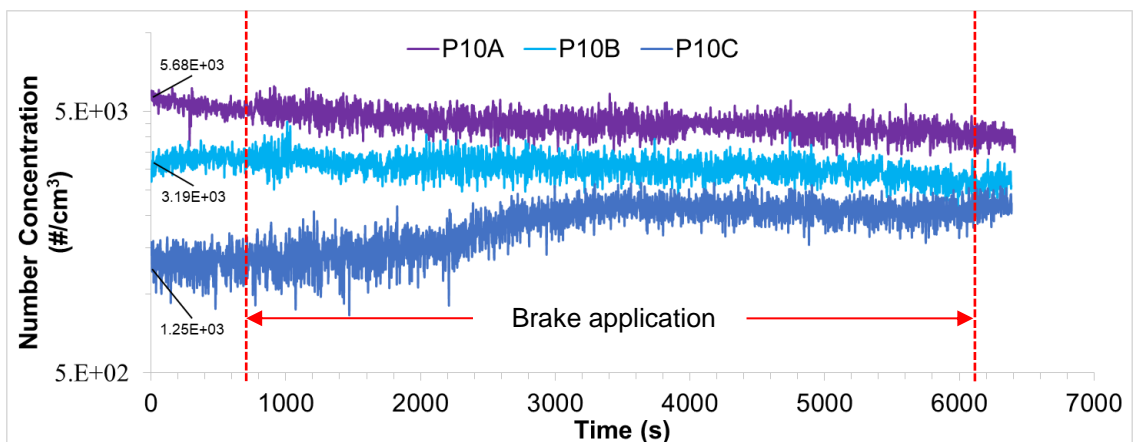
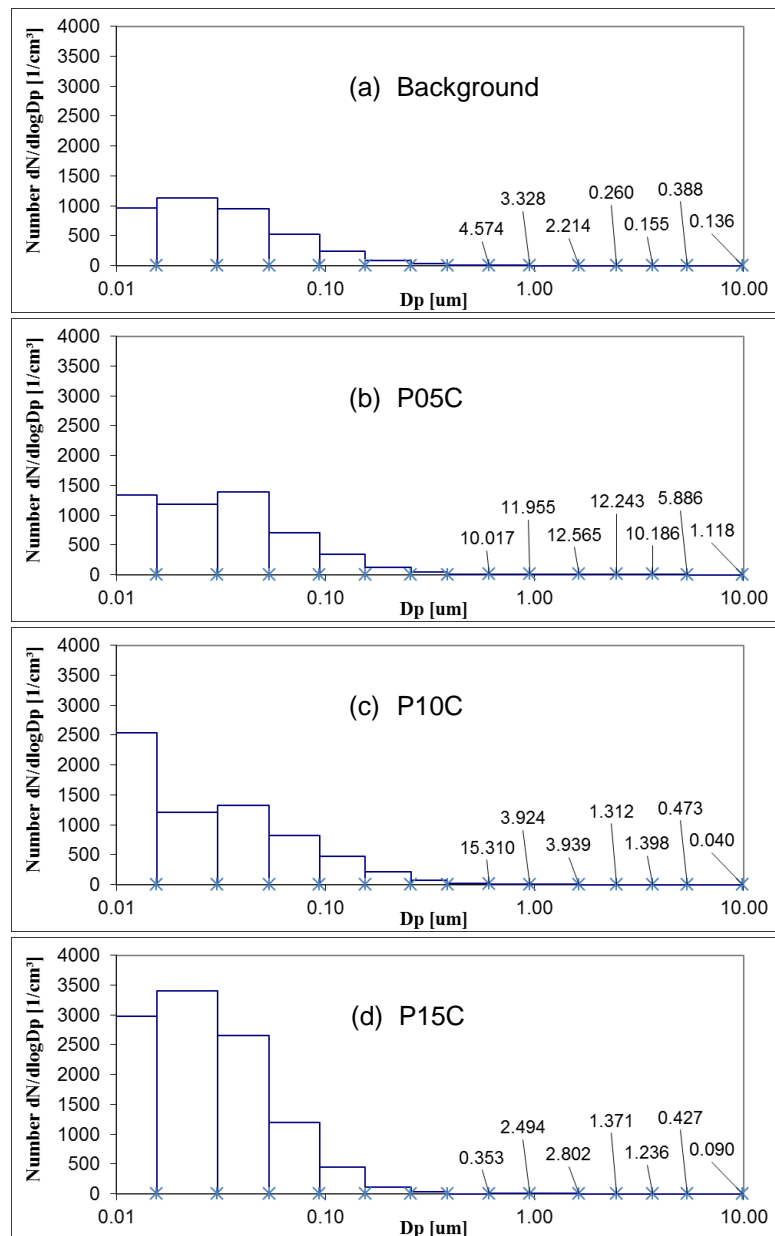


Figure 5.5: Particle concentration variation with time for the three tests of P10.

5.3.2.2 Particle number distribution

From the same results as above, particle number concentration can also be exhibited as a function of aerodynamic particle size. The number distribution was presented from the particle size range of 6 nm to 10 μm with 14 size intervals. All size distributions were averaged over a desired period of time. To compare the effect of a steady-state temperature on the particle number distribution, the measurement data were taken from the beginning to the end of the steady-state condition which is from 4000 to 6120 seconds from the start of each test.

The results of background and brake application number concentration distributions are shown in Figures 5.6 (a) and (b-d), respectively. It can be seen that significant numbers of particles with an aerodynamic diameter of less than 0.1 μm ($\text{PM}_{0.1}$ – ultrafine particles) were measured at all three pressures. The brake application measurements exhibit higher particle concentrations compared to the background measurement particularly for the test P15C. In the fine, $\text{PM}_{2.5}$ and coarse particle, PM_{10} regions (particles with an aerodynamic diameter less than 2.5 μm and 10 μm , respectively), the particle number concentrations recorded were very small. This is may due to the presence of several ducting and probe bends which allow the coarser particles to deposit on the ducting wall owing to the inertia effect. As the brake pressure increases, the distributions in these regions demonstrate a contradictory trend to the one in the $\text{PM}_{0.1}$ region. The particle concentration was greater at the low brake pressure compared to the high ones. Based on this relationship, it was expected that the mass distribution would be higher for the test with lower brake pressure.



increases when the brake pressure decreases from 15 to 10 bar, at a constant speed of 135 rpm. However, a much more significant increase occurs in the 1-10 μm range when the pressure is reduced to 5 bar. This may be because large particles are more readily released when the pad-disc contact pressure is reduced. Based on the obtained results, it is estimated that greater than 90% of the total brake particulate mass is emitted as particle sizes in the 1 to 10 μm range for all the braking conditions studied. This shows that coarse particles within this range dominate the brake wear debris emissions of road vehicles.

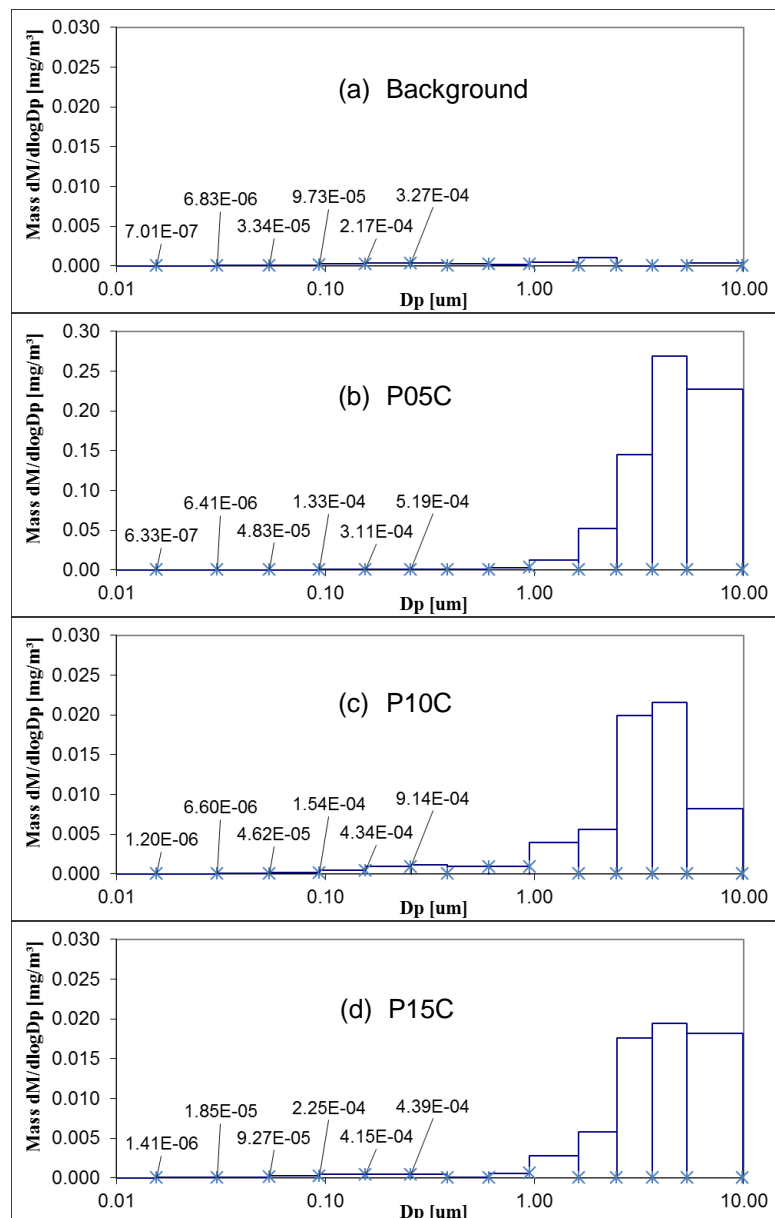


Figure 5.7: Mass distribution measurements for (a) background and (b-d) brake application at 5, 10 & 15 bar hydraulic pressure, respectively.

5.3.2.4 Airborne particulate matter classification

Particulate matter is commonly classified into two size groups which are coarse and fine particles. The previous section has stated that a coarse particle has an aerodynamic diameter between 2.5 to 10 μm (PM_{10}), whereas a fine particle has an aerodynamic diameter up to 2.5 μm ($\text{PM}_{2.5}$). Occasionally the particles in the fine size range which are smaller than 0.1 μm ($\text{PM}_{0.1}$) are recognised as ultrafine particles. In this study, brake wear emissions were evaluated according to three categories namely $\text{PM}_{0.1}$, $\text{PM}_{2.5}$ and PM_{10} with size ranges of 0.006 to 0.0938 μm , 0.0938 to 2.47 μm and 2.47 to 9.90 μm , respectively.

The particle number and mass concentrations recorded from the previous repeatability test (the tests at each of the three conditions were repeated three times) were added up within the same category and the corresponding average was determined for each test condition. Figure 5.8 shows brake wear emissions of the three classified PMs with regard to average particle number and particle mass concentrations. In the case of particle number concentration as shown in Figure 5.8 (a), the $\text{PM}_{0.1}$ dominates greater than 85% of the total airborne brake wear emissions for all three braking conditions. However, the other two categories demonstrate considerably low particle number concentration particularly that of PM_{10} . It can also be seen that the particle number increases as the brake pressure increases. Material softening with temperature as explained before might be the reason behind this occurrence. From Figure 5.8 (b), the particle mass concentration is clearly visible in the $\text{PM}_{2.5}$ and PM_{10} . These two PMs slightly increase as the brake pressure decrease from 15 to 10 bar and conversely, a much more significant increase occurs as the pressure is reduced to 5 bar. The PM_{10} contributes greater than 80% of the total airborne brake wear emissions for all three braking conditions. Figure 5.8 (b) also shows that only a tiny amount of $\text{PM}_{0.1}$ in terms of particle mass concentration is present in the brake wear emissions.

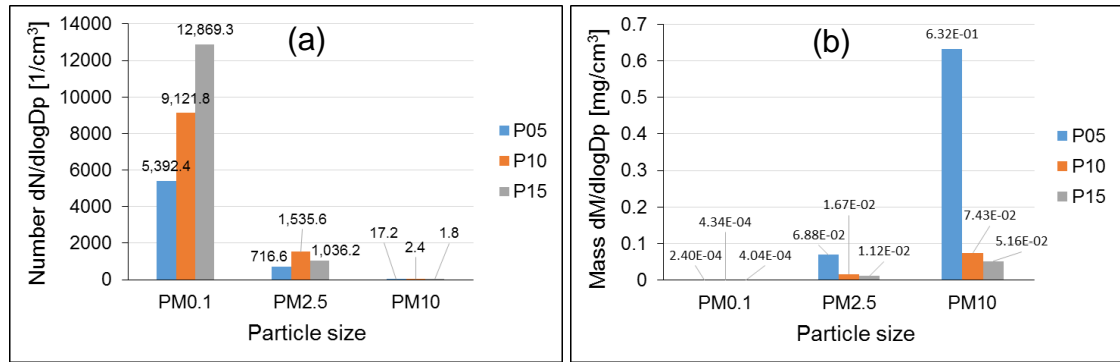


Figure 5.8: Brake wear emissions of PM_{0.1}, PM_{2.5} and PM₁₀ based on average (a) particle number and (b) particle mass concentrations.

5.4 Gravimetric analysis

The determination of particle mass concentration by the gravimetric method was carried out using a Mettler Toledo XP26 Analytical Balance with a resolution of 1 µg. Airborne brake wear particles were collected by following the same sampling procedure as in the previous tests but without background and real-time particle (charger OFF) measurements. In this study, the collection substrates used are the greased Al foils which were placed in the ELPI®+ impactor at every stage except stage number 1. The stage is the last stage of the impactor and measures the particle size range of 0.006 to 0.0156 µm. This stage was designed without a collection plate and so debris in this ultra-fine size range cannot be gravimetrically or chemically analysed. Al foils prior to and after the tests were weighed on the weighing balance in order to determine the mass of the airborne brake wear particles. Readings were taken 3 times to ensure consistent measurement and to avoid any errors that could occur during the weighing process.

The mass of the particles in each size interval was calculated in order to determine the particle mass concentration (mg/m³). The calibrated impactor flow rate value provided by the manufacturer is 9.94 lpm. Assuming a sampling duration of 90 minutes, the volume of air sampled can be determined. The summary of all calculation results is shown in Tables 5.3-5.5 for the three test pressures.

Table 5.3: Mass concentration calculation for the test P05D.

Stage no.	Stage Cut-point D_p (microns)	Initial mass W_1 (mg)	Final mass W_2 (mg)	Particulate mass W ($\times 10^{-3}$ mg)	Concentration ΔC ($\times 10^{-3}$ mg/m ³)	$\log_{10} D_p$	$\Delta \log_{10} D_p$	$\Delta C / \Delta \log_{10} D_p$ (10^{-3} mg/m ³ /log micron)
	0.006	-	-	-	-	-	-	-
1	0.0156	-	-	-	-	-1.8069	-	0
2	0.0305	15.0440	15.0457	1.667	1.863	-1.5157	0.2912	6.40
3	0.0539	15.1377	15.1410	3.333	3.726	-1.2684	0.2473	15.1
4	0.0938	15.0187	15.0210	2.333	2.608	-1.0278	0.2406	10.8
5	0.155	15.5980	15.6020	4.000	4.471	-0.8097	0.2181	20.5
6	0.256	15.0570	15.0587	1.667	1.863	-0.5918	0.2179	8.55
7	0.383	15.1073	15.1090	1.667	1.863	-0.4168	0.1750	10.6
8	0.604	14.9817	14.9847	3.000	3.353	-0.2190	0.1978	17.0
9	0.949	14.8623	14.8660	3.667	4.099	-0.0227	0.1962	20.9
10	1.63	14.9693	14.9743	5.000	5.589	0.2122	0.2349	23.8
11	2.47	15.4557	15.4660	10.33	11.55	0.3927	0.1805	6.40
12	3.66	14.8930	14.9150	22.00	24.59	0.5635	0.1708	144
13	5.37	15.4377	15.4650	27.33	30.55	0.7300	0.1665	184
14	9.9	15.0717	15.0850	13.33	14.90	0.9956	0.2657	56.1

Table 5.4: Mass concentration calculation for the test P10D.

Stage no.	Stage Cut-point D_p (microns)	Initial mass W_1 (mg)	Final mass W_2 (mg)	Particulate mass W (10^{-3} mg)	Concentration ΔC (10^{-3} mg/m ³)	$\log_{10} D_p$	$\Delta \log_{10} D_p$	$\Delta C / \Delta \log_{10} D_p$ (10^{-3} mg/m ³ /log micron)
	0.006	-	-	-	-	-	-	-
1	0.0156	-	-	-	-	-1.8069	-	0
2	0.0305	15.0553	15.0570	1.667	1.863	-1.5157	0.2912	6.40
3	0.0539	15.1877	15.1883	0.6667	0.7452	-1.2684	0.2473	3.01
4	0.0938	14.8153	14.8157	0.3333	0.3726	-1.0278	0.2406	1.55
5	0.155	15.0760	15.0787	2.667	2.981	-0.8097	0.2181	13.7
6	0.256	15.3153	15.3177	2.333	2.608	-0.5918	0.2179	12.0
7	0.383	15.0537	15.0557	2.000	2.236	-0.4168	0.1750	12.8
8	0.604	15.2370	15.2407	3.667	4.099	-0.2190	0.1978	20.7
9	0.949	15.2827	15.2853	2.667	2.981	-0.0227	0.1962	15.2
10	1.63	15.4777	15.4787	1.000	1.118	0.2122	0.2349	4.76
11	2.47	15.1183	15.1277	9.333	10.43	0.3927	0.1805	57.8
12	3.66	15.1257	15.1353	9.667	10.81	0.5635	0.1708	63.3
13	5.37	15.1557	15.1653	9.667	10.81	0.7300	0.1665	64.9
14	9.9	14.8930	14.8990	6.000	6.707	0.9956	0.2657	25.2

Table 5.5: Mass concentration calculation for the test P15D.

Stage no.	Stage Cut-point D_p (microns)	Initial mass W_1 (mg)	Final mass W_2 (mg)	Particulate mass W (10^{-3} mg)	Concentration ΔC (10^{-3} mg/m ³)	$\log_{10} D_p$	$\Delta \log_{10} D_p$	$\Delta C / \Delta \log_{10} D_p$ (10^{-3} mg/m ³ /log micron)
	0.006	-	-	-	-	-	-	-
1	0.0156	-	-	-	-	-1.8069	-	0
2	0.0305	15.1073	15.1087	1.333	1.490	-1.5157	0.2912	5.12
3	0.0539	15.1553	15.1563	1.000	1.118	-1.2684	0.2473	4.52
4	0.0938	15.3997	15.4013	1.667	1.863	-1.0278	0.2406	7.74
5	0.155	15.4343	15.4370	2.667	2.981	-0.8097	0.2181	13.7
6	0.256	15.1303	15.1323	2.000	2.236	-0.5918	0.2179	10.3
7	0.383	14.8290	14.8303	1.333	1.490	-0.4168	0.1750	8.52
8	0.604	15.2943	15.2967	2.333	2.608	-0.2190	0.1978	13.2
9	0.949	15.0743	15.0773	3.000	3.353	-0.0227	0.1962	17.1
10	1.63	15.4323	15.4357	3.333	3.726	0.2122	0.2349	15.9
11	2.47	14.9440	14.9497	5.667	6.334	0.3927	0.1805	35.1
12	3.66	14.8903	14.8970	6.667	7.452	0.5635	0.1708	43.6
13	5.37	15.0097	15.0170	7.333	8.197	0.7300	0.1665	49.2
14	9.9	15.2787	15.2827	4.000	4.471	0.9956	0.2657	16.8

Particle mass distributions were plotted from the calculated values as shown in Figure 5.9. The figure shows that the coarse particle fractions are dominant in all tests. The mass of the coarse particle fractions increases as the brake pressure decreases which is similar to the result obtained from the real-time particle measurements reported in Section 5.3. The actual concentration values are also similar to the real-time measurements. This similarity validated the results of the real-time particle mass distributions for the airborne brake wear particles generated from the grey cast iron rotor and its conforming pads.

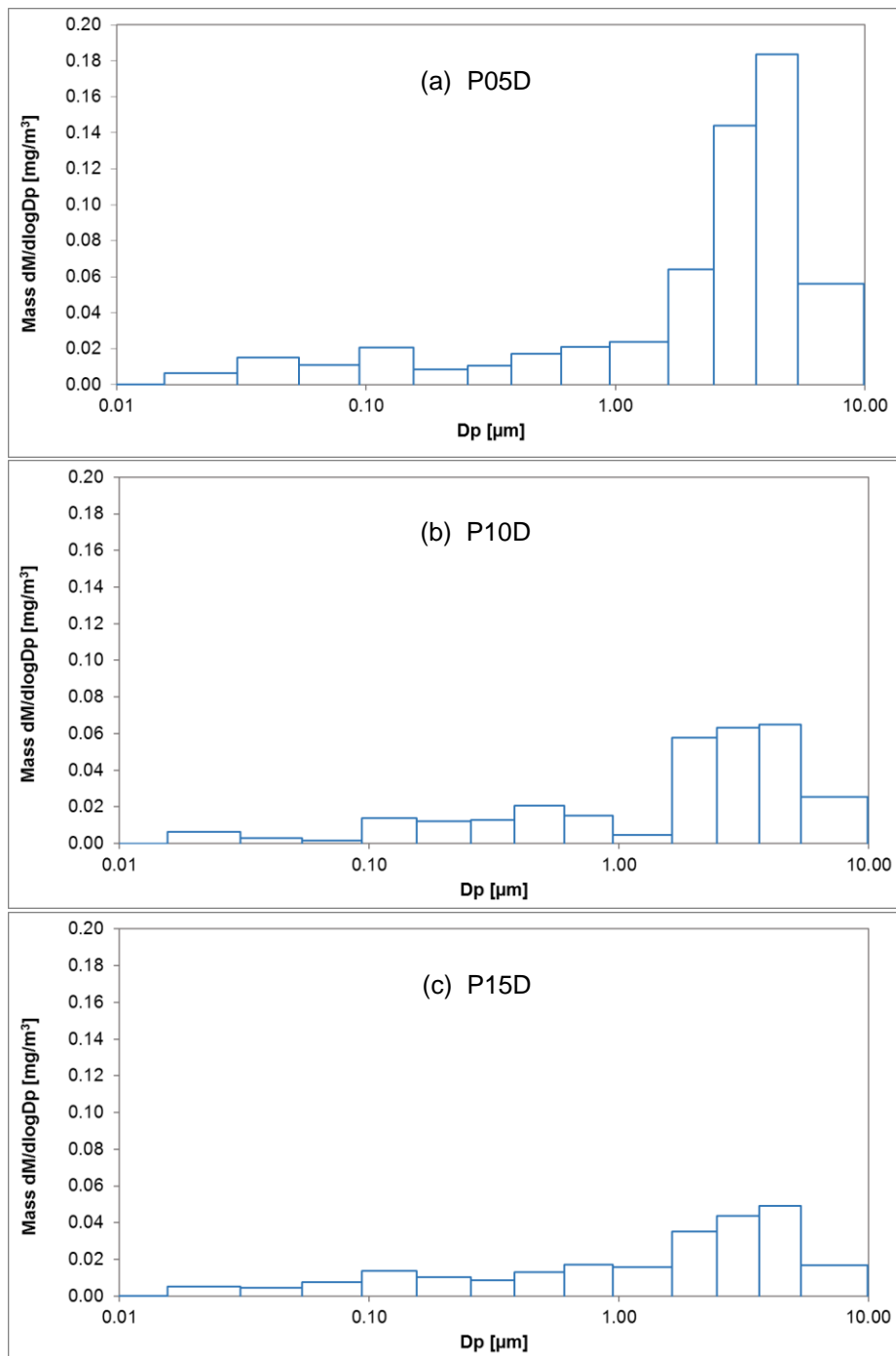


Figure 5.9: Particle mass distributions for (a) test P05D, (b) test P10D and (c) test P15D.

5.5 Microstructural analysis

The morphologies of airborne brake wear debris were examined in a Hitachi TM3030Plus Tabletop Scanning Electron Microscope (SEM). Samples were

collected on greased polycarbonate (PC) foils during a braking test. The same sampling procedure as for the previous tests was followed exactly but without background air measurements. The Dekati ELPI®+ with 14 impactor stages was employed to accumulate samples but only five PC foils were used in order to collect particles in the range of 1 μm – 10 μm (stages 10-14) because this larger scale range was of most interest due to its high mass fraction. In addition, the brake wear particles that fell down on the bottom of the enclosure were also collected on a PC foil. The position of the foil placed on the bottom of the enclosure (underneath the trailing end of the caliper) is shown in Figure 5.10.

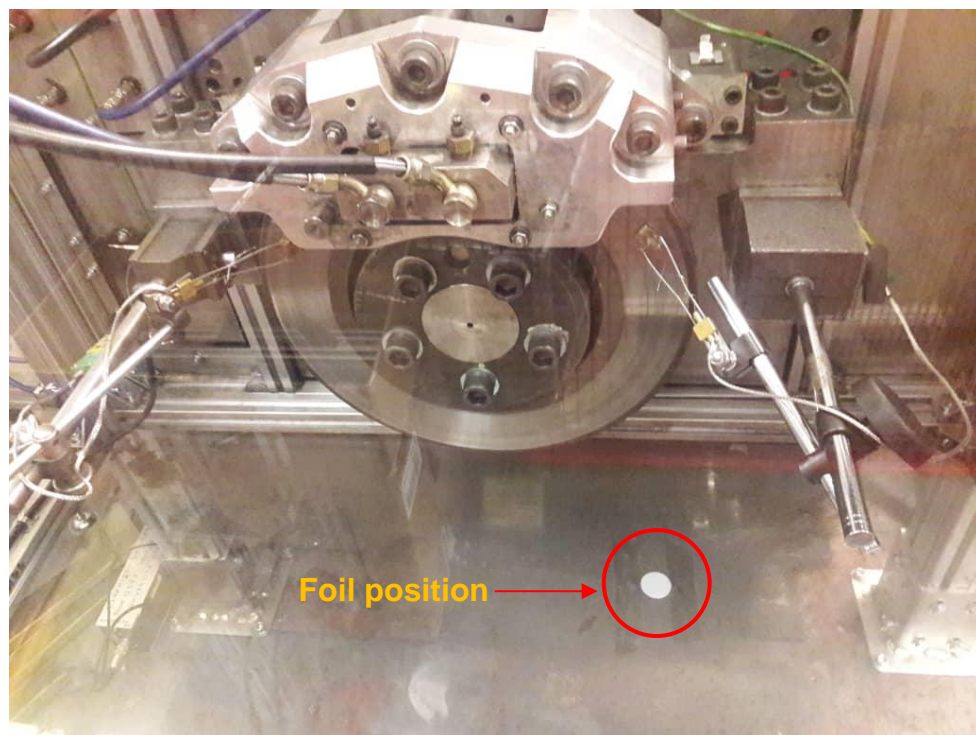


Figure 5.10: PC foil position on the bottom of the enclosure.

Under the same three drag braking conditions as before, the temperature of the rotor rubbing surface was recorded concurrently with the particle collections. Figure 5.11 shows the recorded rotor temperature as a function of time. It is clear that steady-state conditions occur after about 3000 seconds for all three tests. The constant temperatures attained were also closely consistent with the target temperatures, namely 200, 300 and 400°C. This result verifies that the tests can be repeated confidently in order to generate results which are consistent with those shown in Figure 5.2.

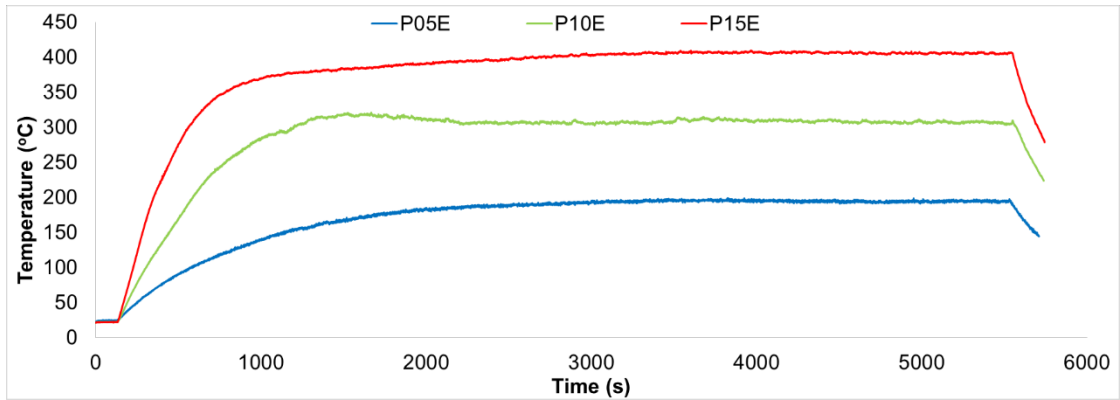


Figure 5.11: Rotor temperature variation with time for the three braking conditions during particle collections.

The presence of the particles deposited on the foils in one of the tests, namely test P05E is displayed in Figure 5.12. The integer number labelled below the PC foil indicates the stage number, with the higher number indicating the larger particle size interval. Dark spots can be seen deposited on the PC foils at certain positions from the centre. Different patterns were clearly formed on each PC foil. These patterns were in fact induced by the jet plate which has a small nozzle or multiple nozzles machined in it. Its positioning on top of the collection plate allows particles with a specified size range to be deposited onto the PC foil. An example of the jet plate for the stage number 12 is shown in Figure 5.12.



Figure 5.12: Brake wear particles collected on polycarbonate foils for the corresponding stage number.

SEM observations were conducted on the brake wear debris collected on the foils at magnification levels of 1200x and 6000x. At a magnification of 1200x, particle distributions can be easily observed and examined, whereas at a magnification of 6000x individual particles can be visibly studied. A location within a typical dark spot was randomly selected on each PC foil (from the impactor) and the micrographs were recorded at this location. All micrographs taken from the different stages of ELPI®+ are exhibited in Figures 5.13-5.15 for brake pressures of 5, 10 and 15 bar, respectively. Moreover, two locations were randomly selected on the PC foils positioned on the bottom of the enclosure. The images taken from the SEM at 3000x magnifications from these foils are exhibited in Figure 5.16 for all three braking conditions.

Generally, it can be seen from the micrographs that the amount of wear debris collected is abundant at the finer particle size range stages. The number of particles visible reduces from fine to coarse particles in all tests. Most of the particles are irregular in shape and there is no apparent difference in the shape of particles at the different stages. The presence of clustered (agglomerated) particles was also not evident even in the small particle size ranges. However, it seems that finer particles have a tendency to form clusters of wear debris (refer to micrographs (a) in Figures 5.13-5.15). This occurrence could be observed undoubtedly if particles less than 1 μm were collected and examined thoroughly. In terms of particle size, most of the particles are classified and registered correctly in the corresponding stages. Nevertheless, some finer particles could be seen on a stage with a larger size interval. This phenomenon might be due to the effects of diffusion as the fine particles passed through the preceding stage. At the same time, there is also a small number of coarse particles deposited on finer stages. This might be caused by the particle bounce and blow-off effects that could happen to larger particles which fall from the stages they should be captured on to lower stages. Another aspect that is worthy of note is that overall airborne brake wear particles are more abundant on the PC foils for the test with lower brake pressure. This qualitative result is consistent with the quantitative measures of particle mass distribution which were obtained from the real-time particle measurement and gravimetric analysis.

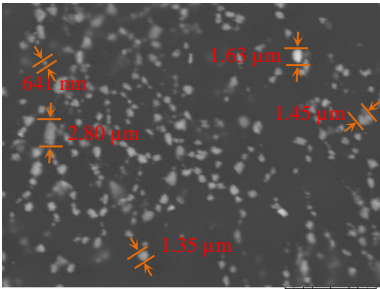
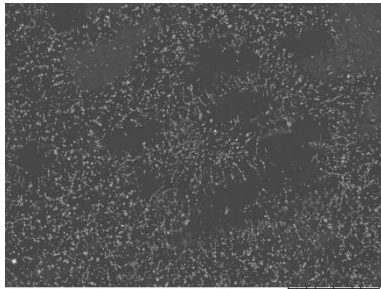
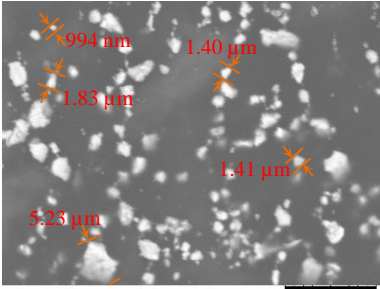
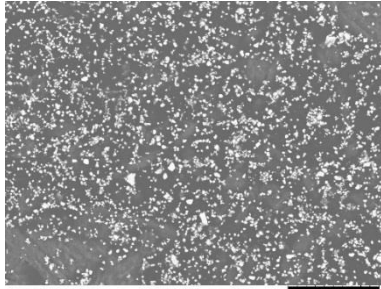
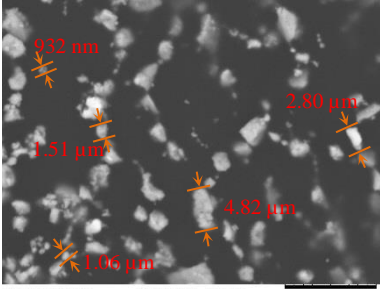
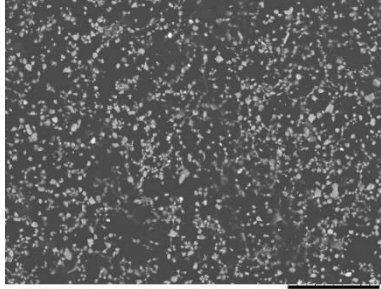
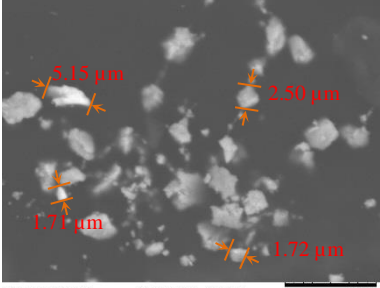
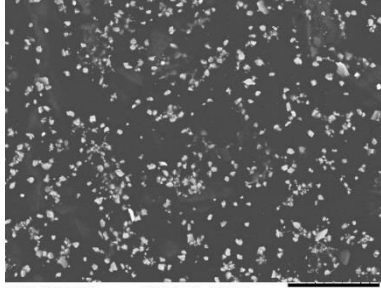
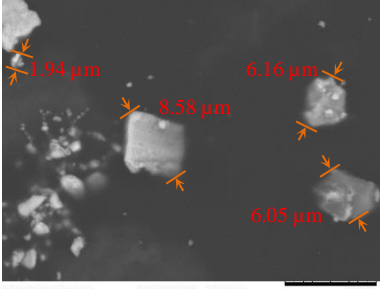
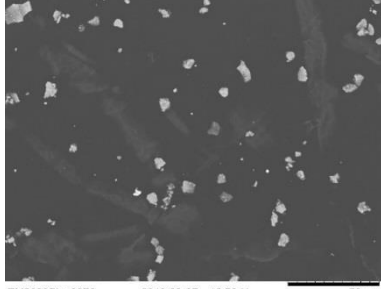
Stage & Size (μm)	Particle images	
	6000x	1200x
(a) Stage 10 (0.949 – 1.63)	 <p>TM3030Plus0047 2019-03-07 11:13 N 10 μm</p>	 <p>TM3030Plus0045 2019-03-07 11:10 N 50 μm</p>
(b) Stage 11 (1.630 – 2.47)	 <p>TM3030Plus0066 2019-03-07 12:25 N 10 μm</p>	 <p>TM3030Plus0064 2019-03-07 12:21 N 50 μm</p>
(c) Stage 12 (2.470 – 3.66)	 <p>TM3030Plus0070 2019-03-07 12:37 N 10 μm</p>	 <p>TM3030Plus0068 2019-03-07 12:34 N 50 μm</p>
(d) Stage 13 (3.660 – 5.37)	 <p>TM3030Plus0074 2019-03-07 12:49 N 10 μm</p>	 <p>TM3030Plus0072 2019-03-07 12:46 N 50 μm</p>
(e) Stage 14 (5.370 – 9.90)	 <p>TM3030Plus0078 2019-03-07 13:01 N 10 μm</p>	 <p>TM3030Plus0076 2019-03-07 12:58 N 50 μm</p>

Figure 5.13: Micrographs for the test P05E.

Stage & Size (μm)	Particle images	
	6000x	1200x
(a) Stage 10 (0.949 – 1.63)	<p>TM3030Plus0029 2019-03-06 16:55 N 10 μm</p>	<p>TM3030Plus0027 2019-03-06 16:48 N 50 μm</p>
(b) Stage 11 (1.630 – 2.47)	<p>TM3030Plus0034 2019-03-06 17:15 N 10 μm</p>	<p>TM3030Plus0032 2019-03-06 17:12 N 50 μm</p>
(c) Stage 12 (2.470 – 3.66)	<p>TM3030Plus0038 2019-03-06 17:28 N 10 μm</p>	<p>TM3030Plus0036 2019-03-06 17:25 N 50 μm</p>
(d) Stage 13 (3.660 – 5.37)	<p>TM3030Plus0042 2019-03-06 17:52 N 10 μm</p>	<p>TM3030Plus0040 2019-03-06 17:44 N 50 μm</p>
(e) Stage 14 (5.370 – 9.90)	<p>TM3030Plus0051 2019-03-07 11:33 N 10 μm</p>	<p>TM3030Plus0049 2019-03-07 11:27 N 50 μm</p>

Figure 5.14: Micrographs for the test P10E.

Stage & Size (μm)	Particle images	
	6000x	1200x
(a) Stage 10 (0.949 – 1.63)	<p>TM3030Plus0092 2019-03-15 16:59 N 10 μm</p>	<p>TM3030Plus0094 2019-03-15 17:01 N 50 μm</p>
(b) Stage 11 (1.630 – 2.47)	<p>TM3030Plus0098 2019-03-18 12:22 N 10 μm</p>	<p>TM3030Plus0097 2019-03-18 12:21 N 50 μm</p>
(c) Stage 12 (2.470 – 3.66)	<p>TM3030Plus0005 2019-03-05 16:00 N 10 μm</p>	<p>TM3030Plus0008 2019-03-05 16:06 N 50 μm</p>
(d) Stage 13 (3.660 – 5.37)	<p>TM3030Plus0009 2019-03-05 16:19 N 10 μm</p>	<p>TM3030Plus0012 2019-03-05 16:25 N 50 μm</p>
(e) Stage 14 (5.370 – 9.90)	<p>TM3030Plus0013 2019-03-05 16:43 H 10 μm</p>	<p>TM3030Plus0016 2019-03-05 16:48 N 50 μm</p>

Figure 5.15: Micrographs for the test P15E.

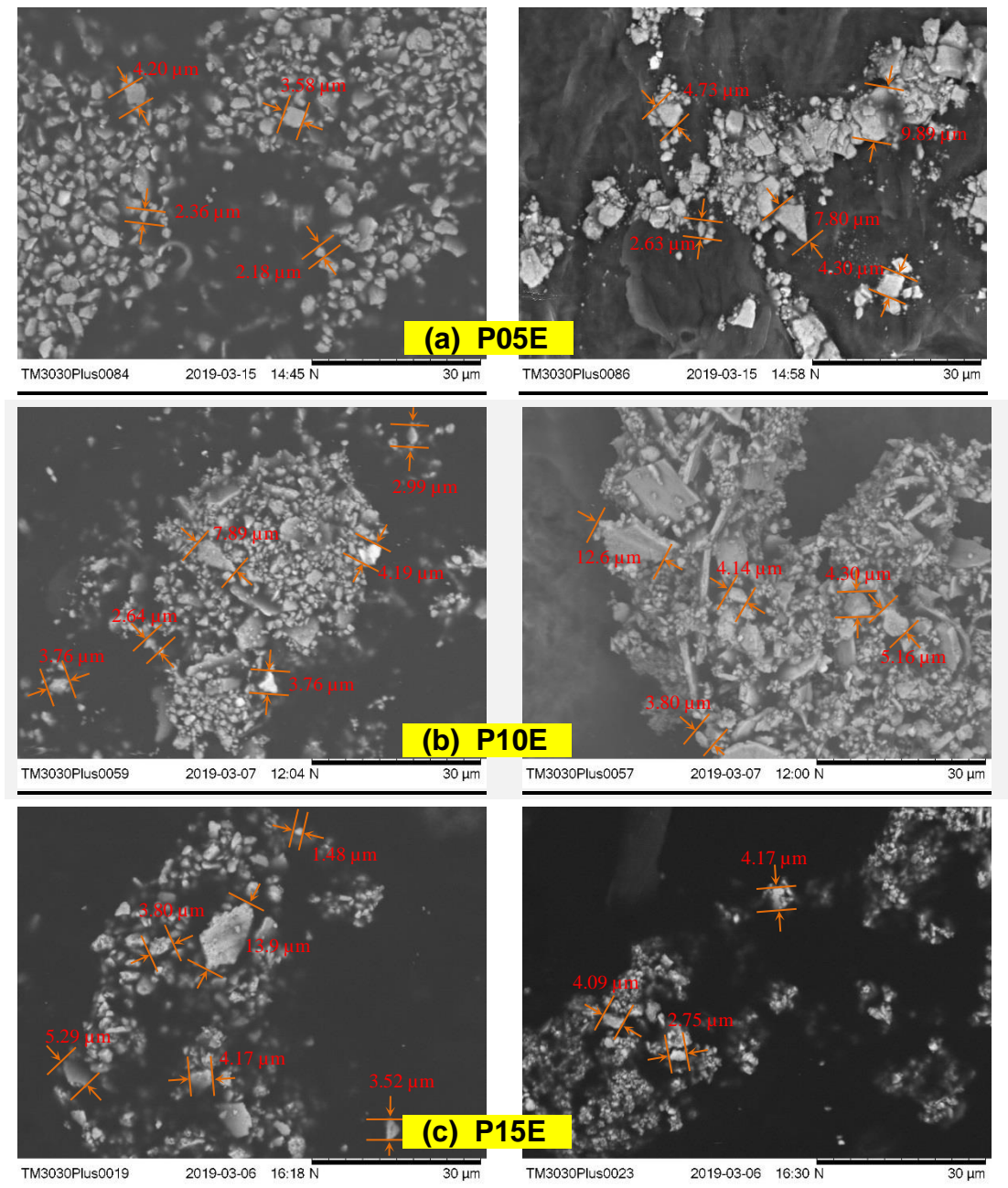


Figure 5.16: Micrographs of the collected particles on the bottom of the enclosure at 3000x magnifications for (a) test P05E, (b) test P10E and (c) test P15E.

Referring to Figure 5.16, it can be seen that particles of different size were deposited on the bottom of the enclosure during the braking process. The size of particles ranges from submicron to 15 μm . Particles with a size of less than 10 μm are quite substantially deposited on the PC foils. This shows that there are many particles that became entrapped inside the enclosed chamber and are then deposited on the bottom of the enclosure. The debris from the test P05E showed

more fragmented particles, while more agglomerated particles were found from the test P15E. The test P10E was also observed to have both fragmented and agglomerated particles. These agglomerates consist of particles with sub-micron to few-micron sizes in a variety of shapes.

5.6 Elemental composition evaluation

5.6.1 EDX mapping analysis for the blank PC foil

To ensure the elements discovered in the EDX analyses described below solely originated from the wear debris, a blank PC foil with grease applied in the same way as for all the other foils was examined. Figure 5.17 summarises the results of this quantitative analysis of the blank PC foil. Two different randomly selected locations were investigated in order to ascertain the consistency of the result. The magnification level employed is 3000x. EDX mapping analysis was conducted on the whole field of view. It can be noticed that the elemental distribution for the two results is just about the same, showing that carbon (C) and oxygen (O) have high percentages while the other elements have very low percentages (<0.5%). The good consistency between the two locations gives confidence in using the results as a reference for subsequent analyses.

5.6.2 EDX mapping analysis for the collected particles

EDX analysis was carried out to evaluate chemical compositions of the collected particles on the PC foils. The same samples as utilised in the SEM examination were analyzed using the integrated EDX system in the Hitachi TM3030Plus SEM. All samples from the tests at the three different pressures were examined at 3000x magnifications. A location within a dark spot was randomly selected as illustrated in Figure 5.18 and the micrographs were taken at this location. EDX mapping analyses were conducted on the whole field of view. At the same time, the relevant spectra were also recorded. Due to a large number of results, only EDX map images that were obtained from samples on stage number 12 (2.47 – 3.66 μm) are exhibited in Figures 5.19-5.21. The corresponding spectrum for each EDX map image is shown separately in Figure 5.22.

Overall, the results for the three different pressures show the samples mostly contain carbon and oxygen elements. Both elements most likely originate from the PC foil. This assumption was verified by referring to the results obtained in Section 5.6.1. The result showed that both C and O have high elemental weight percentages in the sample. Apart from originating from the foil itself, the carbon detected was possibly from the lubricants (graphite) in the brake pads, whereas the oxygen might be derived from oxides used whether as an abrasive (e.g. Al_2O_3) or a filler (e.g. CaCO_3) in the pads.

With carbon and oxygen excluded from the analyses for the above reasons, elemental weight percentages are shown in Figures 5.23-5.25. These figures provide information about elemental composition of all fractions (stages 10-14 and enclosure) collected during the three test conditions. The distributions display no significant differences for the different conditions or from fine to coarser particles. It was found that iron (Fe), barium (Ba), sulphur (S), silicon (Si), chromium (Cr) and calcium (Ca) are the most predominant elements in the samples. Other elements present are chlorine (Cl), sodium (Na), aluminium (Al), potassium (K), magnesium (Mg), tungsten (W), bromine (Br), titanium (Ti), strontium (Sr), molybdenum (Mo), mercury (Hg), terbium (Tb), manganese (Mn) and copper (Cu).

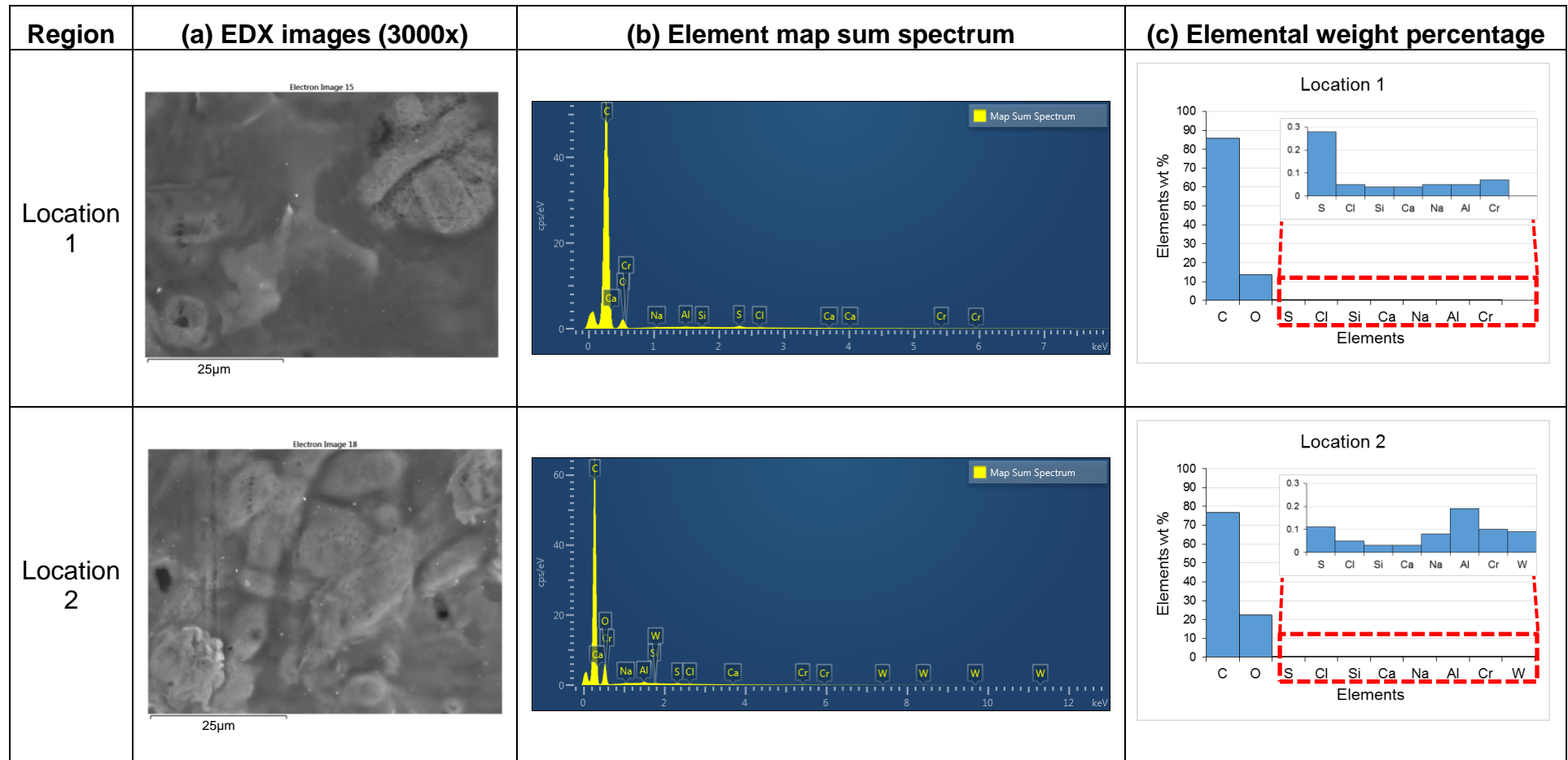


Figure 5.17: EDX images and elemental weight percentages of the greased PC foil.

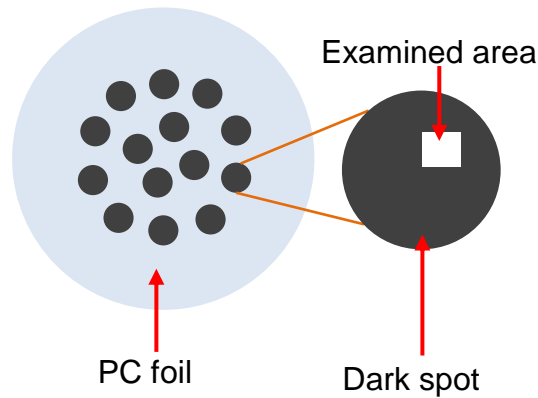


Figure 5.18: An illustration of the examined area within a dark spot on a PC foil.

The abundant Fe that was detected may come from the grey cast iron rotor itself. There is a possibility that this Fe undergoes an oxidation process during the braking event. Thus iron oxide phases such as FeO, Fe₂O₃ and Fe₃O₄ may be formed after completing chemical reactions at the friction interface (Verma et al., 2016). The presence of Ba and S might be derived from the barium sulphate, BaSO₄ compound which is employed as a filler in brake pads in order to improve noise and also reduce manufacturing cost (S. Venkatesh and K. Murugapoopathiraja 2019). The presence of iron oxides and barium sulphate can be speculated from Figures 5.19-5.21. The elements Fe and O were observed overlapping at the same location. The same coincidence was also observed for the elements Ba and S.

The observed Cr and Ca may originate from compounds such as chromium oxide, Cr₂O₃ or calcium carbonate, CaCO₃, respectively in the brake pad material. Similarly the Al and K may come from the compounds such as aluminium oxide, Al₂O₃ (abrasive) and potassium nitrite, KNO₂ (reinforcing fibers). Moreover, Si is utilised in resins for binding the constituents of a brake pad firmly. Other elements which are identified to contribute only a tiny percentage may or may not originate from the brake materials themselves.

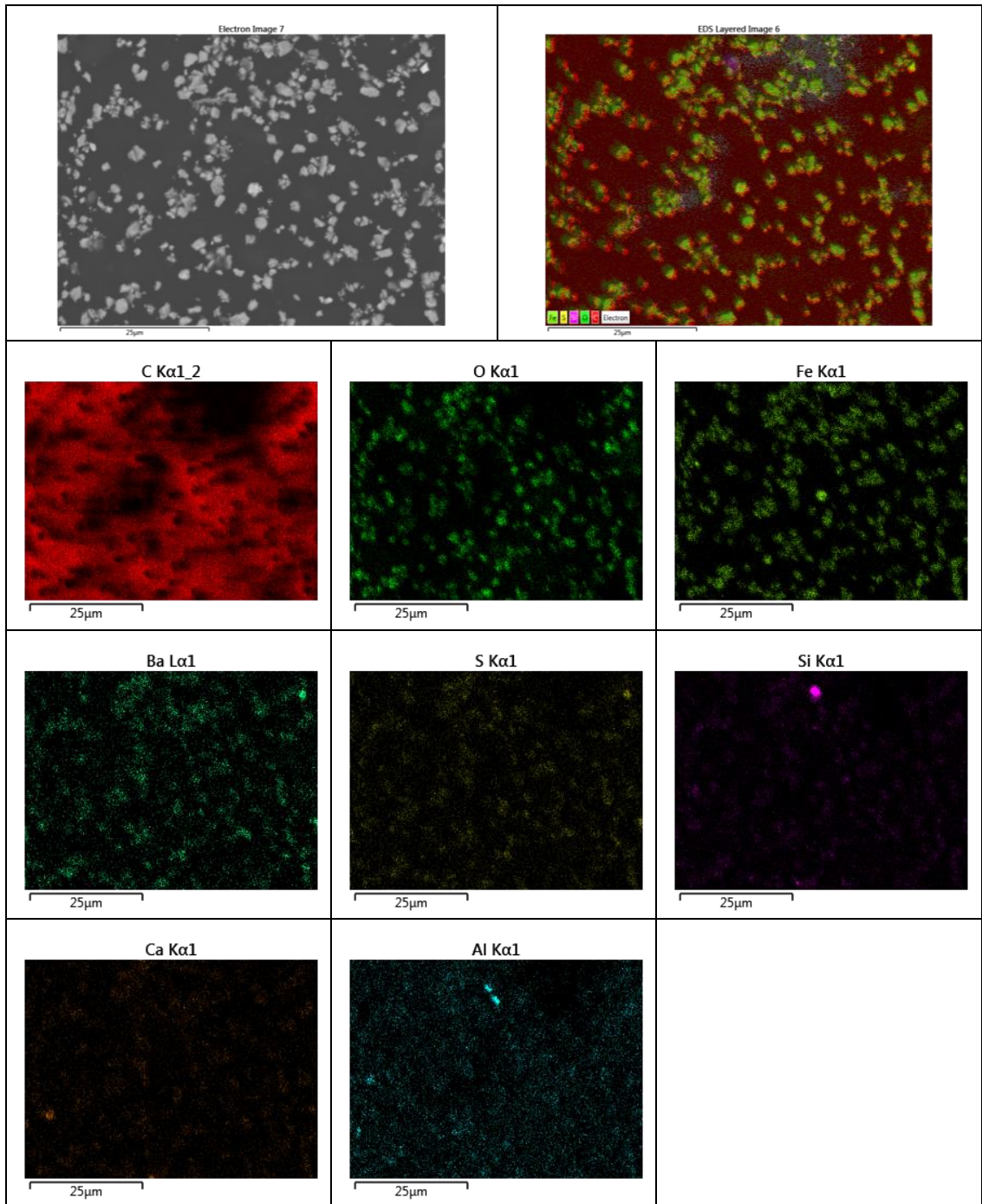


Figure 5.19: EDX map images for the test P05E.

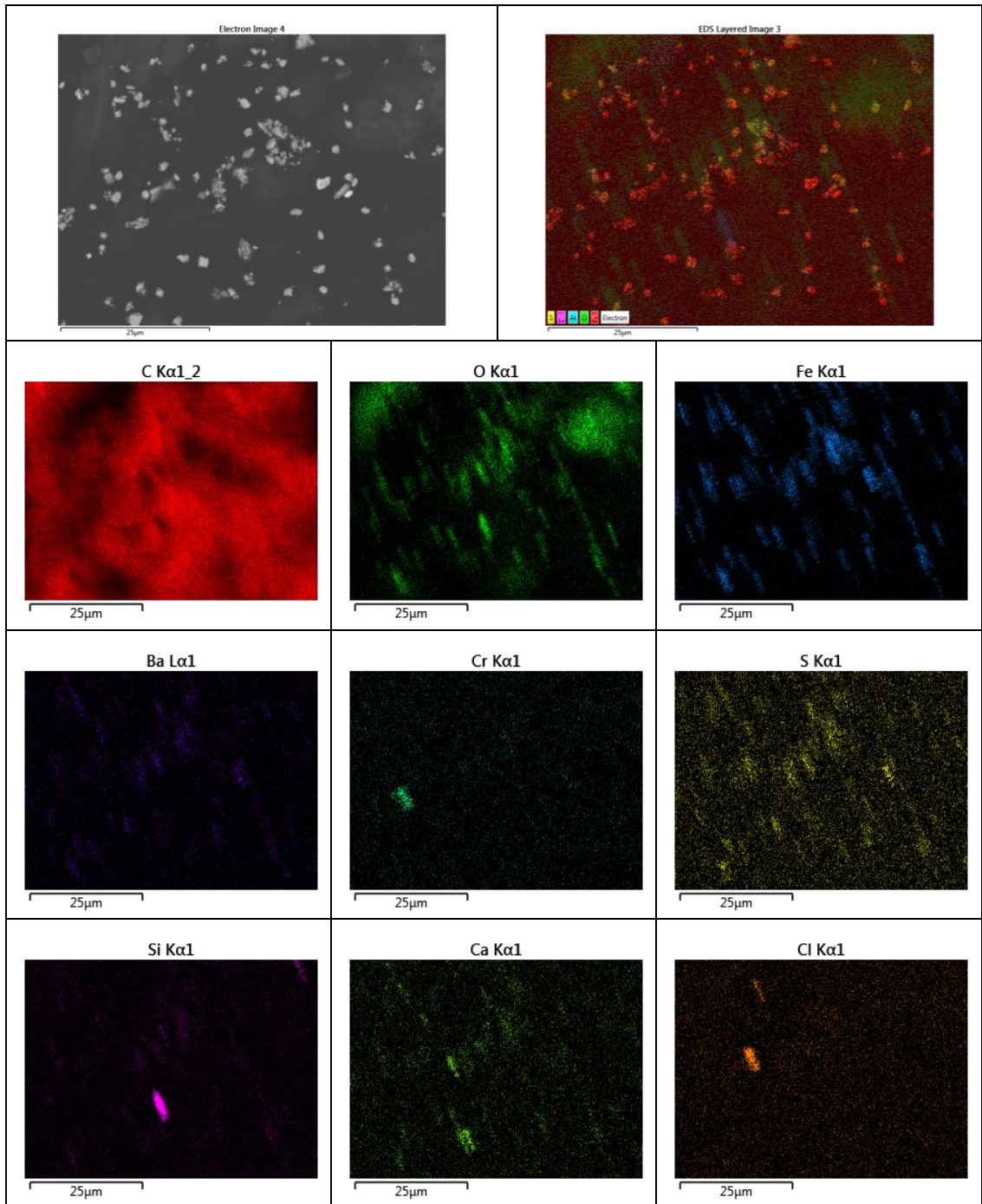


Figure 5.20: EDX map images for the test P10E.

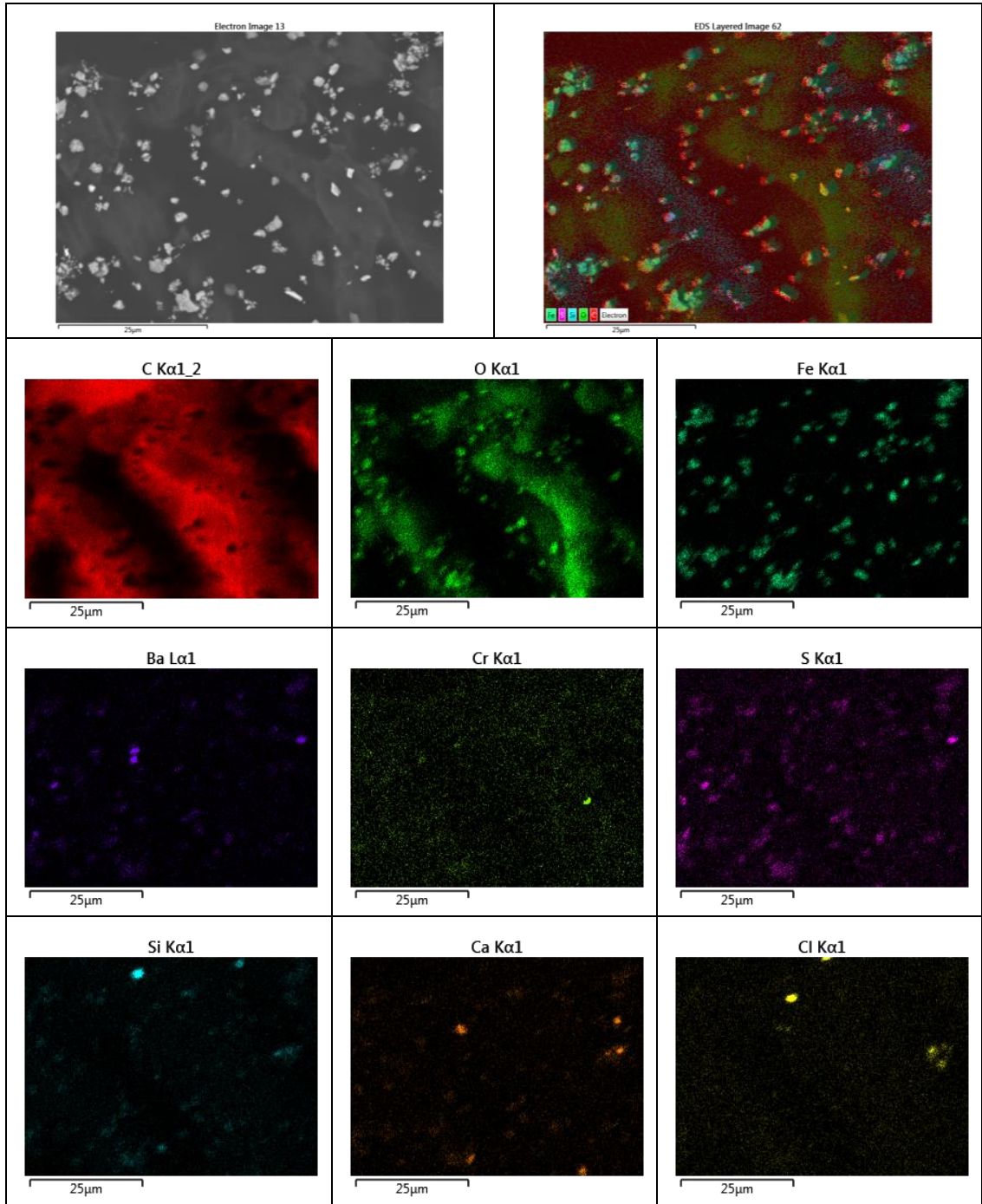


Figure 5.21: EDX map images for the test P15E.

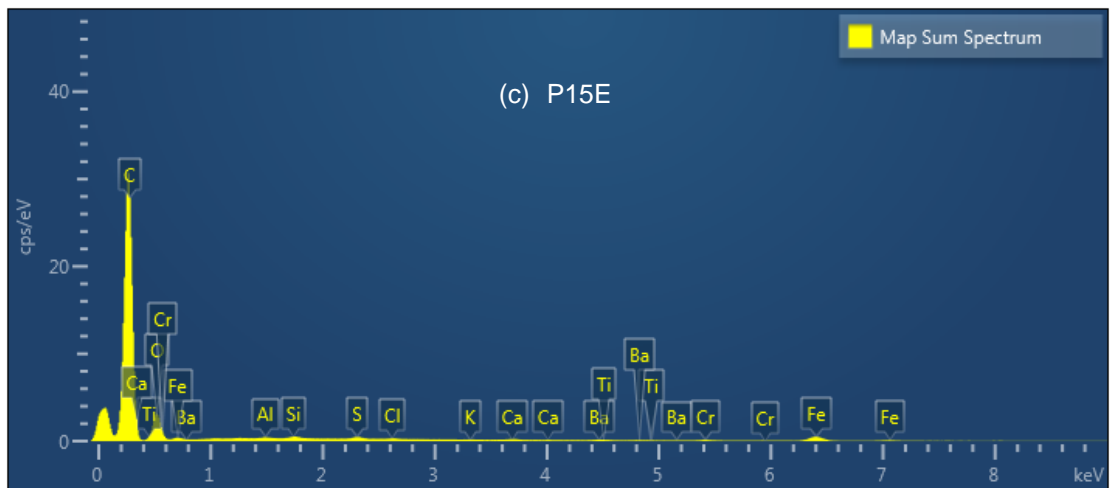
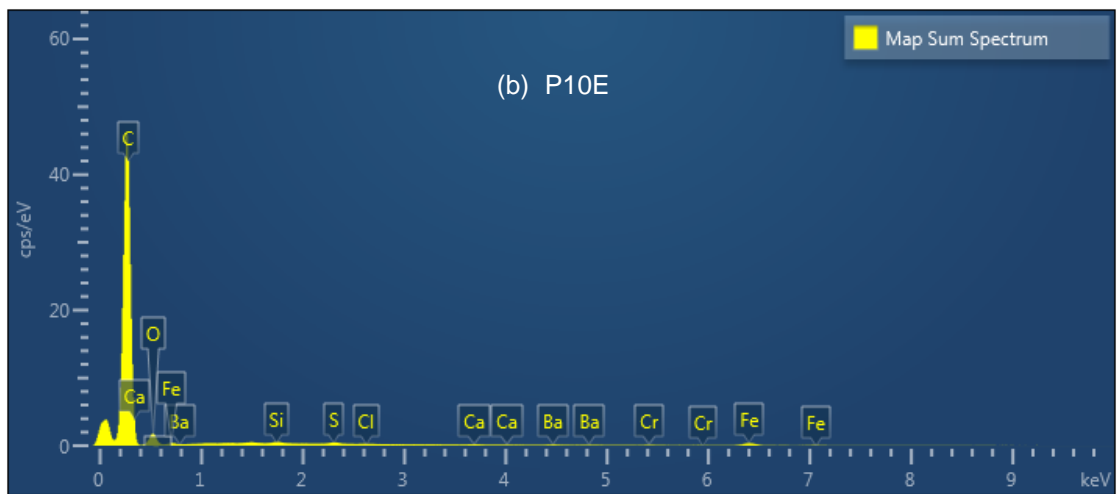
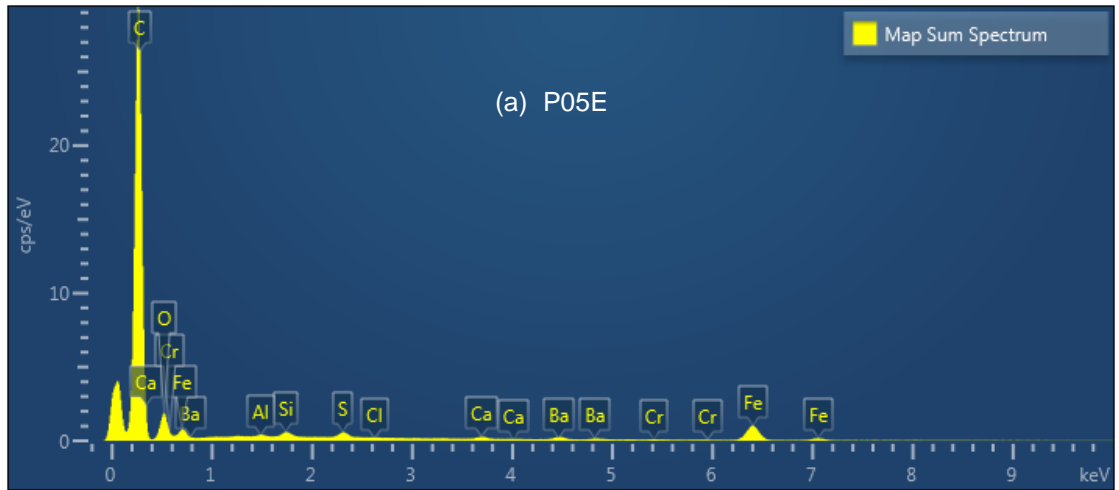


Figure 5.22: EDX spectrum for the corresponding test.

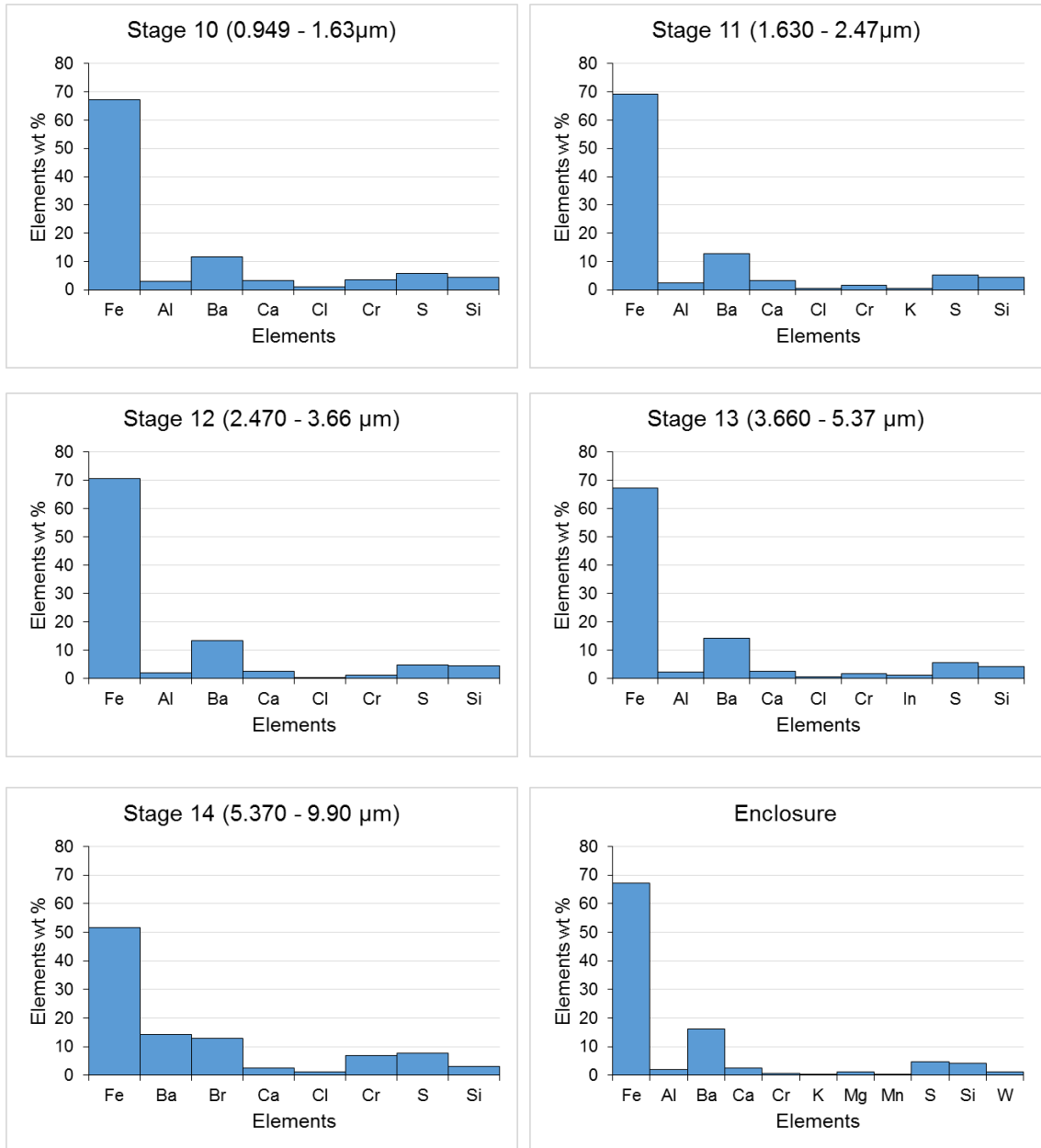


Figure 5.23: Weight percentage of elements for the test P05E.

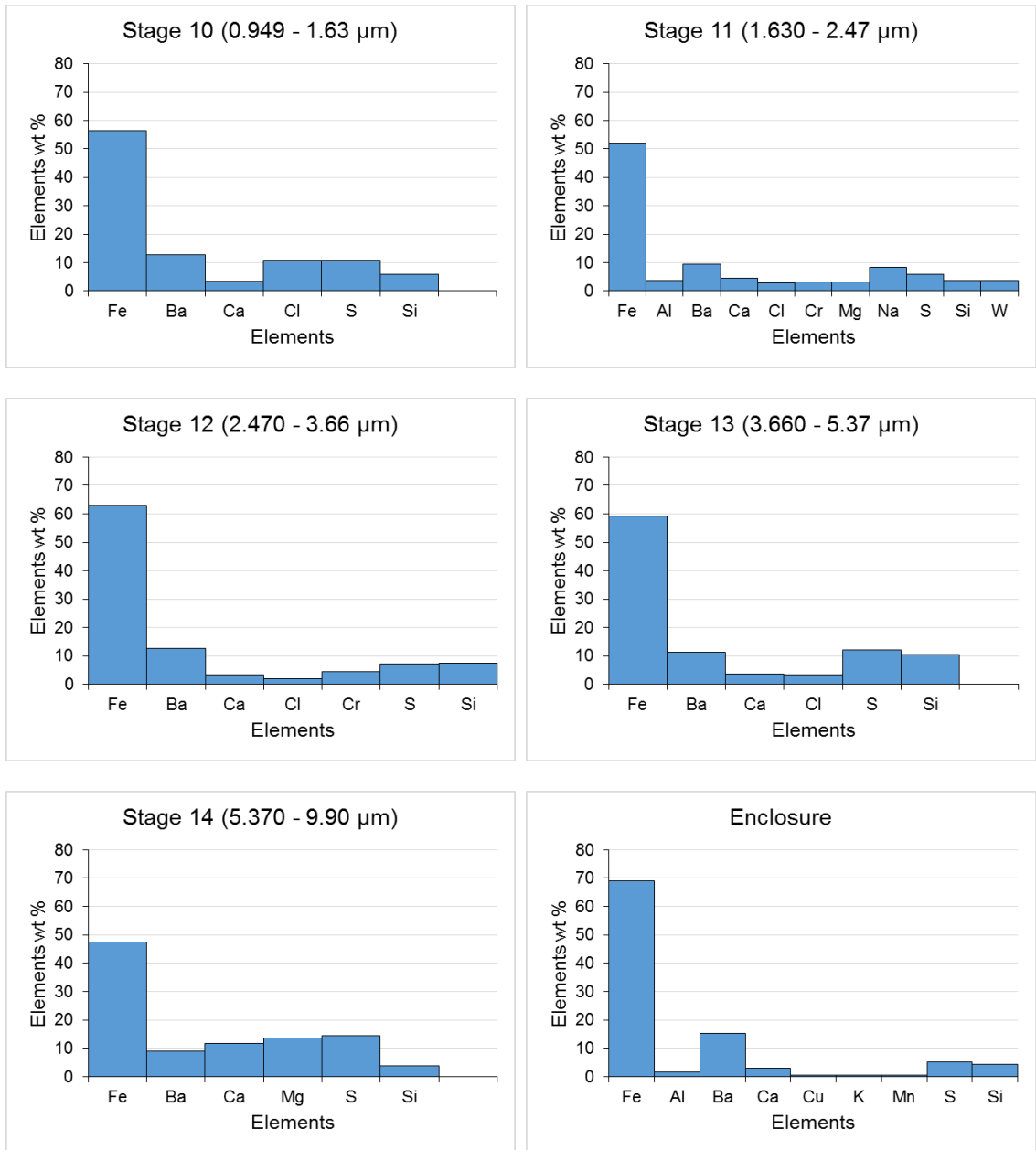


Figure 5.24: Weight percentage of elements for the test P10E.

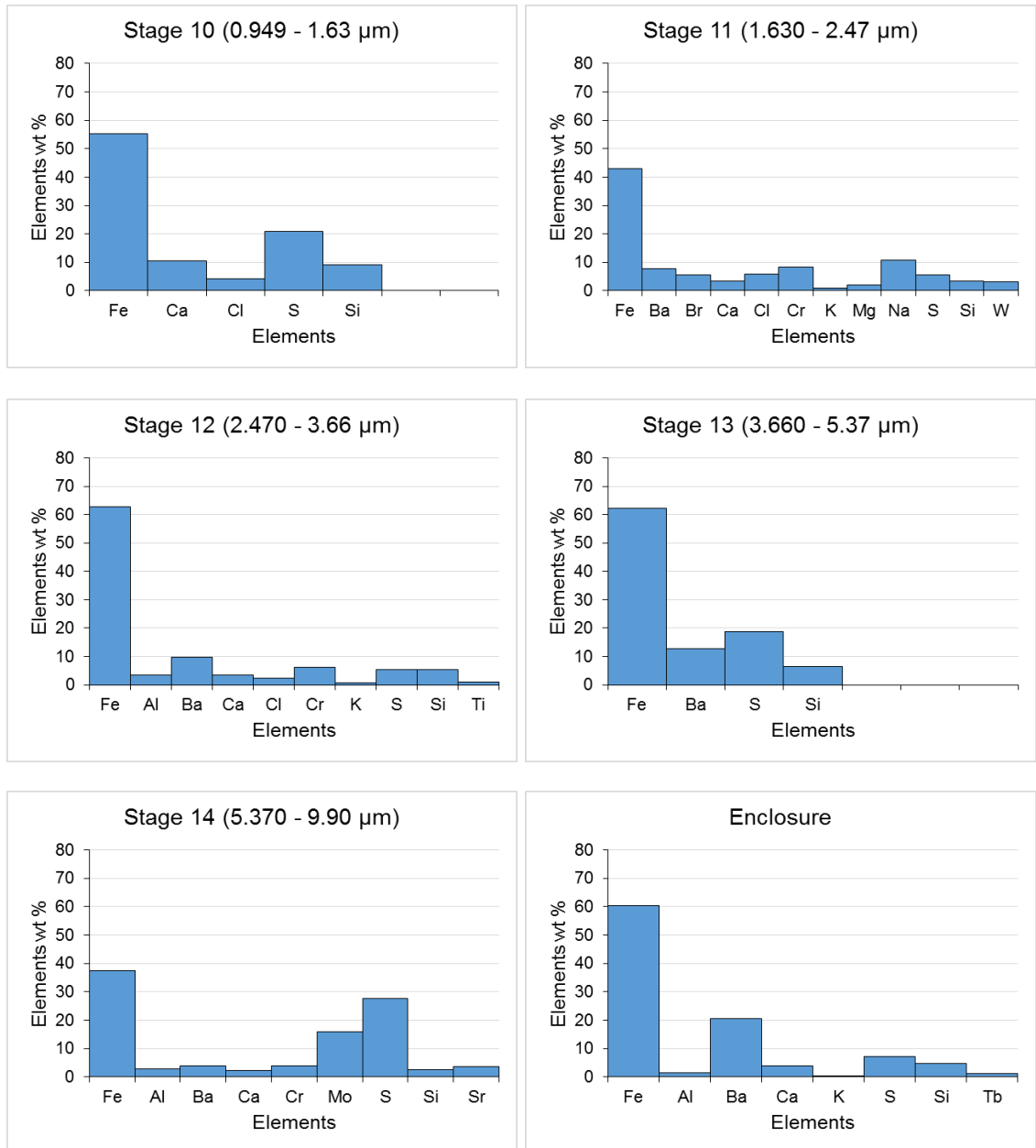


Figure 5.25: Weight percentage of elements for the test P15E.

5.6.3 Elemental weight percentage comparisons

Figure 5.26 exhibits a comparison of elemental percentages by weight for the three braking conditions, excluding the elements of carbon and oxygen. Six main elements (Fe, Ba, Cr, Ca, S and Si) from the results of the previous quantitative analysis were considered in this study. The weight percentages were compared for the samples obtained from the ELPI+ stages of 10 to 14 and also those from the bottom of the enclosure.

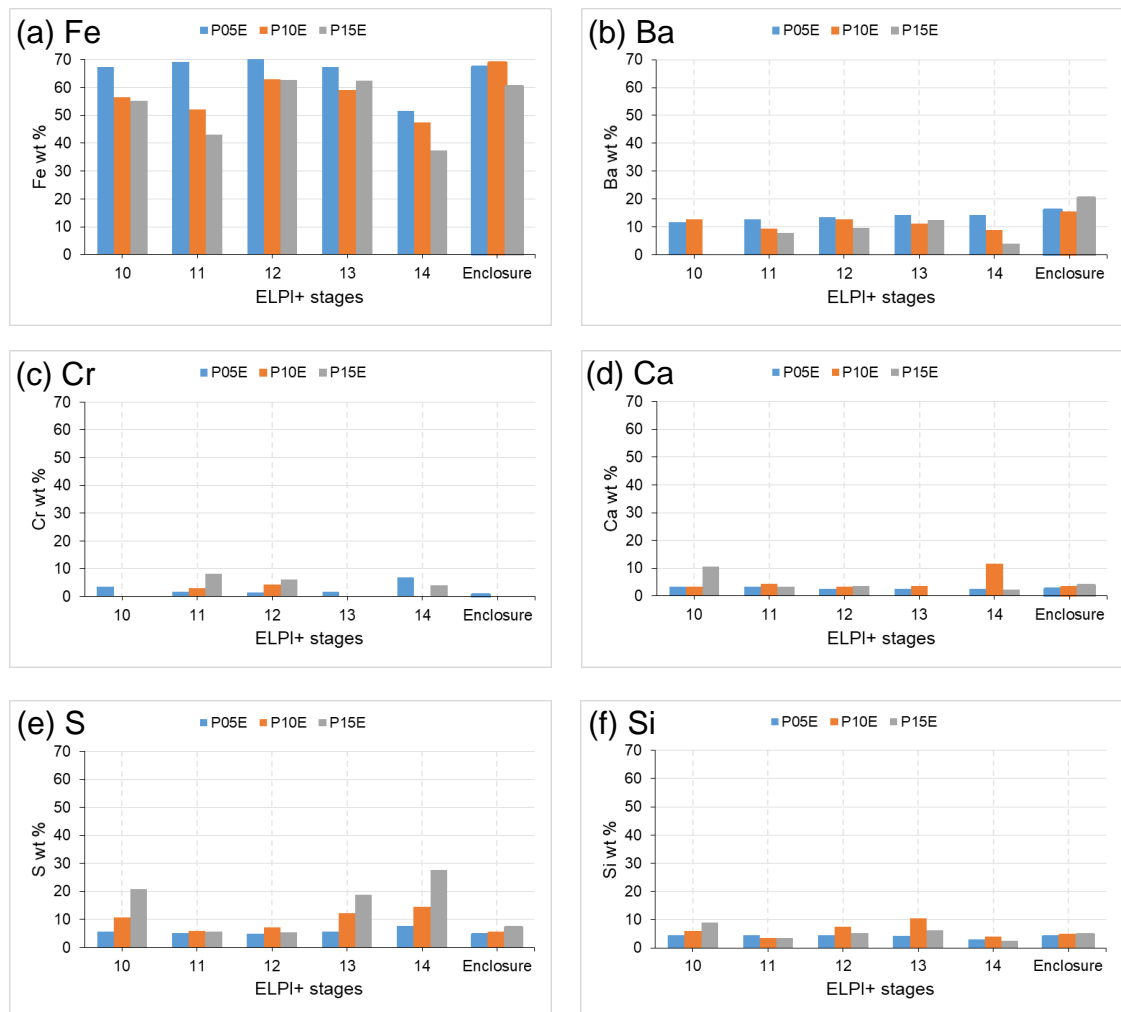


Figure 5.26: Comparison of elemental percentages by weight for the three conditions (a) Fe, (b) Ba, (c) Cr, (d) Ca, (e) S and (f) Si.

Figure 5.26 shows that the percentage of Fe decreases as the brake pressure increases. The Fe is clearly the most predominant element of the collected wear debris, thus proving that the brake rotor becomes worn significantly. A similar

trend can also be seen for Ba. In contrast, the percentage of S increases as the brake pressure and temperature increase. Other elements namely Cr, Ca and Si show less consistency. These elements only contribute small percentages, thus it is not possible to analyse them accurately. However, these elements were produced within all particle ranges with nearly the same proportion.

5.6.4 EDX mapping analysis for the brake pad

In order to correlate the elements found from the wear samples, the brake pad was examined in the same way as the blank foil. Figure 5.27 shows a summary of the quantitative results of EDX analysis on the brake pad. Two different randomly selected locations were investigated in order to ascertain the consistency of the result. The magnification levels employed were 1000x and 100x. EDX mapping analysis was conducted on the whole field of view. It can be noticed that the elemental distribution for the two results is just about the same, showing high percentages of C, O, Fe and Ba while the other elements have low percentages (<1%). A high concentration of Fe was found on the surface of the brake pad. This Fe may originate from the grey cast iron rotor that was transferred during the braking process. Moreover, Cr was not found on the surface of the brake pad. It was presumed that the manufacturer did not employ any materials that contained Cr in the brake pad. However, Cr is frequently used as an alloying element in grey cast iron (Barton, 2011).

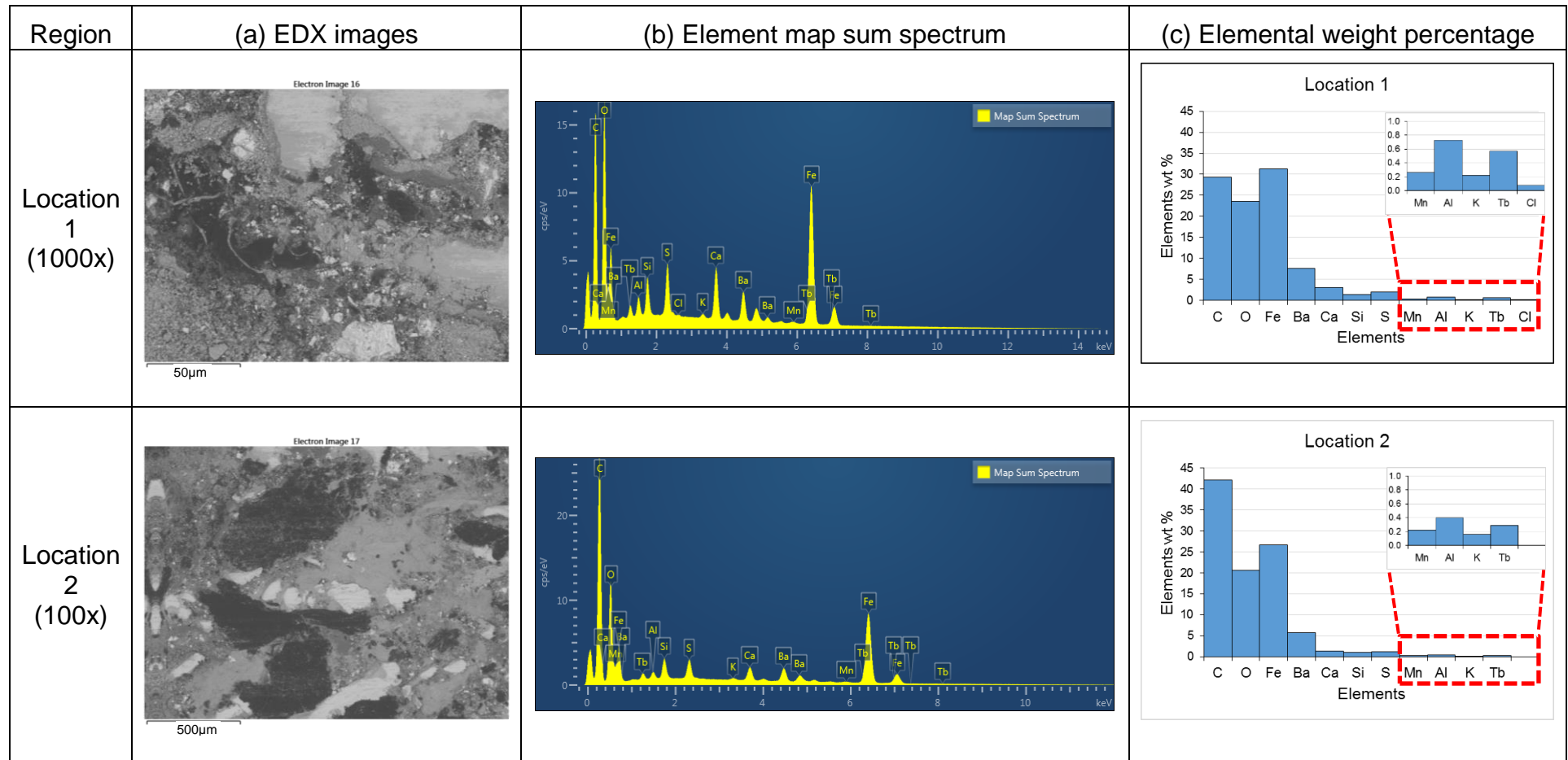


Figure 5.27: EDX images and elemental weight percentages of the brake pad.

5.7 Summary

In this chapter, the evaluation of brake wear particulate matter generated from the grey cast iron rotor and its conforming pads is described. Three brake conditions of different contact pressure and rotor temperature at a constant rotational speed of 135 rpm were selected from the preliminary dynamometer tests. The temperatures recorded during steady-state conditions were approximately 200, 300 and 400°C at the brake pressures of 5, 10 and 15 bar, respectively. The real-time particle measurement, gravimetric analysis and samples for the SEM and EDX analyses were acquired using the Dekati ELPI[®]+ particle analyser. There was a slight increase in the real-time particle number concentration as the brake pressure increased. In terms of particle size distribution, the particle number concentration was found to be higher in the ultrafine particle region (PM_{0.1}) and this concentration increased as the temperature or brake pressure increased. In contrast, the particle mass concentration was found higher in the coarser particle region (PM_{1.0}-PM₁₀) and this concentration reduced as the temperature or brake pressure increased. In all three braking conditions, the PM₁₀ is dominant and accounts for greater than 80% of the total airborne brake wear emissions by mass. Gravimetric analysis was performed to verify the effect of the brake pressure on the particle mass concentration. The results obtained from this analysis showed good agreement with the results acquired from the real-time measurements. The morphological studies revealed that most of the particles observed are irregular in shape at all ELPI[®]+ stages. Airborne brake wear particles are more concentrated at the finer particle size range stages and on the PC foils for the test with lower brake pressure. Besides C and O (which are present anyway in the PC foils), it was found that Fe, Ba, Si, S, Ca and Cr were the main elements contained in the wear particle samples. The Fe, Ba and S constitute around 60%, 15% and 10% of the total elemental percentages, respectively. The Fe is believed to come mainly from the brake rotor while the Ba and S are postulated to originate from the brake pads. Generally speaking, the percentages of Fe and Ba decrease as

the brake pressure increases while the percentage of S increases with brake pressure.

Chapter 6 : Results for PEO-treated lightweight aluminium alloy rotor

6.1 Introduction

This chapter presents the evaluation of brake wear particulate matter generated from the PEO-Al rotor and its conforming pads. Initial brake dynamometer tests were performed in order to gain insight into the rotor temperatures generated when two different brake pressures were applied to the brake system. For each brake condition, the test was conducted three times to check for consistency of results. Real-time particle measurements were conducted concurrently using the Dekati ELPI®+ to investigate the particle number and mass distributions of airborne brake wear particles. The Scanning Electron Microscope (SEM) together with the Energy-Dispersive X-ray spectroscopy (EDX) system were used to study the morphology and elemental composition of the captured wear particles. Finally, quantitative and qualitative comparisons were made based on particle size range and composition for the two brake conditions.

6.2 Brake dynamometer tests

6.2.1 Preliminary tests

For the PEO-Al rotor tests, the same brake conditions were used to allow valid comparisons with those of the GCI rotor. These brake conditions applied hydraulic pressures of 5 and 10 bar to the caliper for a constant rotational speed of 135 rpm. The test under the 15 bar pressure condition used for the GCI rotor could not be conducted for the PEO-Al rotor due to the COVID-19 lock-down restrictions. An initial test was performed in order to get an idea of the PEO-Al rotor temperatures generated during these two drag braking events. Similar to the GCI rotor, the temperature was expected to achieve a steady-state condition

within a few minutes after a test commenced. The fan power of the extraction system and the test duration were identical to those used for the GCI rotor.

Figure 6.1 shows the temperature generated at the rubbing surface of the rotor during steady-state conditions as measured by the rubbing thermocouple. The 'P' and 'F' annotations in the figure legend indicate hydraulic pressure and first test, respectively. It can be seen that the rotor surface attained steady-state temperatures of about 120°C and 210°C for the tests at 5 bar and 10 bar, respectively.

The PEO-Al rotor has a mean rubbing radius of 105 mm and a pad area of 2960 mm². The piston that squeezes the brake pads against the rotor has a diameter of 28.4 mm. By assuming the brake pad was compressed uniformly over its entire surface area by the actuation load, the hydraulic pressures and rotation speed were converted to mean contact pressure and average sliding speed, respectively, as shown in Table 6.1.

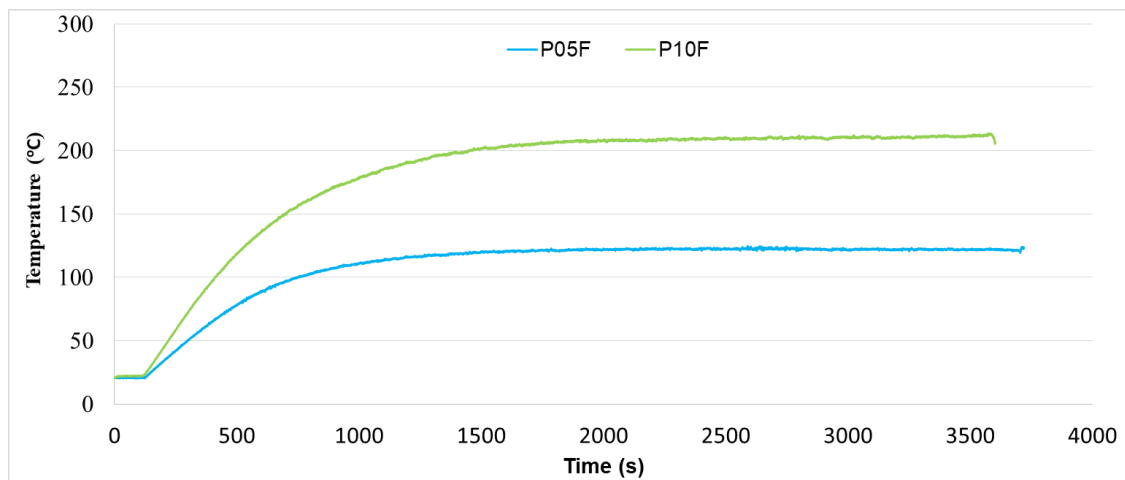


Figure 6.1: Rotor temperature variation with time for the two brake conditions.

Table 6.1: Two brake conditions for subsequent tests.

Condition no.	Hydraulic brake pressure (bar)	Rotation speed (rpm)	Mean contact pressure (MPa)	Average sliding speed (m/s)
1	5	135	0.214	1.48
2	10	135	0.428	1.48

6.2.2 Repeatability tests

Tests were repeated three times at each of the two conditions defined in Table 6.1 in order to check for consistency of results. All tests were carried out using the same dynamometer setup (refer to Chapter 3) and sampling procedure as for the GCI rotor. The temperature-time history plots for all 6 tests are shown in Figure 6.2. The following annotations are used in the figure legend: 'P' is followed by the hydraulic pressure in bar and the repetitions 1, 2, and 3 are represented by the letters 'G,' 'H' and 'I'. The results show that all rotor temperatures attain a steady-state condition after about 3000 seconds from commencement of the braking event.

The test results at 5 bar and 10 bar demonstrate nearly constant steady-state temperatures of 90°C and 150°C, respectively. However, peak temperatures achieved in the first 3000 seconds are significantly higher and more similar to the temperatures measured in the initial tests shown in Figure 6.1. This may be due to the bedding-in process (which transfers pad material to the rotor surface to form a stable transfer layer) not being fully completed in the preliminary tests. Generally, the results in Figure 6.2 suggest that the two brake conditions have achieved good consistency once the transfer layer has been fully established.

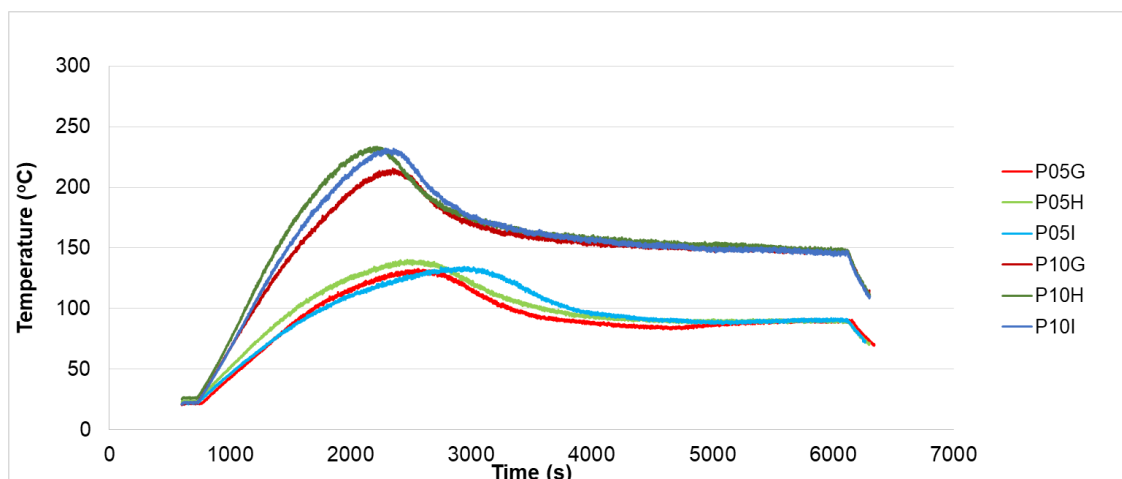


Figure 6.2: Rotor temperature variation with time for the two brake conditions.

6.3 Brake wear emission measurement

As described in Chapter 3, measurements of particle concentration during each braking event were conducted for 90 minutes. Before each brake test, the background level of airborne PM within the system was measured for 10 minutes without the brake running to ensure a consistent and acceptable level of cleanliness. The measurements were then performed at 5 and 10 bar of hydraulic pressure and a constant speed of 135 rpm in order to study the relationship between the rotor temperature and the particle number and mass concentration.

6.3.1 Real-time particle measurement

Figure 6.3 shows temporal changes in real-time particle number concentration for two particular tests at 5 and 10 bar (tests P05H and P10H), respectively. The background number concentration is high for the first 10 minutes of the test P05H when the brake is stationary. This may occur because of the lack of efficacy in completely removing from the system airborne particles produced from the preceding test. Furthermore, the HEPA filter's inefficacy to prevent very fine particles (less than 0.3 μm diameter) from entering the system may also be a factor. It could also be feasible that the local atmospheric conditions or other activities in the laboratory caused more very fine particles to be drawn into the system over this initial time period. Subsequently, the particle number concentration for the P05H test decreases continuously until after about 4000 seconds when it attains an almost constant value until the end of the test. On the other hand, the P10H test starts with a low system background level at the beginning of the test but this increases gradually after about 600 seconds of the test duration. Since the background level is so different in these two tests, the effect of the hydraulic pressure on the particle number concentration cannot easily be inferred from these results. As already stated in Chapter 5, the current system is not able to eliminate the large numbers of very fine particles in the background laboratory air from entering the system and dominating the much smaller numbers of rather larger particles generated by the brake.

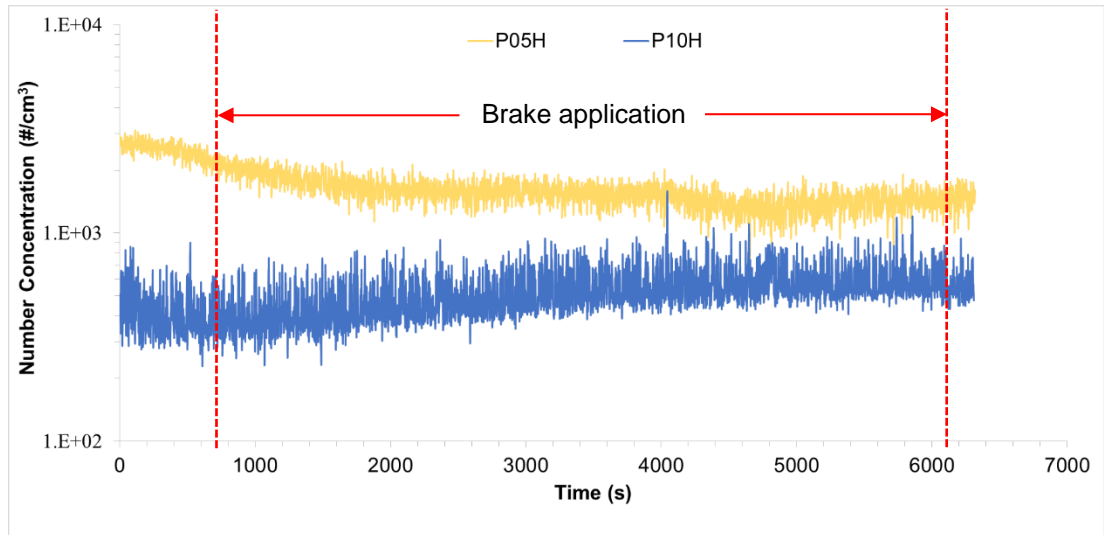


Figure 6.3: Particle number concentration variation with time for two different pressures.

Figure 6.4 shows the results of the real-time particle measurement for the three repeated tests of P10, temperature profiles for which are shown in Figure 6.2. The results were plotted together to check for consistency. From this figure, it can be seen that only the P10H test shows an increasing number concentration with time, while the other two tests demonstrate a marginally decreasing trend over the entire test duration. All tests show a similar level of particle number concentration at the end of the test but have a different background air level at the start of the brake application. This again shows the dominance of the large numbers of ultrafine particles in the background air which depends partly on local laboratory conditions and is probably the main reason why the particle number results appear somewhat inconsistent during the actual brake application.

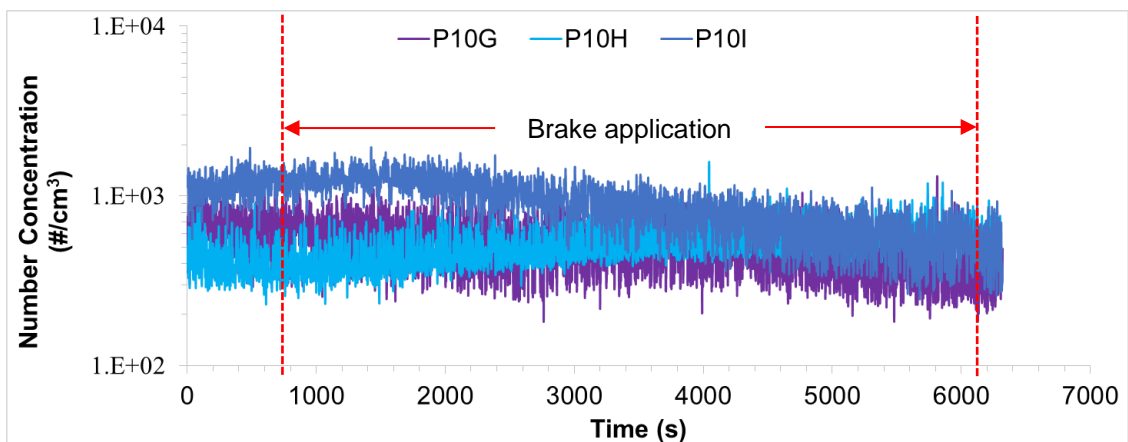


Figure 6.4: Particle number concentration variation with time for the three tests at 10 bar pressure.

6.3.2 Particle number distribution

For further analysis, the Dekati measurements averaged over time are now exhibited as a function of aerodynamic particle size. Since the HEPA filter is ineffective in preventing very fine particles from entering the ducting system, the number distribution is only presented within 7 particle size ranges starting from 0.383 μm up to 10 μm (i.e. particles with diameters of less than 0.383 μm were omitted from this discussion). Measurement data were averaged over a time period from 3600 to 6120 seconds of the duration of each test to compare the effect of the steady-state temperature achieved in this time period on the particle number distribution. Data was also averaged over the initial 600 seconds of each test to obtain the corresponding background air data.

Figures 6.5 (a & c) and (b & d) shows the particle number concentration for background and brake application measurements for pressures of 5 and 10 bar, respectively. A large number of particles were concentrated in the ultrafine particle fraction ($\text{PM}_{0.1}$) for both brake conditions; however, they are omitted from these histograms due to the dominance of such tiny particles in the background air. The particle number concentrations recorded for the background air were very small between $\text{PM}_{2.5}$ and PM_{10} . However, for the P05H test, a significant spike is seen in the 0.383-1.0 μm size range. This corresponds with the overall large total number of particles in the background air indicated in Figure 6.3 which is assumed to be due to local laboratory conditions on the day of this test.

The brake application measurements in the larger particle size ranges shown in Figure 6.5 indicate much higher particle concentrations compared to the background measurements; this confirms that significant numbers of airborne particles generated from the PEO-Al disc brake friction pair were captured during the braking event. The P05H test results demonstrate a decreasing trend from fine to coarse particles while the P10H results show a bell-shaped curve with peak numbers concentrated within the particle size range of 1.0 to 2.5 μm . Overall, the results show that the particle number concentration of coarser particle fractions is marginally greater at the high brake pressure of 10 bar compared to the 5 bar low pressure. Based on this pattern, it was anticipated that the mass distribution would be higher for the test with higher brake pressure.

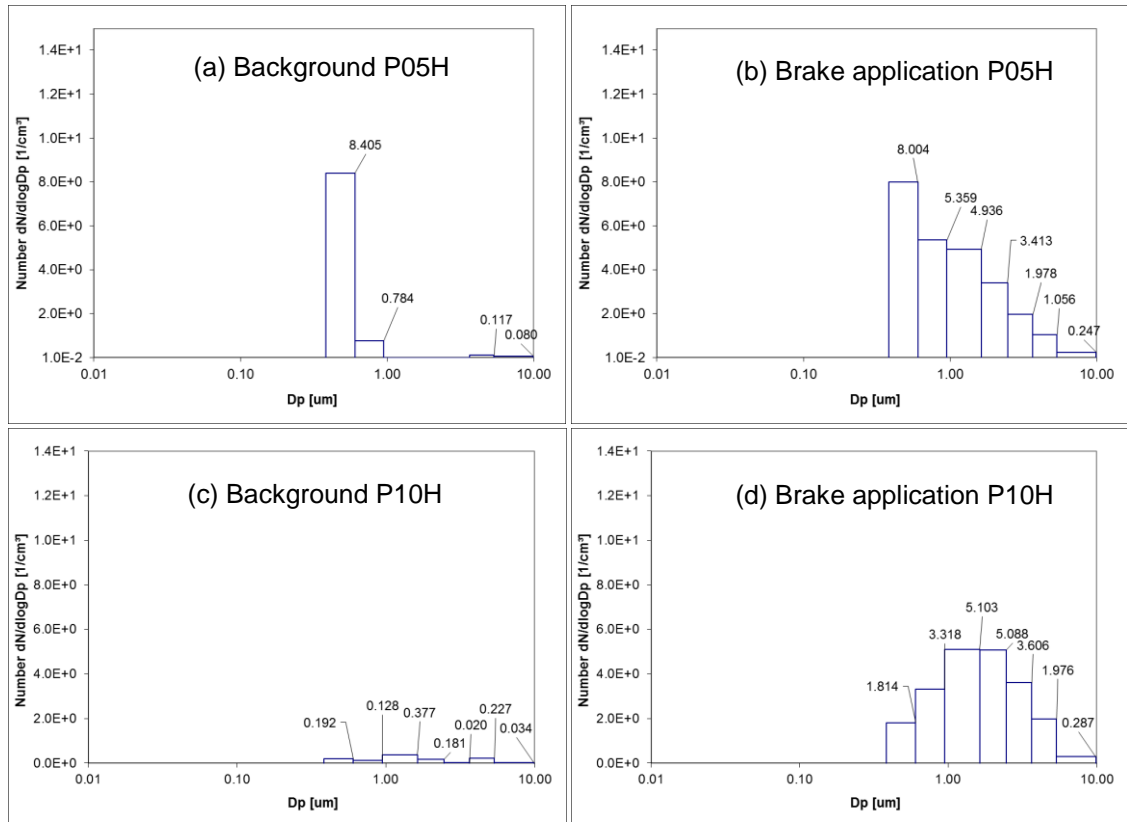


Figure 6.5: Particle number distribution measurements for (a & c) background and (b & d) brake application at 5 & 10 bar hydraulic pressure, respectively.

Figure 6.6 shows the particle number concentration of brake application measurements for the three repeated tests at 5 and 10 bar pressure. The trend of decreasing concentration from fine to coarse particles can be seen for all the tests at 5 bar pressure. In the case of the tests at 10 bar pressure, all results exhibit an approximately normal distribution with a mean value within the particle size range of 1.0 to 2.5 μm . Generally, these results show very good consistency for the applied pressures of 5 and 10 bar where the rotor surface temperatures are approximately 90°C and 150°C, respectively.

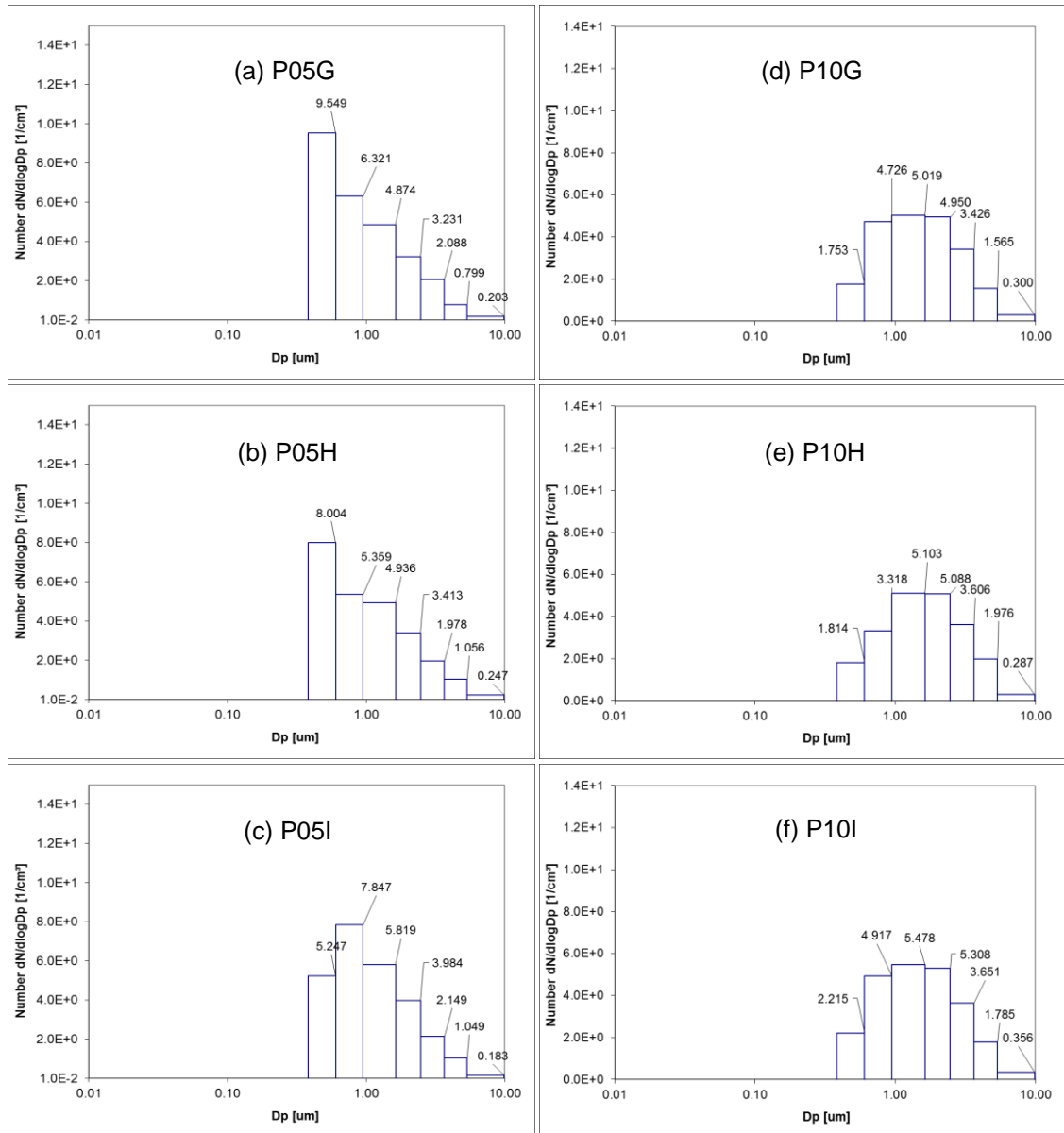


Figure 6.6: Particle number distribution measurements for the brake application at (a-c) 5 bar and (d-f) 10 bar hydraulic pressure.

6.3.3 Particle mass distribution

From the same measurement data, the particle mass concentration can also be exhibited as a function of aerodynamic particle size. The mass concentration distributions of the brake wear particles measured at the two pressures along with their corresponding background levels are shown in Figure 6.7. Again a significant difference between background and brake application measurements can be seen from this figure, particularly for the coarser particle fractions. Thus

the particle mass concentration for both brake conditions is higher at the larger particle size interval. The mass fraction of coarser particles somewhat increases as the brake pressure increases. From these results, it is estimated that greater than 90% of the total brake particulate mass is emitted as particles in the 1 to 10 μm ($\text{PM}_{1.0}$ - PM_{10}) size range for both brake conditions studied. This suggests that coarse particles within this range may primarily contribute to the road vehicles' brake wear debris pollution.

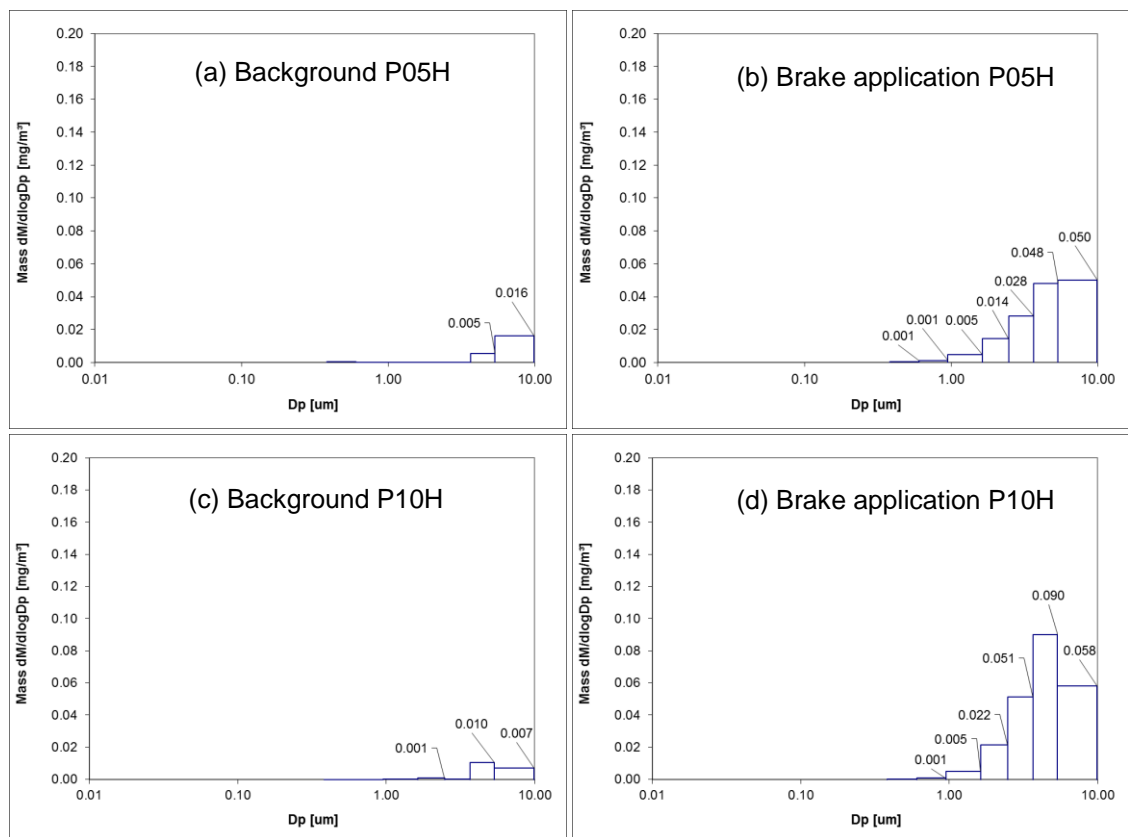


Figure 6.7: Particle mass distribution measurements for (a & c) background and (b & d) brake application at 5 & 10 bar hydraulic pressure, respectively.

In terms of test consistency, the three repeated tests at 5 and 10 bar pressure which generated the rotor surface temperatures of approximately 90°C and 150°C , respectively, demonstrate a very similar pattern of particle mass distribution as shown in Figure 6.8. From the figure, all tests generally show higher particle mass concentration at the larger particle size interval.

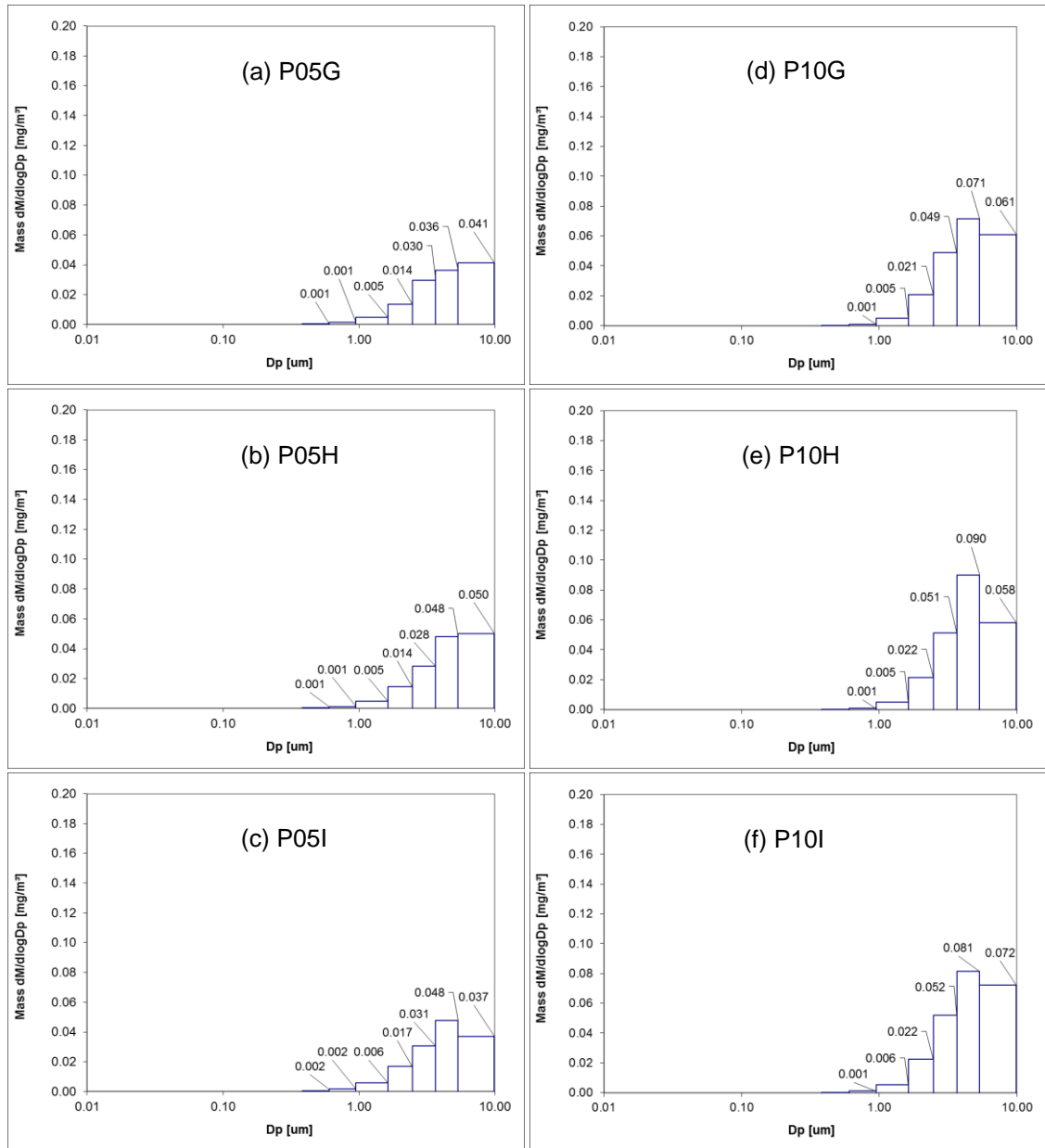


Figure 6.8: Particle mass distribution measurements for the brake application at (a-c) 5 bar and (d-f) 10 bar hydraulic pressure.

6.3.4 Airborne particulate matter classification

In this study, brake wear emissions from the previous repeatability test were evaluated according to $PM_{0.1}$, $PM_{2.5}$ and PM_{10} as for the GCI rotor (refer to Chapter 5). The averages of particle number and particle mass concentrations classified into the three PM categories are shown in Figure 6.9. As can be seen in Figure 6.9 (a), $PM_{0.1}$ contributes more than 90% of the total average particle number concentrations for both brake conditions while the other two categories

show considerably lower particle number concentration, particularly PM₁₀. The particle number concentration decreases as the brake pressure increases. In the case of particle mass concentration, Figure 6.9 (b) shows that PM₁₀ although low in concentration number dominates the total mass of airborne brake wear emissions for both brake conditions while PM_{0.1} contributes only a tiny amount of mass to the total. Generally, the particle mass concentrations in the PM_{2.5} and PM₁₀ size ranges are higher at the higher brake pressure and temperature. The PM₁₀ contributes to approximately 85% of the total airborne brake wear emissions for both braking conditions.

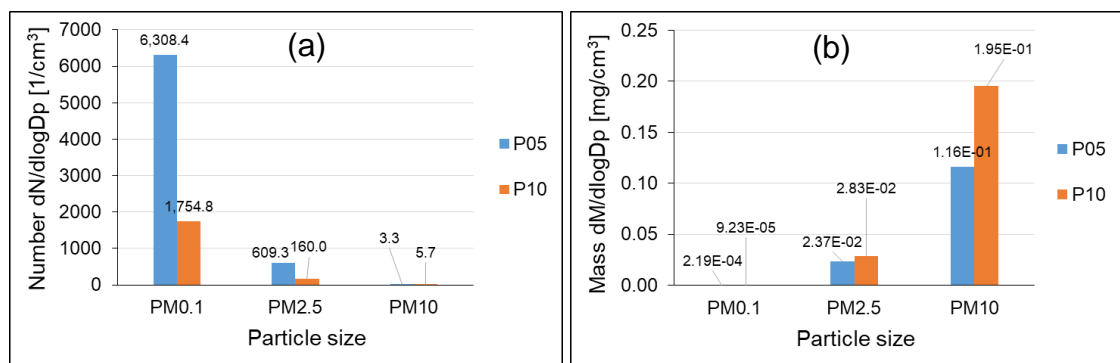


Figure 6.9: Brake wear emissions of PM_{0.1}, PM_{2.5} and PM₁₀ based on average (a) particle number and (b) particle mass concentrations.

6.4 Microstructural analysis

The same sampling procedure as for the grey cast iron rotor was followed to collect particles in the size ranges of 1 μm – 10 μm (Dekati stages 10-14) on the polycarbonate (PC) foils. Brake wear particles that fell down on the bottom of the enclosure were also collected on a PC foil as shown in Figure 6.10.

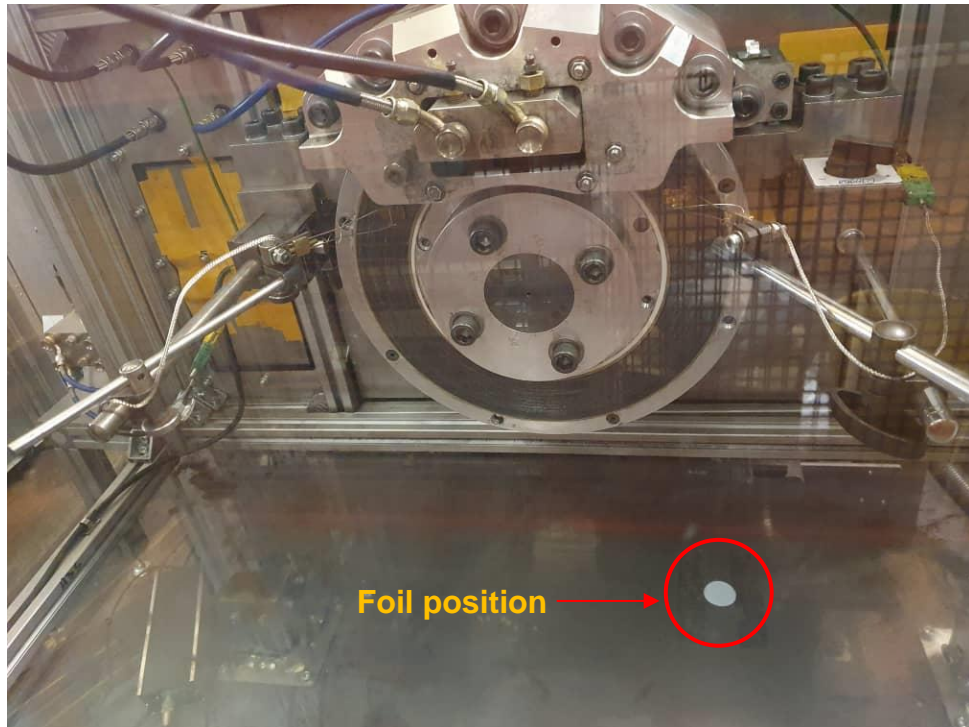


Figure 6.10: PC foil position on the bottom of the enclosure.

As mentioned in Chapter 3, the rotor rubbing surface temperature was measured in parallel with the particle collections. The rotor temperature recorded as a function of time is shown in Figure 6.11. It is clear that steady-state conditions occur in both tests after about 3000 seconds. The constant temperatures attained were also consistent with the previously generated disc temperatures of 90 and 150°C for pressures of 5 and 10 bar, respectively. This result verifies that the tests can be replicated confidently to yield consistent results similar to those shown in Figure 6.2.

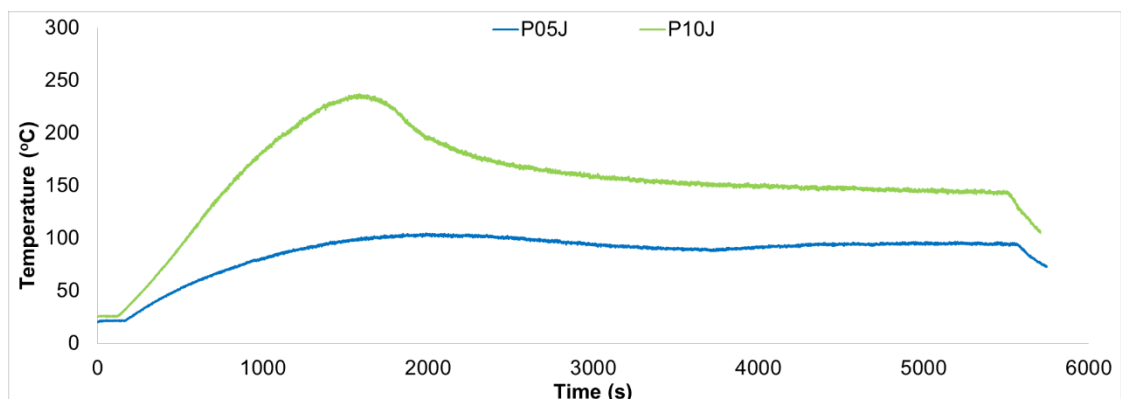


Figure 6.11: Rotor temperature variation with time for the two brake conditions during particle collections.

The brake wear debris accumulated on the foils were observed with the SEM at magnification levels of 1200x and 6000x. Particulate distributions can be easily observed and examined at a magnification of 1200x, whereas individual particles can be readily studied at a magnification of 6000x. A location within a typical dark spot was randomly selected on each PC foil (from each impactor stage) and the micrographs were captured at this location as for cast iron (see Figure 5.12). All micrographs taken from different ELPI® + stages are shown in Figures 6.12 and 6.13 for brake pressures of 5 and 10 bar, respectively. Two locations were also randomly selected on the PC foils positioned at the bottom of the enclosure. The micrographs taken at 3000x magnifications from these foils are shown in Figure 6.14 for both brake conditions.

Generally speaking, the micrographs reveal that large quantities of brake wear debris are accumulated at the finer particle size range stages. The number of observable particles for both tests reduces from fine to coarse particles. There is little noticeable change in the shape of particles at different stages and many particles are irregular in shape. Due to the inadequacy of the SEM resolution, no apparent particle clusters (agglomerations) were observed in the brake wear particles. However, small-scale agglomerations appear to be present in the finer particle stages, particularly in stage 10 (see Figures 6.12 (a) and 6.13 (a)). Overall, most of the particles are graded and properly registered based on their aerodynamic sizes in the respective stages. Nevertheless, some particles were not correctly captured either in the finer or coarser particle stages. This occurrence was similar for the GCI rotor as has been explained in Chapter 5. From the micrographs, it can also be seen that particles are more concentrated in the test with the higher brake pressure. This correlation is consistent with the real-time particle measurements reported in the previous section.

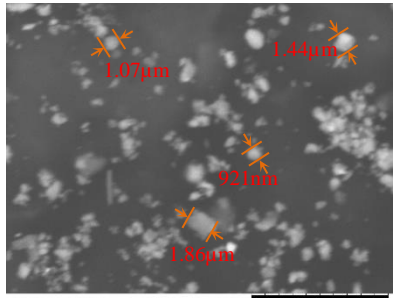
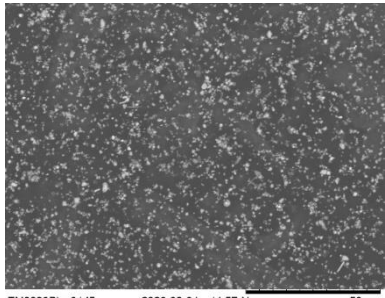
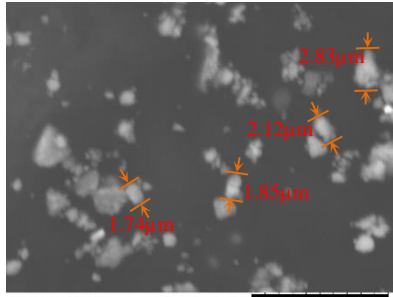
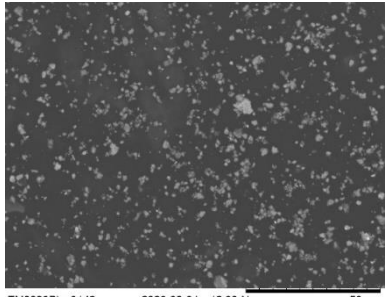
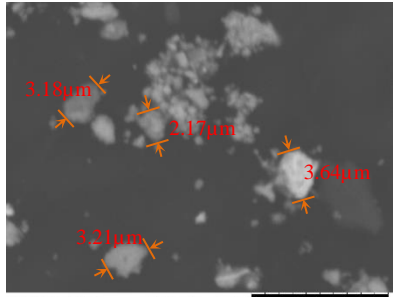
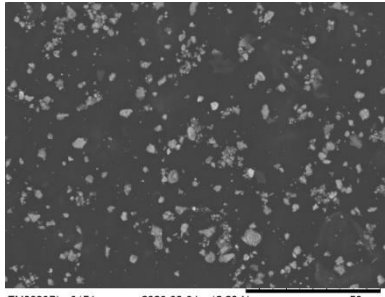
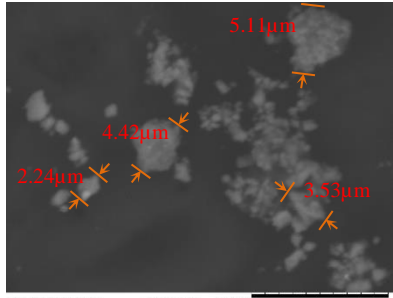
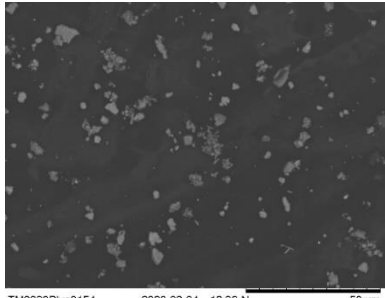
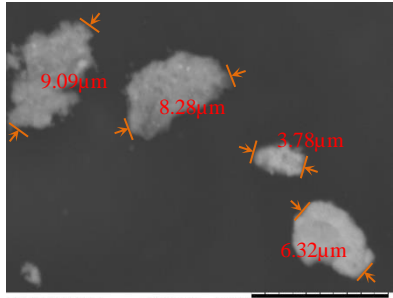
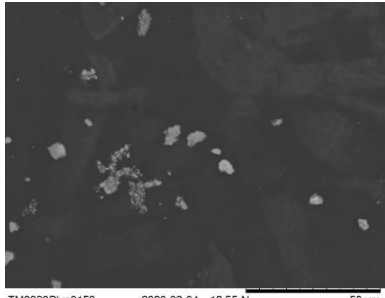
Stage & Size (μm)	Particle images	
	6000x	1200x
(a) Stage 10 (0.949 – 1.63)	 <p>TM3030Plus0146 2020-03-04 11:59 N 10 μm</p>	 <p>TM3030Plus0145 2020-03-04 11:57 N 50 μm</p>
(b) Stage 11 (1.630 – 2.47)	 <p>TM3030Plus0149 2020-03-04 12:12 N 10 μm</p>	 <p>TM3030Plus0148 2020-03-04 12:09 N 50 μm</p>
(c) Stage 12 (2.470 – 3.66)	 <p>TM3030Plus0152 2020-03-04 12:28 N 10 μm</p>	 <p>TM3030Plus0151 2020-03-04 12:23 N 50 μm</p>
(d) Stage 13 (3.660 – 5.37)	 <p>TM3030Plus0155 2020-03-04 12:39 N 10 μm</p>	 <p>TM3030Plus0154 2020-03-04 12:36 N 50 μm</p>
(e) Stage 14 (5.370 – 9.90)	 <p>TM3030Plus0157 2020-03-04 12:52 N 10 μm</p>	 <p>TM3030Plus0159 2020-03-04 12:55 N 50 μm</p>

Figure 6.12: Micrographs for the test P05J.

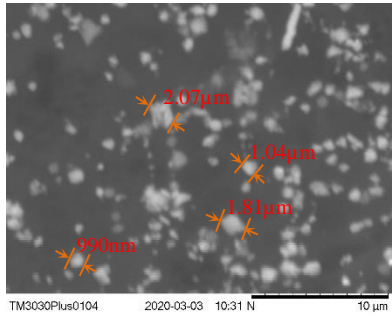
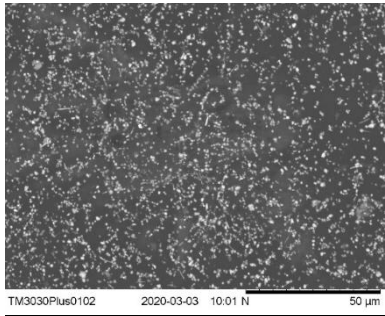
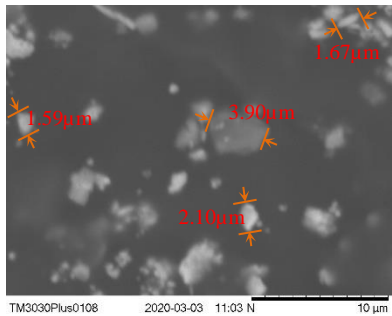
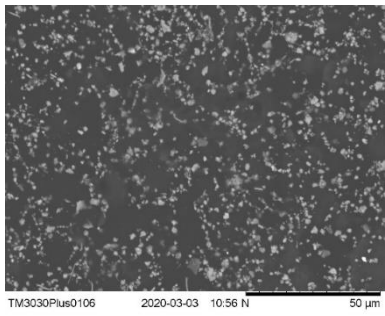
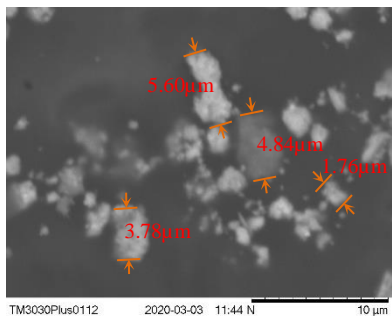
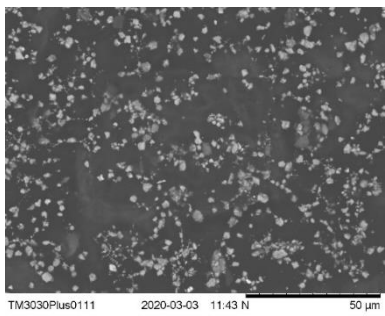
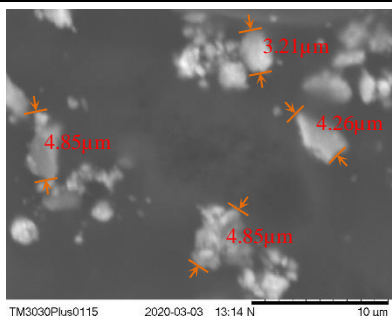
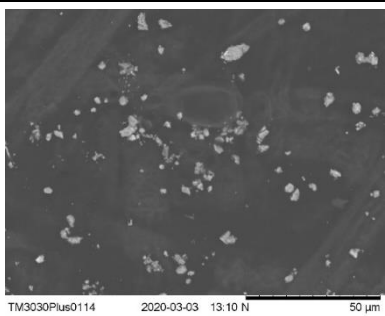
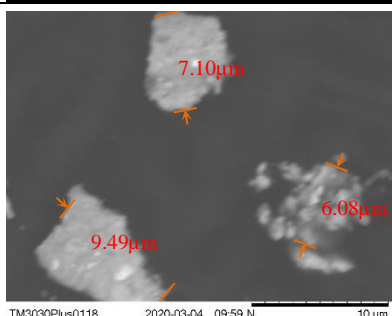
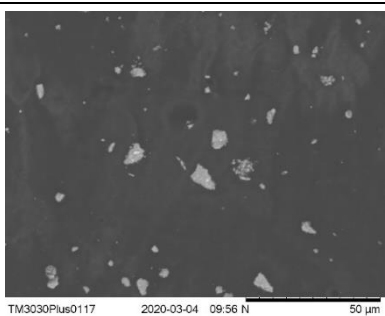
Stage & Size (μm)	Particle images	
	6000x	1200x
(a) Stage 10 (0.949 – 1.63)	 <p>TM3030Plus0104 2020-03-03 10:31 N 10 μm</p>	 <p>TM3030Plus0102 2020-03-03 10:01 N 50 μm</p>
(b) Stage 11 (1.630 – 2.47)	 <p>TM3030Plus0108 2020-03-03 11:03 N 10 μm</p>	 <p>TM3030Plus0106 2020-03-03 10:56 N 50 μm</p>
(c) Stage 12 (2.470 – 3.66)	 <p>TM3030Plus0112 2020-03-03 11:44 N 10 μm</p>	 <p>TM3030Plus0111 2020-03-03 11:43 N 50 μm</p>
(d) Stage 13 (3.660 – 5.37)	 <p>TM3030Plus0115 2020-03-03 13:14 N 10 μm</p>	 <p>TM3030Plus0114 2020-03-03 13:10 N 50 μm</p>
(e) Stage 14 (5.370 – 9.90)	 <p>TM3030Plus0118 2020-03-04 09:59 N 10 μm</p>	 <p>TM3030Plus0117 2020-03-04 09:56 N 50 μm</p>

Figure 6.13: Micrographs for the test P10J.

Figure 6.14 shows particles of varying sizes that were collected on the bottom of the enclosure during the braking event. The particle size varies from submicron to 21 μm . Most of the particles observed have sizes of less than 10 μm . This indicates that many particles in this size range have been deposited within the enclosed chamber. The particles for tests P05J and P10J have no apparent differences in their shape or size. Most of the particles have an irregular shape. The presence of particle agglomeration can also be seen in both tests. Such agglomerates consist of particles with sub-micron to small-micron sizes.

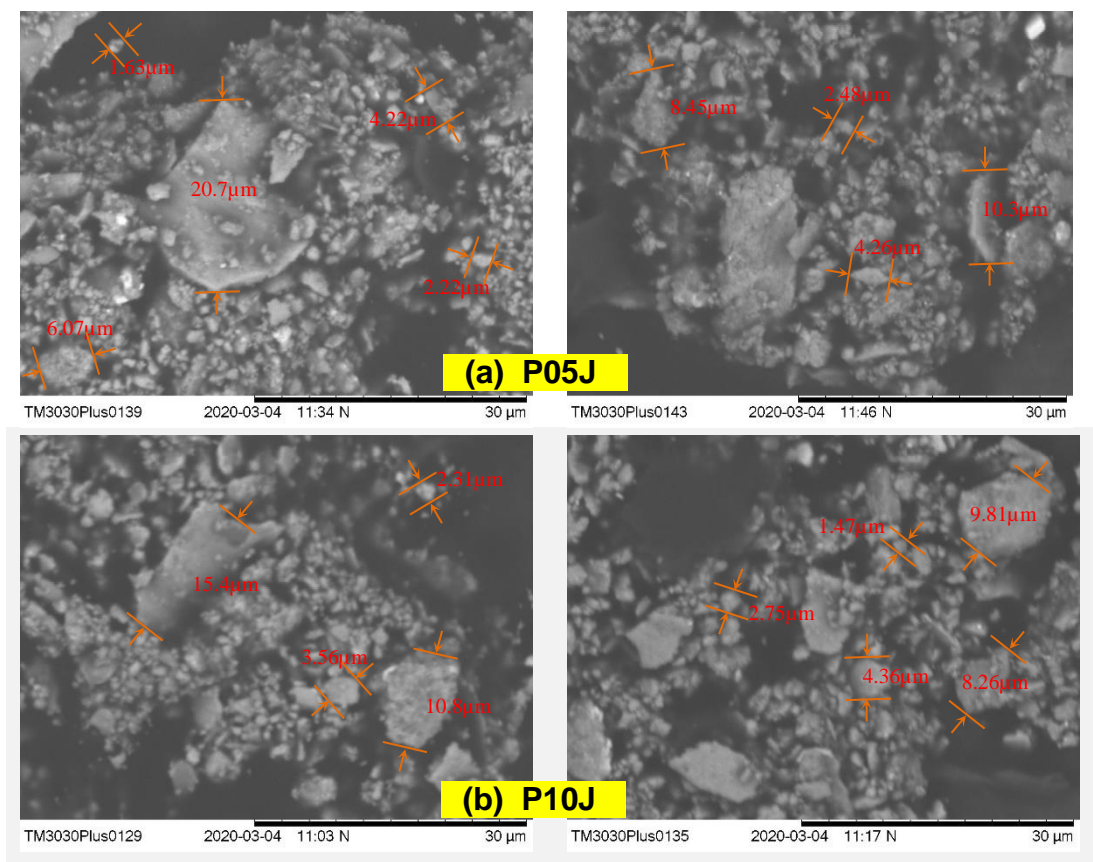


Figure 6.14: Micrographs of the collected particles on the bottom of the enclosure at 3000x magnifications for (a) test P05J and (b) test P10J.

6.5 Elemental composition evaluation

6.5.1 EDX analysis for the collected particles

The chemical composition of the particles collected on the PC foils for the PEO-Al rotor was investigated by EDX analysis. The EDX spectrum was obtained by selecting the whole field of view of the images using a rectangular box. The

relevant elemental compositions were simultaneously acquired from the spectrum generated. The samples used for this analysis were the same as those utilised in the SEM examinations. All samples from the two tests of different pressure were examined at 3000x magnifications. The selection of the desired location is similar to that for the GCI rotor debris (see Figure 5.18). The spectrum (without carbon and oxygen) obtained from samples on stage number 12 (2.47 – 3.66 μm) is exhibited in Figure 6.15 .

Overall, the EDX results of both tests suggest that the samples contain primarily carbon and oxygen elements. Both elements are likely to come from the PC foil. This assumption was verified by referring to the results obtained in Section 5.6.1. The findings revealed that there were high elemental weight percentages of both C and O in the samples. Apart from originating from the foil itself, the carbon found was probably from the lubricants (graphite) in the brake pads, while the oxygen may have come from the alumina surface layer of the PEO-Al rotor itself. The oxygen may also be derived from oxides used either as an abrasive (e.g. Al_2O_3) or as a filler (e.g. CaCO_3) in the pads.

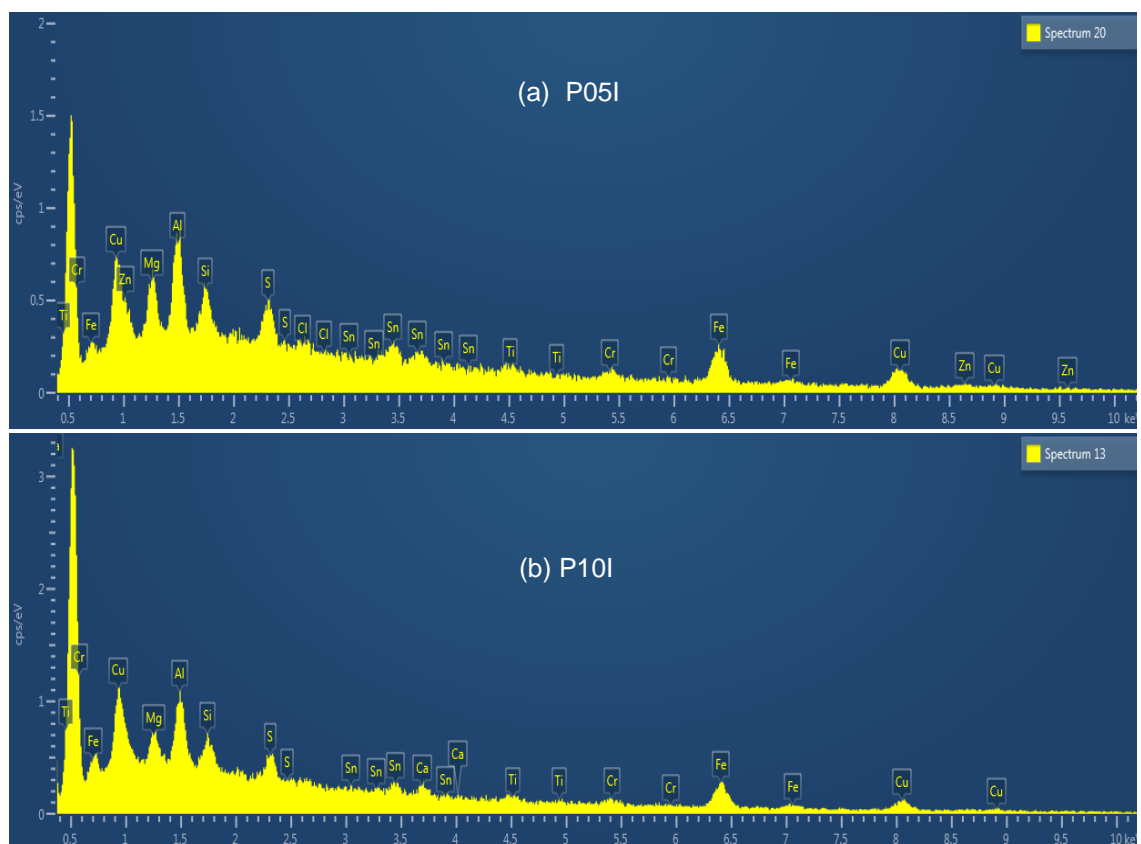


Figure 6.15: EDX spectrum at stage 12 for the two brake conditions.

For the above reasons, the carbon and oxygen were omitted from the subsequent analyses and the elemental weight percentages without these elements are given in Figures 6.16 and 6.17. These figures provide detail on the composition of elements of all fractions (Dekati stages 10-14 and bottom of enclosure) obtained during the two test conditions. There are no major variations in the percentages for the different conditions or from fine to coarser particles. Both test conditions consistently show high percentages of aluminium (Al), copper (Cu) and iron (Fe) in all samples. The samples also contain high percentages of magnesium (Mg), sulphur (S), silicon (Si), tin (Sn) and zinc (Zn). Zn and Si were found to be high in the stages of fine and coarse particle fractions, respectively. It is interesting to note that no barium (Ba) has been discovered in any of the samples. Other elements present are calcium (Ca), chromium (Cr) and titanium (Ti). Elements like chlorine (Cl) and phosphorus (P) appeared at very low concentrations in the debris samples.

Cu usually has the highest weight percentage (excluding C and O) at all size fractions and this most likely comes from the brake pad material. Most brake pad manufacturers have recently reduced and even eliminated copper in their products. The copper has usually been used to help heat dissipation in the pad, but the problem is that it produces dust that can be toxic to aquatic life. However, the pad material used in these tests was a special formulation designed to produce stable friction against the PEO coating and this may have contained more Cu than is now common.

The abundant Fe found may have originated as a steel reinforcing fibre in the brake pad. It is likely that during the braking event, this Fe will be oxidised. As a result, iron oxide phases such as FeO, Fe₂O₃ and Fe₃O₄ may be formed when chemical reactions occur at the friction interface. The presence of Al may be derived from the coating layer of the PEO-Al rotor itself or the aluminium oxide, Al₂O₃ compound which is used as an abrasive or reinforcing fibre in brake pads. The relatively low weight fractions of Al suggest that very little wear of the PEO rotor surface is occurring.

The Mg and Si found may be utilised as a filler and binder, respectively in the brake pad. The Zn used in the brake pad is perhaps for heat conduction purposes

during a braking event. The presence of S might be derived from metal sulphides such as tin sulphate (SnSO_4) or copper sulphate (CuSO_4) which are employed as lubricants in brake pads to modify friction coefficients and wear rates. The observed Cr and Ca may originate from compounds such as chromium oxide (Cr_2O_3) or calcium carbonate (CaCO_3), respectively, in the brake pad material. Other elements identified that contribute only a tiny percentage to the total may or may not originate from the brake materials themselves.

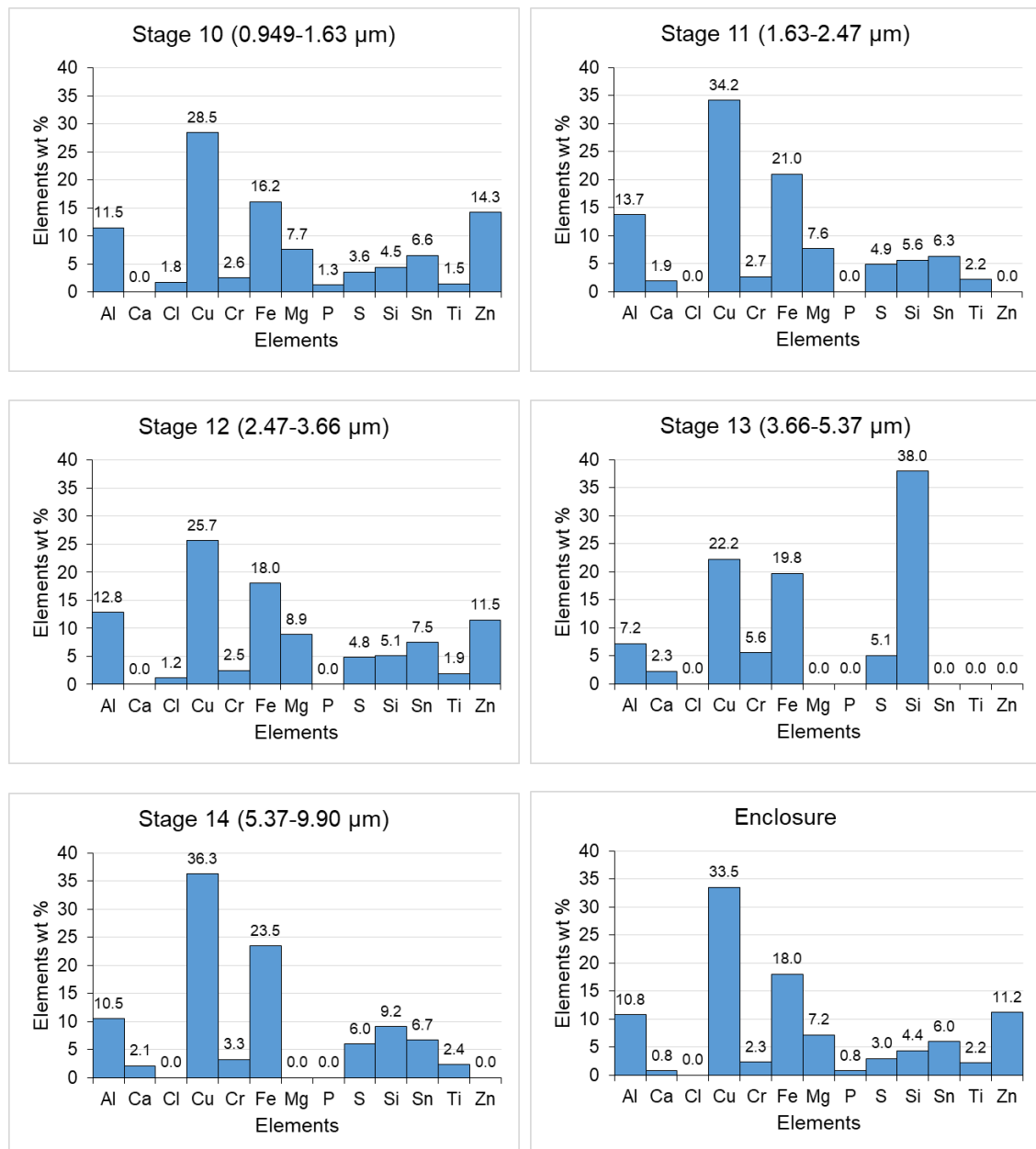


Figure 6.16: Weight percentage of elements for the test P05J.

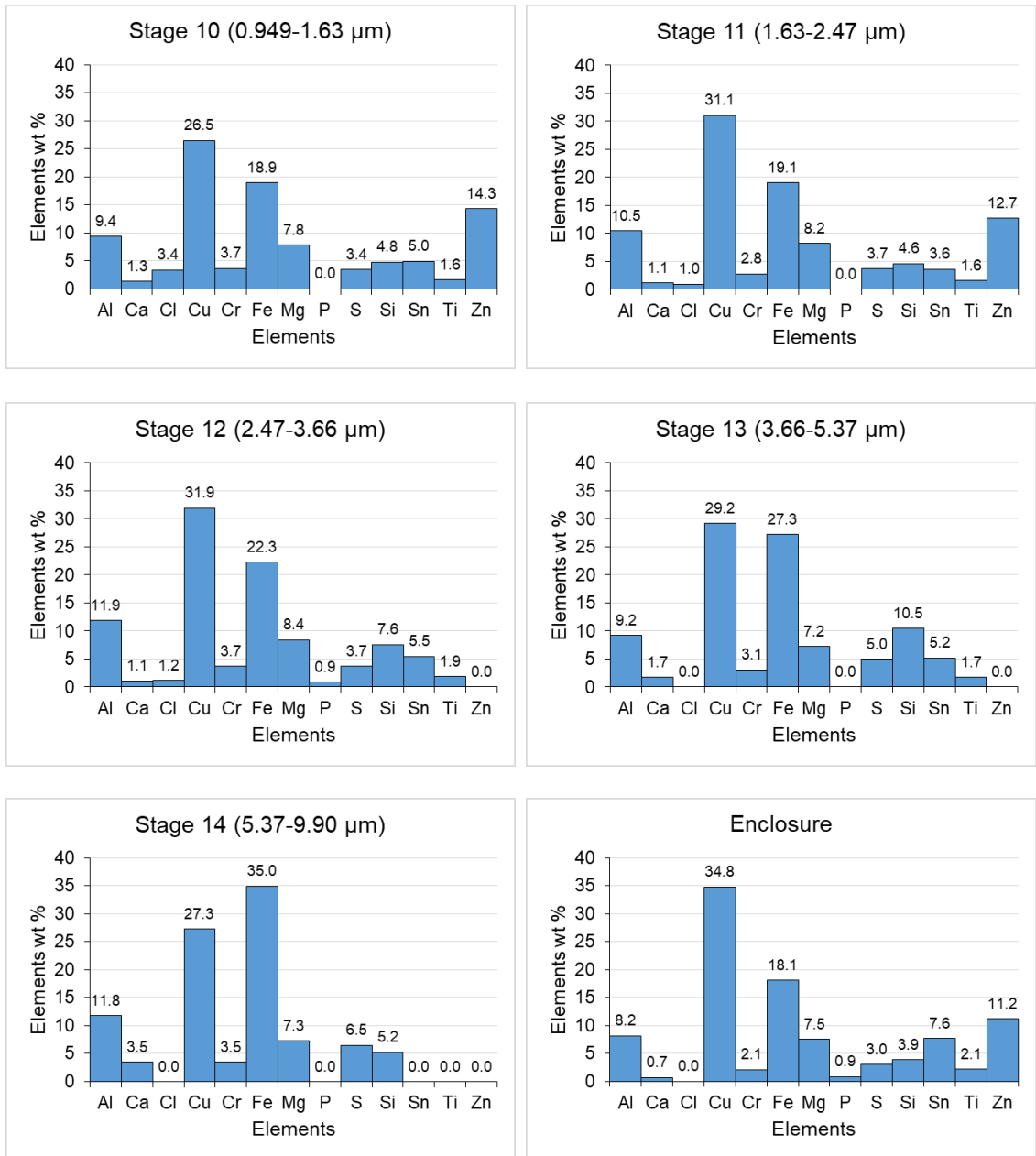


Figure 6.17: Weight percentage of elements for the test P10J.

6.5.2 Elemental weight percentage comparisons

Figure 6.18 shows a comparison of elemental weight percentages for the two brake conditions with the exclusion of carbon and oxygen elements. In this study, eight key elements (Fe, Cu, Cr, Ca, S, Si, Al and Mg) from the quantitative analysis described in the previous section were considered. The weight percentages were compared for the samples obtained from the ELPI+ stages of 10 to 14 and also those from the bottom of the enclosure.

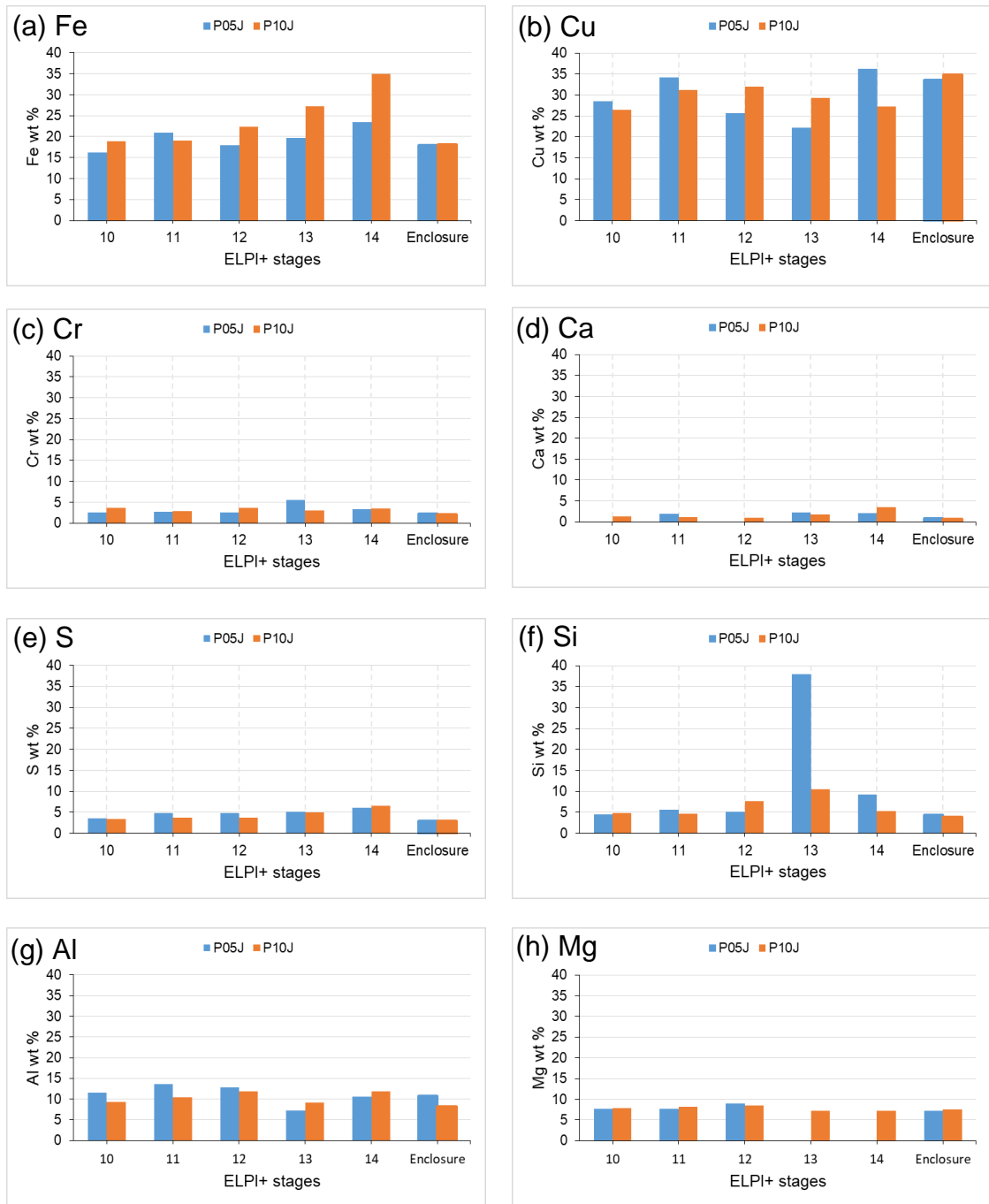


Figure 6.18: Comparison of elemental percentages by weight for the two conditions (a) Fe, (b) Cu, (c) Cr, (d) Ca, (e) S (f) Si, (g) Al and (h) Mg.

Fe and Cu turn out to be the most predominant elements of wear debris, again suggesting that the brake pads became worn significantly. Figure 6.18 (a) indicates that the percentage of Fe increases with the increased brake pressure. In contrast, Figure 6.18 (f) reveals the percentage of Si slightly decreases as the brake pressure increases. It can also be noted that the Si is relatively abundant

at stage 13 of the P05J test. This may be due to the particular location examined, which coincidentally contains more of that element. The weight percentage of Al in Figure 6.18 (g) is somewhat moderate, approximately 10% of the total weight. This finding suggests that only about a tenth of the total wear debris generated comes from the brake rotor material. Mg also has a similar low presence but was not detected at all at stages 13 and 14 of the P05J test. Other elements namely Cr, Ca and S only contribute small percentages; thus, it is not valid to analyse their trends accurately. However, these elements were produced within all particle ranges with nearly the same proportion.

6.5.3 EDX analysis for the brake pad

One of the new brake pads used for the PEO-Al rotor was examined in the same way as the pads used for the GCI rotor to compare with the elements discovered in the samples of brake wear particles. Two locations were analysed to ascertain the consistency of the results. Both locations were randomly selected and examined under SEM at two magnification levels (1000x and 100x). Different magnifications were used to check the result consistency when different area sizes were analysed. EDX analysis was performed on the whole field of view which was approximately 0.15 X 0.20 mm and 1.5 x 2.0 mm for Location 1 and Location 2, respectively.

The results of the EDX analysis on the brake pad are summarised in Figure 6.19. The elemental distributions of the two results are consistent with each other and both show that the brake pad contains high percentages of C, O, Fe and Cu and low percentages of S, Cr, K, P, Ca and Cl (<1%). Other elements identified are Si, Mg, Zn, Sn, Al and Ti which account for about 1-3% of the total weight percentage. The good consistency between the two locations gives confidence that the results are representative of the whole pad surface. These results confirm that the major metallic elements present in the pad are Fe and Cu which correspond with the findings of the wear particle analysis and confirm that the pad is the source for the presence of these elements in the wear debris samples.

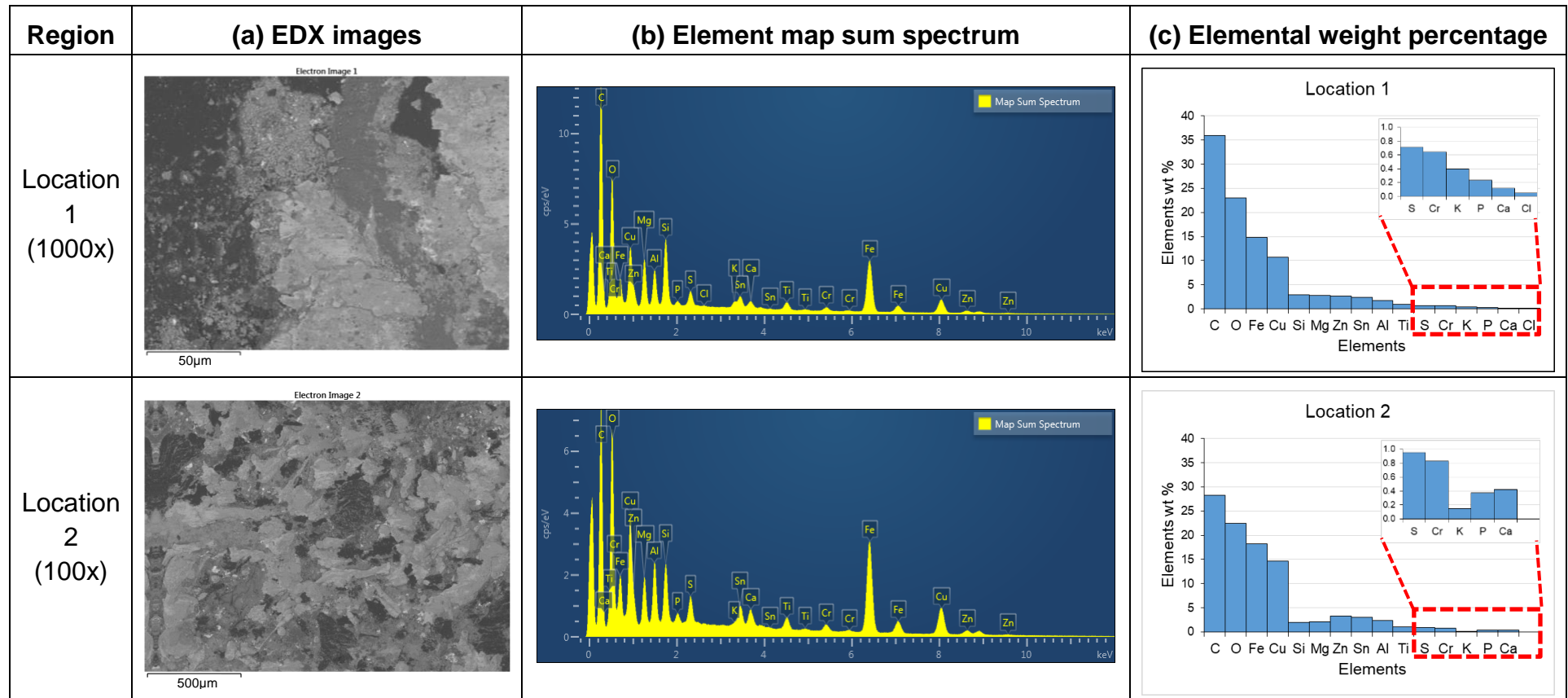


Figure 6.19: EDX images and elemental weight percentages of the brake pad.

6.6 Summary

This chapter describes the collection and evaluation of brake wear particulate matter generated from the PEO-Al rotor and its conforming pads. Preliminary dynamometer tests were carried out using the same brake conditions as those for the GCI rotor in order to ascertain the rotor temperatures during steady-state drag braking conditions. These conditions resulted in rotor surface temperatures of 120°C and 210°C for the tests at 5 and 10 bar braking pressure, respectively. In the repeatability tests, this steady-state condition was again achieved but at lower temperatures of 90°C and 150°C for the tests at 5 and 10 bar, respectively. These lower temperatures, which were subsequently found to be repeatable, are thought to be due to the new PEO rotor having formed a more stable transfer layer on its rubbing surface after the preliminary tests.

The Dekati ELPI®+ particle analyser was utilised to measure and capture brake wear particles for subsequent analysis. The real-time particle measurement results revealed that there was no significant change in particle number concentration with time for the two brake conditions studied. Based on the particle size distribution, the particle number concentration in the coarser particle fractions was found to be slightly higher at the high temperature and brake pressure condition compared to the lower one. Similarly, the mass fraction of coarser particles also slightly increased as the brake pressure was increased. The results also revealed that about 85% of the total airborne brake particulate mass is emitted with particle size ranges from 2.5 to 10 µm for both brake conditions studied. In general, the particle mass concentrations of PM_{2.5} and PM₁₀ were higher at higher brake pressure.

From the subsequent morphological studies, most of the particles observed at all stages were irregular in shape. The number of particles observed on the foils decreased from fine to coarse particle size ranges for both tests and these particles were more abundant at the higher brake pressure. With the exclusion of C and O (which are the dominant elements in the PC foils), the EDX chemical analysis revealed that Fe, Cu, Cr, Ca, S, Si, Al and Mg are the other main elements present in the brake wear particles. Fe and Cu are the most abundant

metallic elements, contributing approximately 20% and 30% of the total elemental percentages, respectively. It is postulated that these two elements originate from the brake pads. Another major contributor is Al which constitutes around 10% of the total elemental composition. The Al may have originated from either the coating layer of the PEO-Al rotor itself or the Al_2O_3 abrasive particles used in the brake pads.

EDX analysis of the brake pad surface confirmed that Fe and Cu are the most abundant metallic elements present and therefore the pad is the most likely source of these elements in the particulate debris. The low percentage of Al in the pad also suggests that the main source of this element in the PM is the PEO alumina surface of the rotor.

Chapter 7 : Discussion

7.1 Introduction

Lightweighting exercises on the disc brake rotor of a vehicle using alternative materials have received increasing attention in recent years. The main reason for utilising such alternative materials is that they will reduce the unsprung mass of the vehicle, and consequently mitigate CO₂ emissions by improving overall fuel efficiency. The reduction in CO₂ emissions is necessary in order to comply with strict exhaust emission regulations. Furthermore, it is anticipated that the first regulations on non-exhaust emissions will be introduced in the near future. As a result, attempts have been made to develop brake rotors that are not only relatively lightweight but also capable of reducing the amount of wear debris generation. The possibility of using such brake rotors is still under research and development. In the present study, the novel PEO-treated aluminium disc brake rotor was characterised and compared to the conventional grey cast iron rotor in relation to tribological performance as well as particulate matter emissions.

This chapter mainly focusses on comparisons between findings obtained from dynamometer tests on GCI and PEO-Al rotors. The discussion includes rotor friction coefficients and surface temperatures, real-time brake wear particle measurements including particle number and mass distributions, post-test classification and microstructural analysis of airborne particulate matter and the evaluation of its elemental composition. In addition, the current test methodology applied in these studies is critically evaluated in the final section.

7.2 Friction performance and temperature

Figure 7.1 shows the variation of the measured coefficient of friction (COF) with time for both GCI and PEO-Al rotors at 5 and 10 bar brake pressures. These

results are typical of the repeatability tests presented in the previous chapters. They were taken from the P05C, P10C, P05H and P10H tests. Due to high frequency fluctuations in the measured torque data, the moving average trendline option in Microsoft Excel was used to display the pattern and trend of the COF time evolution more clearly. From this figure, it can be seen that the COF does not significantly change as the brake pressure for the two brake rotor materials is increased. Initially, the coefficient of friction rises rapidly for both GCI and PEO-Al rotors, and then reaches a peak at about 0.6 for both rotors before dropping to a nearly constant steady-state value in the range 0.43-0.49 for the GCI rotor and in the range 0.25-0.28 for the PEO-Al rotor. The results obtained are closely consistent with other studies; Dahm et al. (2009) reported that the COFs for the standard GCI rotor and a small scale PEO-Al (AA 6082) rotor were 0.5 and 0.30-0.33, respectively, when squeezed against standard NAO brake pads and Alnaqi et al. (2018) found that the COF of a small scale PEO-Al (AA 6082) rotor was in the range of 0.25-0.3.

The present results confirm that the GCI rotor has a significantly higher long term steady-state COF than the PEO-Al rotor. This could be due to the different compositions in the friction material used for the tests on the two rotors which may affect the steady-state COF. The apparent difference is that a high percentage of Ba was found only in the friction material of the GCI rotor while a high percentage of Cu was found only in the friction material of the PEO-Al rotor. The higher and more stable value of COF for the GCI rotor indicates that this rotor-pad system has resulted from a long programme of development to produce the current state-of-the-art friction pair employed by most road vehicles. The lower and more variable COF of the PEO-Al rotor may reflect the much shorter time of development of the friction material for this rotor as compared to that for GCI. It may also reflect the importance of the transfer layer formation on the PEO-Al rotor in establishing a stable COF. It is also worth pointing out that the vast majority of brake applications on the road are of much shorter duration than the long drag applications studied here. The fact that the PEO-Al rotor reaches a relatively high COF of about 0.6 only slightly more slowly after brake application than the GCI rotor is a promising sign that this lightweight rotor may be suitable for on-road use.

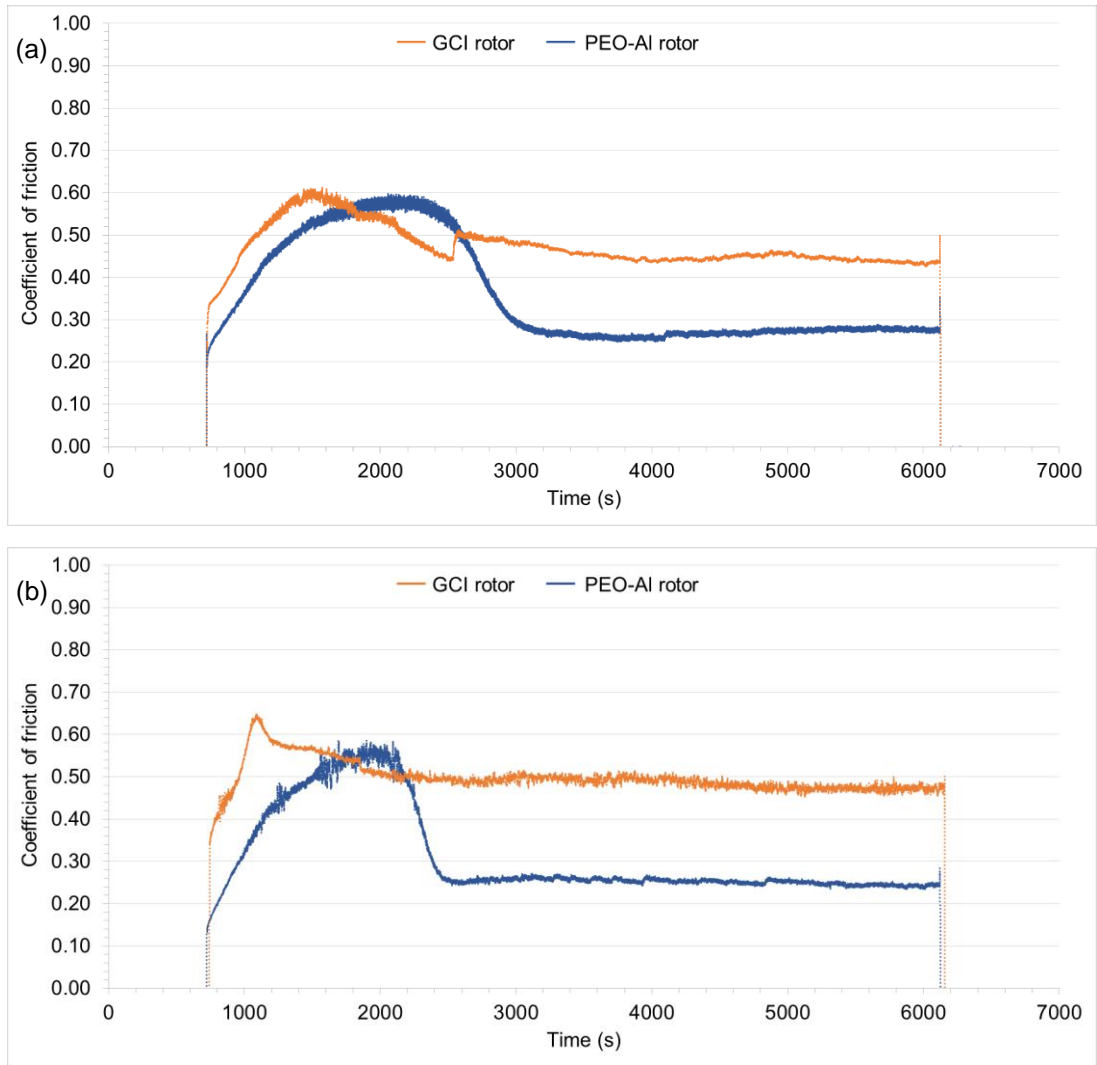


Figure 7.1: Temporal changes in the coefficient of friction for the two brake rotor materials at (a) 5 and (b) 10 bar brake pressures.

To study the relationship between COF and temperature of the rotor for both brake rotor materials at 5 and 10 bar brake pressures, the rotor rubbing surface temperature variation with time was plotted as shown in Figure 7.2 for the same tests as for the COF results presented in Figure 7.1. Overall, the results show that all rotor temperatures attain a nearly steady-state condition within a few minutes from the commencement of the drag braking event. Similar trends can also be seen for all COF plotted in Figure 7.1. The steady-state condition obtained here suggests for the GCI that there is no sign of thermal fade occurring in the rotor during this time period. In contrast, the temperature of the PEO-Al

rotor attains a maximum value after about 2000 seconds and then decreases before reaching a nearly steady-state condition.

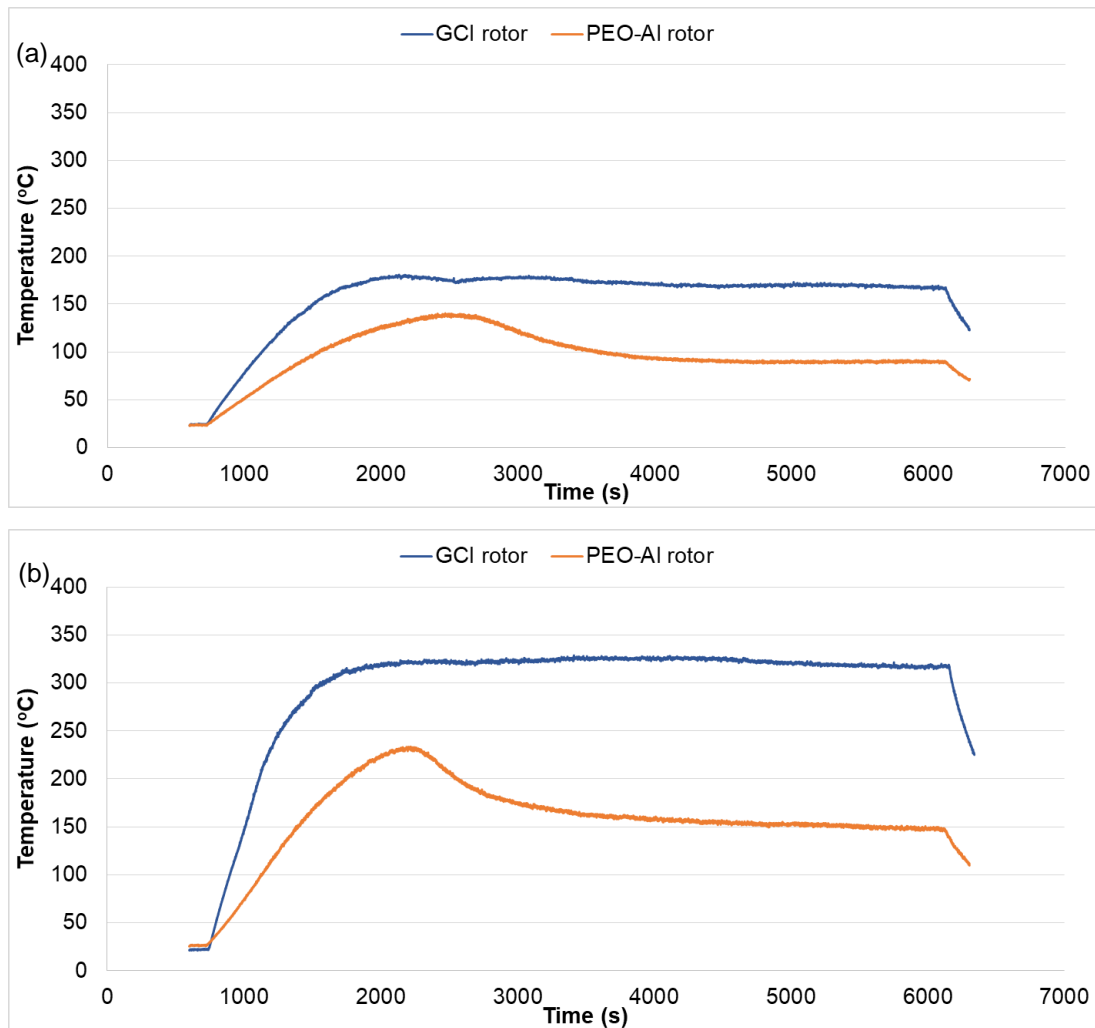


Figure 7.2: Rotor temperature variation with time for the two brake rotor materials at (a) 5 and (b) 10 bar brake pressures.

Likewise, it is evident from Figure 7.1 that the COF plotted for the PEO-Al rotor at the two pressures begins to decrease after 2000 seconds of the braking process before achieving a steady-state value. The measured COF is directly proportional to the torque generated by the disc brake system for these constant applied pressure tests. Therefore, this reduction of COF may be correlated with thermal fade phenomena that may occur when the brake torque is maintained over a long period of time at high rotor temperature (Talib et al., 2018; Hussain, 2018). The thermal fade may be due to the incomplete bedding-in process in the

preliminary tests as the instability of the transfer layer formed on the PEO surface, as already explained in Chapter 6. On the other hand, the GCI rotor shows only a slight reduction in the COF for the two brake pressures applied over the same period of time. This suggests that only a slight amount of thermal fade has occurred for the GCI rotor in these tests, again indicating the robustness of the established GCI system. From the figure, it can also be seen that the temperatures of the GCI rotor are higher than those of the PEO-Al rotor for the same brake pressure applied. This is at least partly due to the higher frictional torque generated by the GCI system leading to a higher thermal power input to the GCI rotor and hence higher temperatures. It is anticipated that the higher the brake rotor temperature, the more brake particulates would be generated. Whether this is in fact the case is discussed in the following section.

7.3 Brake wear emission measurement

7.3.1 Real-time particle measurements

As explained in Chapters 5 and 6, the real-time particle number concentration of both GCI and PEO-Al brake rotors was dominated by a large number of very fine particles due to the inability of the HEPA filter system to remove these very fine particles from the incoming laboratory air. To obtain valid comparisons, the very fine particles within a size range of 6 nm to 0.383 μm were therefore omitted from this analysis. Figures 7.3 (a) and (b) shows the particle number concentration measured in real time for both GCI and PEO-Al rotors at 5 and 10 bar brake pressures. The results used here are similar to Section 7.2. In the figure, the plot area is divided into four time periods to clearly show the different stages of the real-time particle measurements. Periods 1 and 2 indicate the 10-minute system background measurement and the 2-minute free rotation of the brake rotor, respectively. On the other hand, periods 3 and 4 show the measurement of brake wear particles during a brake application for 90 minutes and the final stage where the brake rotor rotates freely without applied brake pressure for 3 minutes, respectively.

From both Figures 7.3 (a) and (b), it can be seen that the particle number concentration measured in the periods 1 and 2 before the brake application commenced is very low in this larger size range. This shows that the extraction and collection system is nearly free from any coarse particles that may come from the laboratory environment. When the brake pressure was applied, wear debris began to be generated as can be seen in period 3 for both brake rotor materials and both brake pressures applied. Initially, the wear debris generated increases as the temperatures of the rotor rubbing surface increase and reaches a peak as the temperatures approach their maximum values (see Figure 7.2). The particle number concentration for both brake rotor materials at 5 and 10 bar brake pressures become approximately constant as the rotor temperatures reach their steady-state values. At the end of the test, the results for time period 4 show that the particle number concentration for all brake conditions dropped when the brake pressure was released from the rotor.

For the applied brake pressure of 5 bar, the particle number concentration generated from the GCI rotor is approximately twice that of the PEO-Al rotor throughout the steady-state braking conditions. However, in the case of 10 bar brake pressure, the particle number concentration of the GCI rotor is actually slightly lower than that of the PEO-Al rotor during these steady-state conditions. The reduction of number concentration of particles for the GCI rotor at the higher brake pressure was quite unexpected. As mentioned in Chapter 5, as the brake pressure was increased to 10 bar, the particle number concentration of GCI always decreased and this trend continued as the pressure was raised to 15 bar.

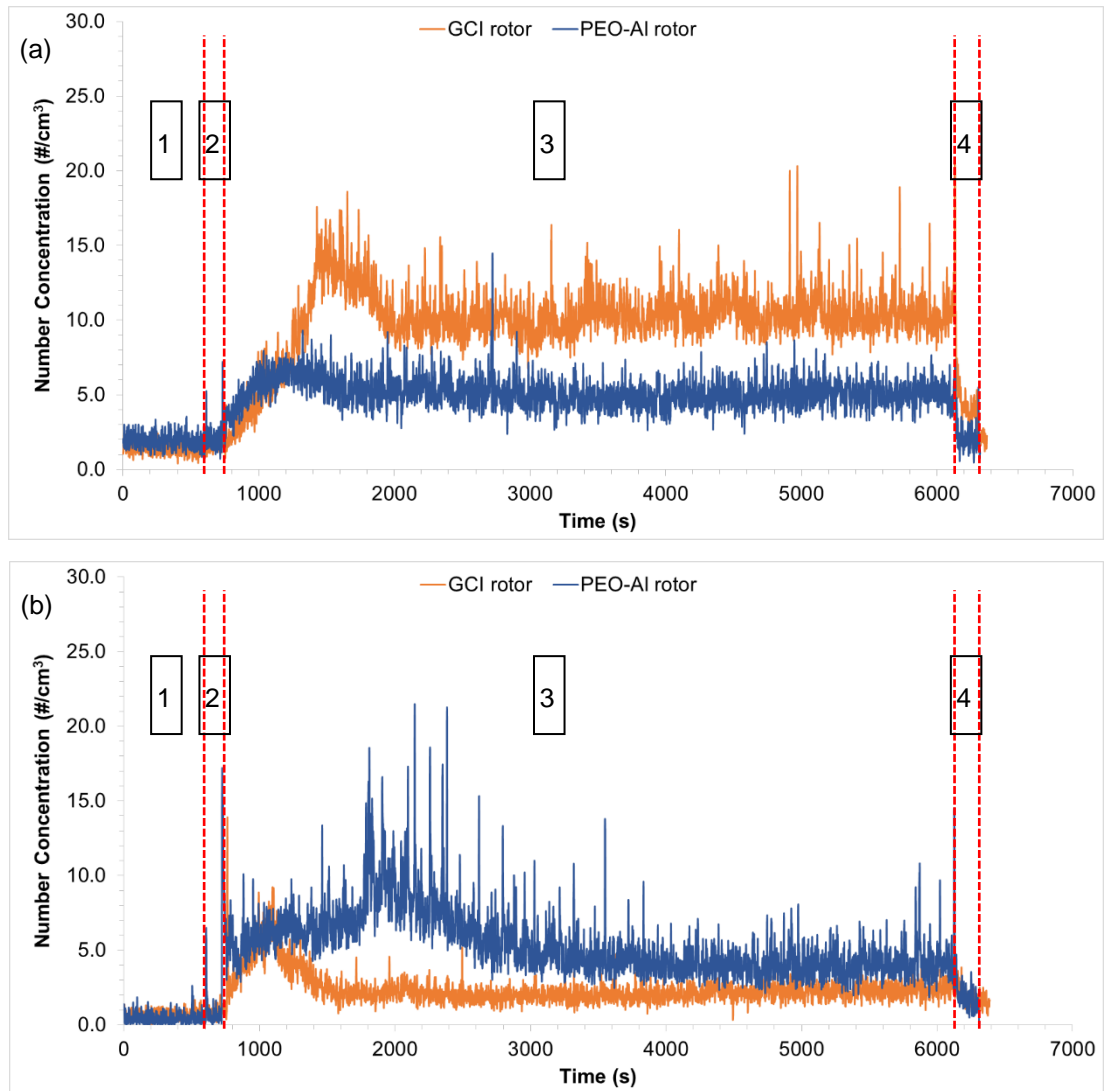


Figure 7.3: Particle number concentration variation with time at (a) 5 bar and (b) 10 bar brake pressures for the two brake rotors studied within the particle size range of 0.383 to 10 μm .

7.3.2 Typical particle number distributions

Figure 7.4 shows the comparison of the particle number concentration over the size range of 0.383 to 10 μm for the two brake rotor materials studied at 5 and 10 bar brake pressures. The data used were the same as in Sections 5.3.2.2 and 6.3.2 for the GCI and PEO rotors, respectively, and their presentation was altered accordingly to allow for an appropriate comparison. The figure clearly shows that the particle number concentration of all the coarser particle fractions at 5 bar brake pressure is significantly greater for the GCI rotor as compared to the PEO-

Al rotor. However, for the brake pressure of 10 bar, the particle number concentration of the PEO-Al rotor for particle size fractions greater than 1 μm is somewhat greater than that of the GCI rotor. This reflects the fact that the time varying total particle number count for the GCI rotor is significantly lower at 10 bar pressure than at 5 bar for the same rotor, as shown in Figure 7.3.

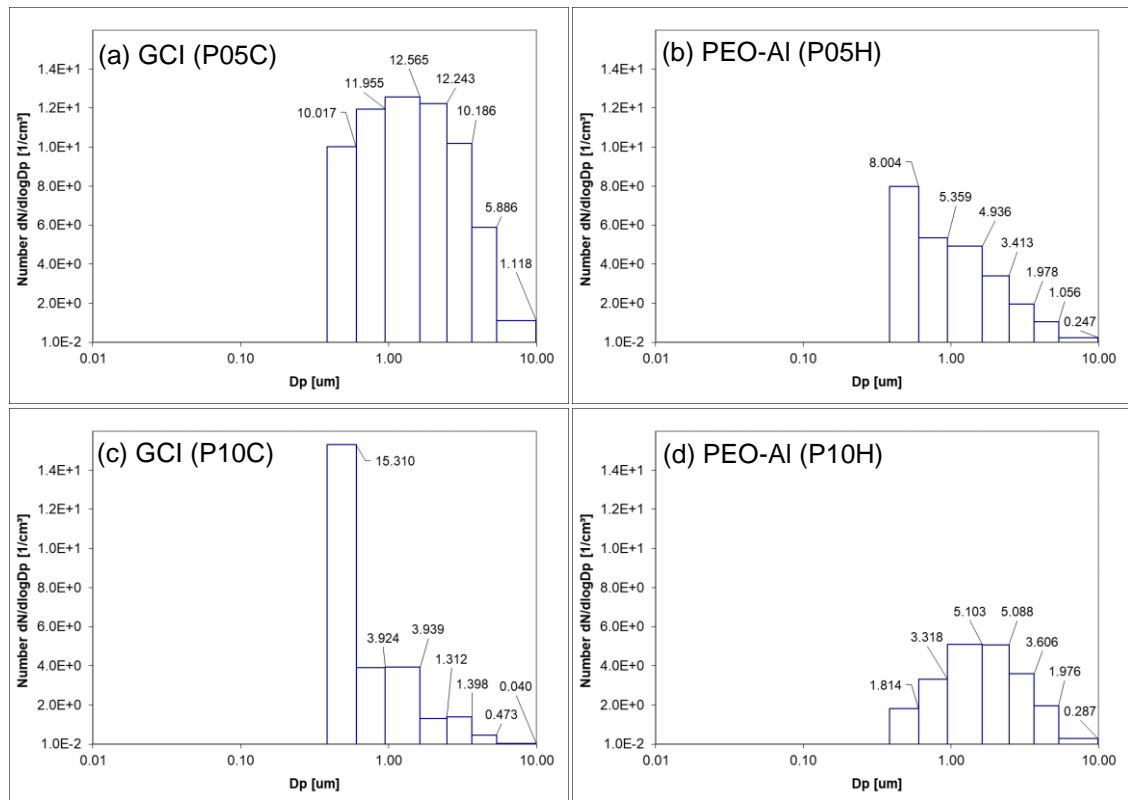


Figure 7.4: Particle number distribution measurements during brake application for (a & c) GCI and (b & d) PEO-Al rotors at the corresponding 5 & 10 bar hydraulic pressures.

7.3.3 Typical particle mass distributions

Figure 7.5 shows the comparison of particle mass concentration for both brake rotor materials studied at 5 and 10 bar brake pressures. The data used and the way they were presented are identical to Section 7.3.2 to allow for an appropriate comparison. It can be seen from Figure 7.5 that all particle mass distributions exhibit peak concentrations within the particle size range of 1 to 10 μm . It is estimated that greater than 90% of the total brake particulate mass is emitted as particles in this 1 to 10 μm ($\text{PM}_{1.0}$ - PM_{10}) size range for both brake rotor materials

and for all brake conditions studied (including the test at 15 bar for the GCI rotor). These results agree with other studies which have demonstrated that coarse particles within this size range dominate the brake wear debris emissions on per mass basis (Sanders et al., 2003; Hagino et al., 2016).

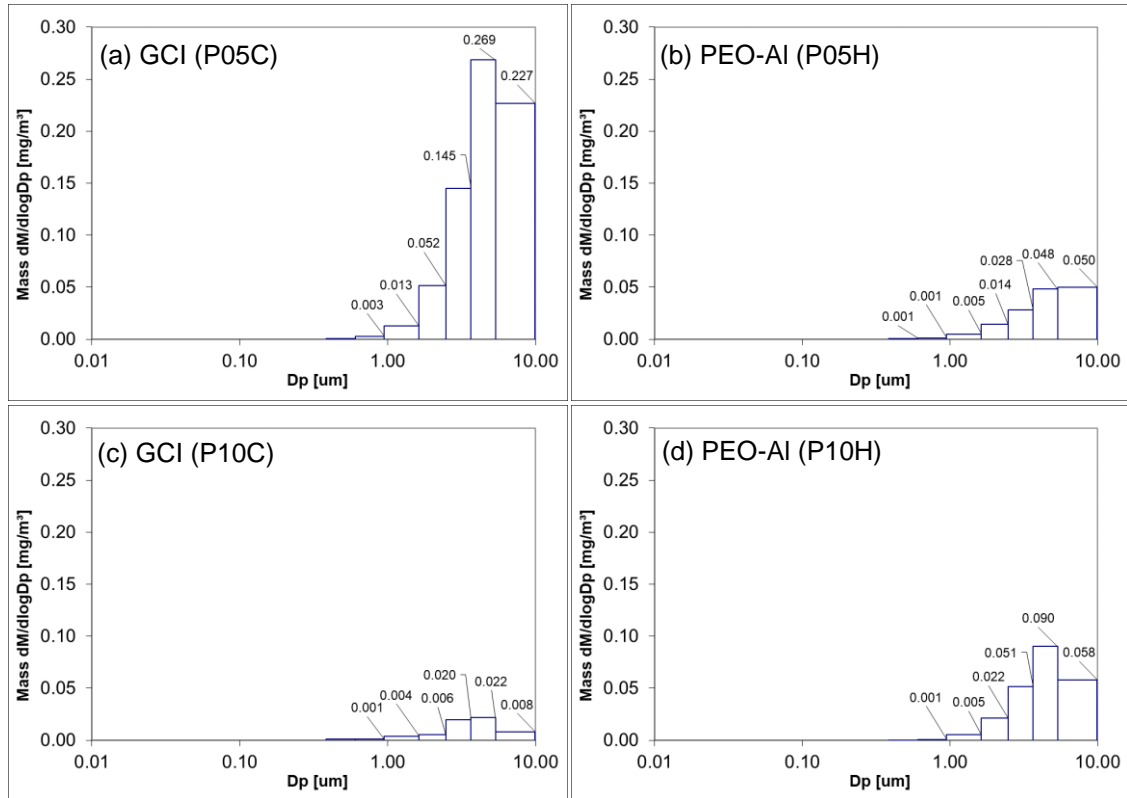


Figure 7.5: Particle mass distribution measurements during brake application for (a & c) GCI and (b & d) PEO-Al rotors at the corresponding 5 & 10 bar hydraulic pressures.

As mentioned in the previous chapters, the particle mass concentration of the coarser particle fractions increased as the brake pressure was increased for the PEO-Al rotor (refer to Chapter 6) but decreased with pressure for the GCI rotor (refer to Chapter 5). Normally, brake wear emissions are expected to be proportional to the frictional work and, hence for constant rotational speed and COF conditions, to the applied brake pressure. The inverse relationship between emissions and pressure suggested by the results for the GCI rotor (including the test at 15 bar for the GCI rotor) may be due to more wear debris becoming trapped between the brake pads and rotor at higher brake pressures. More

precise reasons behind this inverse relationship could not be inferred with the current available data. However, this finding was validated by the gravimetric analysis which was explained in Chapter 5.

7.3.4 Overall average particulate number and mass distributions

Figure 7.6 shows the particle number and particle mass concentrations in the PM_{0.1}, PM_{2.5} and PM₁₀ size ranges averaged over all tests at both pressures for the two brake rotor materials studied. The figure also shows the average concentrations of the test at 15 bar for the GCI rotor. The data used for the GCI and PEO rotors is the same as shown in Sections 5.3.2.4 and 6.3.4, respectively. It can be seen from Figures 7.6 (a) and (b) that the PM_{0.1} size range accounts for more than 85% and 90% of the total average particle number concentrations at both brake pressures for the GCI and PEO rotors, respectively. These large numbers of very fine particles may primarily be contributed by particles from the laboratory air since the current filtration system is not able to efficiently eliminate them. The other two larger size categories are comparatively low in particle number concentration, particularly PM₁₀ for both brake rotor materials and brake conditions studied. Generally, the particle number concentration in the smaller size ranges increases as the brake pressure increases in the case of the GCI rotor. However, this relationship is opposite for the PEO rotor.

From Figure 7.6 (c), the particle mass concentrations in the PM_{2.5} and PM₁₀ are higher at the lower brake pressure and temperature for the GCI rotor. From Figure 7.6 (d), however, the concentrations in these two larger PM size ranges are higher at the higher brake pressure and temperature for the PEO-Al rotor. At 5 bar brake pressure, the PM₁₀ category contributes 90% and 83% of the total airborne brake wear emissions by mass for the GCI and PEO-Al rotors, respectively. At 10 bar brake pressure, the corresponding proportions are 81% and 87% of the total mass, respectively. These results show that GCI emissions of coarser particle fractions (2.5 to 10 µm) are slightly higher than PEO-Al emissions at 5 bar brake pressure whereas the latter are slightly higher at 10 bar brake pressure. For the brake pressure of 5 bar, the particle mass concentration for the PEO-Al rotor in the PM_{2.5} and PM₁₀ categories is reduced by factors of

2.9 and 5.4, respectively, compared with the GCI rotor. On the other hand, for the brake pressure of 10 bar, the particle mass concentration of PEO-Al rotor in the PM_{2.5} and PM₁₀ categories is increased by factors of 1.7 and 2.6, respectively. These findings indicate that PM_{2.5} and PM₁₀ emissions of the PEO-Al rotor are much lower than those of GCI rotor at 5 bar brake pressure whilst, for the higher brake pressure, these two PM categories are marginally higher for the PEO-Al rotor.

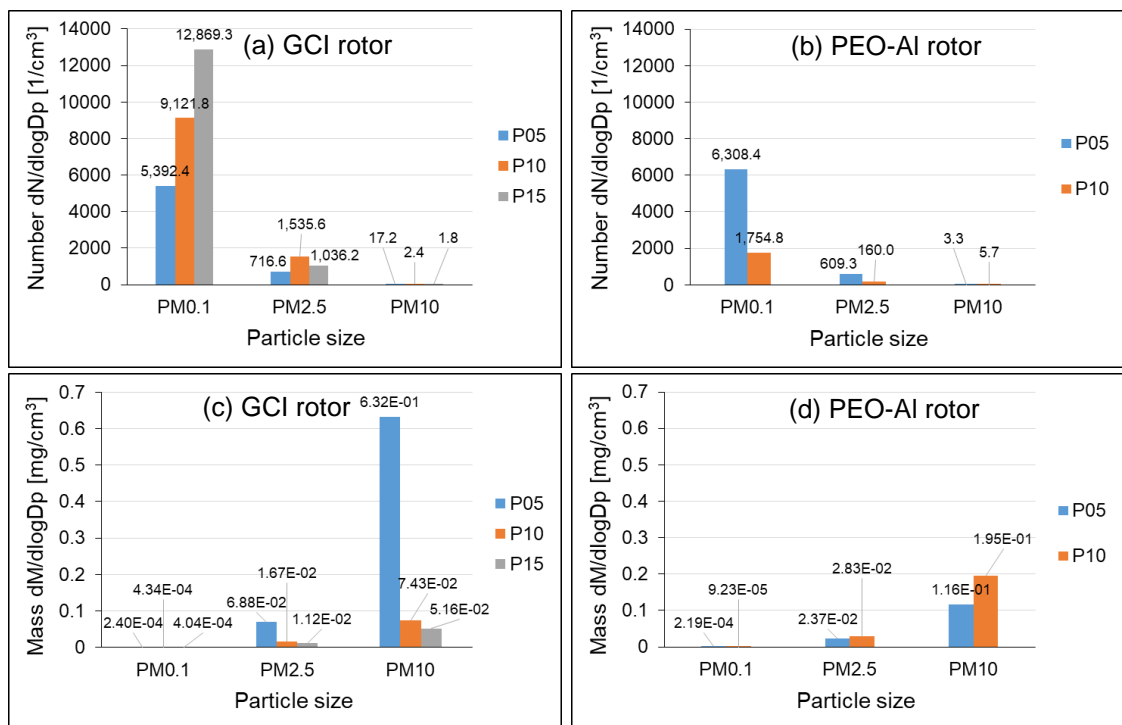


Figure 7.6: Brake wear emissions of PM_{0.1}, PM_{2.5} and PM₁₀ based on average (a & b) particle number and (c & d) particle mass concentrations for the two brake rotor materials.

7.4 Post-test PM characterisation

7.4.1 Microstructural analysis

In this section, qualitative comparisons were made by referring to figures in previous chapters, namely Figures 5.13, 5.14, 6.12 and 6.13. For the test at 5 bar brake pressure, it can be seen from the comparison of Figures 5.13 and 6.12 that the distribution of brake wear debris for both GCI and PEO-Al rotors

demonstrates a similarity whereby the number of observable particles for both results reduces from fine to coarse particles. However, greater numbers of brake wear debris can be noticed for the GCI rotor when comparing the same ELPI+ stage results. Micrographs obtained from both brake rotor materials do not reveal any significant differences in the particle shape for the different stages, most particles being irregular in shape. The micrographs (Figures 5.13-5.15 and Figures 6.12 and 6.13) for these two rotor materials also do not show the presence of wear particle agglomerates. For the test at 10 bar brake pressure (see Figures 5.14 and 6.13), the results also show no difference in particle shape and agglomerated formation. However, particles are noticeably more concentrated in the results for the PEO-Al rotor. These micrographs indicate that the higher the brake pressure the more abundant the particles collected in the case of PEO-Al rotor but the opposite is apparent for the GCI rotor where more particles are observed at the lower brake pressure. These basic findings are consistent with other researches showing that particles generated from the wear of brake friction pair were mostly different in size and irregular in shape (Verma et al. 2016; Kukutschová et al., 2011; Hinrichs et al., 2011; Hussain et al., 2014). For the particles collected on the foils at the bottom of the enclosure (see Figure 5.16 and 6.14), both micrographs show the presence of particles with varying sizes, most of which are less than 10 μm in size. There are no significant differences between the results of GCI and PEO-Al rotors for the two brake conditions applied (5 and 10 bar). Particle agglomeration and numerous particles with an irregular shape were observed in all these enclosure debris results.

7.4.2 Elemental composition evaluation

Figure 7.7 shows the weight percentage comparison of the key elements found in the GCI and PEO-Al brake wear debris. All results were taken from Sections 5.6 and 6.5 in previous chapters. The EDX quantitative analysis was determined without considering oxygen and carbon due to the overabundance of these elements in the PC foils as mentioned in the previous chapters. Moreover, this quantitative analysis is not reliable for light elements (Verma et al., 2016).

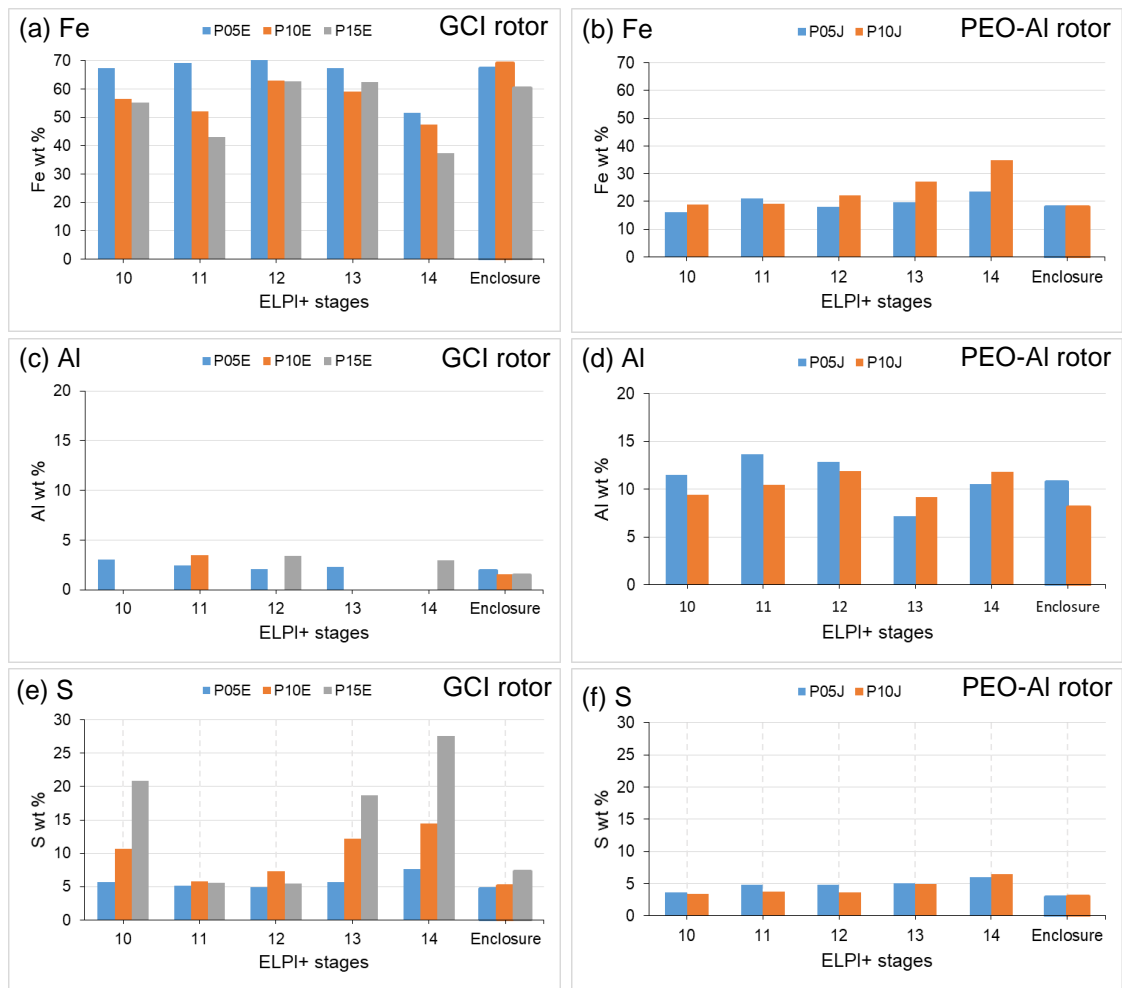


Figure 7.7: Comparison of elemental percentages by weight for two brake rotor materials at 5 and 10 bar brake pressures (a & b) Fe, (c & d) Al and (e & f) S.

Overall, it can be estimated from Figure 7.7 that the percentage of Fe in the PEO-Al debris is about threefold lower than that from the GCI rotor. The distributions of the Fe percentage are somewhat uniform across all the size ranges for both brake conditions and rotor materials studied. A similar pattern of the results was obtained in a previous study (Verma et al., 2016). In the case of the GCI rotor, Iijima et al. (2007) and Hagino et al., (2016) also found that Fe was a major element of wear debris and that large amounts of Fe were assumed to come from the brake rotor. At a much smaller proportion, the percentage of Al in the PEO-Al debris is about four times greater than that for the GCI rotor. The distribution of the Al percentage is quite uniform for the PEO-Al rotor but this is not the case for the GCI rotor where it appears quite random. The percentage of

S in the PEO-Al debris is nearly double lower than that from the GCI rotor and the distribution of the S is more uniform in the PEO-Al rotor.

The EDX analysis also revealed high percentages of Ba and Cu found only in the GCI and PEO-Al brake rotors, respectively. It might also be worth comparing the weight percentages of these two elements which are assumed to originate from the respective brake pad materials. Figure 7.8 shows a comparison of elemental weight percentages of Ba (from GCI rotor) and of Cu (from PEO-Al rotor) for the two brake pressures studied. The percentage of Cu in the PEO-Al rotor is shown to be about twice that of Ba in the GCI rotor across all size ranges.

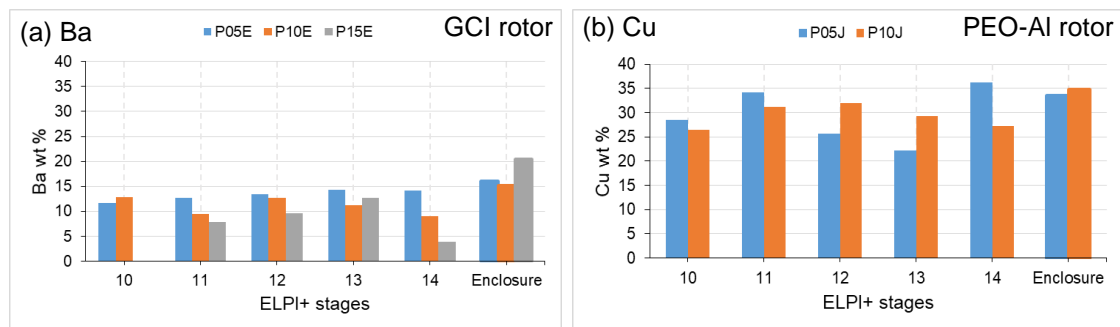


Figure 7.8: Comparison of weight percentages for two different elements, (a) Ba and (b) Al at 5 and 10 bar brake pressures.

7.5 Health relevance of brake wear particles

Particle size is an important factor that can cause adverse effects on human health. The present study showed that particle mass distributions for all braking conditions and materials studies exhibit peak concentrations in the coarse particle fraction (PM_{10}). These coarse particles are most likely to be deposited in the nose and throat and may be responsible for causing irritations (Ciudin et al., 2014). According to Samet et al. (2000), they have found consistent evidence to associate the level of PM_{10} with the rate of death from all causes, especially from cardiovascular and respiratory illnesses.

The key elements found in the GCI brake wear debris are Fe, Ba, Cr, Ca, S and Si while for the PEO-Al debris, Fe, Cu, Cr, Ca, S, Si, Al and Mg were discovered. The presence of these key elements were also reported in previous studies. Iijima et al. (2007) found that Fe, Ba and Cu are to be most abundant elements

in the brake wear debris which were generated from a cast iron brake rotor and NAO brake pads. Hjortenkrans et al. (2007) reported that brake wear debris mainly contained Fe with significant amounts of other elements such as Ba, Sb, Cu, Si, S, Ti, Ni, Zn, Cr and Pb. Furuta et al. (2005) found that the brake dust to be predominantly composed of elements such as Na, Mg, Al, K, Ca and Fe. Hagino et al. (2016) identified Fe, Cu, Ba and Sb as the key traces of the brake wear debris. In addition, the presence of Fe, Ba, Sb, Cu, Si, Ti, Ni, Zn, Cr and Pb in the brake dust was also mentioned in The Brake Report (2021).

Chemical composition of brake wear debris can also negatively affect human health. In this study, it was shown that Fe, Ba and S is the most dominant elements in the GCI debris. For PEO-Al debris, Fe, Al and Cu were recorded the highest percentages. The high level of these elements may have a tendency to cause health problems. For example, Liu et al. (2018) has linked high Fe levels to Alzheimer's disease. This relationship could be because of the excess Fe in the brain that may impair normal cognitive function and behaviour. A review carried out by Grigoratos and Martini (2015) mentioned that Cu and S had been associated with the increased monthly mortality. Moreover, high concentrations of Fe and Cu have also been connected to pulmonary injury and inflammation (Ghio et al. 2004).

7.6 Evaluations of current methodology

Wear debris emitted from automotive friction braking can pollute the atmosphere and thereby impact human health and the environment. Emissions from this source are widely discussed in the scientific community but as yet no regulations are in place to control it. Various test stands, particle capture instruments and test cycles have been utilised in recent years to measure the emissions of the brake wear debris. Most of the test stand used has been designed and manufactured using in house facilities. The particle capture instruments commonly used by researchers include the Micro-Orifice Uniform Deposited Impactor (MOULDI), Aerodynamic Particle Sizer Spectrometer (APS), Optical Particle Sizer (OPS), Electric Low-Pressure Impactor (ELPI), etc. In the literature, most braking tests were conducted using repetitive braking in short

time intervals, often following some standard test cycles such as the AK Master or WLTP. However, variations in these approaches have resulted in different findings, frequently leading to contradictory comparisons. In the present study, the test stand with the new ducting system installed and fitted with the Dekati ELPI®+ was also fabricated using in house facilities and the test cycle used was based on continuous drag braking which are the only conditions available on the Leeds non-inertial dynamometer. Therefore, the findings of this research have to be seen in the light of some limitations of this set-up as described below;

- 1) The existing extraction and collection system has outlet ducting with several 90 degree bends. Such bends are undesirable because of increased particle loss during aerosol transport in the ducting which may subsequently affect sampling efficiencies. Generally, larger particles are more influenced by inertial forces and they are driven more easily towards the wall of the ducting bends. This may cause losses of these larger particles on the ducting wall (Brockmann, 2011).
- 2) The sampling probe was designed to be isokinetic. However, in this study the actual flow velocity in the vicinity of the probe was not measured precisely during the particle measurement tests. Therefore, the extent to which airborne brake wear particles deviate from the streamlines of the flow into the sampling probe inlet could not be evaluated. Also, the lowest air velocity (6 m/s) that the fan of the system can achieve is rather high, leading to a relatively small internal diameter of the sampling probe compared with the diameter of the outlet duct.
- 3) As mentioned above, the existing Leeds full-scale disc brake dynamometer is only available for use under drag brake conditions. To the best author's knowledge, no research regarding the use of such brake conditions has been found in the literature. Since the test cycles developed in this study were based on these drag brake conditions, comparisons with other findings under different conditions are not trivial.
- 4) The bedding-in method applied to the PEO-Al rotor was taken from the previous student's work (Hussain, 2018) since no established method has yet been developed. This may have affected the COF results for this rotor particularly during the initial stages of a test due to the fact that the transfer

of pad material to the rotor surface had not been fully established in the preliminary tests.

7.7 Overall assessment of GCI and PEO-Al rotors

GCI is the most commonly used brake rotor material in automotive industries due to low production costs and excellent tribological properties. Over the past decade, much effort has been spent to improve the friction performance of both the GCI rotor and its friction materials. The GCI rotor is now regarded as a reliable and robust system. Similarly, well developed compatible friction materials with the limited use of copper have also been created. It has been shown that the GCI rotor has a stable and consistent COF over a wide range of temperatures. This means the GCI rotor has shown little evidence of brake fade in the current tests. However, such GCI rotors are prone to corrosion and have a high weight which leads to higher fuel consumption. The present tests have demonstrated that the GCI rotor also has relatively high emissions, especially under light braking pressure. These brake wear emissions contain a lot of Fe and also Ba which were thought to originate from the rotor and the conforming pads, respectively.

The PEO-Al rotor is a newly developed brake rotor developed using in-house facilities and the expertise of Keronite. The rotor is lightweight and the mass saved can be estimated at around 20 kg as compared to the conventional GCI brake rotor for a medium-sized passenger car. Although no studies have been reported, the PEO-Al rotor is also potentially more corrosion resistant. At low brake pressure, the PEO-Al rotor produced lower emissions than the GCI rotor and especially a much lower proportion of Fe in the wear debris. However, a major disadvantage of the PEO-Al rotor is that it produces a more variable COF than that of the GCI rotor. This COF tends to be lower during long brake applications which may arise from the phenomenon known as thermal fade. The PEO-Al rotor is also more dependent on the establishment of a transfer layer in order to function under stable tribological conditions. Moreover, the current PEO-compatible brake pad material contains Cu that is not considered environmentally safe. However, the compatible friction material is still at an early

stage of development and it could be expected that future pad formulations will not require the addition of Cu and will produce a more stable and consistent COF.

Chapter 8 : Conclusions and future work

8.1 Conclusions

Non-exhaust emissions are a significant source of traffic-related particulate matter which can cause adverse health effects to humans (Perricone et al., 2016). Stringent regulations on exhaust emissions have been put in place to reduce public health but there are no such regulations for non-exhaust emissions. As a result, the proportion of non-exhaust emissions in the atmosphere is significantly growing. This has increased interest in using lightweight materials not only to reduce CO₂ emissions but also to control pollution from non-exhaust sources, particularly from automotive brakes. Studies both in the field and under laboratory conditions have shown that brake-related particulate matter is likely to remain one of the major contributors to the non-exhaust emissions (Harrison et al., 2012; Grigoratos and Martini, 2015).

In the present study, all experiments have been carried out based on laboratory measurements to avoid contamination from other sources such as road dust and tyre wear. Unlike previous laboratory studies based on complex braking cycles which attempt to simulate real-world driving conditions, the present study has aimed to carefully control the basic tribological parameters of sliding speed, contact pressure and surface temperature under nearly steady-state drag braking conditions. Moreover, the aim has been not only to further understand the basic wear debris generation process but also to seek solutions through the investigation of alternative aluminium-based rotor materials which may give lower emissions compared with the traditional grey cast iron as well as offering a significant mass saving.

The new air extraction system installed on the Leeds brake dynamometer has been successfully commissioned and utilised to allow particle measurements and collections under controlled drag brake conditions of constant sliding speed

and applied braking pressure. The performance of the novel PEO-treated lightweight disc brake rotor has been investigated and compared with a grey cast iron rotor (GCI), particularly with respect to the emission of the brake wear particles in the environment. Overall, it was concluded that the PEO-treated lightweight aluminium alloy rotor (PEO-Al) showed a better performance than the conventional GCI rotor in terms of both mass reduction and fewer wear debris particle emissions, especially at low applied pressures. This is an encouraging results because friction brakes on current and future electric vehicles are predicted to operate at lower applied pressures due to the availability of regenerative braking. However, the PEO-Al rotor showed less consistent and generally lower friction coefficients than the GCI, indicating the need to further develop and optimise the pad material for rubbing against the PEO-Al disc.

Other more detailed findings of the current research can be summarised as follows:

- A detailed CFD study of the test set up showed good levels of turbulence in the enclosure, particularly around the brake assembly, which indicated a well-mixed regime to enable efficient transport of brake wear particles of varying sizes into the ducting system, where they are sampled. The predicted velocity profiles at the duct cross-section containing the anemometer probe were shown to be consistent with the experimental results, thereby validating the CFD analysis. The simulation results showed that the flow is more stable at the left-hand side of the outlet duct (recall Figure 4.6 for a better illustration) and this suggested that the sampling probe should be placed in this region. It was also confirmed from this study that the purpose-built sampling probe achieved near isokinetic conditions which is a fundamental requirement.
- The developed test protocol using the newly commissioned Dekati ELPI[®]+ showed good potential and repeatability for investigating airborne brake wear particles of the different brake rotors in the laboratory.

- The preliminary tests were successfully carried out on the modified brake dynamometer for the brake rotors under investigation. The temperatures recorded at the rubbing surface of the GCI rotor during steady-state conditions were approximately 200, 300 and 400 °C for brake hydraulic pressures of 5, 10 and 15 bar, respectively. In contrast, the temperatures recorded for the PEO-Al rotor under the same drag braking conditions were approximately 120 and 210 °C for brake pressures of 5 and 10 bar, respectively. (Due to the COVID-19 lock-down restrictions, it did not prove possible to test the PEO-Al rotor under 15 bar pressure conditions).
- The coefficient of friction for the GCI and PEO-Al rotors during steady-state conditions was found to be in the range of 0.43-0.49 and 0.25-0.28, respectively. The effect of thermal fade was found to be more significant in the PEO-Al rotor as compared to the GCI rotor.
- Not all brake wear particles were emitted as airborne particles and this was observed from the larger particles that were deposited on the PC foil at the bottom of the enclosure.
- The particle number and mass concentrations in the coarser particle fractions (1.0-10 µm) collected by the Dekati impactor showed a decreasing trend as the brake pressure was increased for the GCI rotor. However, this relationship was opposite for the PEO-Al rotor for the two braking conditions studied i.e. the emissions were increased at 10 bar compared with 5 bar brake pressure.
- The results revealed that the PM₁₀ (PM_{2.5}-PM₁₀) category contributed about 85% of the total airborne brake particulate mass emissions for the PEO-Al rotor at both brake pressures studied, while the PM₁₀ also accounted for greater than 80% of the total mass for the GCI rotor at 5, 10 and 15 bar brake pressures.

- The particle mass concentrations in the PM_{2.5} (PM_{0.1}-PM_{2.5}) and PM₁₀ categories for the PEO-Al rotor were greater for higher brake pressure (and thus higher temperature), while the concentrations in these two larger PM size ranges for the GCI rotor were greater at the lowest brake pressure and temperature.
- The particle mass concentrations of the PEO-Al rotor in the PM_{2.5} and PM₁₀ categories for the brake pressure of 5 bar were reduced by factors of 2.9 and 5.4, respectively, compared with the GCI rotor. At the higher pressure of 10 bar, these concentrations were increased by factors of 1.7 and 2.6, respectively.
- The morphological studies showed that most of the particles observed for both PEO-Al and GCI rotors were irregular in shape at all ELPI+ stages and brake conditions studied.
- With the exclusion of the carbon and oxygen prevalent in the PC foils, the key elements of brake wear particles in the PEO-Al rotor debris were Fe, Cu, Cr, Ca, S, Si, Al and Mg while, for the GCI rotor, main debris elements were Fe, Ba, Cr, Ca, S and Si.
- Based on the EDX analysis, the Fe content in the PEO-Al debris was found to be about threefold lower than that from the GCI rotor. The percentage of Fe increased with the increased brake pressure for the PEO-Al rotor whereas this relationship was opposite for the GCI rotor results. However, the content of Al in the former was about four times greater than that for the GCI. This is as expected given the main constituent elements of the two brake rotors. The lower proportion of Fe in the PEO-Al rotor debris, especially at the low braking pressures expected for electric vehicle friction brakes, is an important result given the reported link between sub-micron airborne particles containing Fe oxides and neurological diseases such as Alzheimers

- The Cu and Ba present in the PEO-Al and GCI debris, respectively, were postulated to originate from the brake pads. If these two elements were compared, it was found that the content of Cu from the PEO-Al test was about twice that of Ba from the GCI test. However, it must be emphasised that the compatible pad material for the PEO-Al rotor has not been fully developed or optimised and a production version would almost certainly not contain Cu as this element has been recognised as non environmentally-friendly.

The present research has provided important insights into generating, measuring and collecting airborne brake wear particles using the newly developed test protocol and the modified brake dynamometer. The originality of the work lies in the application of prescribed steady-state tribological conditions of sliding speed, contact pressure and surface temperature. In contrast nearly all previous research in this area has attempted to simulate real driving conditions where these tribological parameters are highly variable. Moreover, the present research has aimed to investigate potential solutions to reduce brake wear emissions rather than just defining the nature of the problem. The present work thereby offers a good starting point for discussion and further research on wear emissions from lightweight disc brake rotors. The results presented in this thesis give important information to encourage the automotive industry to consider the potential use of lightweight disc brake rotors for replacing the conventional ferrous ones.

8.2 Suggestions for future work

The following recommendations offer further improvements to the current research work that may prove useful to academics and industry practitioners:

- Further braking tests should be carried out using repetitive braking in short time intervals such as the AK Master or WLTP test cycles to allow for

appropriate comparisons with the steady-state results presented in this thesis.

- In order to replicate real-world conditions such as variable speeds and weather conditions, measurement of airborne brake wear particles during on-road driving, particularly in urban areas, should be conducted to compare various disc brake rotors including the novel PEO-treated lightweight design. However, such testing requires specialised equipment and careful consideration to separate out brake wear debris from all other forms of airborne particulate emissions.
- The present extraction and particle capture system could be redesigned to increase sampling efficiencies by reducing particle losses in the system. Several bends in the current outlet ducting could potentially be eliminated or at the least minimised in number. For the same reason, a straight sampling probe should also be utilised in the system.
- More advanced test methods such as X-ray diffraction analysis should be used to characterise the phase formation in airborne brake wear particles samples obtained from the braking tests. Through this examination, oxide phases such as FeO, Fe₃O₄, MgO, ZnO and Fe₂O₃ could be identified and used to provide useful information e.g. for toxicological studies.
- Further information regarding mass concentrations of metallic elements in the brake wear particles according to their size ranges could be investigated using inductively coupled plasma mass spectrometry (ICP-MS).
- Different rotor surfaces should be investigated such as Al Metal Matrix Composite rotors and hard-coated ferrous rotors. Although the latter would not significantly reduce rotor mass, such coatings would be expected to reduce wear particle emissions compared with uncoated GCI rotors.

References

- Agbeleye, A.A., Esezobor, D.E., Balogun, S.A., Agunsoye, J.O., Solis, J. and Neville A. 2020. Tribological properties of aluminium-clay composites for brake disc rotor applications. *Journal of King Saud University – Science*. **32**(1), pp.21-28.
- Agudelo, C., Vedula, R., Capecelatro, J. and Wang, Q. 2019. Design of experiments for effects and interactions during brake emissions testing using high-fidelity computational fluid dynamics. *SAE Technical Paper*.
- Akebono. 2020. *Drum brakes*. [Online]. [Accessed 18 April 2020]. Akebono Brake Industry Co., Ltd. Available from: https://www.akebono-brake.com/english/product_technology/product/automotive/drum/.
- Alemani, M., Perricone, G., Olofsson, U., Söderberg, A., Wahlström, J. and Ciotti, A. 2014. A proposed dyno bench test cycle to study particle emissions from disc brakes. *Eurobrake 2014 conference*. Lille, France: London: FISITA.
- Alnaqi, A.A. 2014. *Characterisation of coated lightweight brake rotors*. Doctor of Philosophy thesis, University of Leeds.
- Alnaqi, A.A., Kosarieh, S., Barton, D.C., Brooks, P.C. and Shrestha, S. 2018. Material characterisation of lightweight disc brake rotors. *Proceedings of the Institution of Mechanical Engineers, Part L: Journal of Materials: Design and Applications*. **232**(7), pp.555-565.
- Alnaqi, A.A., Shrestha, S., Barton, D.C. and Brooks, P.C. 2014. Optimisation of alumina coated lightweight brake rotor. *SAE Technical Paper*.
- Andrade-Lima, M., Pereira, L.F.F. and Fernandes, A.L.G. 2012. Pharmaceutical equivalence of the combination formulation of budesonide and formoterol in a single capsule with a dry powder inhaler. *Jornal Brasileiro de Pneumologia*. **38**(6), pp.748-756.
- Barton, D.C. 2011. Materials design for disc brakes. In: Day, A.J., Klaps, J. and Ross, C.F. ed. *Braking of road vehicles*. 1st ed. Bradford: University of Bradford.
- Bielaczyc, P. and Woodburn, J. 2019. Trends in automotive emission legislation: impact on LD engine development, fuels, lubricants and test methods: a global view, with a focus on WLTP and RDE regulations. *Emission Control Science and Technology*. **5**, pp.86-98.
- Belhocine, A. and Wan Omar, W.Z. 2018. Computational fluid dynamics (CFD) analysis and numerical aerodynamic investigations of automotive disc brake rotor. *International Journal on Interactive Design and Manufacturing*. **12**, pp.421–437.
- Belyaev, S.P. and Levin, L.M. 1974. Techniques for collection of representative aerosol samples. *Journal of Aerosol Science*. **5**(4), pp.325-338.

- Bensalah, W., Elleuch, K., Feki, M., Depetris-Wery, M. and Ayedi, H.F. 2009. Comparative study of mechanical and tribological properties of alumina coatings formed on aluminium in various conditions. *Materials & Design*, **30**(9), pp.3731-3737.
- Berghmans, P., Bleux, N., Int Panis, L., Mishra, V.K., Torfs, R. and Van Poppel, M. 2009. Exposure assessment of a cyclist to PM₁₀ and ultrafine particles. *Science of The Total Environment*. **407**(4), pp.1286-1298.
- Blau, P.J. 2001. *Composition, functions and testing of friction brake materials and their additives*. Oak Ridge National Laboratory Report for U.S. Department of Energy, ORNL/TM-2001/64, Oak Ridge, Tennessee.
- Blau, P.J. and Meyer, H.M. 2003. Characteristics of wear particles produced during friction tests of conventional and unconventional disc brake materials. *Wear*. **255**(7-12), pp.1261-1269.
- Borja-Aburto, V.H., Castillejos, M., Gold, D.R., Bierzwinski, S. and Loomis, D. 1998. Mortality and ambient fine particles in southwest Mexico City, 1993-1995. *Environmental health perspectives*. **106**(12), pp.849-855.
- Brockmann, J.E. 2011. Aerosol transport in sampling lines and inlets. In: Kulkarni, P., Baron, P.A. and Willeke, K. ed. *Aerosol measurement: principles, techniques, and applications*. 3rd ed. New Jersey: John Wiley & Sons, Inc.
- Budinsky, T. 2018. Towards the active suppression of disc brake squeal. Doctor of Philosophy thesis, University of Leeds.
- Calcabrini, A., Meschini, S., Marra, M., Falzano, L., Colone, M., Berardis, B.D., Paoletti, L., Arancia, G. and Fiorentini, C. 2004. Fine environmental particulate engenders alterations in human lung epithelial A549 cells. *Environmental Research*. **95**(1), pp.82-91.
- Carley, L. 2008. *Brake rotors & calipers: the when, where, why and how of brake system service and component replacement* [online]. [Accessed 13 November 2020]. ImportCAR. Available from: <https://www.import-car.com/brake-rotors-calipers-the-when-where-why-and-how-of-brake-system-service-and-component-replacement>.
- Cengel Y.A and Cimbala, J.M. 2006. *Fluid mechanics: fundamentals and applications*. 1st ed. New York: McGraw-Hill.
- Chan, D. and Stachowiak, G. 2004. Review of automotive brake friction materials. *Proceedings of the Institution of Mechanical Engineers, Part D: Journal of Automobile Engineering*. **218**(9), pp.953-966.
- Ciudin, R., Verma, P. C., Gialanella, S. and Straffelini, G. 2014. Wear debris materials from brake systems: environmental and health issues. *WIT Transactions on Ecology and the Environment*. **191**, pp.1423-1434.
- Dahm, K.L., Black, A.J., Shrestha, S., and Dearnley, P.A. 2009. Plasma Electrolytic Oxidation treatment of aluminium alloys for lightweight disc brake rotors. *IMEchE Conference on Braking*, York: United Kingdom.
- Day, A. 2014. *Braking of road vehicles*. 1st ed. Oxford: Butterworth-Heinemann.

- DEFRA. 2019a. *Non-exhaust emissions from road traffic*. United Kingdom: Department for Environment, Food and Rural Affairs.
- DEFRA. 2019b. *What is the daily air quality index?* [Online]. [Accessed 1 October 2019]. Department for Environment Food & Rural Affairs. Available from: <https://uk-air.defra.gov.uk/air-pollution/daq?view=more-info>.
- DEKATI. 2016. Dekati ELPI®+ User Manual.
- Dutta, P., Saha S. K., Nandi N., and Pal N. 2016. Numerical study on flow separation in 90° pipe bend under high Reynolds number by k-ε modelling. *Engineering Science and Technology, an International Journal*. **19**(2), pp.904-910.
- Ebnesajjad, S. 2014. Chapter 4 - Surface and material characterization techniques. In: Ebnesajjad, S. ed. *Surface treatment of materials for adhesive bonding*. 2nd ed. Oxford: William Andrew Publishing.
- EEA. 2016. *Air quality standards under the air quality directive, and WHO air quality guidelines* [Online]. [Accessed 23 October 2019]. European Environment Agency. Available from: <https://www.eea.europa.eu/data-and-maps/figures/air-quality-standards-under-the>.
- EPUK. 2019. *National air quality law and policy* [Online]. [Accessed 23 October 2019]. Environmental protection UK. Available from: <https://www.environmental-protection.org.uk/policy-areas/air-quality/air-pollution-law-and-policy/air-pollution-laws/>.
- European Federation for Transport and Environment. 2011. *Consultation response: reducing CO₂ emissions from road vehicles*. [Online]. [Accessed 20 December 2016]. Available from: <http://www.transportenvironment.org/>.
- Furuta, N., Iijima, A., Kambe, A., Sakai, K. and Sato, K. 2005. Concentrations, enrichment and predominant sources of Sb and other trace elements in size classified airborne particulate matter collected in Tokyo from 1995 to 2004. *Journal of Environmental Monitoring*. **7**, pp.1155-1161.
- Garg, B.D., Cadle, S.H., Mulawa, P.A., Groblicki, P.J., Laroo, C. and Parr, G.A. 2000. Brake wear particulate matter emissions. *Environmental Science & Technology*. **34**(21), pp.4463-4469.
- Galindo-López, C.H. and Tirovic, M. 2012. Maximising heat dissipation from ventilated wheel-hub-mounted railway brake discs. *Proceedings of the Institution of Mechanical Engineers, Part F: Journal of Rail and Rapid Transit*. **227**(3), pp.269-285.
- Gasser, M., Riediker, M., Mueller, L., Perrenoud, A., Blank, F., Gehr, P. and Rothen-Rutishauser, B. 2009. Toxic effects of brake wear particles on epithelial lung cells in vitro. *Particle and Fibre Toxicology*. **6**(30), pp.1-13.
- Ghio, A.J., Churg, A. and Roggli, V.L. 2004. Ferruginous bodies: Implications in the mechanism of fiber and particle toxicity. *Toxicologic Pathology*. **32**(6), pp.643-649.
- Glišović, J., Pešić, R., Lukić, J. and Miloradović, D. 2016. Airborne wear particles from automotive brake systems: environmental and health issues. *1st*

International Conference on Quality of Life. Faculty of Engineering, University of Kragujevac.

- Gorjan, L., Boretius, M., Blugan, G., Gili, F., Mangherini, D., Lizarralde, X., Ferraris, M., Graule, T., Igartua, A., Mendoza, G. and Kuebler, J. 2016. Ceramic protection plates brazed to aluminum brake discs. *Ceramics International*. **42**(14), pp.15739-15746.
- Grieve, D.G., Barton, D.C., Crolla, D.A. and Buckingham, J.T. 1998. Design of a lightweight automotive brake disc using finite element and Taguchi techniques. *Proceedings of the Institution of Mechanical Engineers, Part D: Journal of Automobile Engineering*. **212**(4), pp.245-254.
- Grigoratos, T. and Martini, G. 2015. Brake wear particle emissions: a review. *Environmental Science and Pollution Research*. **22**, pp.2491-2504.
- Gulden, F., Reinhold, B., Gramstat, S., Stich, A., Tetzlaff, U. and Höppel, H.W. 2020. Investigation of the run-in and corrosion behavior of a PEO-coated aluminum brake disc. In: Pfeffer, P. ed. *10th International Munich Chassis Symposium 2019*. Proceedings. Wiesbaden: Springer Vieweg, pp.611-631.
- Hagino, H., Oyama, M. and Sasaki, S. 2015. Airborne brake wear particle emission due to braking and accelerating. *Wear*. **334-335**, pp.44-48.
- Hagino, H., Oyama, M. and Sasaki, S. 2016. Laboratory testing of airborne brake wear particle emissions using a dynamometer system under urban city driving cycles. *Atmospheric Environment*. **131**, pp.269-278.
- Harrison, R.M., Jones, A. M., Gietl, J., Yin, J. and Green, D.C. 2012. Estimation of the contributions of brake dust, tire wear, and resuspension to nonexhaust traffic particles derived from atmospheric measurements. *Environmental Science & Technology*. **46**(12), pp.6523-6529.
- Hinds, W.C. 1982. *Aerosol technology: properties, behavior, and measurement of airborne particles*. 1st ed. New York: John Wiley & sons.
- Hinrichs, R., Marcio R.F.S., Lamb, R.G., Marcos R.F.S. and Vasconcellos, M.A. Z. 2011. Phase characterization of debris generated in brake pad coefficient of friction tests. *Wear*. **270**(7-8), pp.515-519.
- Hjortenkrans, D.S., Bergbäck, B.G. and Häggerud, A.V. 2007. Metal emissions from brake linings and tires: Case studies of Stockholm, Sweden 1995/1998 and 2005. *Environmental Science & Technology*. **41**(15), pp.5224–5230.
- Hulskotte, J.H.J., Roskam, G.D. and Denier Van Der Gon, H.A.C. 2014. Elemental composition of current automotive braking materials and derived air emission factors. *Atmospheric Environment*. **99**, pp.436-445.
- Hussain, J. 2018. *Thermal and material characterisation of coated lightweight disc brake rotor*. Doctor of Philosophy thesis, University of Leeds.
- Hussain, S., Abdul Hamid, M.K., Mat Lazim, A.R. and Abu Bakar, A.R. 2014. Brake wear particle size and shape analysis of non-asbestos organic (NAO) and semi metallic brake pad. *Jurnal Teknologi*. **71**(2), pp.129-134.

- Iijima, A., Sato, K., Yano, K., Kato, M., Kozawa, K. and Furuta, N. 2008. Emission factor for antimony in brake abrasion dusts as one of the major atmospheric antimony sources. *Environmental Science & Technology*. **42**(8), pp.2937-2942.
- Iijima, A., Sato, K., Yano, K., Tago, H., Kato, M., Kimura, H. and Furuta, N. 2007. Particle size and composition distribution analysis of automotive brake abrasion dusts for the evaluation of antimony sources of airborne particulate matter. *Atmospheric Environment*. **41**(23), pp.4908-4919.
- Jiang, L., Jiang, Y.L., Yu, L., Su, N. and Ding, Y.D. 2012. Thermal analysis for brake disks of SiC/6061 Al alloy co-continuous composite for CRH3 during emergency braking considering airflow cooling. *Transactions of Nonferrous Metals Society of China*. **22**(11), pp.2783-2791.
- Kelly, F.J. and Fussell J.C. 2012. Size, source and chemical composition as determinants of toxicity attributable to ambient particulate matter. *Atmospheric Environment*. **60**, pp.504-526.
- Keronite. 2017. *What is plasma electrolytic oxidation?* [online]. [Accessed 6 October 2020]. Available from: <https://blog.keronite.com/what-is-plasma-electrolytic-oxidation-article>.
- Keronite. 2020. *Surface technology* [online]. [Accessed 6 October 2020]. Available from: <https://www.keronite.com/surface-technology/>.
- Kukutschová, J., Moravec, P., Tomášek, V., Matějka, V., Smolík, J., Schwarz, J., Seidlerová, J., Šafářová, K. and Filip, P. 2011. On airborne nano/micro-sized wear particles released from low-metallic automotive brakes. *Environmental Pollution*. **159**(4), pp.998-1006.
- Kulkarni, P., Baron, P.A. and Willeke, K. 2011. Introduction to aerosol characterization. In: Kulkarni, P., Baron, P.A. and Willeke, K. ed. *Aerosol measurement: principles, techniques, and applications*. 3rd ed. New Jersey: John Wiley & Sons, Inc.
- Kumar, P., Pirjola, L., Ketzel, M., and Harrison, R.M. 2013. Nanoparticle emissions from 11 non-vehicle exhaust sources - a review. *Atmospheric Environment*, **67**, pp.252–277.
- Kwak, J.-H., Kim, H., Lee, J. and Lee, S. 2013. Characterization of non-exhaust coarse and fine particles from on-road driving and laboratory measurements. *Science of The Total Environment*. **458-460**, pp.273-282.
- Lapinus. 2020. *Trends in automotive braking* [online]. [Accessed 19 April 2020]. The brake report. Available: <https://thebrakereport.com/trends-in-automotive-braking/>.
- Launder, B.E., Reece, G.J. and Rodi, W. 1975. Progress in the development of a Reynolds-stress turbulence closure. *Journal of Fluid Mechanics*. **68**(3), pp.537-566.
- Lazaridis, M. and Colbeck, I. 2014. Introduction. In: Lazaridis, M. and Colbeck, I. (eds.) *Aerosol science technology and applications*. 1st ed. West Sussex: John Wiley & Sons, Inc.

- Limpert, R. 1999. *Brake design and safety*. 2nd ed, Warrendale, Pa: Society of Automotive Engineers, Inc.
- Liu, J.L., Fan, Y.G., Yang, Z.S., Wang, Z.Y., and Guo, C. 2018. Iron and Alzheimer's disease: From pathogenesis to therapeutic implications. *Frontiers in neuroscience*. **12**, pp.1-14.
- Lü, H. and Yu, D. 2016. Optimization design of a disc brake system with hybrid uncertainties. *Advances in Engineering Software*. **98**, pp.112-122.
- Magari, S.R., Schwartz, J., Williams, P.L., Hauser, R., Smith, T.J. and Christiani, D.C. 2002. The association of particulate air metal concentrations with heart rate variability. *Environmental health perspectives*. **110**(9), pp.875-880.
- Malayoglu, U., Tekin, K.C., Malayoglu, U. & Shrestha, S. 2011. An investigation into the mechanical and tribological properties of plasma electrolytic oxidation and hard-anodized coatings on 6082 aluminum alloy. *Materials Science and Engineering: A*. **528**(24), pp.7451-7460.
- Manisalidis, I., Stavropoulou, E., Stavropoulos, A., and Bezirtzoglou, E. 2020. Environmental and health impacts of air pollution: A review. *Frontiers in public health*. **8**, pp.1-13.
- Marple, V.A. and Olson, B.A. 2011. Sampling and measurement using inertial, gravitational, centrifugal, and thermal techniques. In: Kulkarni, P., Baron, P.A. and Willeke, K. ed. *Aerosol measurement: principles, techniques, and applications*. 3rd ed. New Jersey: John Wiley & Sons, Inc.
- Mathissen, M., Grigoratos, T., Lahde, T. and Vogt, R. 2019. Brake wear particle emissions of a passenger car measured on a chassis dynamometer. *Atmosphere*. **10**(9), pp.1-15.
- Menter, F.R. 1994. Two-equation eddy-viscosity turbulence model for engineering applications. *American Institute of Aeronautics and Astronautics Journal*. **32**, pp.1598-1605.
- Mew, T.D., Kang, K.-J., Kienhöfer, F.W. and Kim, T. 2015. Transient thermal response of a highly porous ventilated brake disc. *Proceedings of the Institution of Mechanical Engineers, Part D: Journal of Automobile Engineering*. **229**(6), pp.674-683.
- Mosleh, M., Blau, P.J. and Dumitrescu, D. 2004. Characteristics and morphology of wear particles from laboratory testing of disk brake materials. *Wear*. **256**(11-12), pp.1128-1134.
- Nosko, O., Alemani, M. and Olofsson, U. 2015. Temperature effect on emission of airborne wear particles from car brakes. *Europe's braking conference and exhibition*. Dresden, Germany.
- Nutwell, B. and Ramsay, T. 2009. Modeling the cooling characteristics of a disk brake on an inertia dynamometer, using combined fluid flow and thermal simulation. *SAE Technical paper*, 2009-01-0861.
- Oh, J., Choi, S. and Kim, J. 2015. Numerical simulation of an internal flow field in a uniflow cyclone separator. *Powder Technology*. **274**, pp.135-145.

- Ostro, B., Feng, W.Y., Broadwin, R., Green, S. and Lipsett, M. 2007. The effects of components of fine particulate air pollution on mortality in California: results from CALFINE. *Environmental Health Perspectives*. **115**(1), pp.13-19.
- Palmer, E., Mishra, R. and Fieldhouse, J. 2009. An optimization study of a multiple-row pin-vented brake disc to promote brake cooling using computational fluid dynamics. *Proceedings of the Institution of Mechanical Engineers, Part D: Journal of Automobile Engineering*. **223**(7), pp.865-875.
- Peikertova, P. and Filip, P. 2016. Influence of the automotive brake wear debris on the environment - a review of recent research. *SAE International Journal of Materials and Manufacturing*. **9**(1), pp.133-146.
- Perricone, G., Wahlström, J. and Olofsson, U. 2016. Towards a test stand for standardized measurements of the brake emissions. *Proceedings of the Institution of Mechanical Engineers, Part D: Journal of Automobile Engineering*. **230**(11), pp.1521-1528.
- Pevec, M., Potrc, I., Bombek, G. and Vranesevic, D. 2012. Prediction of the cooling factors of a vehicle brake disc and its influence on the results of a thermal numerical simulation. *International Journal of Automotive Technology*. **13**, pp.725-733.
- Pope III, C.A., Burnett, R.T., Thun, M.J., Calle, E.E., Krewski, D., Ito, K. and Thurston, G.D. 2002. Lung cancer, cardiopulmonary mortality, and long-term exposure to fine particulate air pollution. *The Journal of the American Medical Association*. **287**(9), pp.1132-1141.
- Pope III, C.A. and Dockery, D.W. 2006. Health effects of fine particulate air pollution: lines that connect. *Journal of the Air & Waste Management Association*. **56**(6), pp.709-742.
- Pope III, C.A., Rodermund, D.L. and Gee, M.M. 2007. Mortality effects of a copper smelter strike and reduced ambient sulfate particulate matter air pollution. *Environmental Health Perspectives*. **115**(5), pp.679-683.
- Post, W. 2014. Car braking systems. In: REIF, K. ed. *Fundamentals of automotive and engine technology*. 1st ed. Wiesbaden: Springer Vieweg.
- Qian, C. 2002. Aerodynamic shape optimization using CFD parametric model with brake cooling application. *SAE Technical Paper*, 2002-01-0599.
- Samet, J.M., Dominici, F., Curriero, F.C., Coursac, I. and Zeger, S.L. 2000. Fine particulate air pollution and mortality in 20 U.S. cities, 1987–1994. *New England Journal of Medicine*. **343**, pp.1742-1749.
- Sanders, P.G., Xu, N., Dalka, T.M. and Maricq, M.M. 2003. Airborne brake wear debris: size distributions, composition, and a comparison of dynamometer and vehicle tests. *Environmental Science & Technology*. **37**(18), pp.4060-4069.
- Shrestha, S., Shashkov, P. and Dunn, B.D. 2006. Microstructural and thermo-optical properties of black Keronite PEO coating on aluminium alloy

- AA7075 for spacecraft materials. *10th Symposium on Materials in a Space Environment*. Colliour, France.
- Shrestha, S. and Dunn, B.D. 2007. Advanced plasma electrolytic oxidation treatment for protection of light weight materials and structures in a space environment. *Advanced Surface Treatment*. pp.40-44.
- Sisson, A.E. 1978. Thermal analysis of vented brake rotors. *SAE Technical Papers 780352*, pp.1685-1694.
- Spalart, P.R. and Allmaras, S.A. 1992. A one-equation turbulence model for aerodynamic flows. *American Institute of Aeronautics and Astronautics Journal*, Paper No. 92-0439.
- Talib, R.J., Aznifa, M.Z., Arif, P., Ramlan, K. and Eliasidi, A.O. 2018. Effect of carbon in brake friction materials on friction characteristics. *Journal of Engineering Science*. **14**, pp.47-59.
- The Brake Report. 2021. *Brake wear enviro impact; trends to combat them (Part One)* [online]. [Accessed 8 February 2021]. Available from: <https://thebrakereport.com/brake-wear-enviro-impact-trends-to-combat-them/>.
- Thornton, R., Slatter, T., Jones, A.H. and Lewis, R. 2011. The effects of cryogenic processing on the wear resistance of grey cast iron brake discs. *Wear*. **271**(9-10), pp.2386-2395.
- Tsai, D.S. and Chou, C.C. 2018. Review of the soft sparking issues in plasma electrolytic oxidation. *Metals*. **8**(2), pp.1-22.
- Tu, J., Yeoh, G.H. and Liu, C. 2012. *Computational fluid dynamics: a practice approach*. 2nd edition, Oxford, United kingdom: Butterworth-Heinemann.
- USEPA. 2018. *Particulate matter (PM) basics* [Online]. [Accessed 28 December 2018]. Available from: <<https://www.epa.gov/pm-pollution/particulate-matter-pm-basics#PM>>.
- USEPA. 2020. *Basic information about visibility* [Online]. [Accessed 20 May 2020]. Available from: <https://www.epa.gov/visibility/basic-information-about-visibility>.
- Venkatesh S. and Murugapoopathiraja K. 2019. Scoping review of brake friction material for automotive. *Materials Today: Proceedings*. **16**, pp.927-933.
- Verma, P.C., Alemani, M., Gialanella, S., Lutterotti, L., Olofsson, U. and Straffelini, G. 2016. Wear debris from brake system materials: a multi-analytical characterization approach. *Tribology International*. **94**, pp.249-259.
- Vernon-Parry, K.D. 2000. Scanning electron microscopy: an introduction. *III-Vs Review*. **13**(4), pp.40-44.
- Versteeg, H.K. and Malalasekera, W. 2007. *An Introduction to Computational Fluid Dynamics: the finite volume method*. 2nd ed. Harlow, England: Pearson Education Ltd.
- Wahid, S.M.S. 2018. Automotive brake wear: a review. *Environmental Science and Pollution Research*. **25**, pp.174-180.

- Wahlström, J. 2009. *Towards a simulation methodology for prediction of airborne wear particles from disc brakes: licentiate thesis*. KTH Royal Institute of Technology.
- Wahlström, J., Lyu, Y., Matjeka, V. and Söderberg, A. 2017. A pin-on-disc tribometer study of disc brake contact pairs with respect to wear and airborne particle emissions. *Wear*. **384-385**, pp.124-130.
- Wahlström, J., Olander, L. and Olofsson, U. 2010. Size, shape, and elemental composition of airborne wear particles from disc brake materials. *Tribology Letters*. **38**, pp.15-24.
- Wahlström, J. and Olofsson, U. 2015. A field study of airborne particle emissions from automotive disc brakes. *Proceedings of the Institution of Mechanical Engineers, Part D: Journal of Automobile Engineering*, **229**(6), pp.747-757.
- Watremez, M., Bricout, J.P., Marguet, B. and Oudin, J. 1996. Friction, temperature, and wear analysis for ceramic coated brake disks. *Journal of Tribology*. **118**(3), pp.457-465.
- Welker, R.W. 2012. Chapter 1 - Basics and sampling of particles for size analysis and identification. In: Kohli, R. and Mittal, K.L. ed. *Developments in surface contamination and cleaning*. Oxford: William Andrew Publishing.
- WHO 2006. Air quality guidelines for particulate matter, ozone, nitrogen dioxide and sulphur dioxide. *Global Update 2005, Summary of Risk Assessment*. Geneva, The Swiss: World Health Organization.
- Wilcox, D.C. 1998. *Turbulence modeling for CFD*. 2nd ed. DCW Industries, Inc., 5354 Palm Drive, La Canada, California, ISBN 0963605100.
- Wilcox, J.D. 1956. Isokinetic flow and sampling. *Journal of the Air Pollution Control Association*. **5**(4), pp.226-245.
- Xiao, X., Yin, Y., Bao, J., Lu, L. and Feng, X. 2016. Review on the friction and wear of brake materials. *Advances in Mechanical Engineering*. **8**(5), pp.1-10.
- Yan, H.B., Feng, S.S., Yang, X.H. and Lu, T.J. 2015a. Role of cross-drilled holes in enhanced cooling of ventilated brake discs. *Applied Thermal Engineering*. **91**, pp.318-333.
- Yan, H.B., Zhang, Q.C. and Lu, T.J. 2015b. An X-type lattice cored ventilated brake disc with enhanced cooling performance. *International Journal of Heat and Mass Transfer*. **80**, pp.458-468.
- Yan, H.B., Zhang, Q.C. & Lu, T.J. 2016. Heat transfer enhancement by X-type lattice in ventilated brake disc. *International Journal of Thermal Sciences*. **107**, pp.39-55.

Appendix A

Readings of air velocity at the velocity test points.

Width	LOCATION A		LOCATION B	
	Velocity range	Average velocity	Velocity range	Average velocity
0	0.00	0.00	0.00	0.00
16	11.2 - 11.4	11.30	12.0 - 12.1	12.05
26	11.1 - 11.2	11.15	11.7 - 11.9	11.80
36	10.9 - 11.0	10.95	11.7 - 11.8	11.75
46	10.8 - 10.9	10.85	11.1 - 11.2	11.15
56	10.7 - 10.8	10.75	11.4 - 11.6	11.50
66	10.8 - 10.9	10.85	10.9 - 11.0	10.95
76	10.6 - 10.8	10.70	10.9 - 11.0	10.95
86	10.4 - 10.6	10.50	10.6 - 10.7	10.65
96	10.2 - 10.4	10.30	10.4 - 10.5	10.45
106	10.2 - 10.5	10.35	10.1 - 10.2	10.15
112.5	9.9 - 10.0	9.95	9.9 - 10.1	10.00
119	9.8 - 10.2	10.00	9.6 - 9.7	9.65
129	9.9 - 10.2	10.05	9.0 - 9.2	9.10
139	9.7 - 10.0	9.85	8.8 - 9.0	8.90
149	9.9 - 10.5	10.20	8.6 - 8.9	8.75
159	10.0 - 10.3	10.15	8.2 - 8.6	8.40
169	10.1 - 10.2	10.15	8.1 - 8.5	8.35
179	10.1 - 10.3	10.20	8.4 - 8.9	8.65
189	10.4 - 10.5	10.45	8.8 - 9.2	9.00
199	10.6 - 10.7	10.65	9.0 - 9.3	9.15
209	10.5 - 10.6	10.55	8.9 - 9.5	9.20
213	10.6 - 10.7	10.65	8.8 - 9.2	9.00
217	10.9 - 11.1	11.00	8.8 - 9.3	9.05
221	10.9 - 11.1	11.00	8.5 - 9.1	8.80
225	0.00	0.00	0.00	0.00

Appendix B

List of publications

Some parts of the current research work have been published or accepted as follows:

Paper	Status
A. B. Sanuddin, S. Kosarieh, C. A. Gilkeson, P. C. Brooks and D. C. Barton, "Design and assessment of a test rig for airborne brake wear debris measurements", Proceedings of the Eurobrake 2019 Conference, Paper EB2019-MDS-005. EuroBrake 2019, Dresden, Germany, 2019.	Published
A. B. Sanuddin, S. Kosarieh, C. A. Gilkeson, P. C. Brooks and D. C. Barton, "Airflow Simulation and Measurement of Brake Wear Particle Emissions with a Novel Test Rig", Journal of Engineering, 2020.	Published
A. B. Sanuddin, S. Kosarieh, C. A. Gilkeson, P. C. Brooks, D. C. Barton and S. Shrestha, "Preliminary comparisons of particulate emissions generated from different disc brake rotor". The abstract has been accepted for inclusion at Eurobrake 2021 at Mainz, Germany in May 2021	Accepted (Abstract)